Supporting Information For

Synthesis, Characterization and Coordination Chemistry of Pincer Ligands Based on (Benzannulated) Pyridines: An Investigation into Their Electronic Structure and Applications

by

Jason Braun

A Thesis submitted to the Faculty of Graduate Studies of

The University of Manitoba

in partial fulfilment of the requirements of the degree of

Doctor of Philosophy

Department of Chemistry

University of Manitoba

Winnipeg, MB, Canada

TABLE OF CONTENTS

Chapter 2

General methodology: charge/discharge measurements

Cycling measurements were carried out inside an N_2-filled glovebox. Potential was applied by a potentiostat and recorded over time using a CHI760C electrochemical workstation. In order to perform battery tests, both the electrolyte and active species solutions were placed in a custom-built air-tight H-cell made up of two chambers separated by a fine porosity glass frit. In one of the chambers, a solution made up of the active species (2 mM) and the electrolyte nBu$_4$PF$_6$ (0.4 M) was stored along with the working and reference electrodes inserted in two outputs. In the other chamber, the 0.4M nBu$_4$PF$_6$ solution was placed as well as the counter electrode. Reticulated vitreous carbon (RVC) counter and working electrodes were used, with a non-aqueous Ag/Ag$^+$ quasi-reference electrode. Potential cutoffs, voltages at which the reversible couples start and finish, were set according to CV results. Cycling experiments were executed at a variety of anodic and cathodic currents (0.5, 1.1, 1.5 and 2.2 mA) with different (dis)charge times (3600 or 7200 s), corresponding to 0.5, 1, and 2 C charging rates assuming a 2e$^-$ reduction process.

Figure S1. H-cell[1] used for cycling measurements.

Cycling Measurements / Coulombic Efficiency / Capacitance Figures
Cycling of 1 at 2.2 mA, (dis)charge time = 1 h, 2.0 C charging rate, potential cut-offs: 1 V to -2.6 V, cathodic charging

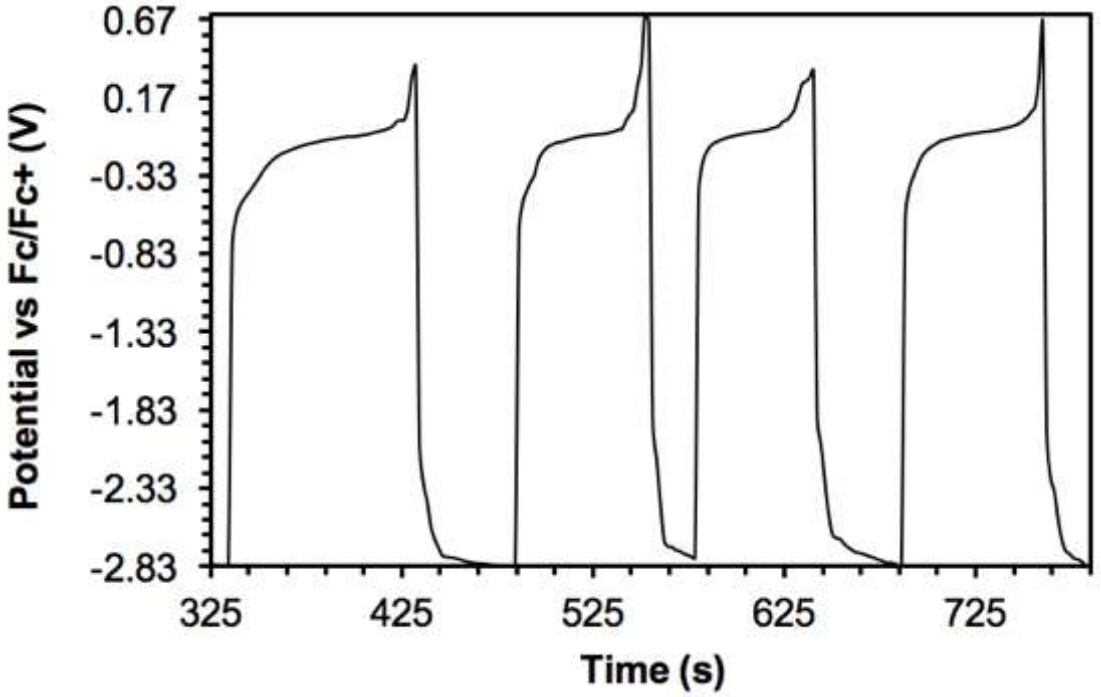

Figure S2. Potential curves for **2a** (1 V to -2.6 V, cathodic charging at 2 C)

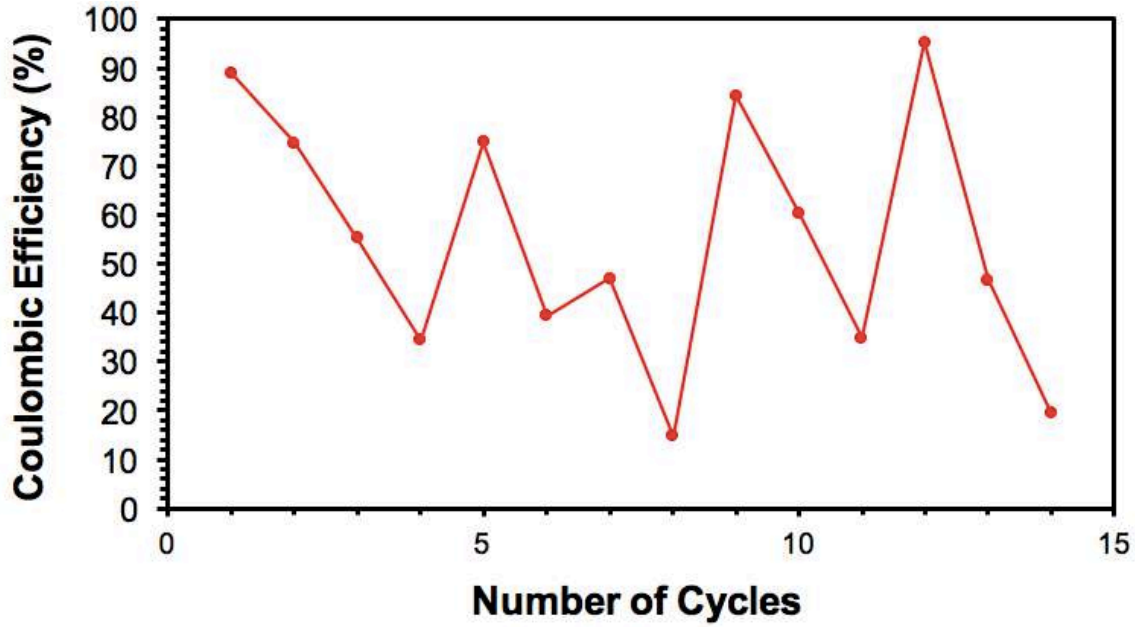

Figure S3. Coulombic Efficiency for **2a** (1 V to -2.6 V, cathodic charging at 2 C)

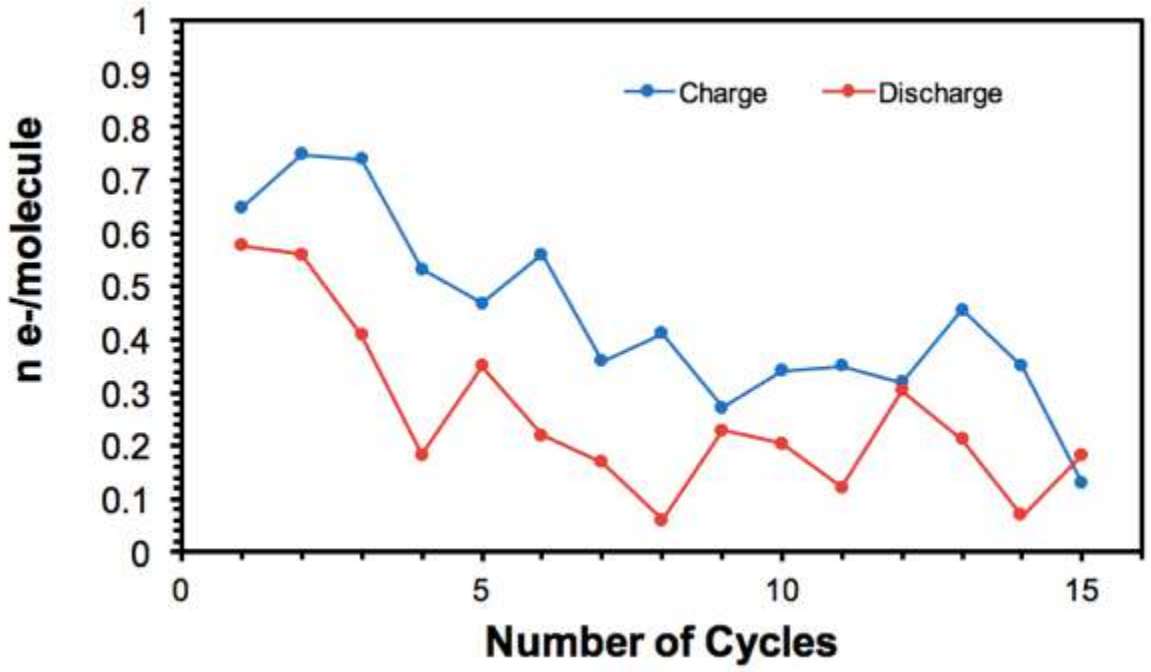

Figure S4. Capacitance for **2a** (1 V to -2.6 V, cathodic charging at 2 C)

Allowing the cell to reach -2.6 V led to irreversible reduction of the MCC, consistent with the cyclic voltammogram shown in Figure S5. The absence of significant plateaus in Figure S2 suggests no redox processes were accessed in the experiment. Additionally, the time span to cover each cycle was roughly 150 seconds, which despite the accelerated C-rate, is fast, having an unsatisfactory impact on the capacitance, as confirmed by the low number of electrons per molecule on Figure S6.

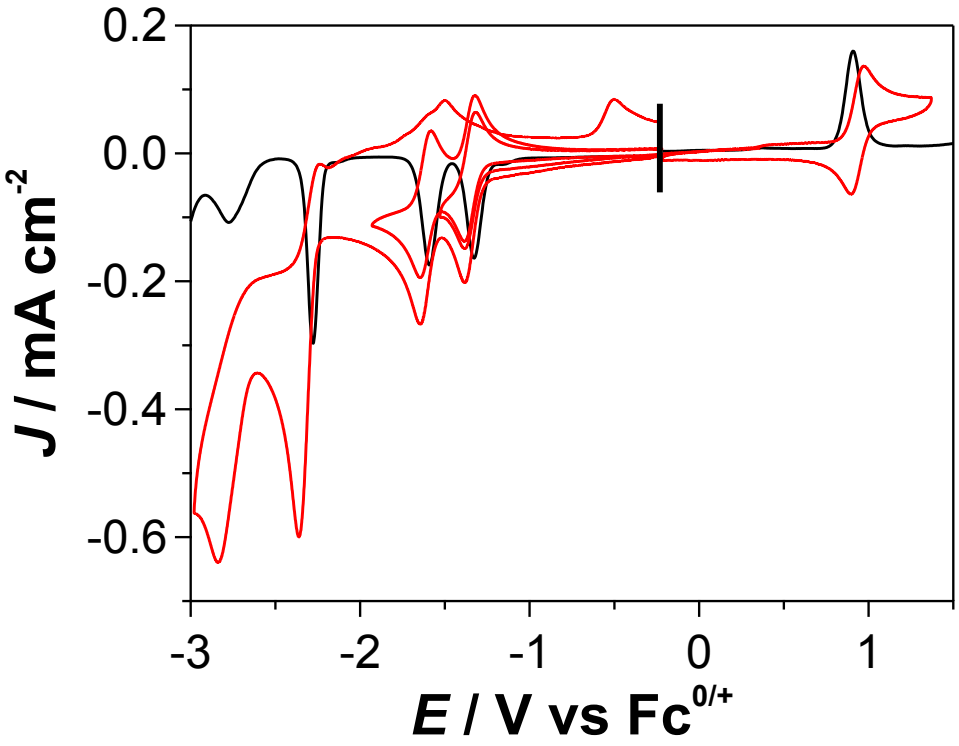

Figure S5. Wide CV of **2a** confirming irreversible redox processes below -2.2 V

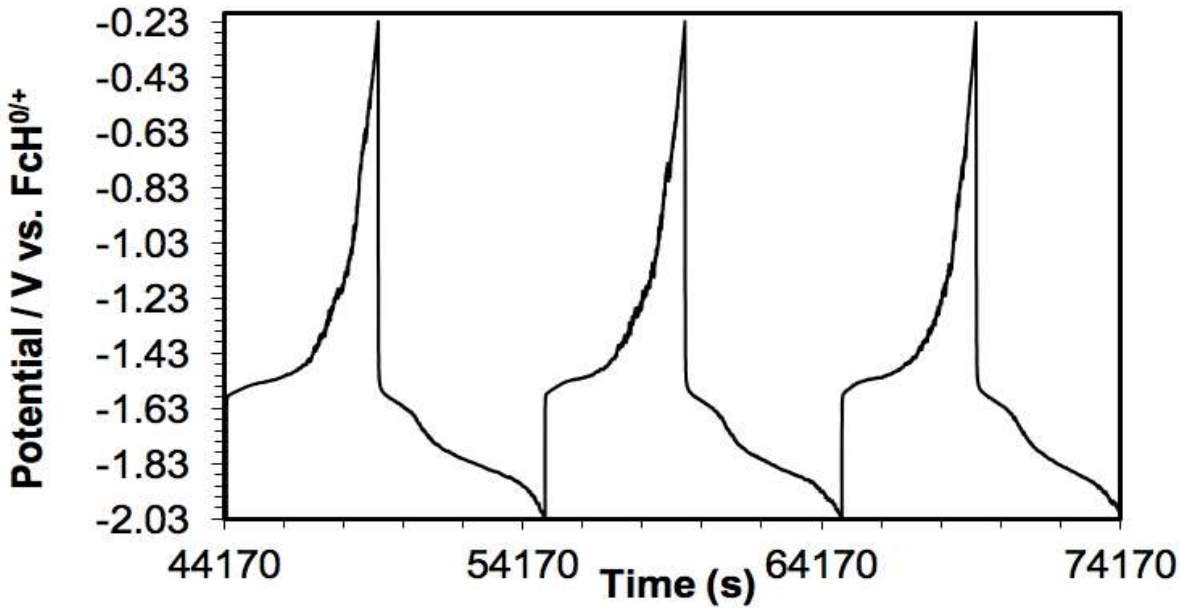

Figure S6. Potential curves for **2a** (-0.2 to -2 V, cathodic charging at 0.5 C)

Cycling of 2 at 0.5 mA, (dis)charge time = 2h, rate of 0.5 C; potential cutoffs: 0.23 V to -2.03 V, cathodic charging

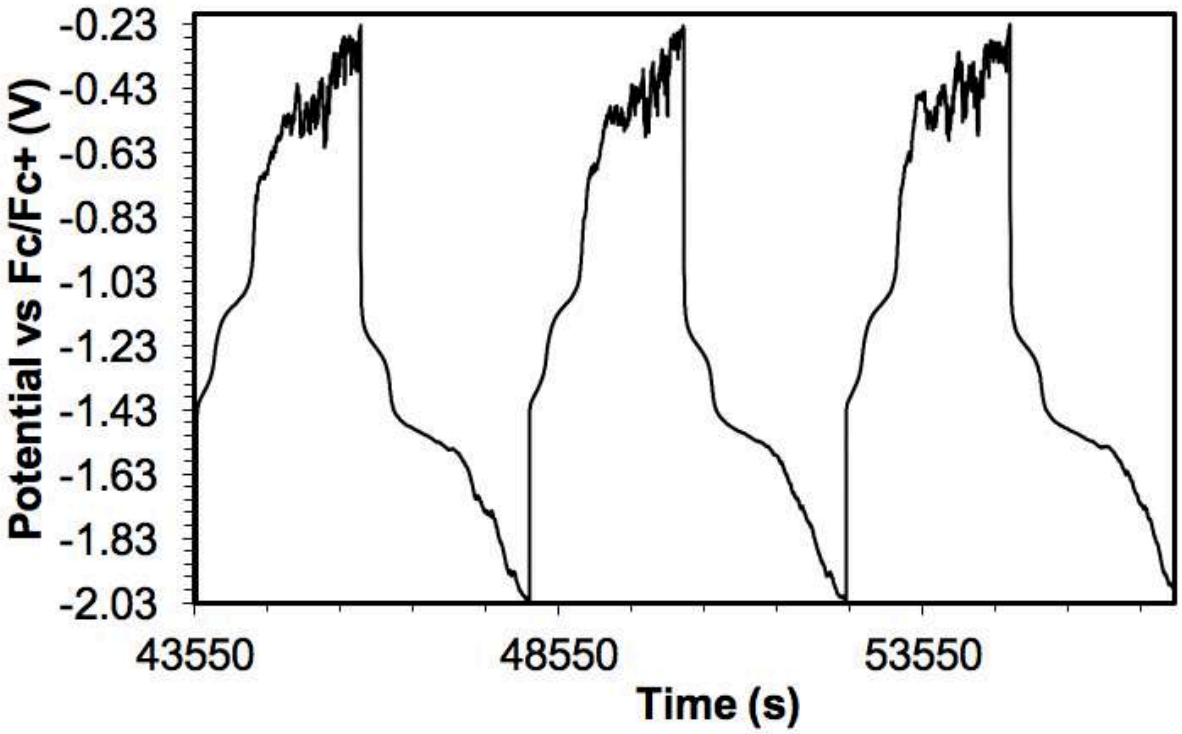

Figure S7. Potential curves for **2b** (-0.2 V to -1.8 V, cathodic charging at 0.5 C)

The potential curves shown in Figure S7 clearly exhibits two plateaus on both charging and discharging segments, indicating that the two redox couples are being accessed. An increase in capacitance is observed when compared to a charging rate of 0.5 C.

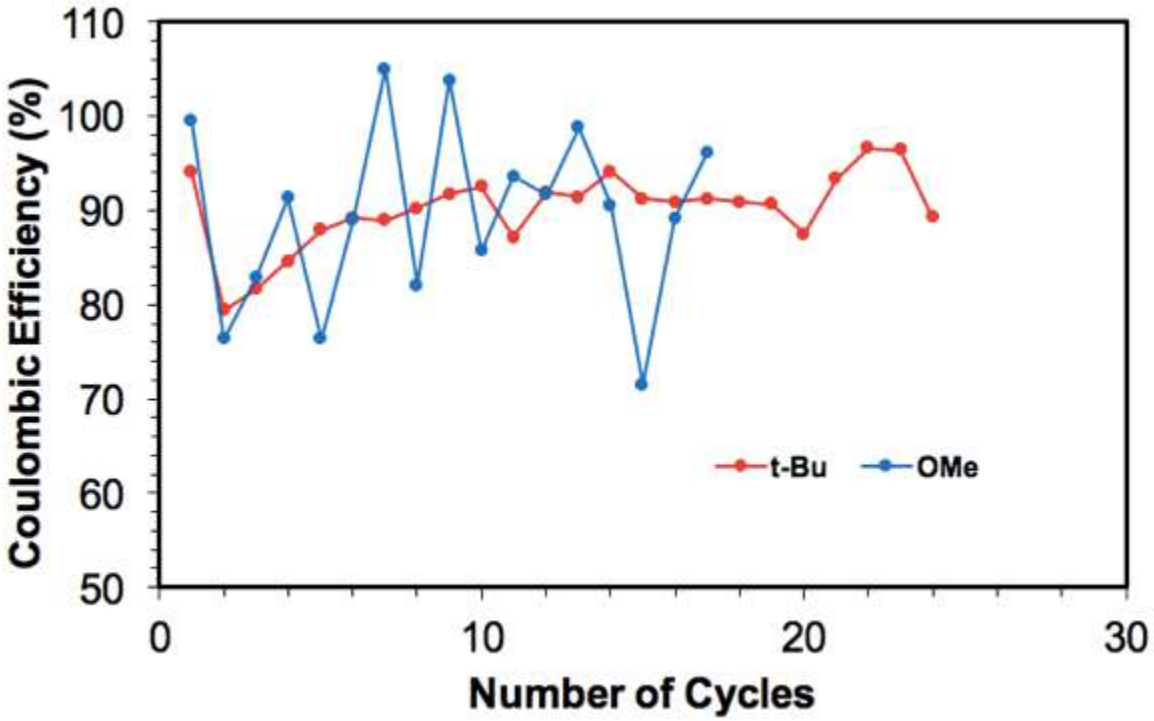

Figure S8. Coulombic efficiency at charging rate of 0.5 C

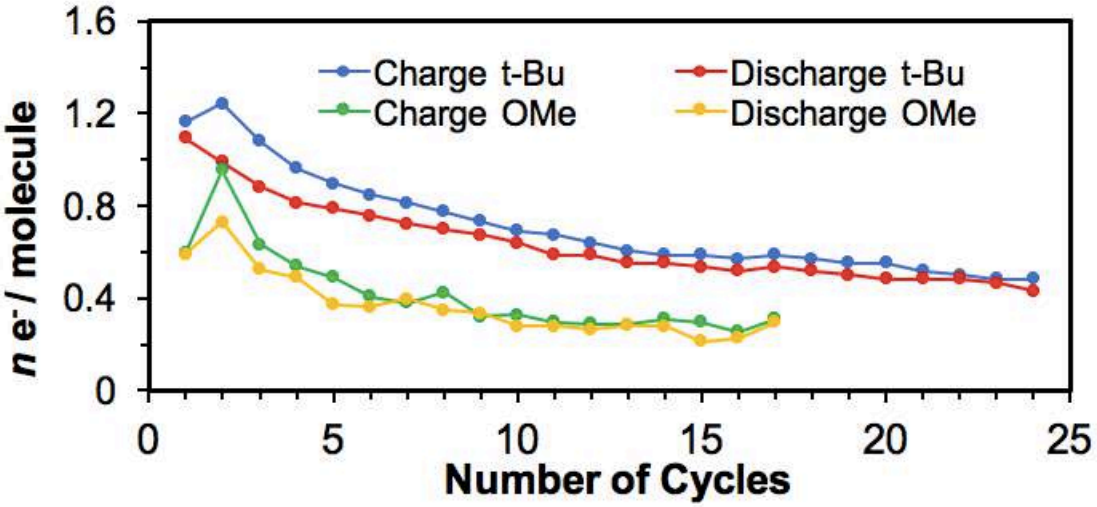

Figure S9. Capacitance at charging rate of 0.5 C

Solution Characterization of 1

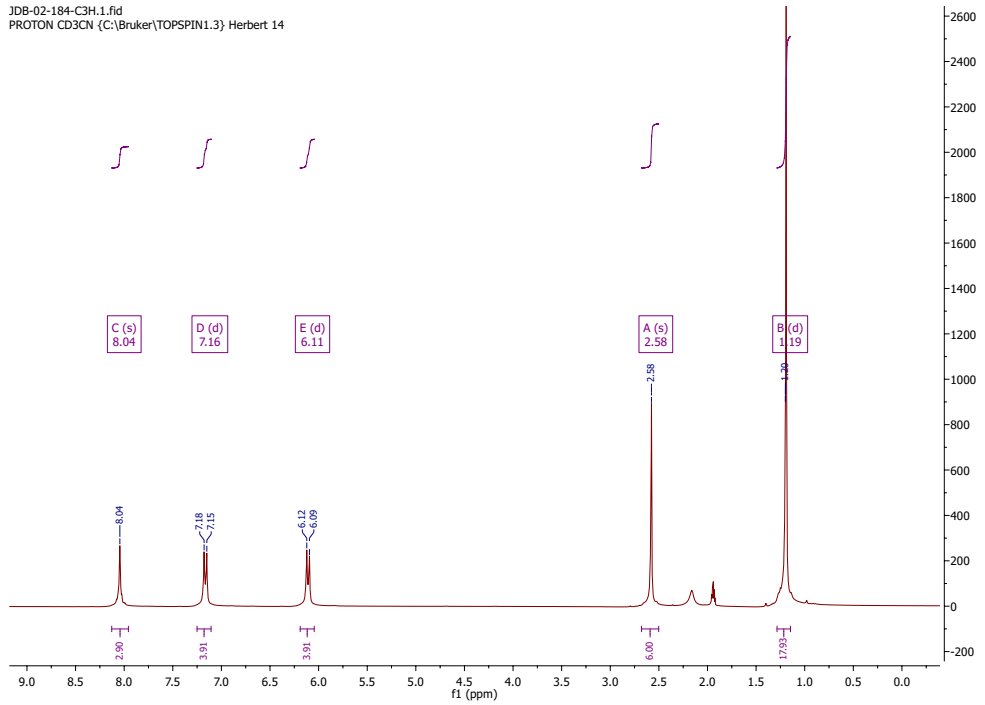

Figure S10. ^{1}H NMR (300 MHz, CD_3CN) of **2a** at 25 °C

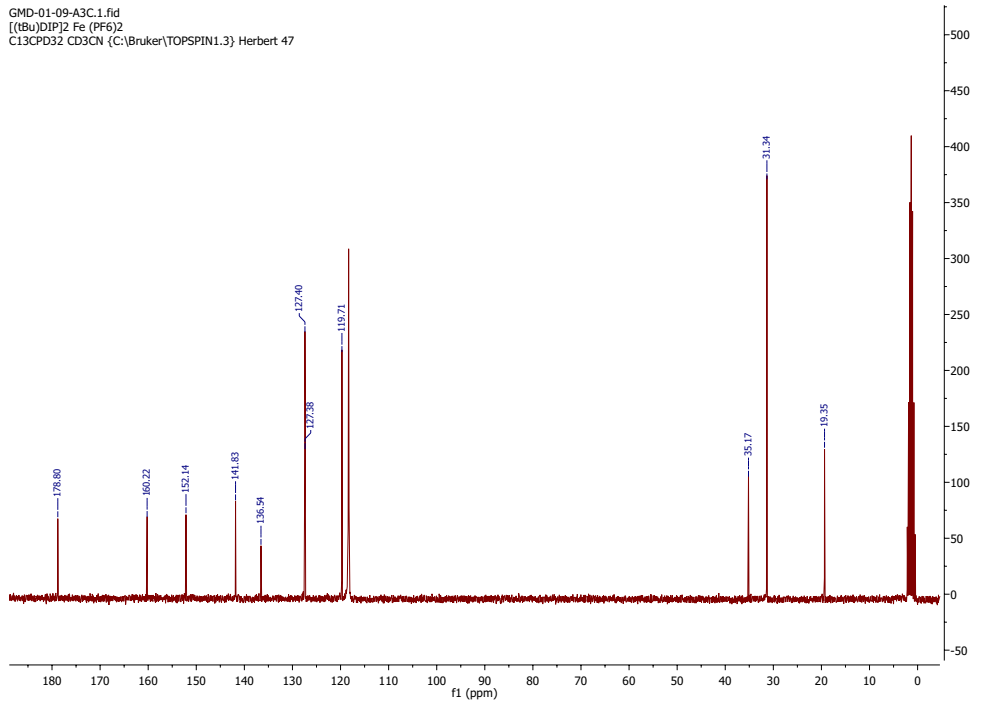

Figure S11. ^{13}C{^{1}H} NMR (75 MHz, CD_3CN) of **2a** at 25 °C

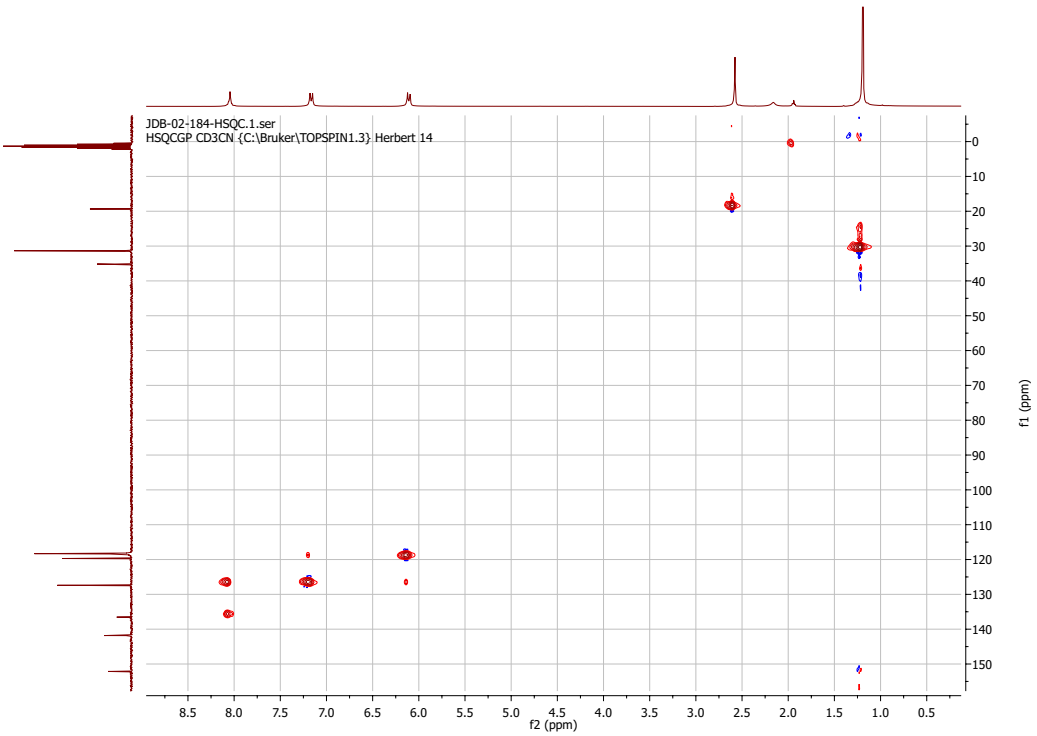

Figure S12. HSQC NMR (300, 75 MHz, CD_3CN) of **2a** at 25 °C

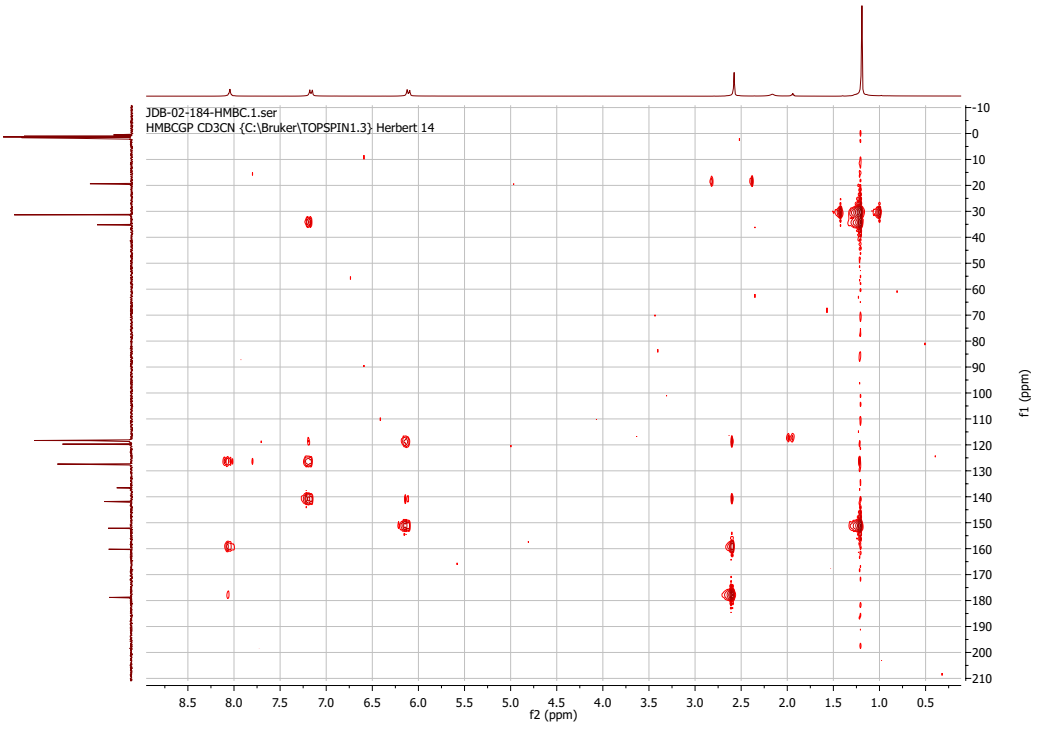

Figure S13. HMBC NMR (300, 75 MHz, CD_3CN) of **2a** at 25 °C

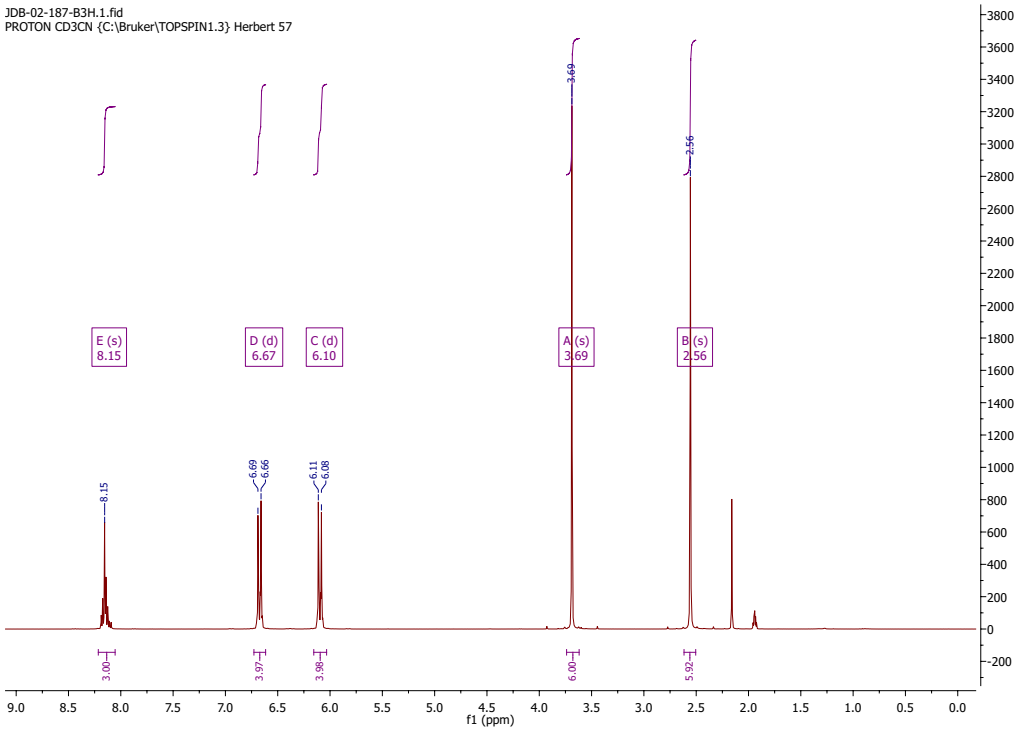

Figure S14. ^{1}H NMR (300 MHz, CD_3CN) of **2a** at 25 °C

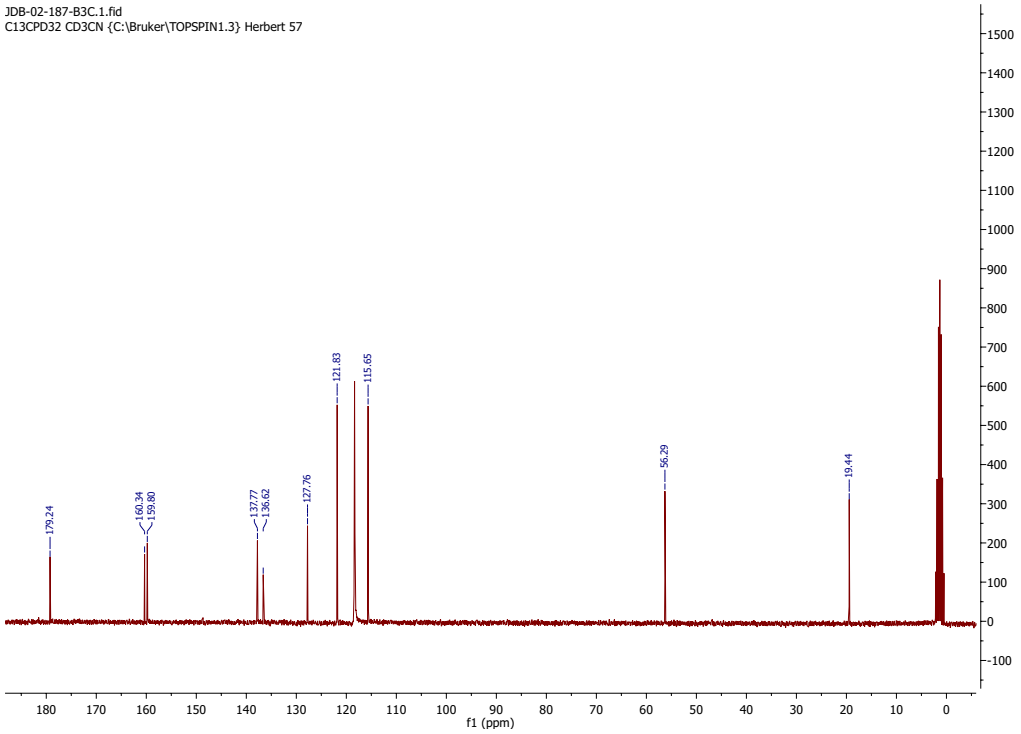

Figure S15. $^{13}C\{^{1}H\}$ NMR (75 MHz, CD_3CN) of **2a** at 25 °C

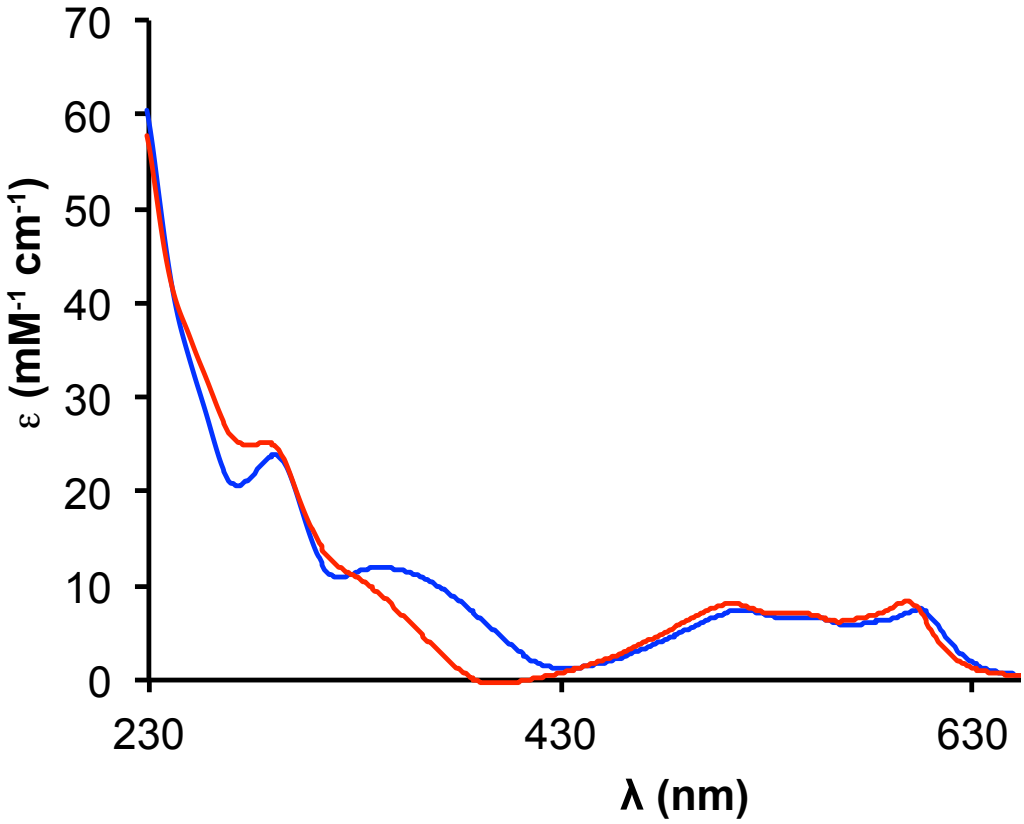

Figure S16. UV-visible spectrum of **2a** (red) and **2b** (blue) in acetonitrile solution using an Agilent Technologies Cary 5000 Series spectrophotometer (range: 230 – 1600 nm)

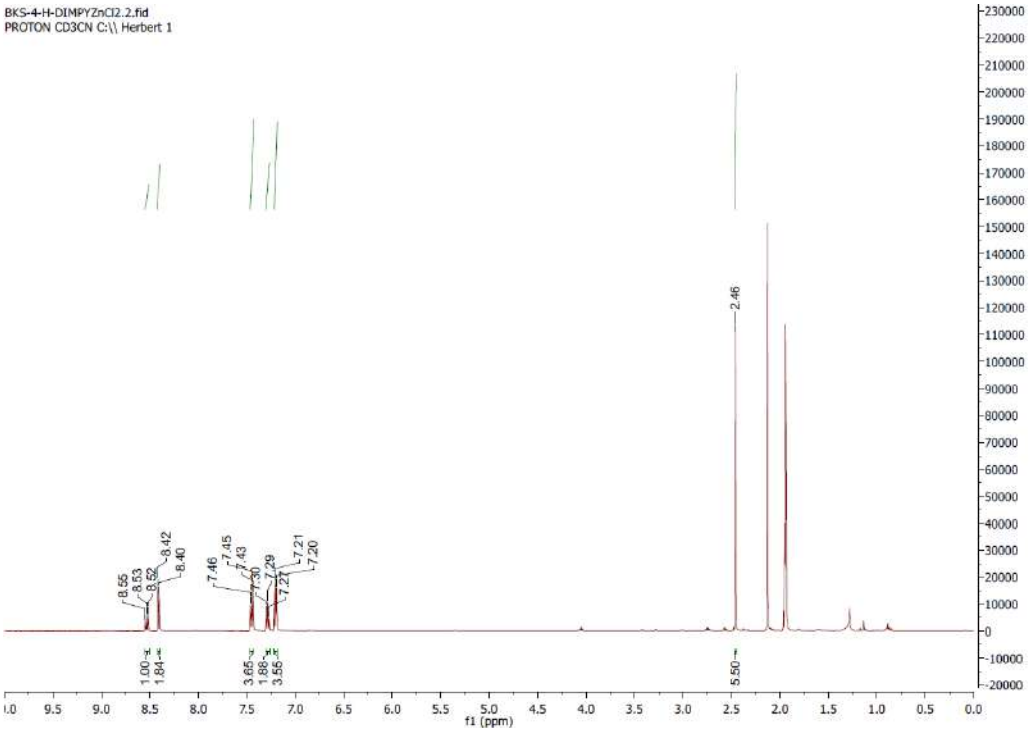

Figure S17. ^{1}H NMR (CD_3CN, 500 MHz, 25°C, ppm) of **3c**.

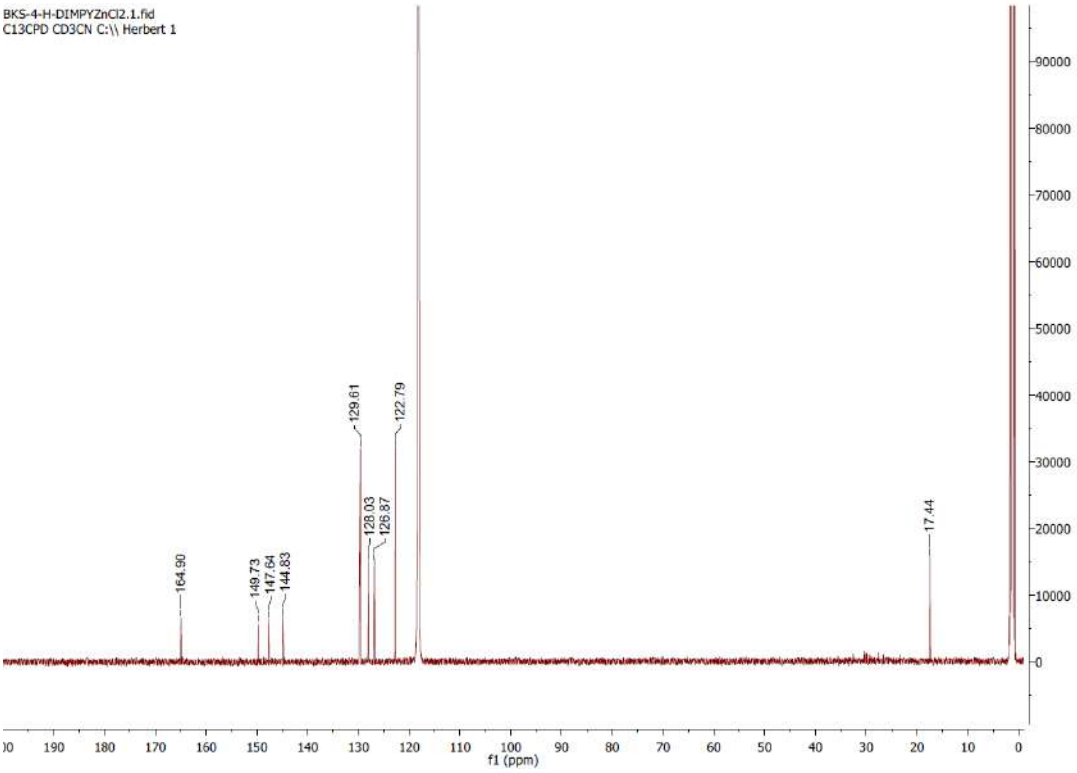

Figure S18. $^{13}C\{^{1}H\}$ NMR (CD_3CN, 125 MHz, 25°C, ppm) of **3c**.

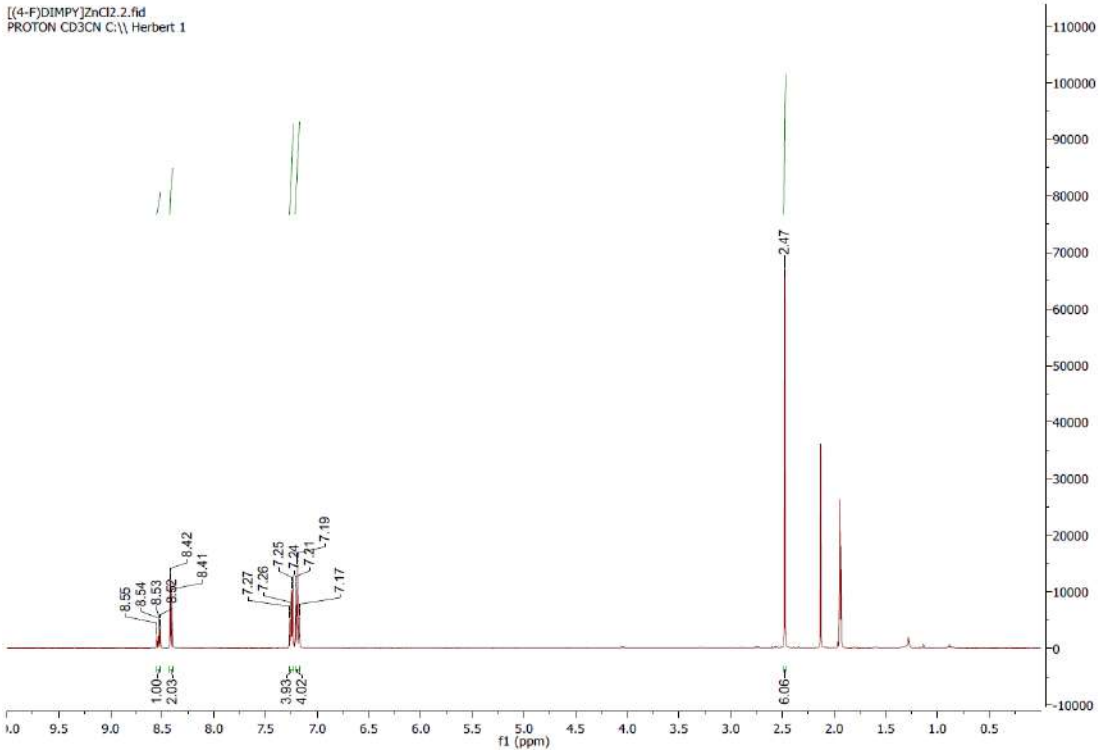

Figure S19. ^{1}H NMR (CD_3CN, 500 MHz, 25°C, ppm) of **3d**.

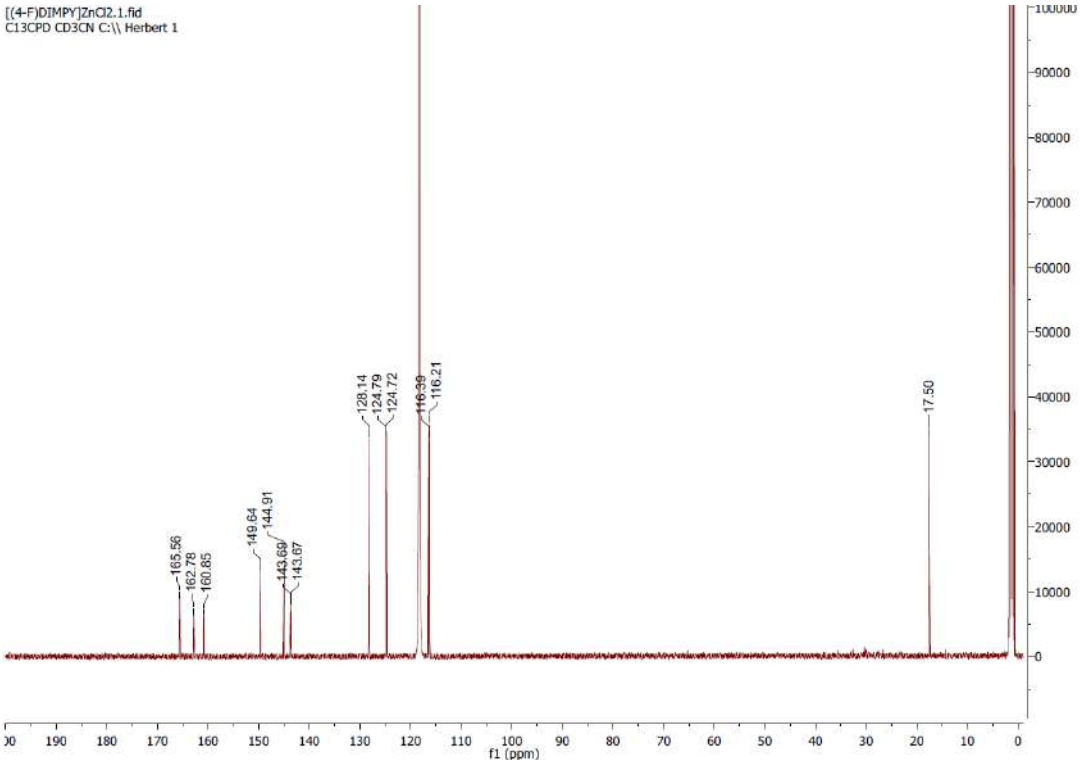

Figure S20. $^{13}C\{^{1}H\}$ NMR (CD_3CN, 125 MHz, 25°C, ppm) of **3d**.

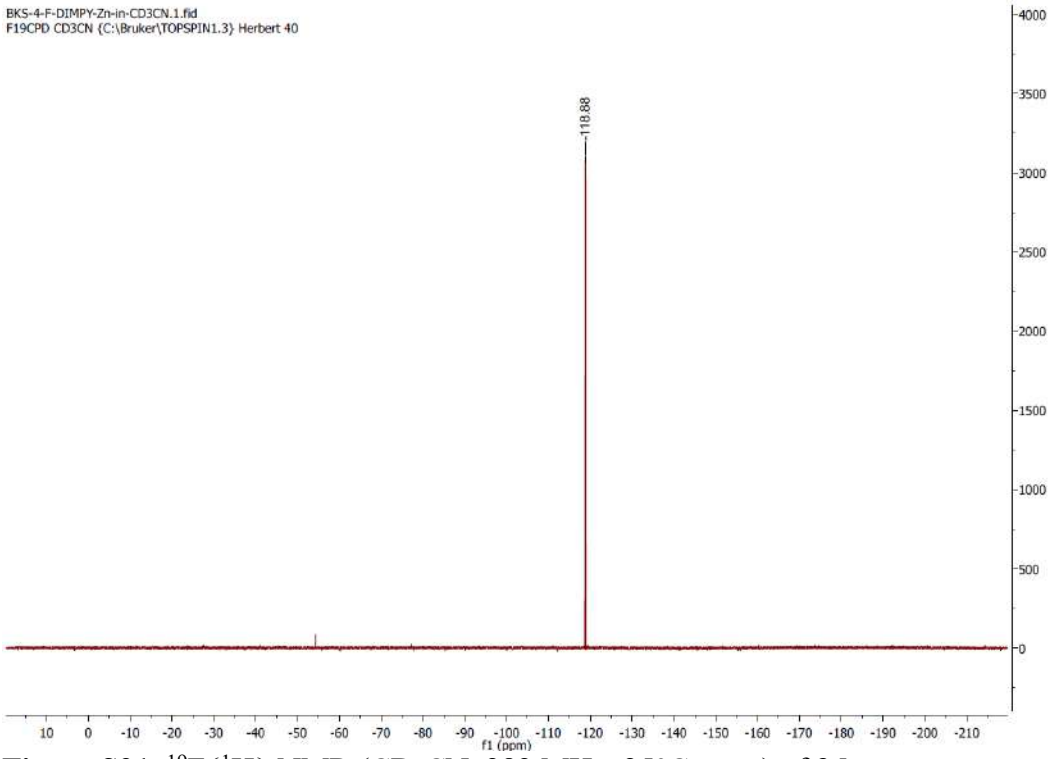

Figure S21. $^{19}F\{^{1}H\}$ NMR (CD_3CN, 282 MHz, 25°C, ppm) of **3d**.

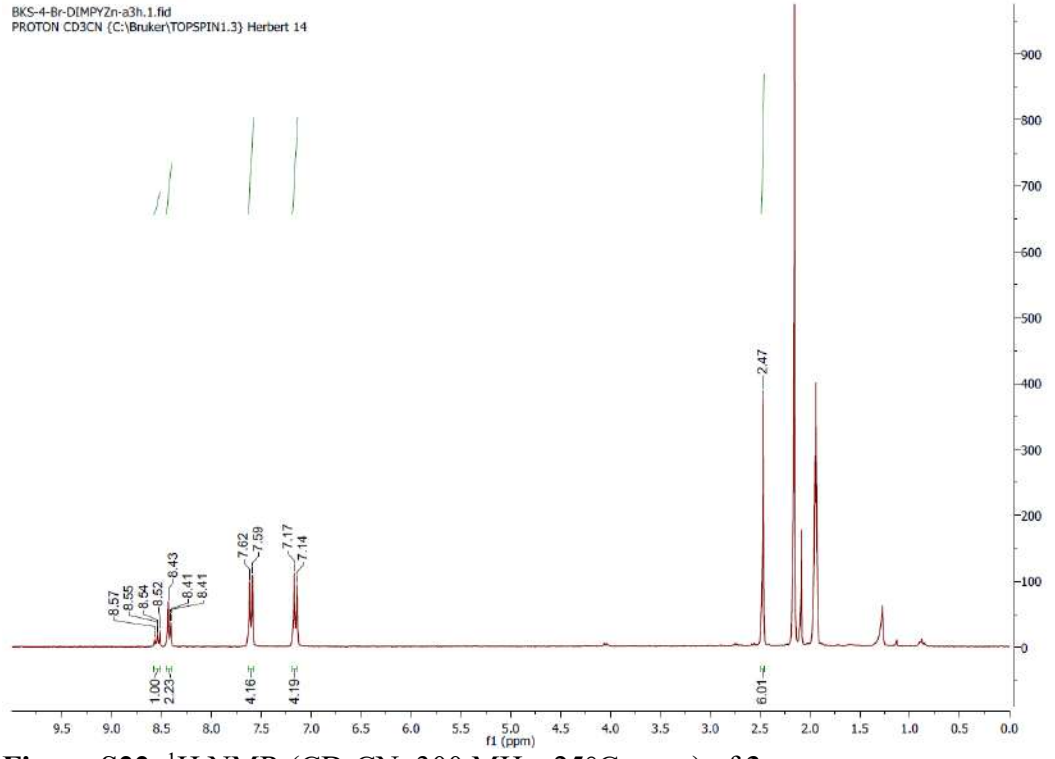

Figure S22. ^{1}H NMR (CD_3CN, 300 MHz, 25°C, ppm) of **3e**.

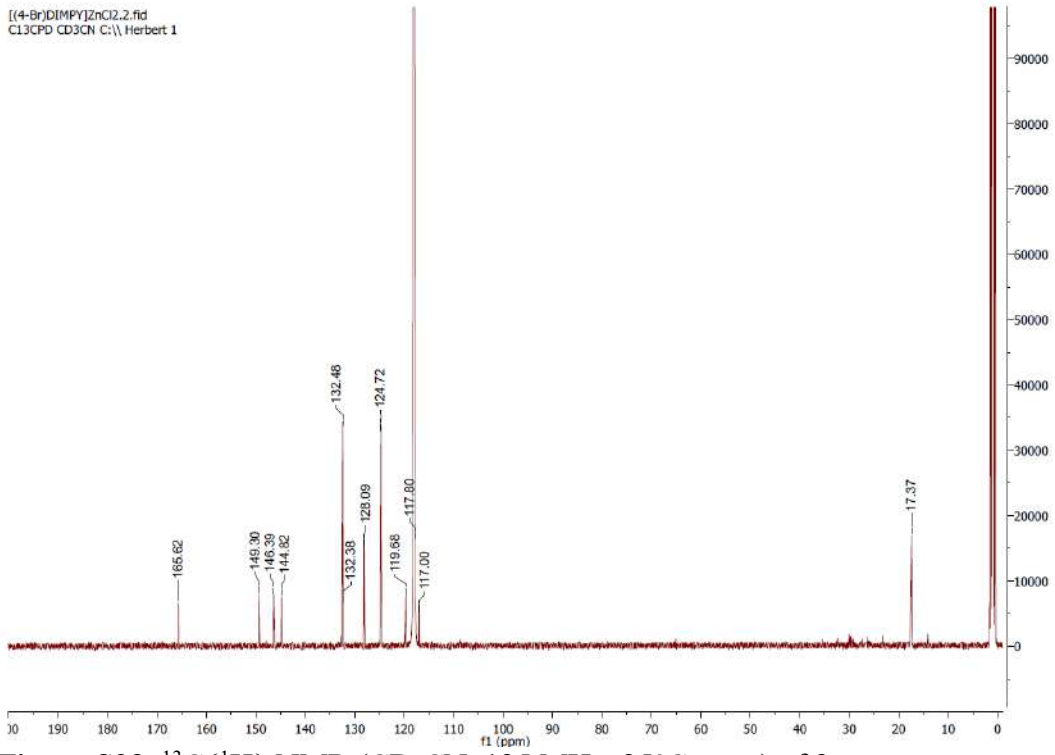

Figure S23. $^{13}C\{^{1}H\}$ NMR (CD_3CN, 125 MHz, 25°C, ppm) of **3e**.

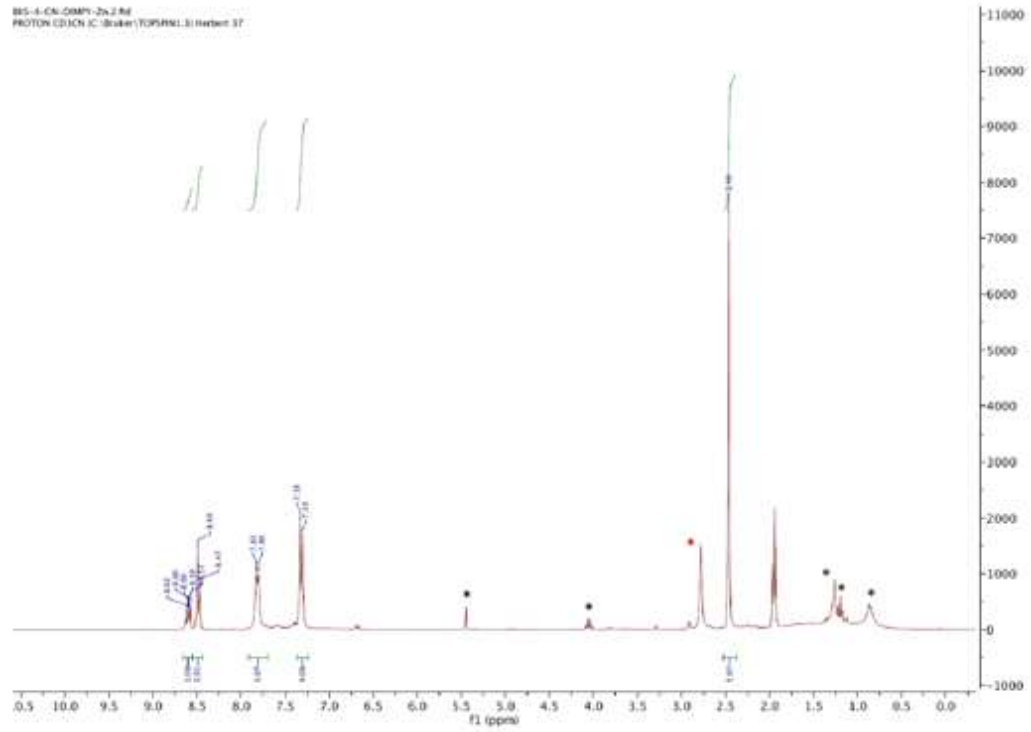

Figure S24. ^{1}H NMR (CD_3CN, 300 MHz, 25°C, ppm) of **3f**. Asterisks (black) represent solvent impurities (n-pentane, ethyl acetate, dichloromethane) and an unknown impurity (red).

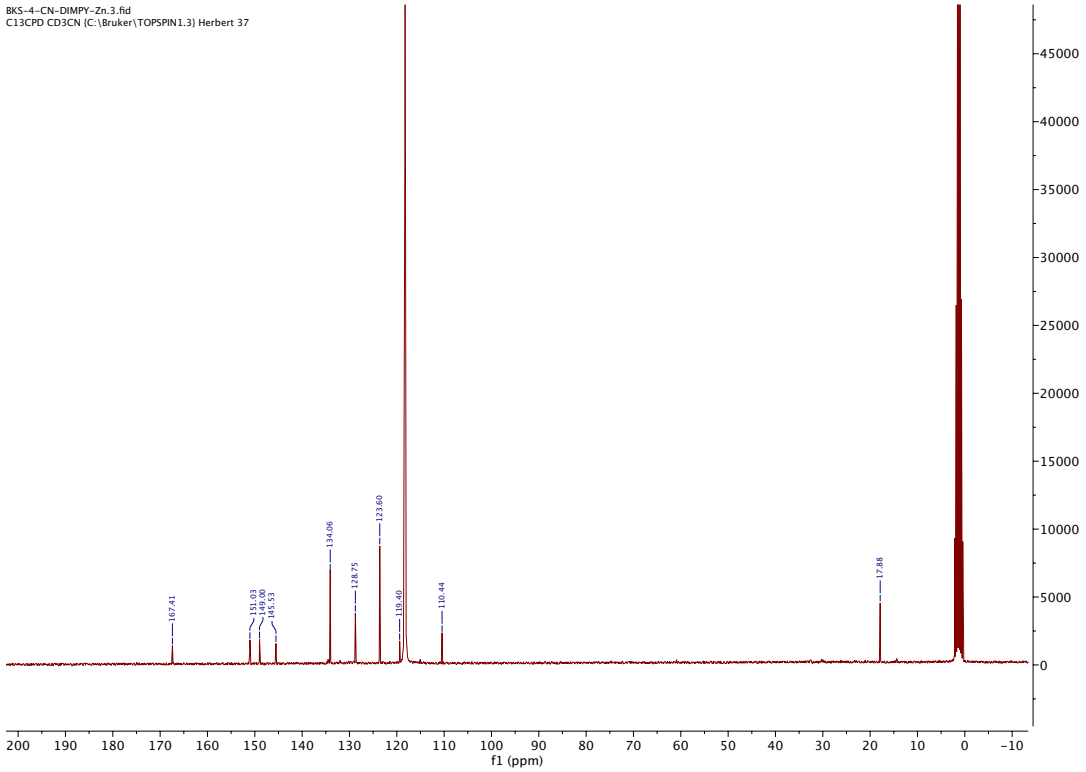

Figure S25. $^{13}C\{^{1}H\}$ NMR (CD_3CN, 125 MHz, 25°C, ppm) of **3f**.

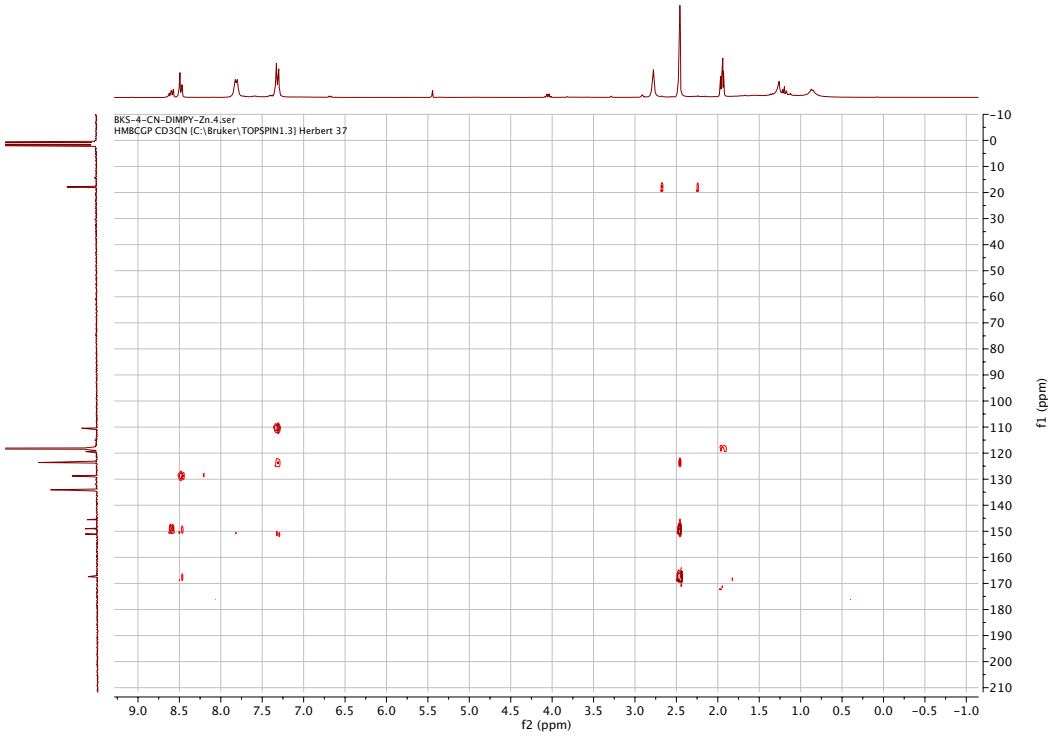

Figure S26. HMBC NMR (CD_3CN, 300/75 MHz, 25°C, ppm) of **3f**.

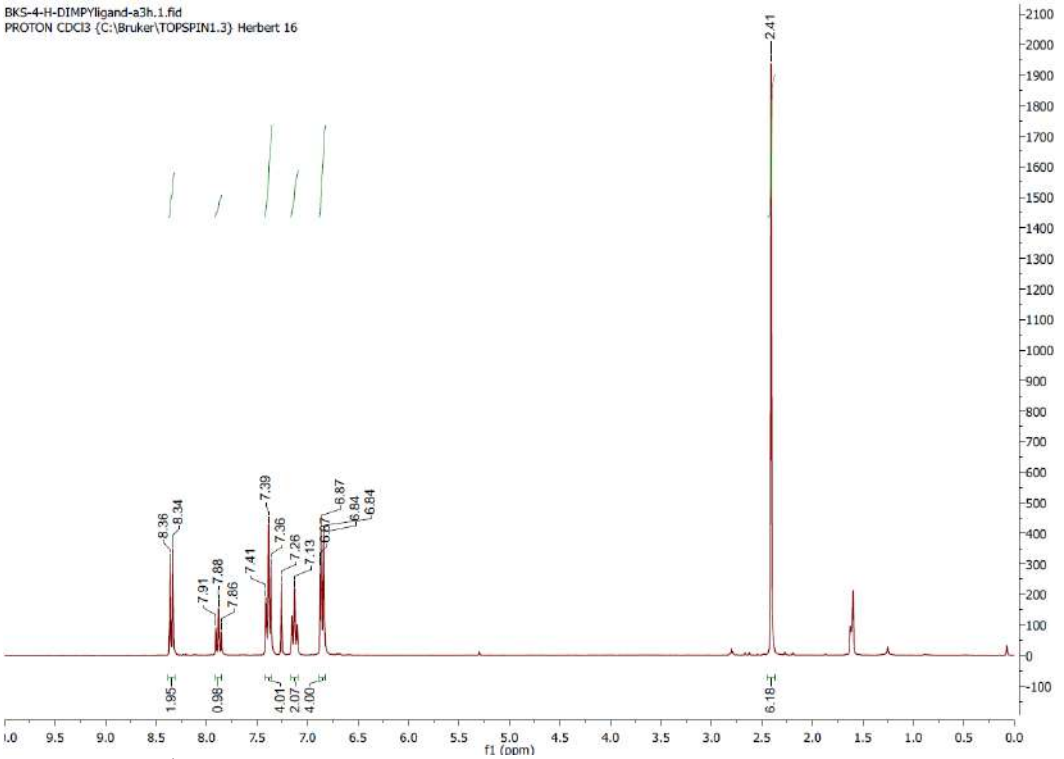

Figure S27. ^{1}H NMR ($CDCl_3$, 300 MHz, 25°C, ppm) of **1c**.

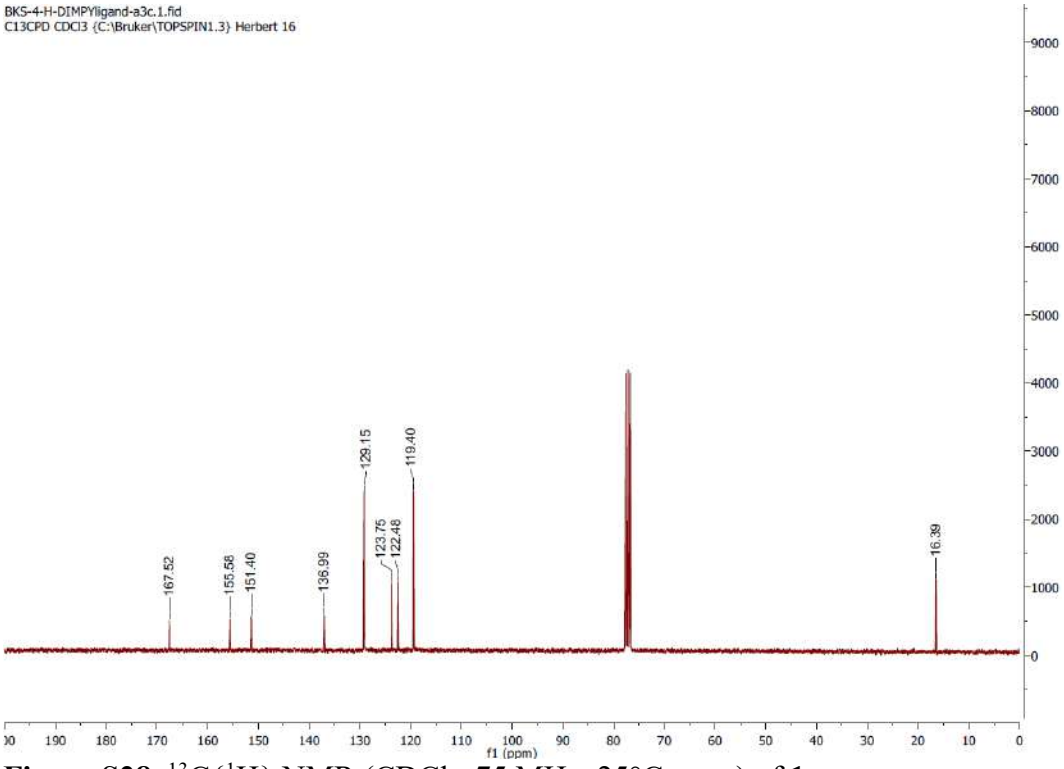

Figure S28. $^{13}C\{^{1}H\}$ NMR ($CDCl_3$, 75 MHz, 25°C, ppm) of **1c**.

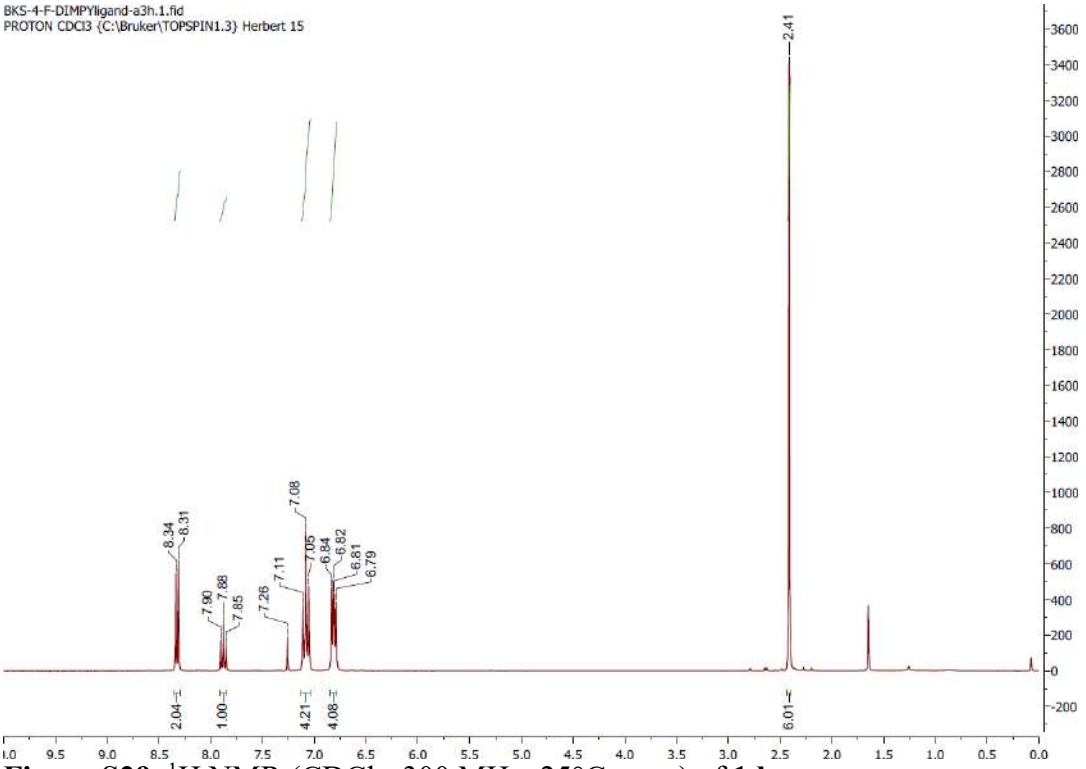

Figure S29. ^{1}H NMR ($CDCl_3$, 300 MHz, 25°C, ppm) of **1d**.

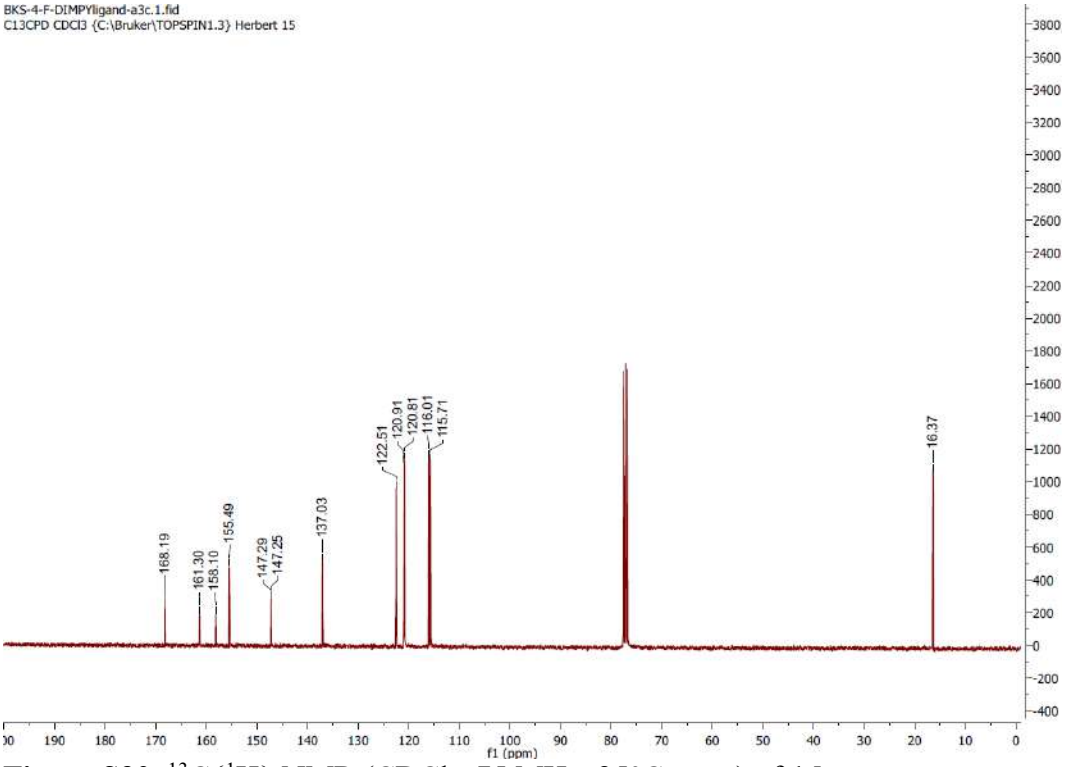

Figure S30. $^{13}C\{^{1}H\}$ NMR ($CDCl_3$, 75 MHz, 25°C, ppm) of **1d**.

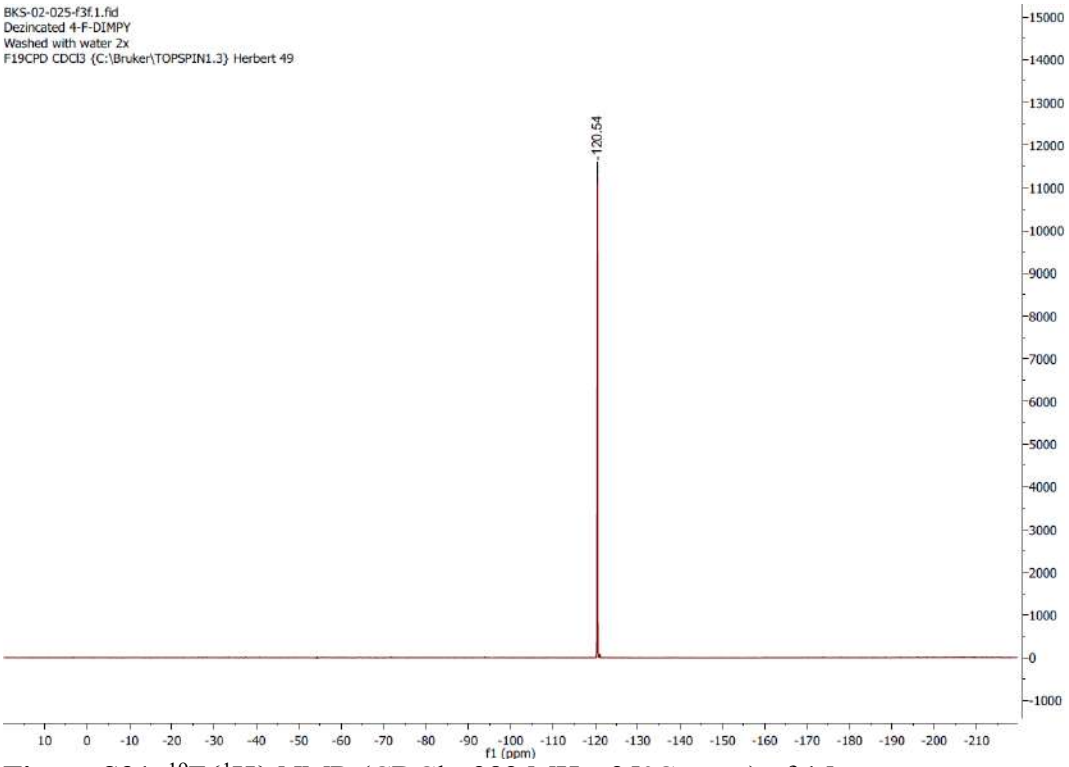

Figure S31. $^{19}F\{^{1}H\}$ NMR ($CDCl_3$, 282 MHz, 25°C, ppm) of **1d**.

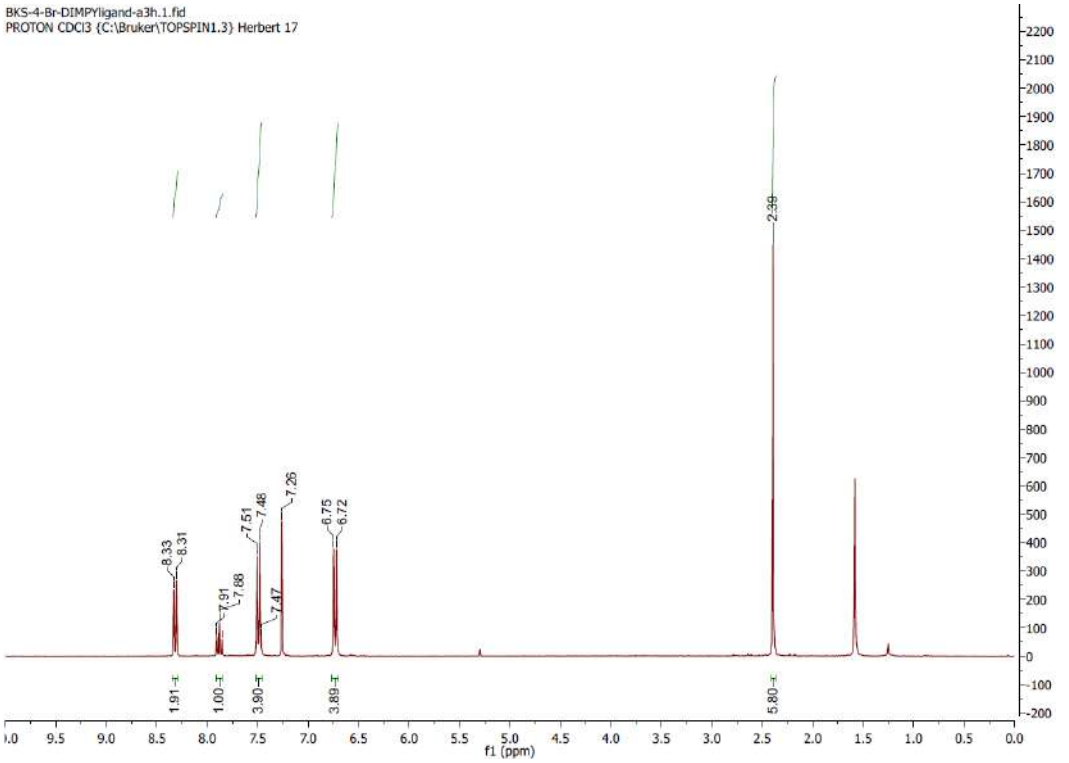

Figure S32. ^{1}H NMR ($CDCl_3$, 300 MHz, 25°C, ppm) of **1e**.

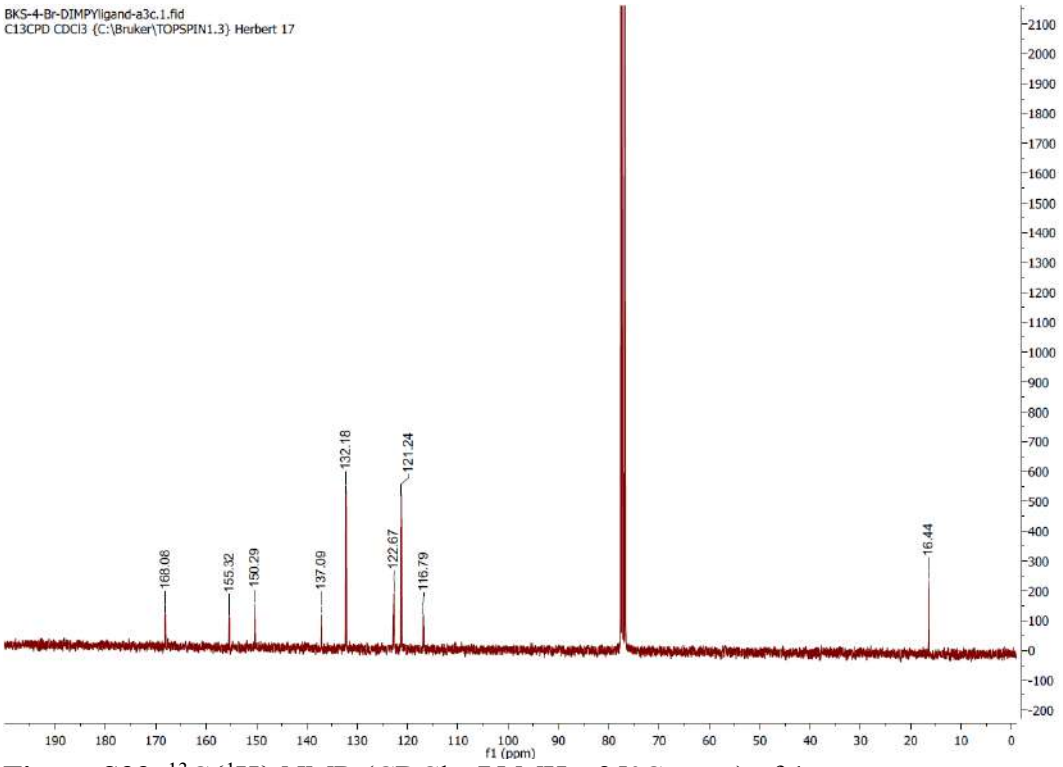

Figure S33. $^{13}C\{^{1}H\}$ NMR ($CDCl_3$, 75 MHz, 25°C, ppm) of **1e**.

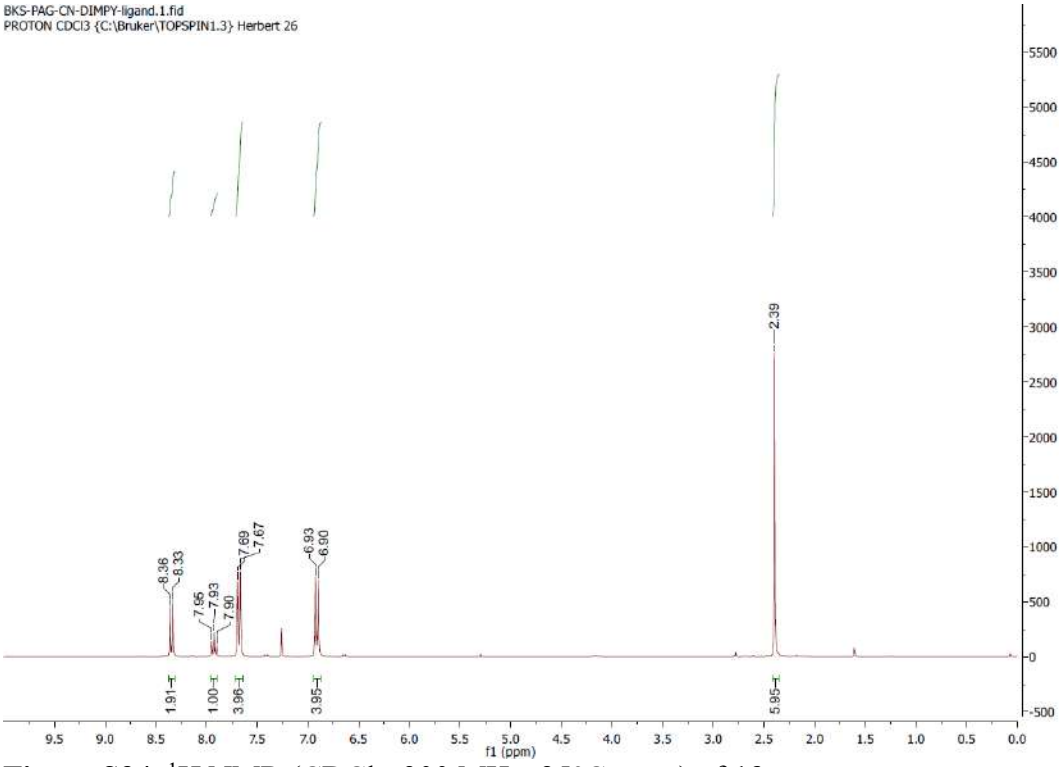

Figure S34. ^{1}H NMR ($CDCl_3$, 300 MHz, 25°C, ppm) of **1f**.

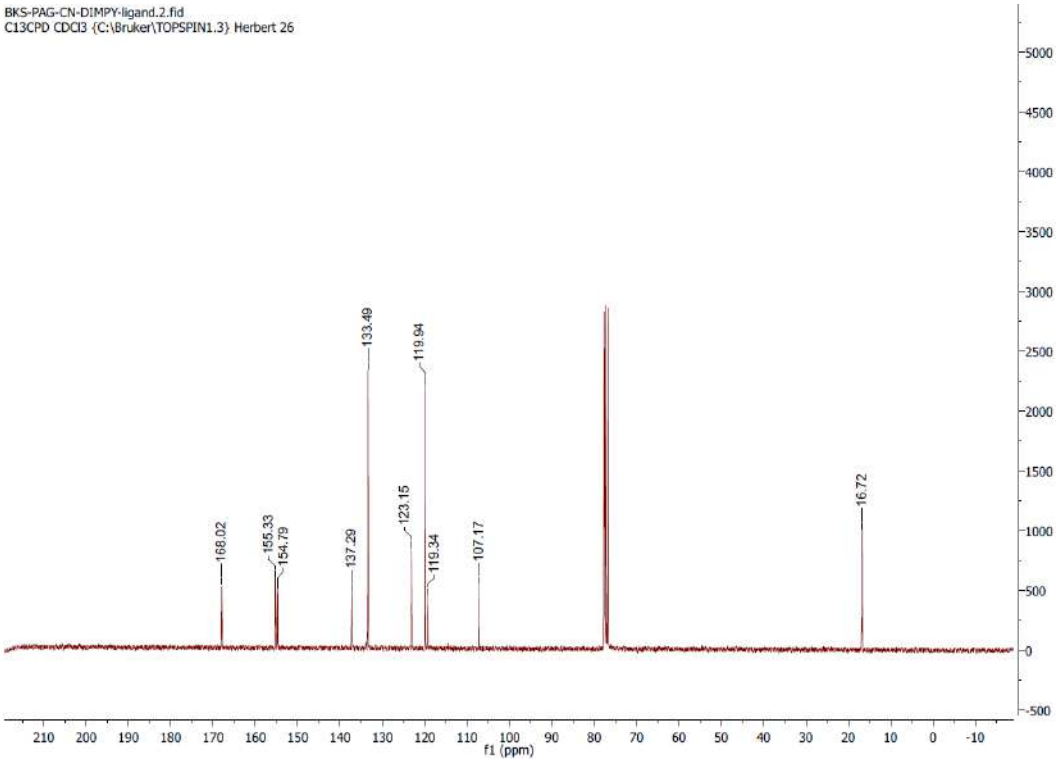

Figure S35. $^{13}C\{^{1}H\}$ NMR ($CDCl_3$, 75 MHz, 25°C, ppm) of **1f**.

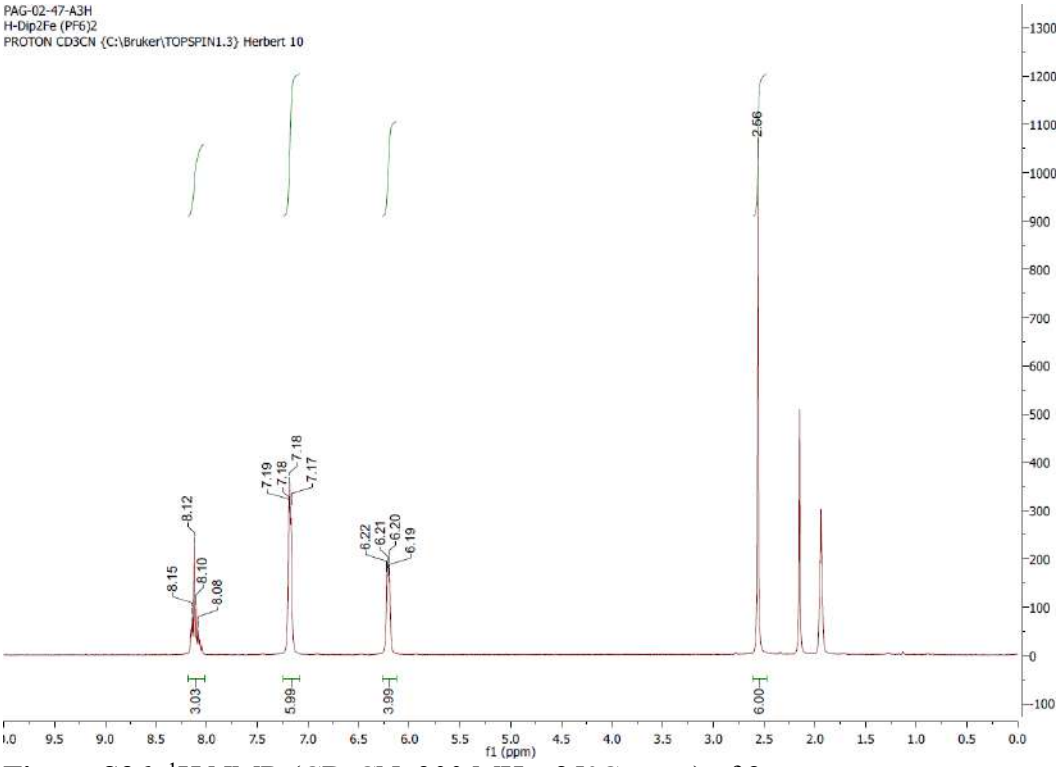

Figure S36. ^{1}H NMR (CD_3CN, 300 MHz, 25°C, ppm) of **2c**.

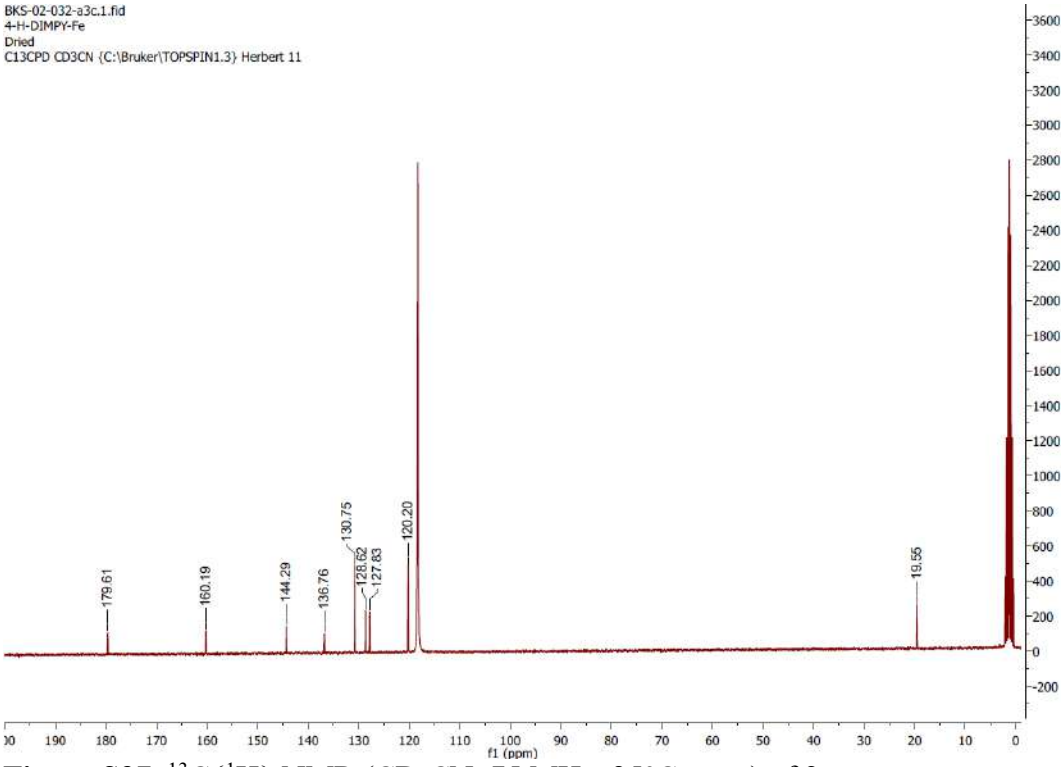

Figure S37. $^{13}C\{^{1}H\}$ NMR (CD_3CN, 75 MHz, 25°C, ppm) of **2c**.

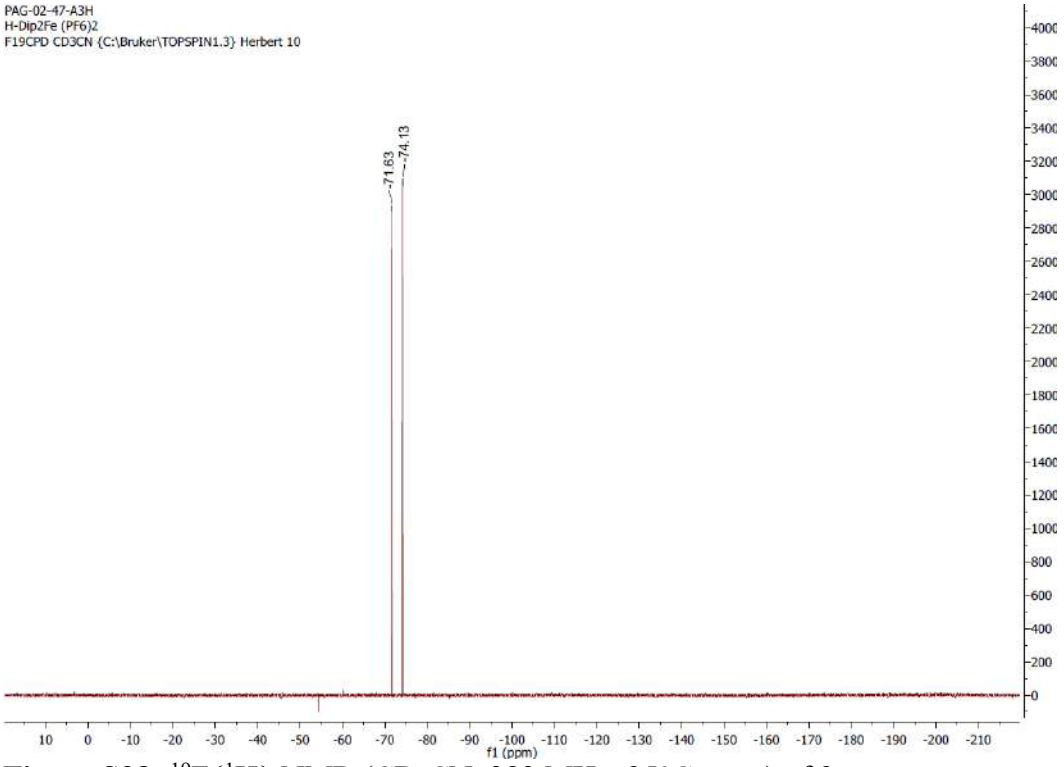

Figure S38: $^{19}F\{^{1}H\}$ NMR (CD_3CN, 282 MHz, 25°C, ppm) of **2c**.

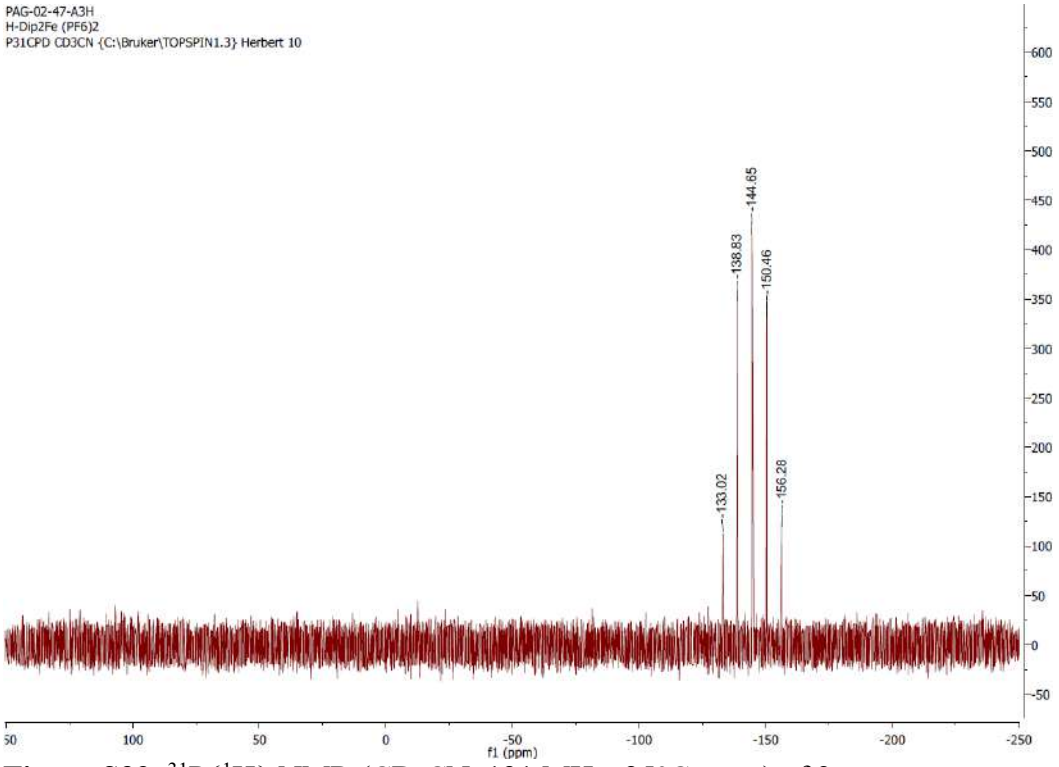

Figure S39. $^{31}P\{^{1}H\}$ NMR (CD_3CN, 121 MHz, 25°C, ppm) of **2c**.

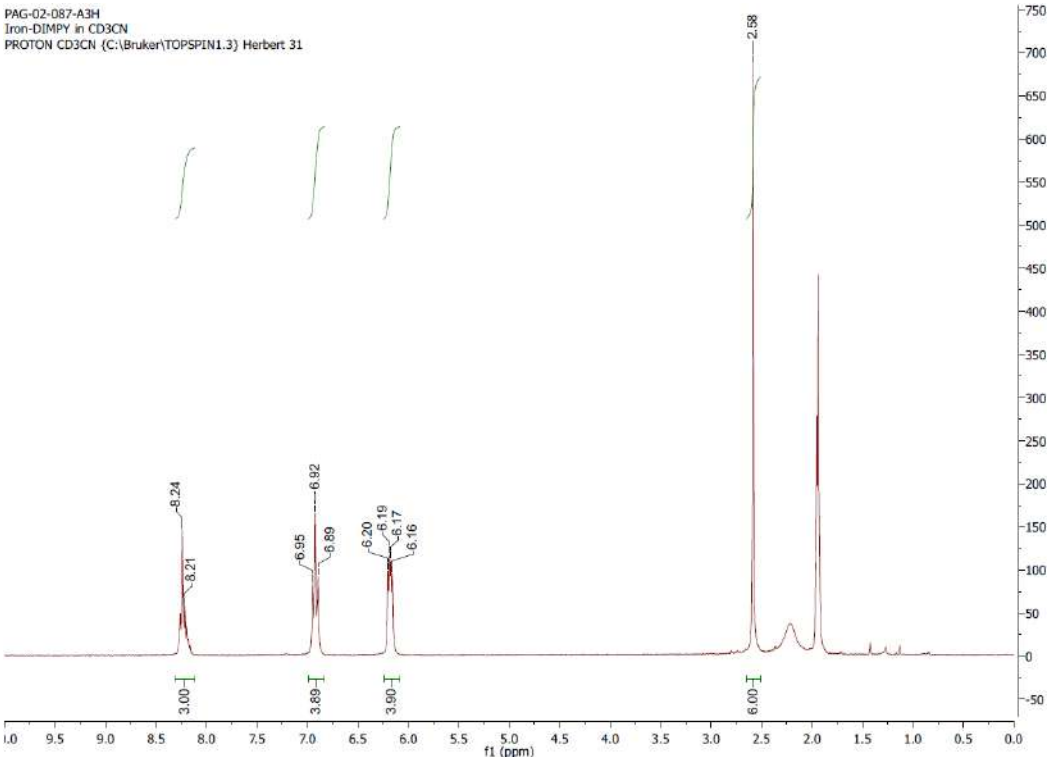

Figure S40. ^{1}H NMR (CD_3CN 300 MHz, 25°C, ppm) of **2d**.

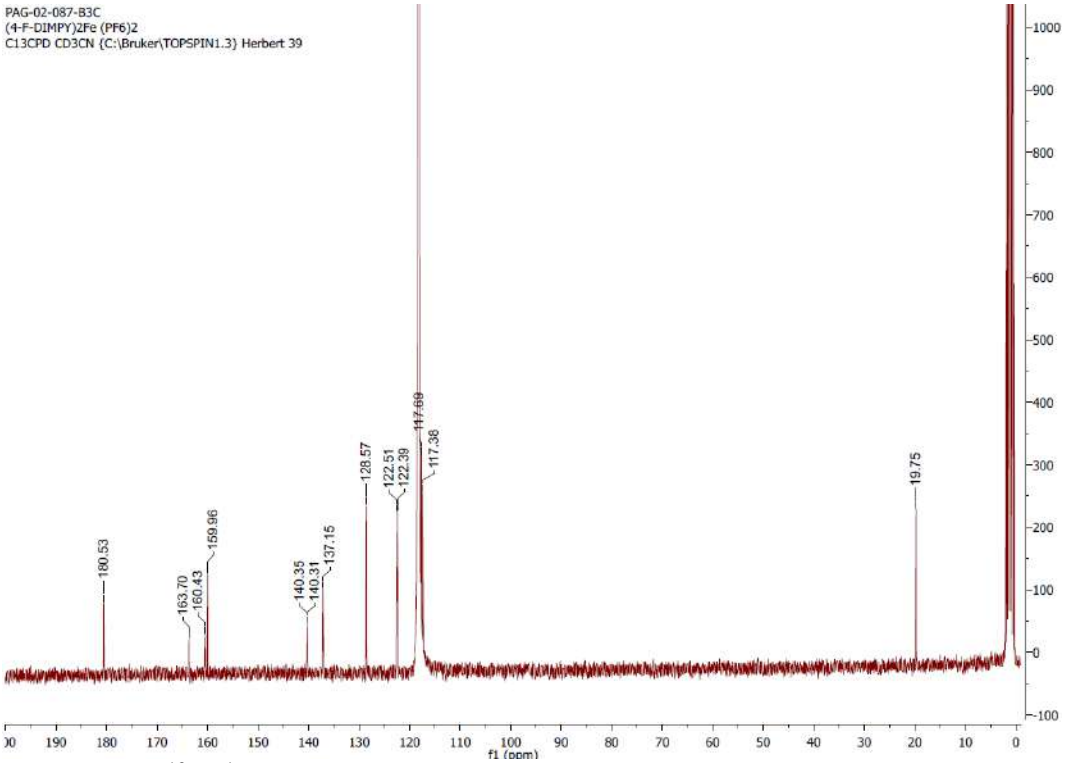

Figure S41. $^{13}C\{^{1}H\}$ NMR (CD_3CN, 75 MHz, 25°C, ppm) of **2d**.

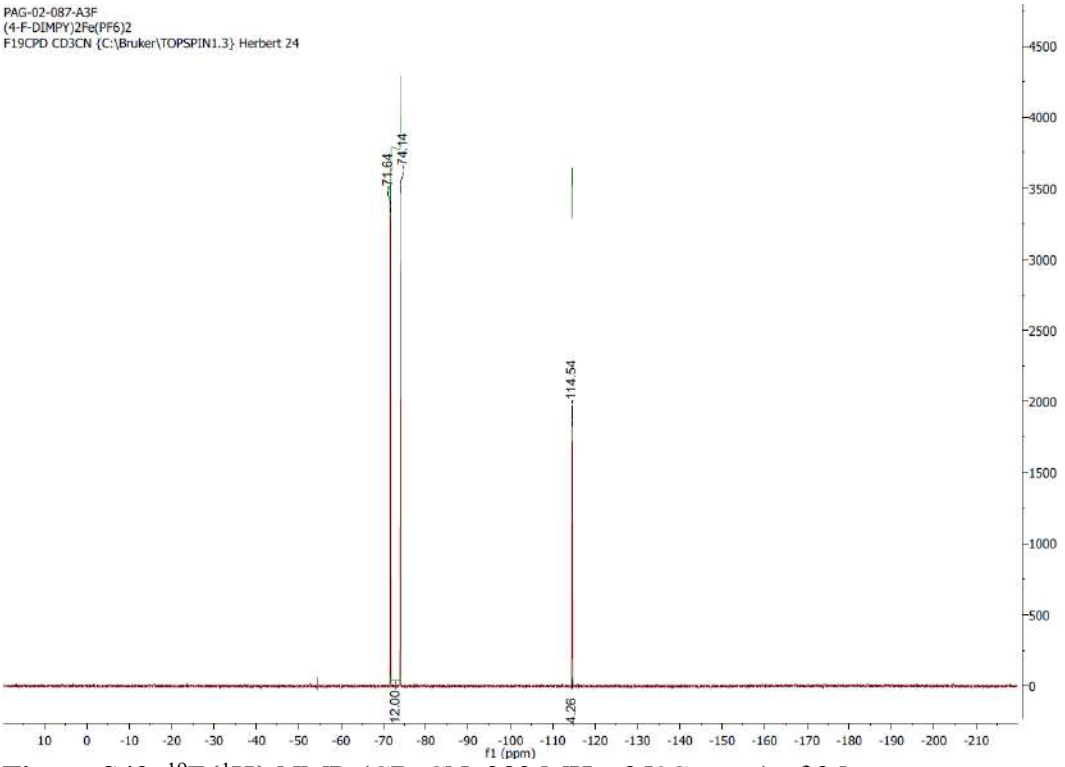

Figure S42. $^{19}F\{^{1}H\}$ NMR (CD_3CN, 282 MHz, 25°C, ppm) of **2d**.

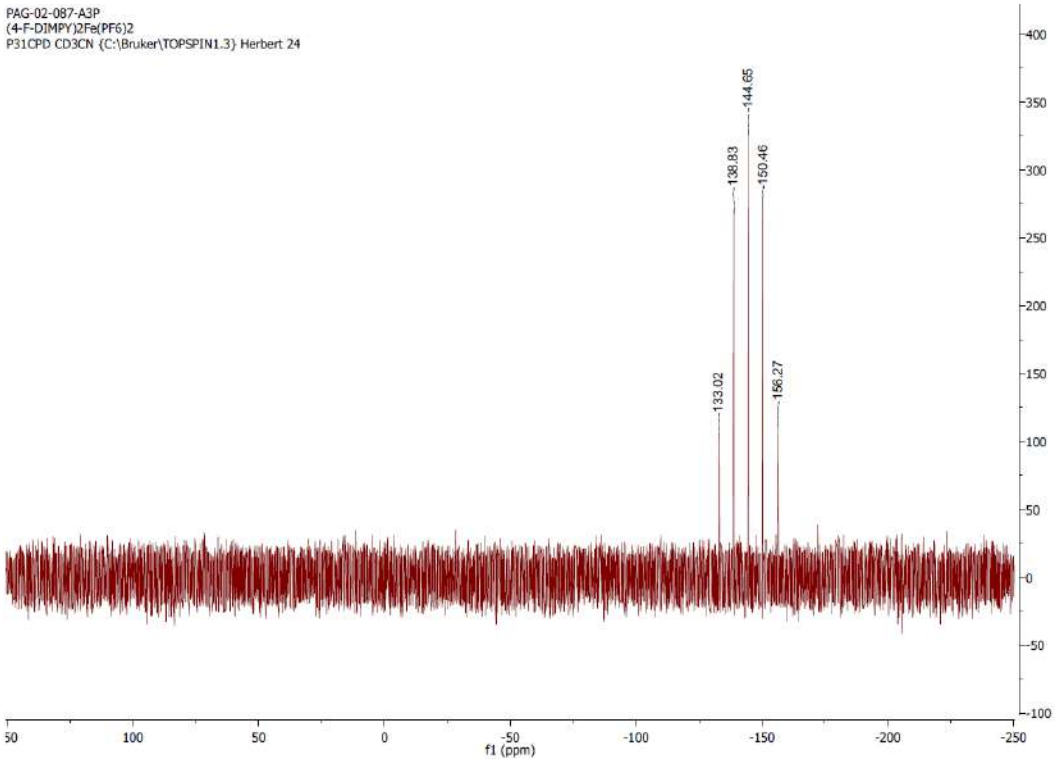

Figure S43. $^{31}P\{^{1}H\}$ NMR (CD_3CN, 121 MHz, 25°C, ppm) of **2d**.

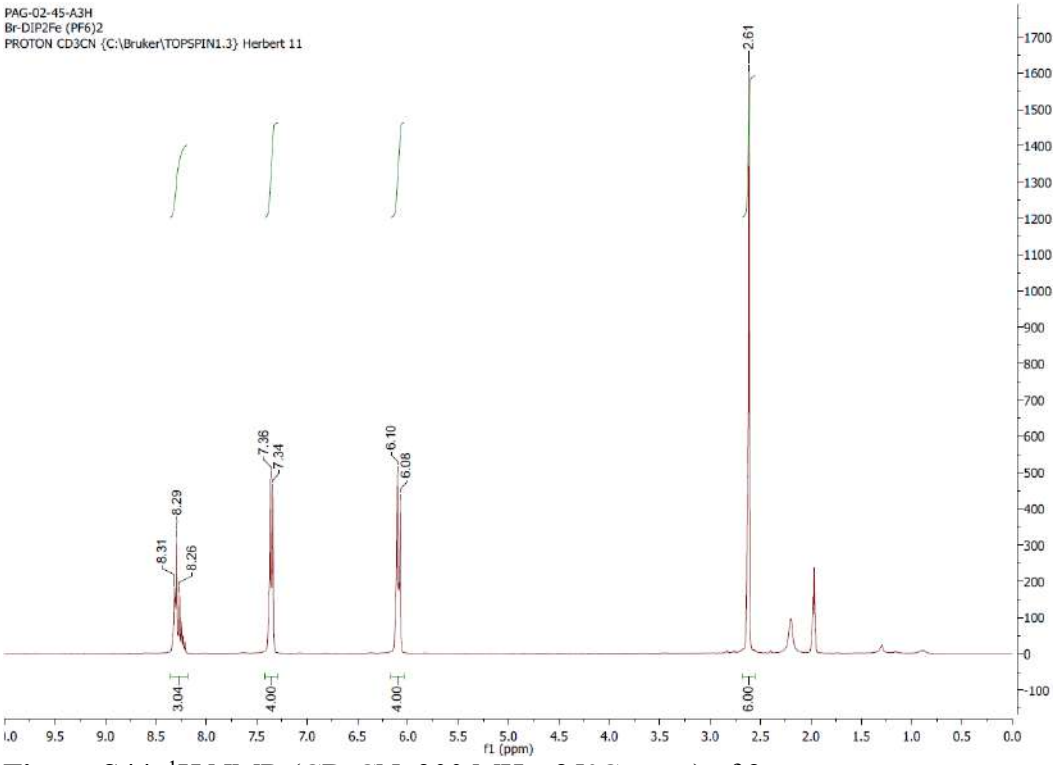

Figure S44. ^{1}H NMR (CD_3CN, 300 MHz, 25°C, ppm) of **2e**.

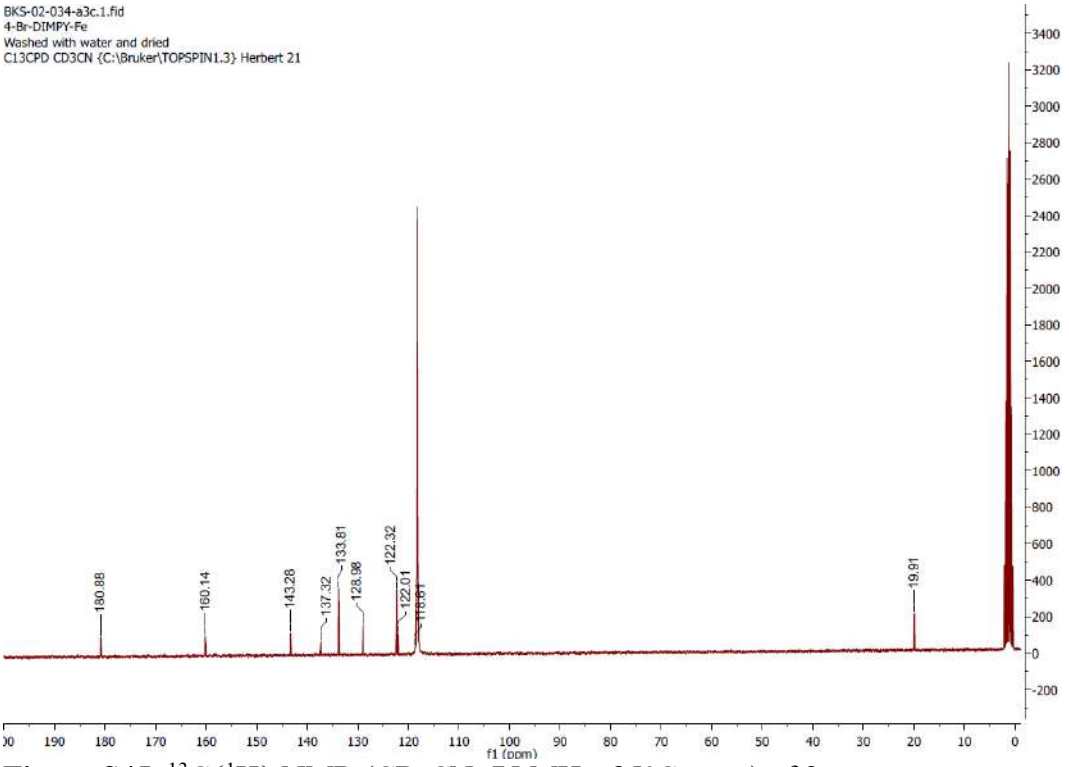

Figure S45. $^{13}C\{^{1}H\}$ NMR (CD_3CN, 75 MHz, 25°C, ppm) of **2e**.

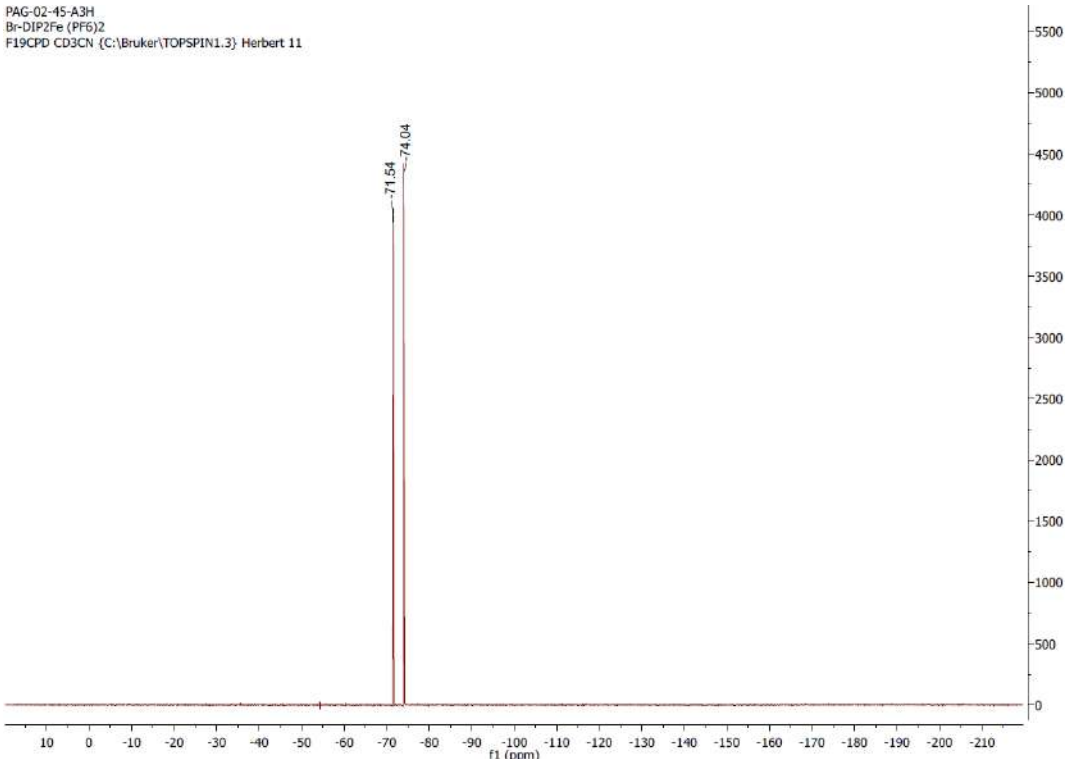

Figure S46. $^{19}F\{^{1}H\}$ NMR (CD_3CN, 282 MHz, 25°C, ppm) of **2e**.

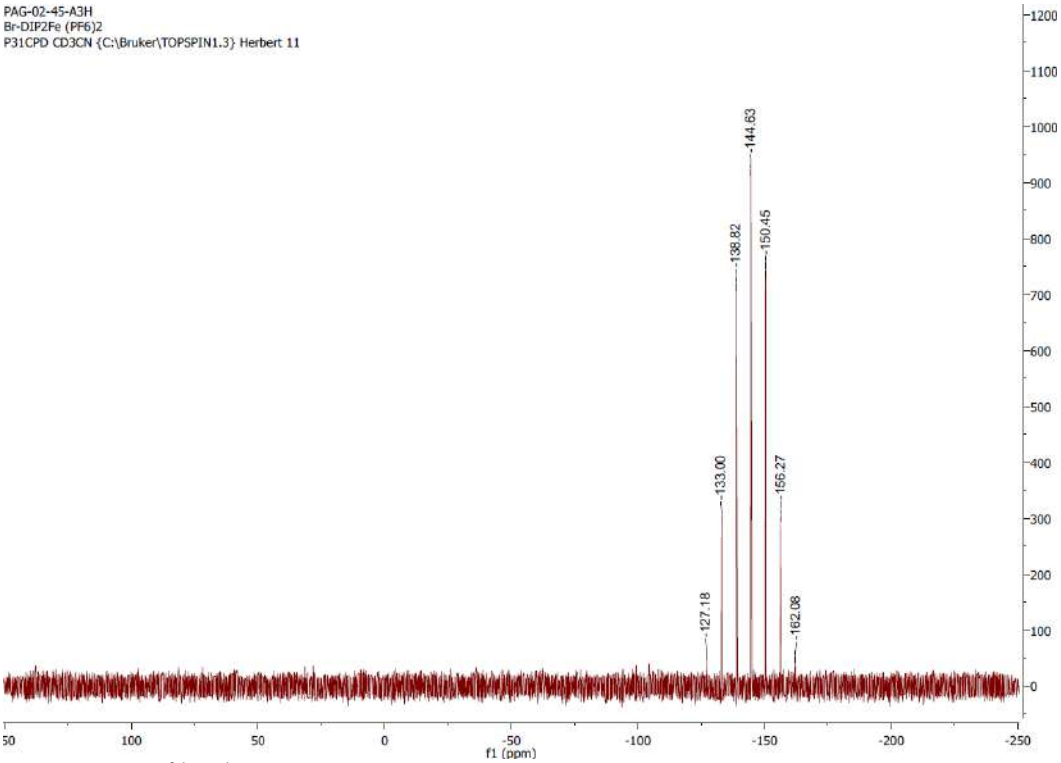

Figure S47. $^{31}P\{^{1}H\}$ NMR (CD_3CN, 121 MHz, 25°C, ppm) of **2e**.

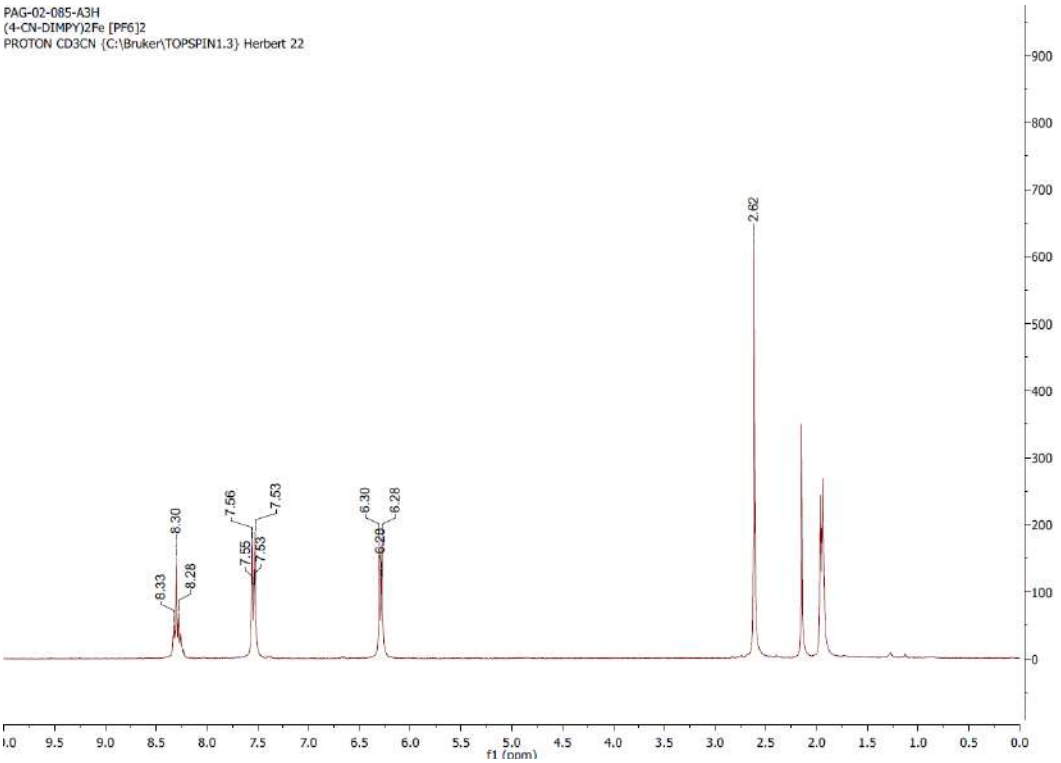

Figure S48. ^{1}H NMR (CD_3CN, 300 MHz, 25°C, ppm) of **2f**.

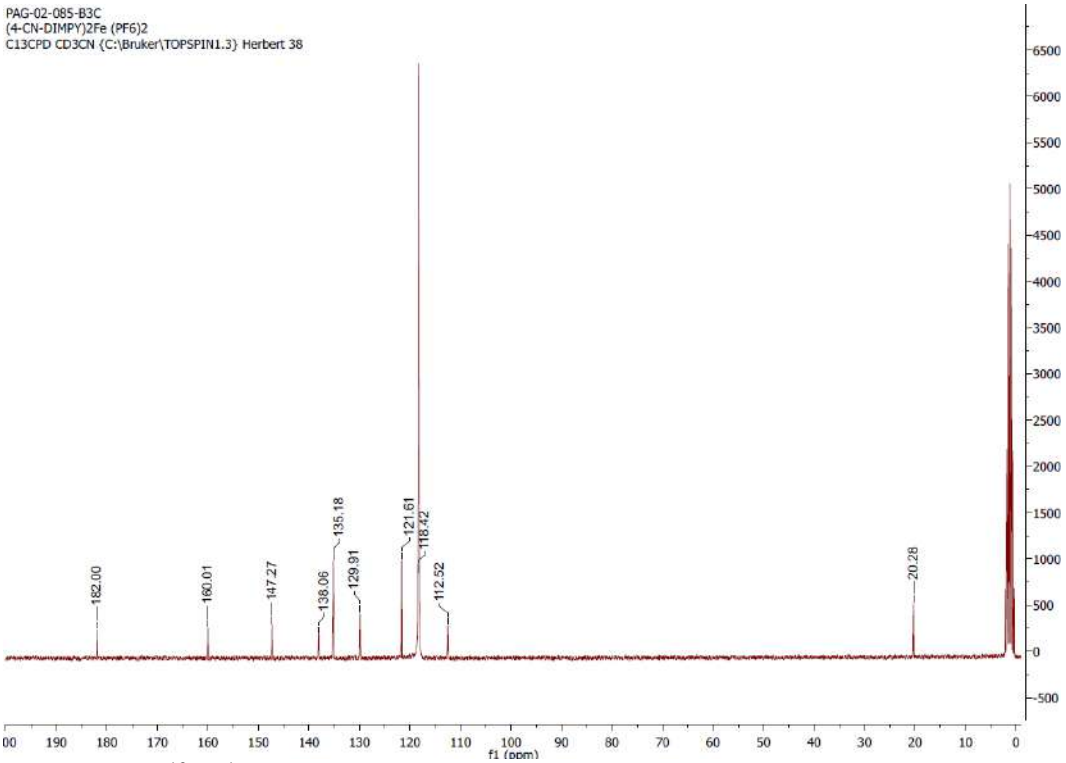

Figure S49. $^{13}C\{^{1}H\}$ NMR (CD_3CN, 75 MHz, 25°C, ppm) of **2f**.

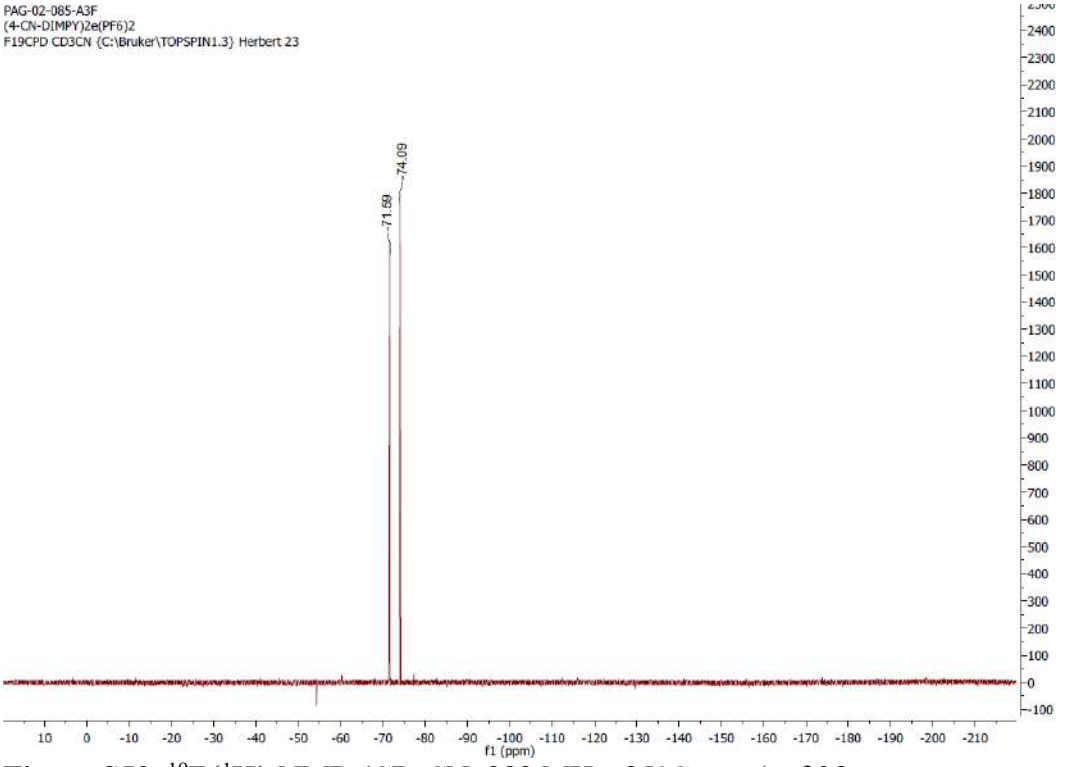

Figure S50. $^{19}F\{^{1}H\}$ NMR (CD_3CN, 282 MHz, 25°C, ppm) of **2f**.

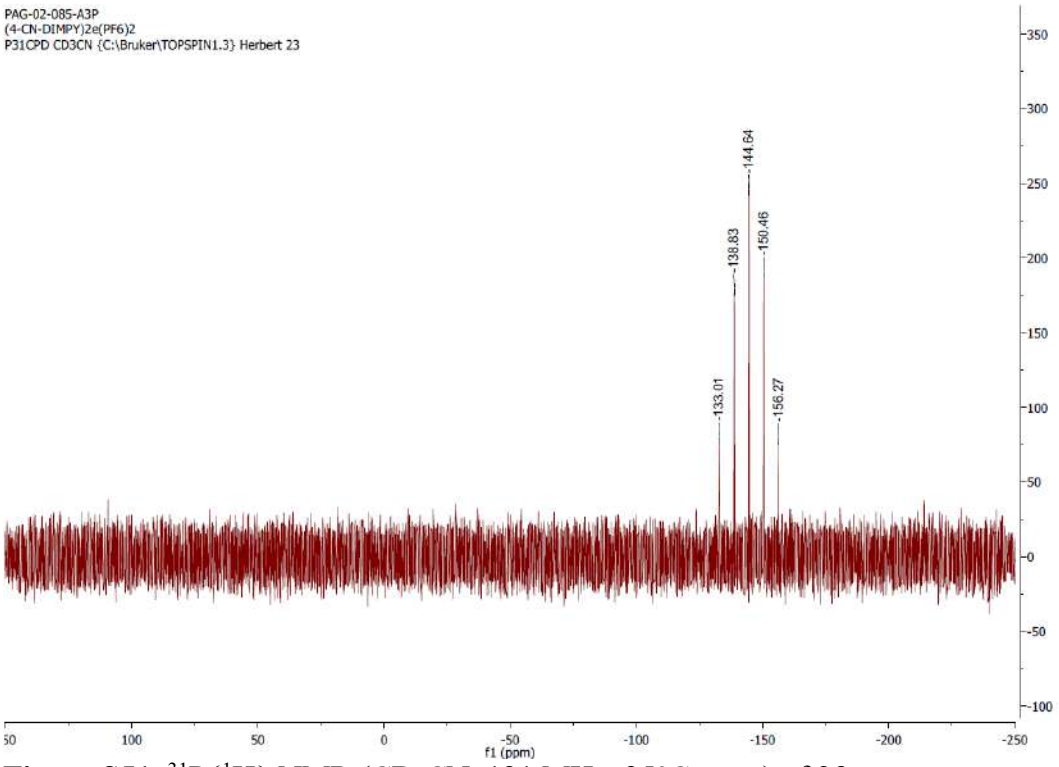

Figure S51. $^{31}P\{^{1}H\}$ NMR (CD_3CN, 121 MHz, 25°C, ppm) of **2f**.

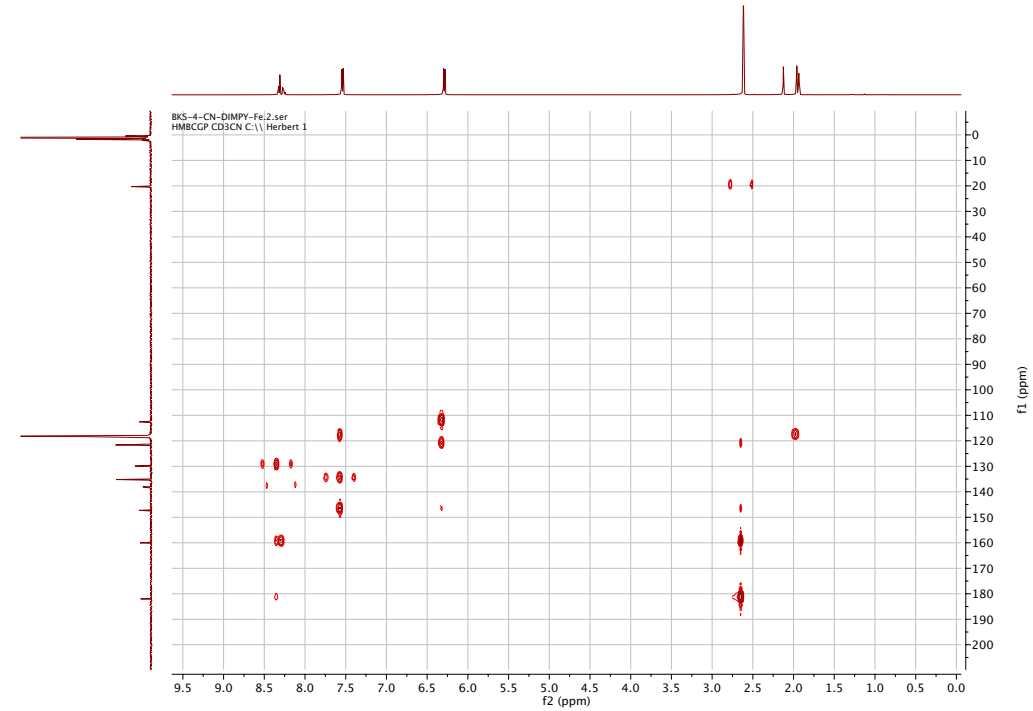

Figure S52. HMBC NMR (CD_3CN, 300/75 MHz, 25°C, ppm) of **2f**.

Table S1. Selected bond angles (°) for **3d-f** (Zn) and **2e-f** (Fe).

	3d	**3e**	**3f**	**2e**	**2f**
Intraligand angles					
N1 – M1 – N3	**147.86(11)**	**147.58(15)**	**147.44(15)**	159.71(12)	159.98(14)
N1 – M1 – N2	74.00(11)	73.75(16)	73.80(15)	80.16(12)	79.97(14)
N2 – M1 – N3	73.87(11)	73.90(16)	73.72(15)	79.56(12)	80.05(14)
N4(6) – Fe1 – N6(8)[a]	-	-	-	158.95(12)	160.18(14)
N4(6) – Fe1 – N5(7)[a]	-	-	-	79.52(13)	80.44(15)
N5(7) – Fe1 – N6(8)[a]	-	-	-	79.68(13)	79.75(15)
N4 – Zn2 – N6	**147.49(11)**	**147.90(15)**	-	-	-
N4 – Zn2 – N5	74.24(11)	74.19(15)	-	-	-
N5 – Zn2 – N6	73.29(11)	73.81(15)	-	-	-
Interligand angles					
N2 – M1 – N5(7)	-	-	-	173.65(14)	177.45(15)
N1 – M1 – N6(8)	-	-	-	91.42(12)	90.99(14)
N2 – M1 – N4(6)	-	-	-	94.82(12)	101.45(14)
N2 – M1 – N6(8)	-	-	-	106.10(13)	98.34(14)
N1 – M1 – N5(7)	-	-	-	102.58(13)	101.70(14)
N3 – M1 – N5(7)	-	-	-	97.65(12)	98.31(14)
N3 – M1 – N4(6)	-	-	-	92.28(12)	89.29(14)
N1 – Zn1 – Cl1	95.97(8)	96.97(11)	93.02(10)	-	-
N1 – Zn1 – Cl2	98.82(8)	99.72(11)	100.05(11)	-	-
N2 – Zn1 – Cl1	114.79(8)	111.14(12)	116.75(10)	-	-
N2 – Zn1 – Cl2	**128.78(8)**	**129.44(12)**	**123.28(10)**	-	-
N3 – Zn1 – Cl1	97.03(9)	96.55(12)	99.49(10)	-	-
N3 – Zn1 – Cl2	101.44(8)	99.01(11)	99.47(11)	-	-
Cl1 – Zn1 – Cl2	116.40(4)	119.41(5)	119.88(5)	-	-
N4 – Zn2 – Cl3	99.14(8)	98.37(11)	-	-	-
N4 – Zn2 – Cl4	97.84(8)	97.51(11)	-	-	-
N5 – Zn2 – Cl3	**126.73(8)**	**122.22(12)**	-	-	-
N5 – Zn2 – Cl4	115.97(8)	117.26(12)	-	-	-
N6 – Zn2 – Cl3	98.79(8)	96.45(12)	-	-	-
N6 – Zn2 – Cl4	97.69(8)	99.19(11)	-	-	-
Cl3 – Zn2 – Cl4	117.30(4)	120.52(6)	-	-	-
τ_5[b]	0.32, 0.35	0.30, 0.31	0.40	-	-

[a] Atom labels in parentheses are for cyano derivatives **3f** and **2f**

[b] $\tau_5 = (\beta-\alpha)/60°$ where β and α are the largest valence angles (bolded in table) and $\beta > \alpha$.[2] Where two values are given, values correspond to the two molecules in asymmetric unit (Zn1 and Zn2)

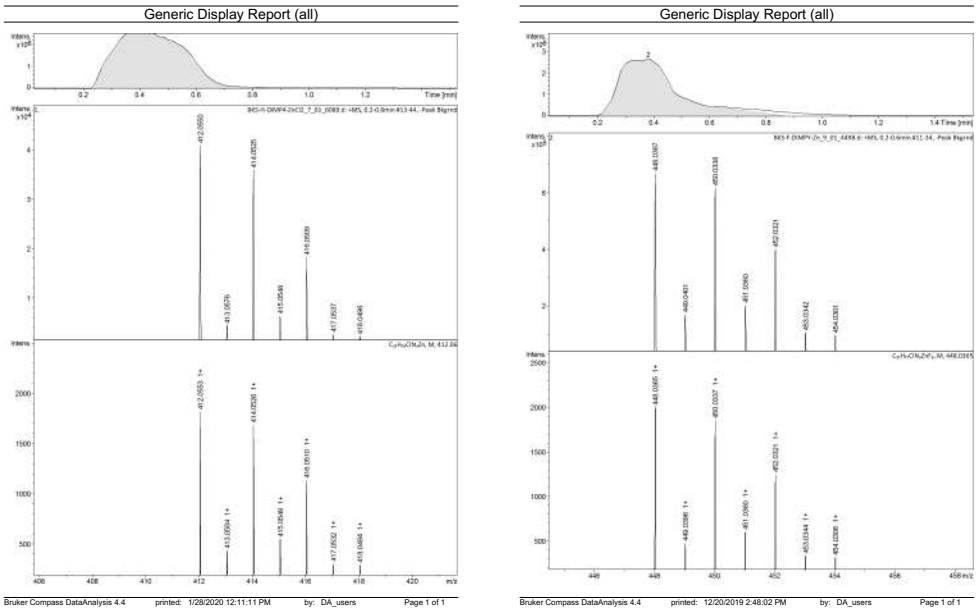

Figure S53. MS (ESI-TOF/MS, m/z) for **3c** and **3d**.

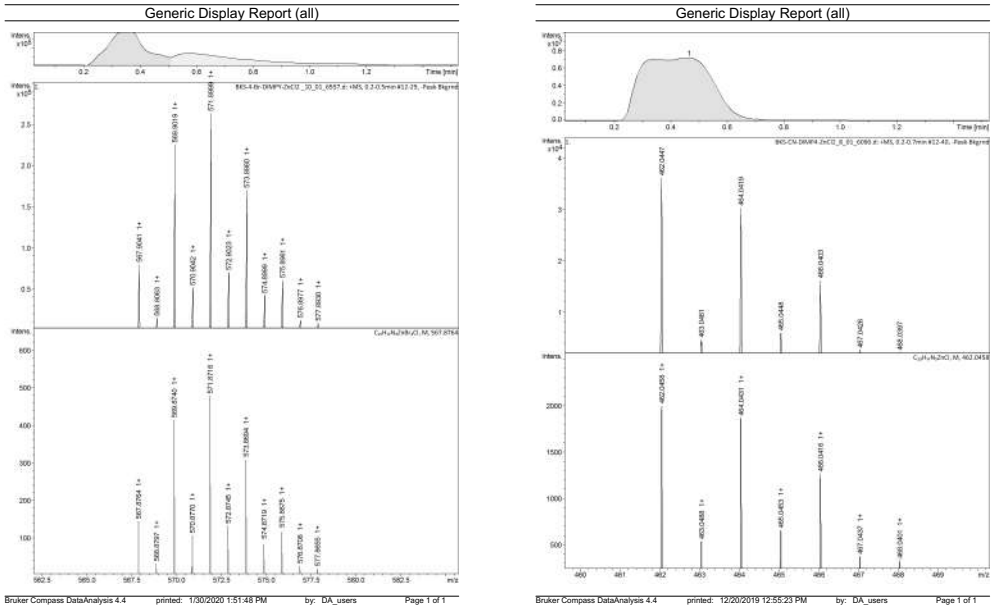

Figure S54. MS (ESI-TOF/MS, m/z) for **3e** and **3f**.

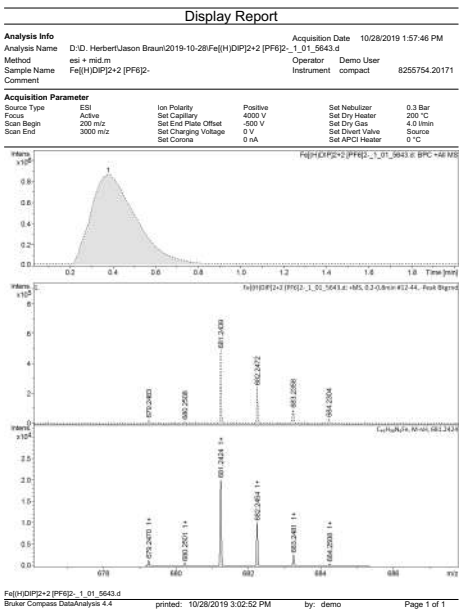

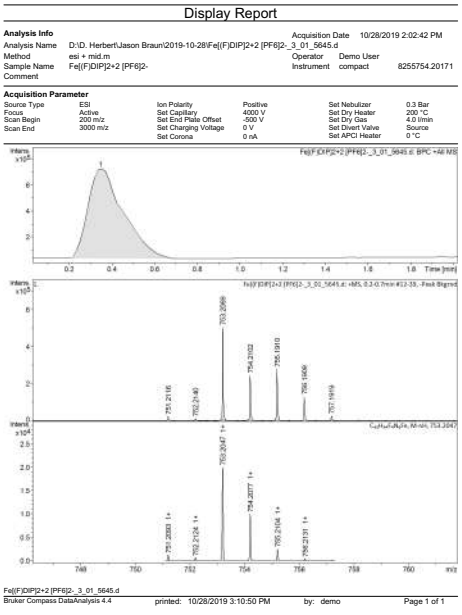

Figure S55. MS (ESI-TOF/MS, m/z) for **2c** and **2d**.

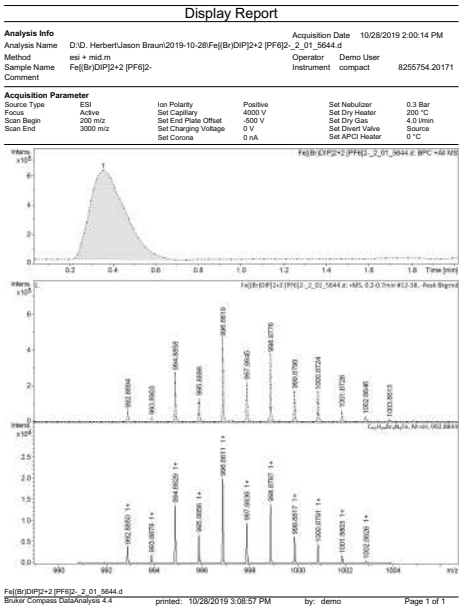

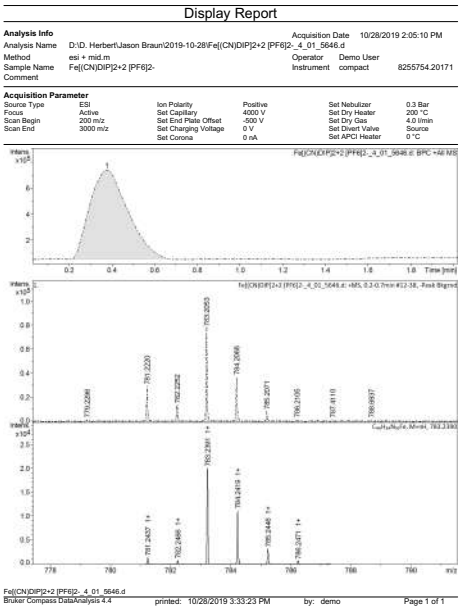

Figure S56. MS (ESI-TOF/MS, m/z) for **2e** and **2f**.

Chapter 3

Computational Details

Calculations were conducted using Gaussian 16, Revision B01.[3] Geometry optimizations were performed with M06 hybrid functional[4] and the Def2-SVP[5] basis set for all atoms. Stationary points were confirmed as true minima by vibrational frequency analysis (no negative eigenvalues). Solvent effects were included using the 'solvation model based on density' protocol (SMD, solvent = CH_2Cl_2).[6] Full TD-DFT treatment with solvation was carried out for the first 50 states at the SMD-M06/Def2-SVPD level of theory. All spectra were simulated using the GaussSum software.[7] Electron density distribution maps (green = electron, blue = hole) were generated using Multiwfn software.[8] Natural transition orbitals[9] were calculated for vertical excitations and are provided in addition to electron density distribution maps where relevant.

Table S2. Energies (Hartrees) and Cartesian Coordinates for **[(^{dipp}DIP^{tBu})P]$^+$**.

[(^{dipp}DIP^{tBu})P]$^+$

HF=	-2022.60506
Zero-point correction=	0.865871
Thermal correction to Energy=	0.911392
Thermal correction to Enthalpy=	0.912336
Thermal correction to Gibbs Free Energy=	0.790602
Sum of electronic and zero-point Energies=	-2021.739189
Sum of electronic and thermal Energies=	-2021.693668
Sum of electronic and thermal Enthalpies=	-2021.692724
Sum of electronic and thermal Free Energies=	-2021.814458

Atomic Label	X Coord.	Y Coord.	Z Coord.
C	-2.31025	1.51664	0.34864
C	-3.72557	1.99834	0.69843
C	-3.64791	2.74941	2.04656
H	-3.28885	2.07444	2.83778
H	-4.65585	3.08795	2.32444
H	-2.99236	3.62759	2.03273
C	-4.28557	2.90198	-0.41891
H	-3.66033	3.77107	-0.65311
H	-5.27222	3.27436	-0.10875
H	-4.42453	2.32925	-1.34711
C	-4.74093	0.86429	0.9003
H	-4.9453	0.30898	-0.02219
H	-5.68335	1.3203	1.23384
H	-4.42089	0.15004	1.66856
C	-1.19018	2.40129	0.19278
C	-1.17034	3.80498	0.20167
H	-2.09097	4.35176	0.37993
C	0.00406	4.49124	-0.02542
H	0.01674	5.57997	-0.03444
C	1.18634	3.7706	-0.24186
H	2.11138	4.3075	-0.42457
C	1.1928	2.38884	-0.22012
C	2.3463	1.49034	-0.35784
C	3.75559	2.00173	-0.69601
C	4.29936	2.9472	0.39459
H	3.66205	3.81065	0.61369
H	5.27576	3.32979	0.06514
H	4.46143	2.40415	1.33651
C	3.67312	2.70838	-2.06822
H	3.31049	2.00897	-2.83642

H	4.68171	3.03338	-2.3594
H	3.02119	3.58928	-2.08106
C	4.78319	0.87189	-0.85202
H	4.97334	0.3434	0.08954
H	5.72896	1.32382	-1.18155
H	4.47976	0.13371	-1.60444
C	-2.64369	-0.9452	0.08144
C	-3.25652	-1.22666	-1.15678
C	-3.89848	-2.45817	-1.29266
H	-4.38719	-2.70657	-2.2356
C	-3.92593	-3.37532	-0.24457
H	-4.43398	-4.3319	-0.37178
C	-3.30643	-3.0727	0.96074
H	-3.33226	-3.79784	1.77612
C	-2.64383	-1.85427	1.15129
C	-3.22447	-0.24864	-2.32243
H	-3.00285	0.75208	-1.9238
C	-2.09826	-0.6067	-3.2988
H	-1.11853	-0.59239	-2.79911
H	-2.07329	0.10408	-4.13767
H	-2.25231	-1.61704	-3.70764
C	-4.56735	-0.15362	-3.05139
H	-4.79482	-1.07631	-3.60422
H	-4.53881	0.66409	-3.78573
H	-5.39874	0.03652	-2.35642
C	-1.97818	-1.57255	2.4896
H	-1.57085	-0.54922	2.46656
C	-2.98075	-1.64542	3.64728
H	-3.82872	-0.96096	3.50147
H	-2.48691	-1.38026	4.5929
H	-3.38629	-2.6615	3.75945
C	-0.81164	-2.53921	2.72439
H	-1.16951	-3.57939	2.75051
H	-0.32596	-2.3268	3.68763
H	-0.05697	-2.46085	1.92719
C	2.66936	-0.95526	-0.07924
C	3.28542	-1.23487	1.16099
C	3.88149	-2.48546	1.32091
H	4.37279	-2.72804	2.26367
C	3.86582	-3.4293	0.29596
H	4.34304	-4.39905	0.44074
C	3.24189	-3.13298	-0.90771
H	3.23402	-3.87668	-1.70674

C	2.6179	-1.89748	-1.11994
C	3.28988	-0.22672	2.30051
H	3.20736	0.77849	1.86293
C	4.58329	-0.24852	3.11722
H	4.67259	-1.16866	3.71231
H	4.59496	0.59388	3.82345
H	5.47323	-0.17274	2.47486
C	2.06989	-0.42963	3.2063
H	1.13044	-0.34307	2.63883
H	2.0591	0.31411	4.0165
H	2.09614	-1.43273	3.65816
C	1.95343	-1.62497	-2.46078
H	1.50987	-0.6168	-2.43003
C	2.97409	-1.64779	-3.60501
H	3.78473	-0.92203	-3.44639
H	2.48374	-1.40861	-4.55949
H	3.43227	-2.64281	-3.70506
C	0.82395	-2.62692	-2.72303
H	1.21371	-3.65479	-2.76456
H	0.33928	-2.41588	-3.68708
H	0.06083	-2.58595	-1.93091
N	-1.88354	0.27399	0.19333
N	-0.00419	1.70941	-0.01638
N	1.94743	0.26815	-0.21181
P	-0.07343	-0.02456	-0.03116

Table S3. Energies (Hartrees) and Cartesian Coordinates for **[(^{dipp}DIP^{tBu})PCl]$^{2+}$**.

[(^{dipp}DIP^{tBu})PCl]$^{2+}$

HF=	-2482.319702
Zero-point correction=	0.869252
Thermal correction to Energy=	0.915727
Thermal correction to Enthalpy=	0.916671
Thermal correction to Gibbs Free Energy=	0.794882
Sum of electronic and zero-point Energies=	-2481.45045
Sum of electronic and thermal Energies=	-2481.403974
Sum of electronic and thermal Enthalpies=	-2481.40303
Sum of electronic and thermal Free Energies=	-2481.52482

Atomic Label	X Coord.	Y Coord.	Z Coord.
C	-2.39912	1.44589	-0.30965
C	-3.79629	1.95579	-0.6572
C	-3.7092	2.69493	-2.01409
H	-3.05432	3.57335	-2.02495
H	-4.71822	3.03903	-2.27831
H	-3.37713	2.00828	-2.80723
C	-4.302	2.87405	0.47832
H	-4.30554	2.34214	1.4394
H	-5.3394	3.15487	0.2494
H	-3.73902	3.80503	0.60834
C	-4.83012	0.83666	-0.84862
H	-4.52796	0.1263	-1.62577
H	-5.76732	1.30998	-1.1701
H	-5.03342	0.27617	0.06819
C	-1.2237	2.38723	-0.26514
C	-1.24011	3.77915	-0.28114
H	-2.17671	4.32108	-0.35744
C	-0.03835	4.47642	-0.18221
H	-0.04351	5.56755	-0.1711
C	1.16913	3.78739	-0.10282
H	2.10818	4.32973	-0.04265
C	1.1548	2.39594	-0.10089
C	2.34119	1.46974	-0.05613
C	3.75038	2.05773	-0.02903
C	4.88608	1.03199	-0.1698
H	4.92449	0.31907	0.65668
H	5.82726	1.59866	-0.16913
H	4.82987	0.47155	-1.10972
C	3.89209	2.70951	1.37298
H	3.18298	3.52549	1.56251
H	4.90649	3.1249	1.45059
H	3.77413	1.96034	2.16775
C	3.92723	3.11253	-1.16771
H	3.05087	3.23417	-1.81783
H	4.75214	2.80869	-1.8237
H	4.1898	4.09728	-0.75549
C	-2.75838	-0.9797	0.05025
C	-3.37031	-1.29838	1.28231
C	-4.03229	-2.5274	1.3545
H	-4.52582	-2.807	2.2867
C	-4.0791	-3.39857	0.27189
H	-4.60528	-4.34958	0.35999

C	-3.45742	-3.05529	-0.92264
H	-3.50486	-3.74166	-1.76967
C	-2.77904	-1.84201	-1.06394
C	-3.38504	-0.40064	2.5138
H	-2.78461	0.49972	2.30077
C	-4.81016	0.04088	2.88161
H	-5.33489	0.54741	2.06145
H	-4.78139	0.72469	3.74205
H	-5.41959	-0.82643	3.17284
C	-2.76798	-1.10888	3.72973
H	-3.42799	-1.91534	4.08008
H	-2.65146	-0.40049	4.56199
H	-1.79184	-1.55769	3.50782
C	-2.14307	-1.51193	-2.40744
H	-1.71488	-0.49477	-2.36159
C	-3.1673	-1.5199	-3.55044
H	-3.59398	-2.52319	-3.68898
H	-2.68036	-1.23721	-4.49414
H	-4.00093	-0.82593	-3.37678
C	-1.00591	-2.48853	-2.72146
H	-0.23551	-2.48915	-1.93522
H	-0.53537	-2.22717	-3.67898
H	-1.39049	-3.51507	-2.80999
C	2.74	-0.96499	-0.0329
C	3.27885	-1.49061	1.15892
C	4.03256	-2.66477	1.04786
H	4.46979	-3.09871	1.9484
C	4.23861	-3.28341	-0.17596
H	4.83723	-4.19297	-0.23453
C	3.67283	-2.75019	-1.3308
H	3.83792	-3.25714	-2.2799
C	2.90028	-1.58756	-1.29516
C	3.11062	-0.88586	2.54768
H	2.51997	0.03938	2.45818
C	2.35176	-1.85998	3.46438
H	1.451	-2.26797	2.98929
H	2.06566	-1.35986	4.40093
H	2.99673	-2.7095	3.73189
C	4.44977	-0.53566	3.21386
H	5.06292	-1.43573	3.36158
H	4.26448	-0.10243	4.2071
H	5.05141	0.18255	2.64196
C	2.32097	-1.0203	-2.59214

H	1.29232	-0.67597	-2.37753
C	2.22265	-2.06861	-3.70305
H	3.21882	-2.32118	-4.09356
H	1.6444	-1.66403	-4.54503
H	1.74133	-2.99495	-3.36326
C	3.11639	0.17771	-3.12684
H	3.11971	1.03612	-2.44309
H	2.68969	0.51657	-4.08137
H	4.16233	-0.10896	-3.31284
Cl	-0.08107	-0.34581	1.92102
N	-2.00097	0.24854	-0.06864
N	-0.03221	1.75385	-0.16957
N	1.94461	0.24868	0.00072
P	-0.03199	-0.08405	-0.10508

Table S4. Selected solid-state and optimized gas-phase bond lengths (Å) and angles (°) for **[(^{dipp}DIP^{tBu})P]$^{+}$** and **[(^{dipp}DIP^{tBu})PCl]$^{2+}$**

	[(^{dipp}DIP^{tBu})P]$^{+}$		**[(^{dipp}DIP^{tBu})PCl]$^{2+}$**	
	Solid-state	**DFT**	**Solid-state**	**DFT**
N1-P1	1.8933(19)	1.848	1.9989(19)	2.007
N2-P1	1.7111(17)	1.735	1.7752(18)	1.839
N3-P1	2.0055(18)	2.05	2.0009(19)	1.997
P1-Cl1	--	--	2.0192(8)	2.044
C1-N1	1.318(3)	1.323	1.285(3)	1.285
C11-N3	1.309(3)	1.294	1.294(3)	1.285
N1-P1-N3	162.75(8)	162.4	161.47(8)	160.4
N1-P1-N2	81.26(8)	82.9	81.36(8)	80.6
N2-P1-N3	80.49(8)	79.6	81.66(8)	80.5

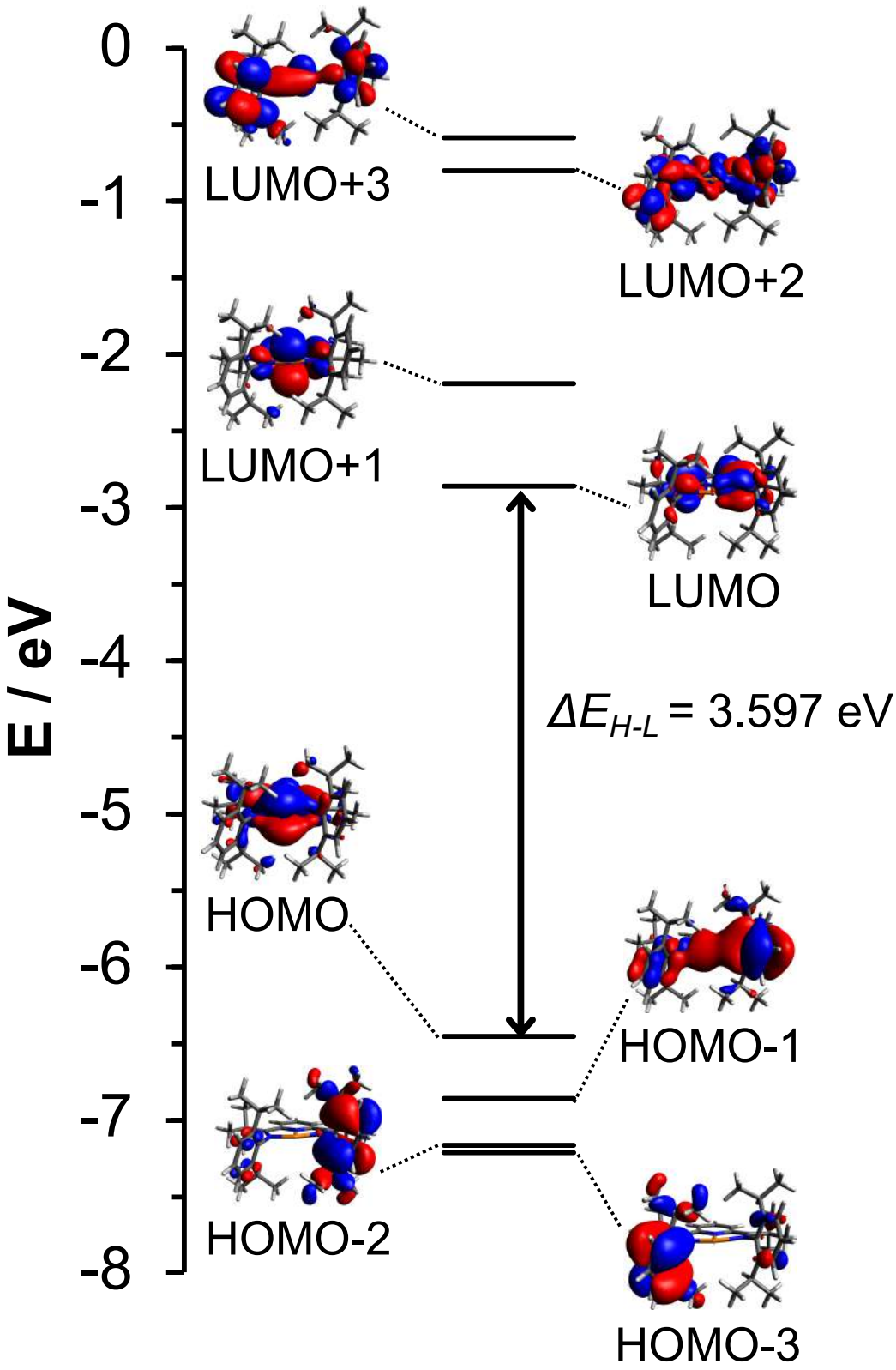

Figure S57. DFT optimized molecular orbital energy level diagrams (SMD-M06/def2SVP, CH_2Cl_2 solvent field) of **[(**^{dipp}**DIP**^{tBu}**)P]**$^{+}$.

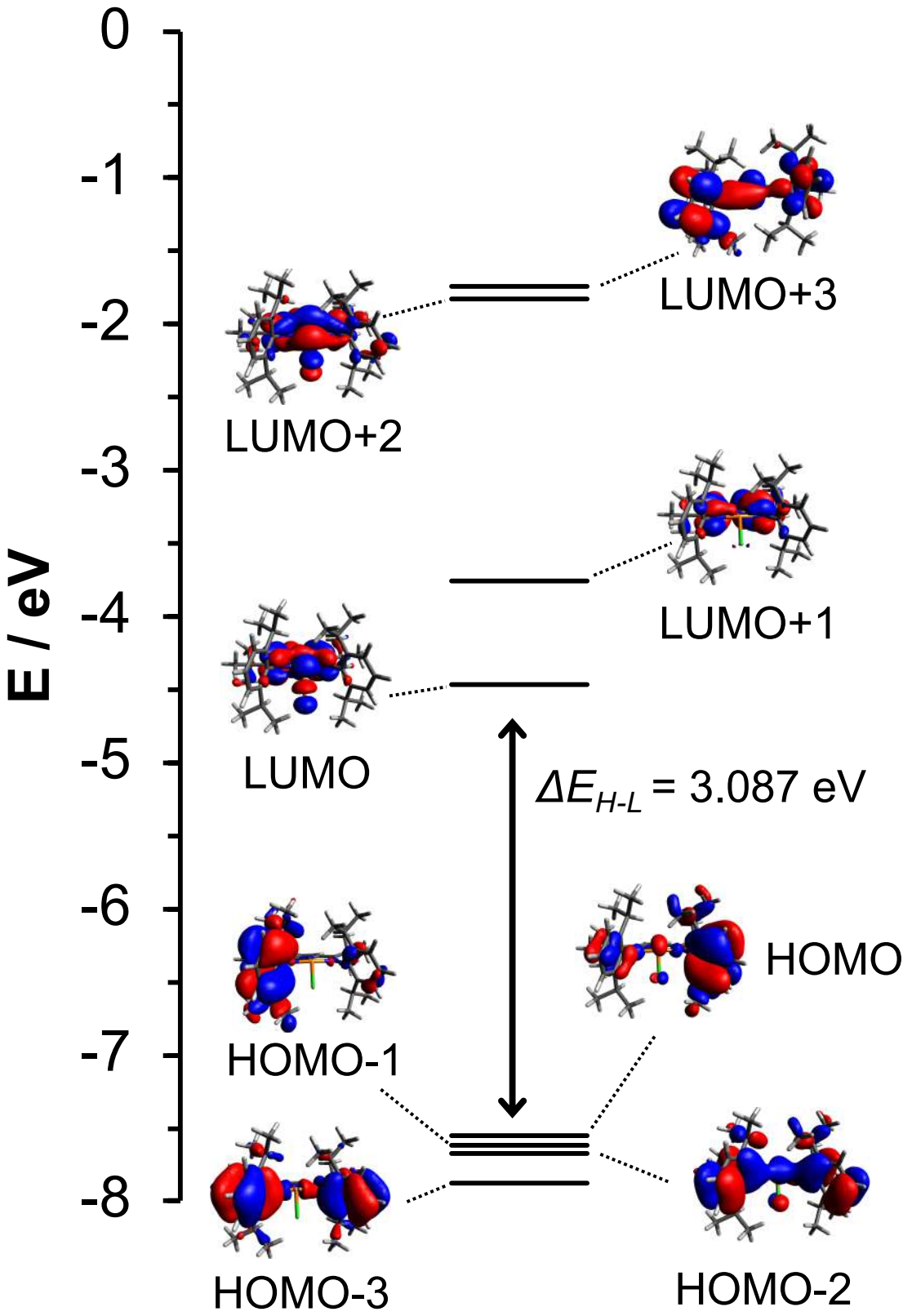

Figure S58. DFT optimized molecular orbital energy level diagrams (SMD-M06/def2SVP, CH_2Cl_2 solvent field) of **[(dippDIPtBu)PCl]$^{2+}$**.

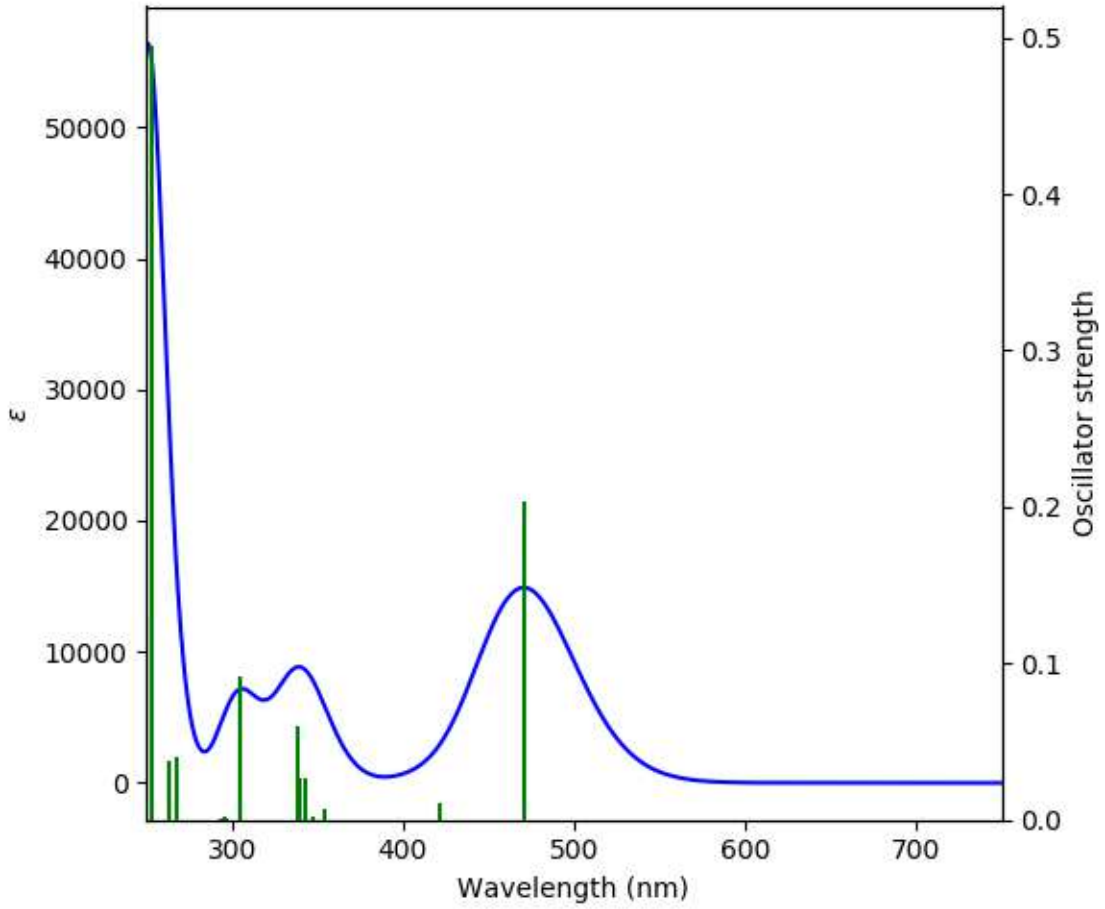

Figure S59. TD-DFT simulated spectrum (blue) and vertical excitation energies (green) for **[(dippDIPtBu)P]**$^{+}$in CH_2Cl_2 (SMD-M06/Def2-SVP; FWHM = 3000 cm^{-1}).

Table S5. TD-DFT predicted vertical excitation energies, wavelengths, oscillator strengths (*f* >0.01) and MO contributions (>10%) for **[(^{dipp}DIP^{tBu})P]$^+$**.

No.	E / eV	λ / nm	*f*	MO Contribution
1	2.63	471	0.204	HOMO->LUMO (98%)
2	2.94	421	0.010	H-1→LUMO (94%)
5	3.62	343	0.027	H-3→LUMO (50%), H-1→L+1 (10%), HOMO→L+1 (31%)
6	3.65	340	0.027	H-4→LUMO (23%), H-3→LUMO (43%), HOMO→L+1 (23%)
7	3.67	338	0.060	H-4→LUMO (36%), H-1→L+1 (19%), HOMO→L+1 (35%)
8	4.07	305	0.092	H-5→LUMO (80%)
9	4.17	297	0.001	H-2→L+1 (93%)
10	4.19	296	0.002	H-4→L+1 (75%), H-3→L+1 (10%)
11	4.23	293	0.001	H-4→L+1 (10%), H-3→L+1 (86%)
12	4.64	267	0.041	H-6→LUMO (31%), H-5→L+1 (13%), HOMO→L+2 (49%)
13	4.70	264	0.038	H-5→L+1 (76%)
14	4.89	254	0.495	H-6→LUMO (43%), HOMO→L+2 (36%)
15	4.95	250	0.130	HOMO→L+3 (63%)
16	5.00	248	0.020	H-1→L+2 (35%), H-1→L+5 (15%), HOMO→L+3 (16%)
17	5.07	245	0.028	H-1→L+2 (16%), H-1→L+5 (12%)
18	5.09	243	0.012	H-1→L+2 (22%), HOMO→L+4 (21%)
19	5.11	243	0.137	H-7→LUMO (12%), H-6→L+1 (60%)
20	5.19	239	0.038	HOMO→L+4 (45%), HOMO→L+5 (32%)
21	5.21	238	0.043	HOMO→L+4 (20%), HOMO→L+5 (48%)
22	5.26	236	0.073	H-7→LUMO (75%), H-6→L+1 (16%)
23	5.32	233	0.052	HOMO→L+6 (71%)
25	5.43	228	0.022	H-8→LUMO (17%), H-1→L+3 (13%), H-1→L+5 (12%), H-1→L+6 (15%)
33	5.70	218	0.067	H-2→L+2 (57%), H-1→L+4 (12%), H-1→L+5 (10%)
34	5.71	217	0.066	H-3→L+2 (19%), H-1→L+4 (21%), HOMO→L+7 (27%)
35	5.73	217	0.031	H-14→LUMO (24%), HOMO→L+7 (46%)
36	5.73	216	0.056	H-14→LUMO (25%), H-1→L+4 (26%), HOMO→L+7 (12%)
37	5.77	215	0.040	H-14→LUMO (14%), H-4→L+2 (24%), H-3→L+2 (10%), H-3→L+3 (10%)
38	5.79	214	0.076	H-16→LUMO (32%), H-15→LUMO (36%)
41	5.90	210	0.028	H-7→L+1 (86%)
42	5.91	210	0.229	H-2→L+3 (23%), H-2→L+5 (19%), H-1→L+6 (25%)

Transition	Natural Transition Orbitals	Electron Density Distribution Map
1	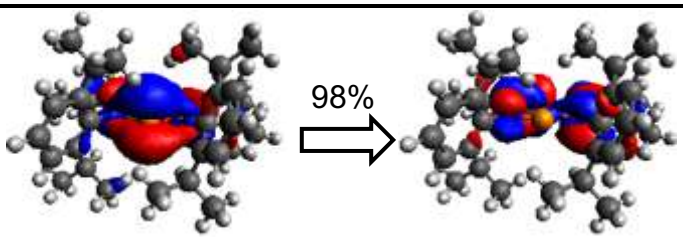	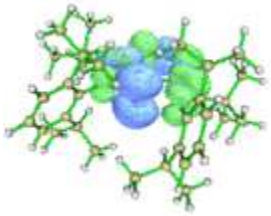
2	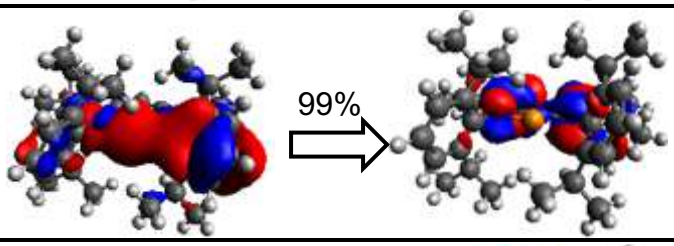	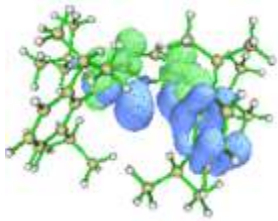
5	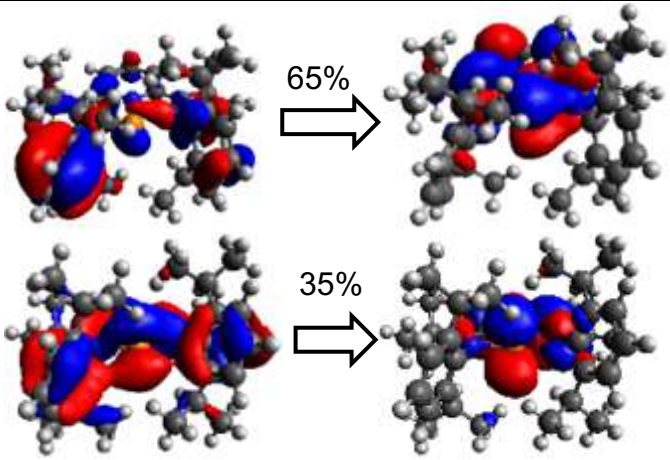	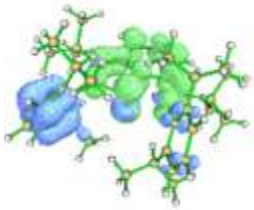

Figure S60. Natural transition orbitals (NTOs: isosurface = 0.05) and TD-DFT calculated electron density gain (green) and depletion (blue) distribution maps (isosurface = 0.003) for the lowest energy transitions (1, 2 and 5) in **[(dippDIP*t*Bu)P]**$^+$ (SMD-M06/Def2-SVP).

Transition	Natural Transition Orbitals	Electron Density Distribution Map
6	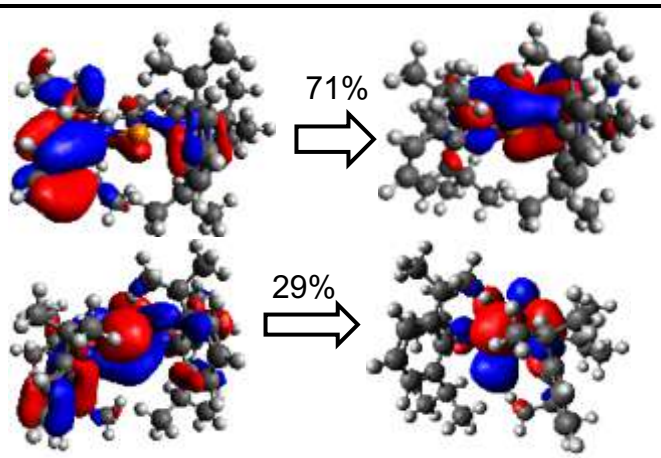	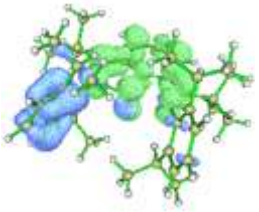
7	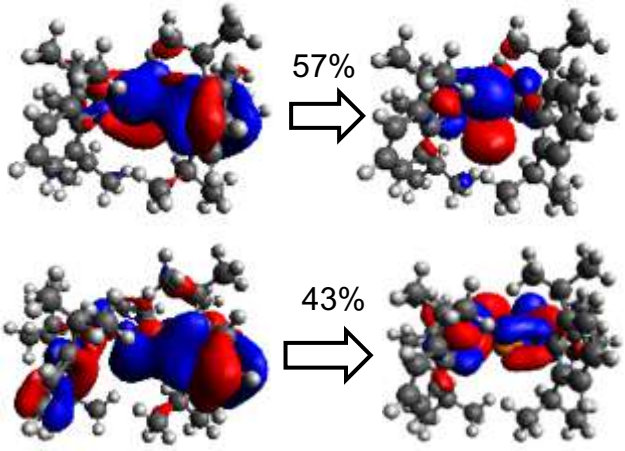	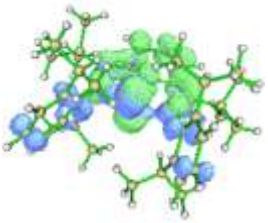
8	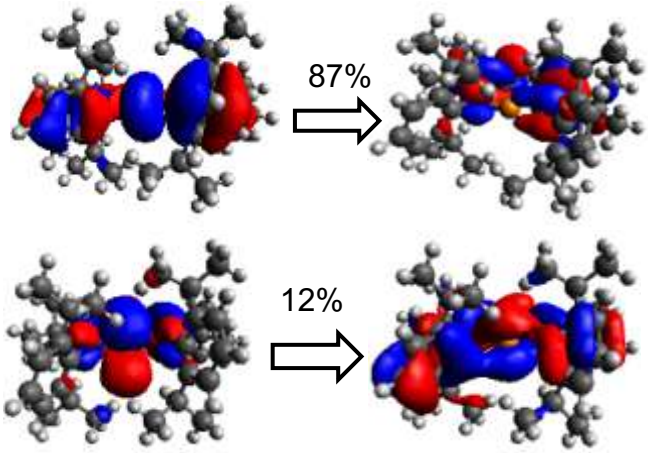	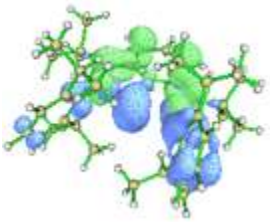

Figure S61. Natural transition orbitals (NTOs: isosurface = 0.05) and TD-DFT calculated electron density gain (green) and depletion (blue) distribution maps (isosurface = 0.003) for the next lowest energy transitions (6, 7 and 8) in **[(dippDIP^{t}Bu)P]$^{+}$** (SMD-M06/Def2-SVP).

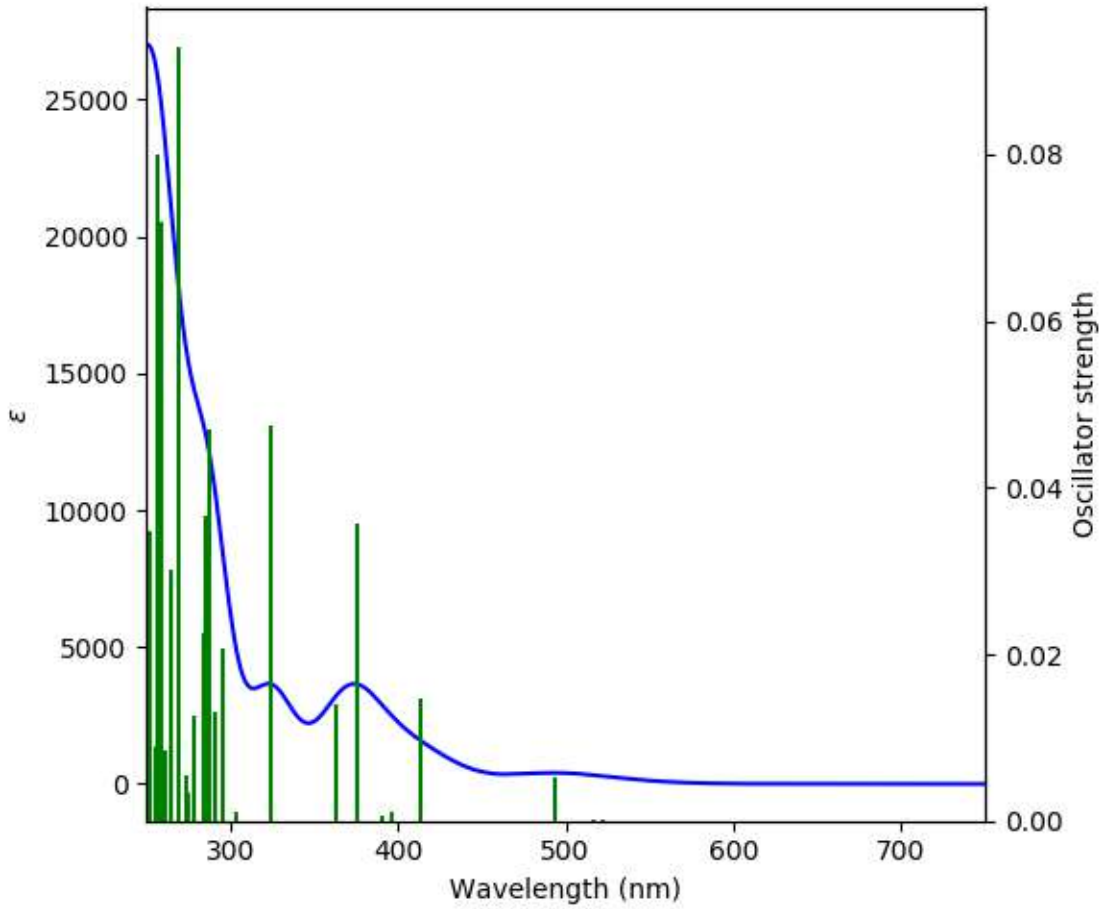

Figure S62. TD-DFT simulated spectrum (blue) and vertical excitation energies (green) for **[(dippDIP^{t}Bu)PCl]$^{2+}$** in CH_2Cl_2 (SMD-M06/Def2-SVP; FWHM = 3000 cm^{-1}).

Table S6. TD-DFT predicted vertical excitation energies, wavelengths, oscillator strengths (*f* >0.01) and MO contributions (>10%) for **[(^{dipp}DIP^{rBu})PCl]$^{2+}$**.

No.	E / eV	λ / nm	*f*	MO Contribution
4	2.51	494	0.005	H-3->LUMO (90%)
5	3.00	413	0.015	H-2->L+1 (38%), HOMO->L+1 (47%)
8	3.30	375	0.036	H-4->LUMO (11%), H-3->L+1 (86%)
9	3.41	363	0.014	H-4->LUMO (84%), H-3->L+1 (10%)
10	3.82	325	0.047	H-5->LUMO (87%)
12	4.20	295	0.021	H-6->LUMO (86%)
13	4.27	291	0.013	H-7->LUMO (86%)
14	4.30	288	0.047	H-8->LUMO (78%)
15	4.35	285	0.037	H-10->LUMO (73%)
16	4.37	284	0.023	H-9->LUMO (84%)
17	4.46	278	0.013	H-12->LUMO (45%), H-11->LUMO (44%)
20	4.60	270	0.093	H-14->LUMO (72%)
21	4.68	265	0.030	H-17->LUMO (31%), H-15->LUMO (19%), H-5->L+1 (27%)
24	4.80	258	0.072	H-17->LUMO (14%), H-5->L+1 (17%), H-2->L+3 (24%), HOMO->L+3 (12%)
25	4.81	258	0.011	H-17->LUMO (14%), H-16->LUMO (13%), H-2->L+3 (27%), HOMO->L+3 (12%)
26	4.83	256	0.080	H-18->LUMO (15%), H-17->LUMO (18%), H-16->LUMO (17%), H-5->L+1 (16%)
28	4.92	252	0.035	H-2->L+2 (32%), H-1->L+2 (13%), HOMO->L+3 (19%)
29	4.96	250	0.015	H-6->L+1 (10%), H-1->L+2 (22%), H-1->L+3 (20%), H-1->L+4 (12%)
30	4.97	249	0.032	H-19->LUMO (50%)
31	4.98	249	0.027	H-6->L+1 (46%), HOMO->L+3 (16%)
33	5.01	248	0.016	H-20->LUMO (18%), H-2->L+2 (14%), H-1->L+3 (22%)
36	5.05	246	0.013	H-2->L+3 (14%), H-1->L+3 (22%), H-1->L+4 (22%)
38	5.09	244	0.012	H-24->LUMO (13%), H-10->L+1 (14%), H-9->L+1 (17%), H-8->L+1 (19%)
39	5.11	243	0.039	H-3->L+2 (13%), H-3->L+3 (52%), H-1->L+2 (17%)
41	5.14	241	0.019	H-3->L+2 (11%), H-1->L+2 (38%), H-1->L+4 (11%)
42	5.16	240	0.024	H-24->LUMO (11%), H-10->L+1 (12%), H-9->L+1 (25%)
43	5.16	240	0.020	H-3->L+2 (18%), HOMO->L+2 (16%), HOMO->L+5 (17%)
44	5.17	240	0.016	H-21->LUMO (67%)
48	5.26	236	0.011	H-3->L+2 (24%), H-3->L+3 (13%)
49	5.27	235	0.065	H-25->LUMO (11%), H-12->L+1 (44%)
50	5.29	234	0.069	H-13->L+1 (71%)

Transition	Natural Transition Orbitals	Electron Density Distribution Map
4	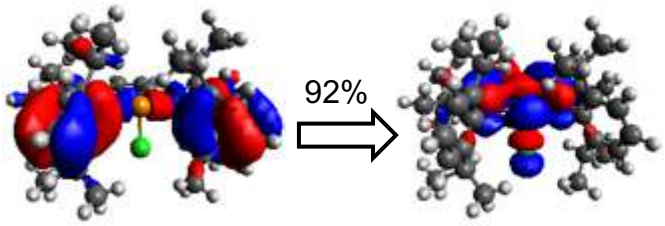	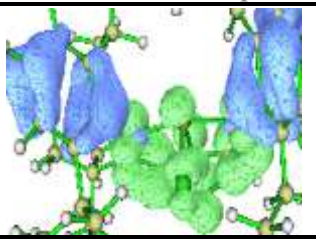
5	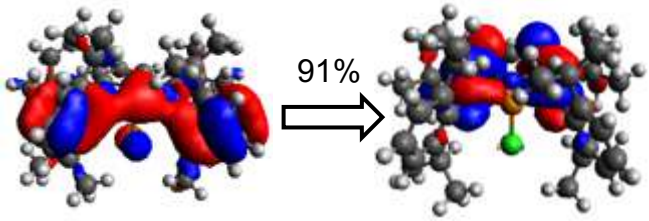	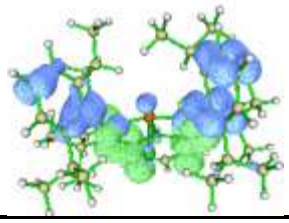
8	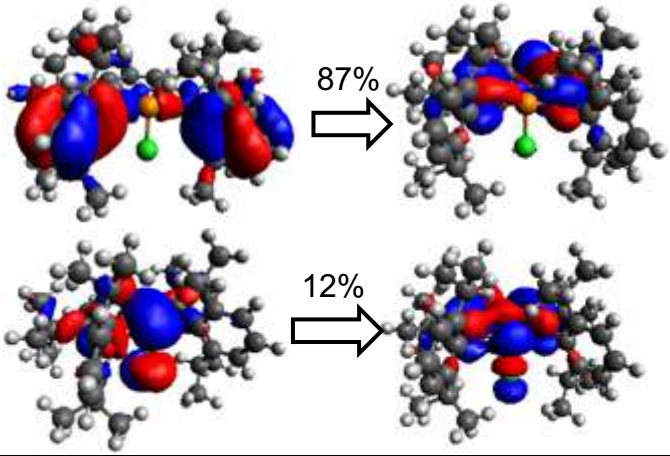	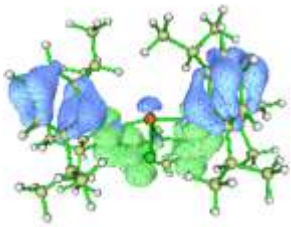

Figure S63. Natural transition orbitals (NTOs: isosurface = 0.05) and TD-DFT calculated electron density gain (green) and depletion (blue) distribution maps (isosurface = 0.003) for the lowest energy transitions (4, 5 and 8) in **[(^{dipp}DIP^{tBu})PCl]$^{2+}$** (SMD-M06/dev2SVP).

Transition	Natural Transition Orbitals	Electron Density Distribution Map
9	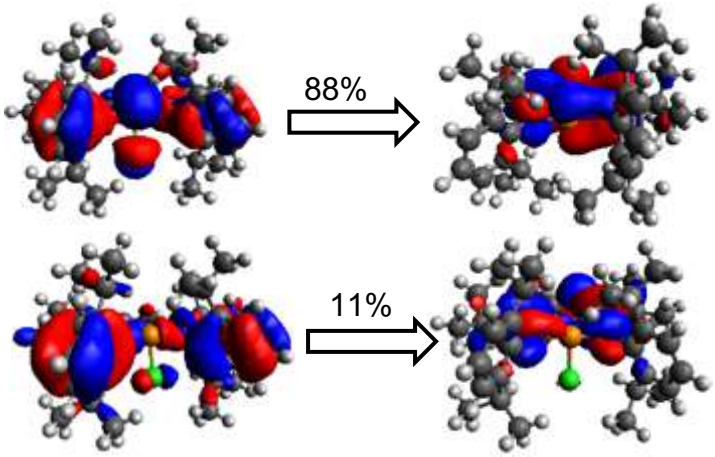	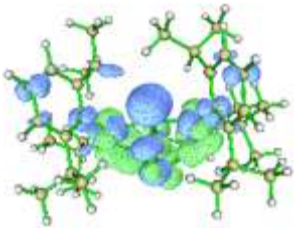
10	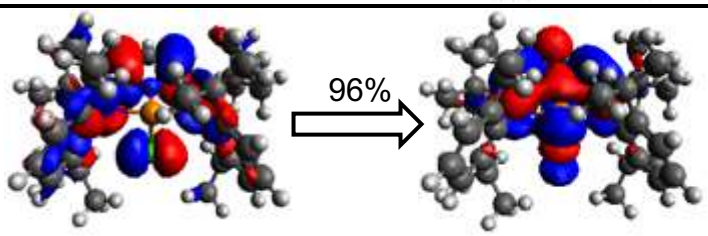	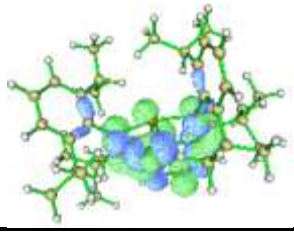

Figure S64. Natural transition orbitals (NTOs: isosurface = 0.05) and TD-DFT calculated electron density gain (green) and depletion (blue) distribution maps (isosurface = 0.003) for the next lowest energy transitions (9 and 10) in **[(^{dipp}DIP^{tBu})PCl]$^{2+}$** (SMD-M06/dev2SVP).

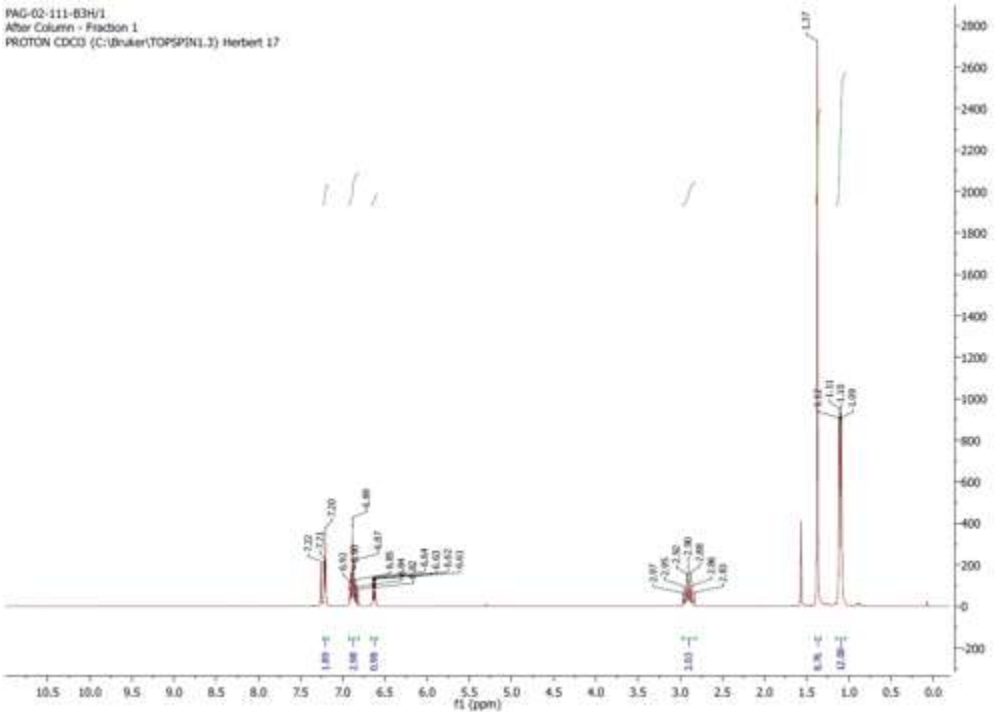

Figure S65. ^{1}H NMR ($CDCl_3$, 300 MHz, 25 °C) of [1-(6-bromo-pyridin-2-yl)-2,2-dimethyl-propylidene]-(2,6-diisopropyl-phenyl)amine.

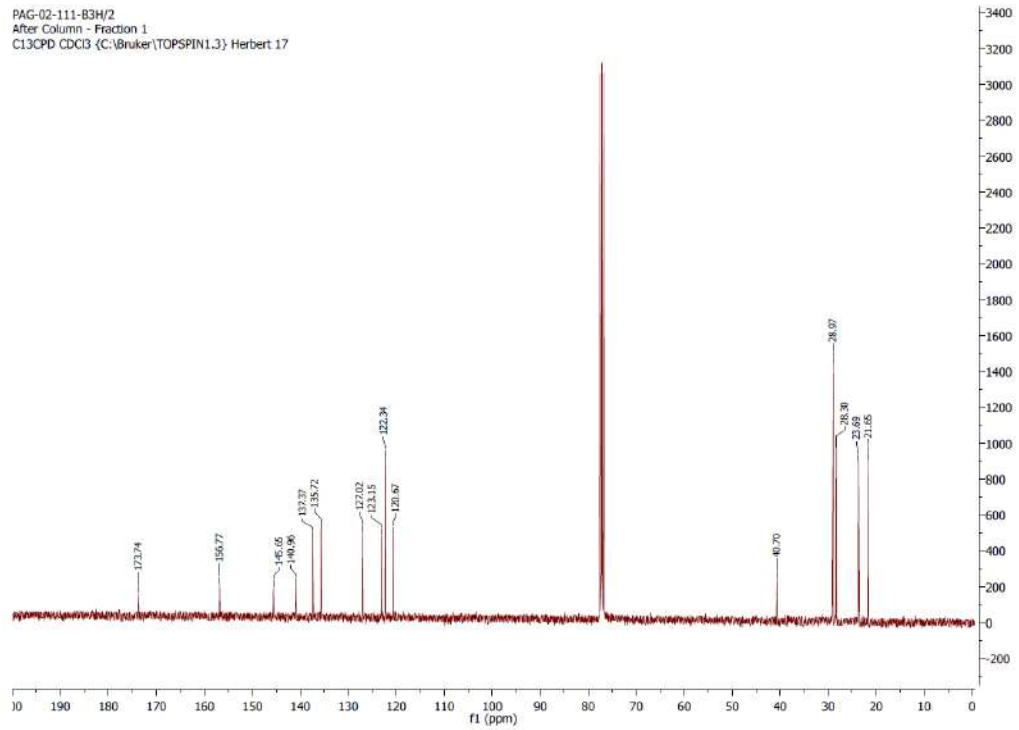

Figure S66. $^{13}C\{^{1}H\}$ NMR ($CDCl_2$, 75 MHz, 25 °C) of [1-(6-bromo-pyridin-2-yl)-2,2-dimethyl-propylidene]-(2,6-diisopropyl-phenyl)amine.

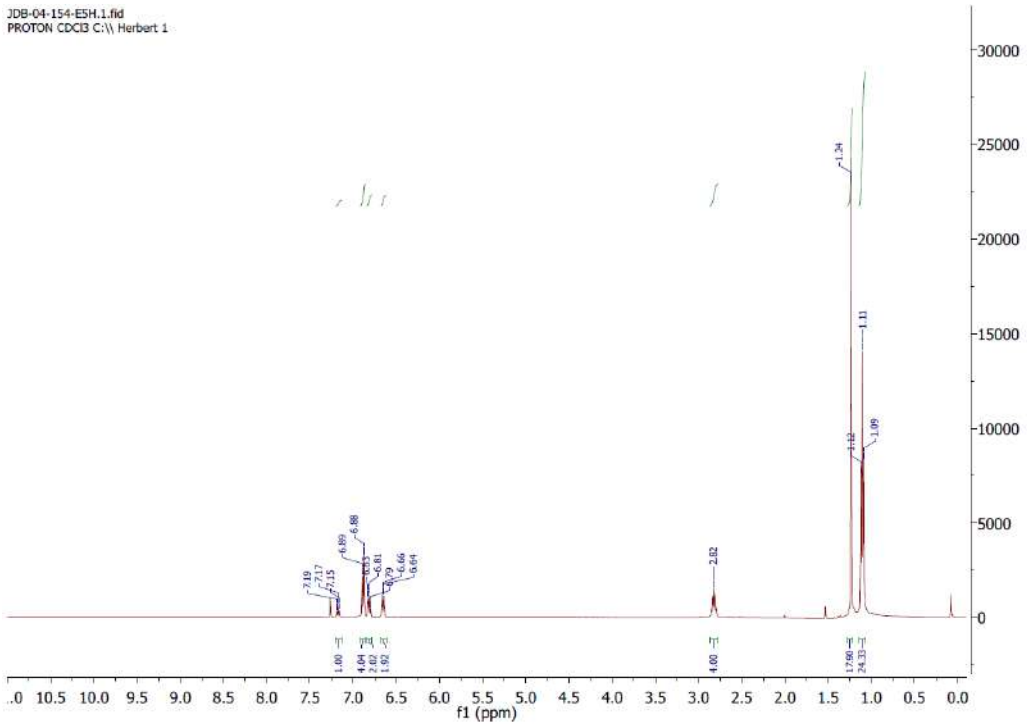

Figure S67. ^{1}H NMR ($CDCl_3$, 500 MHz, 25°C) of ^{dipp}**DIP**$^{t\mathbf{Bu}}$.

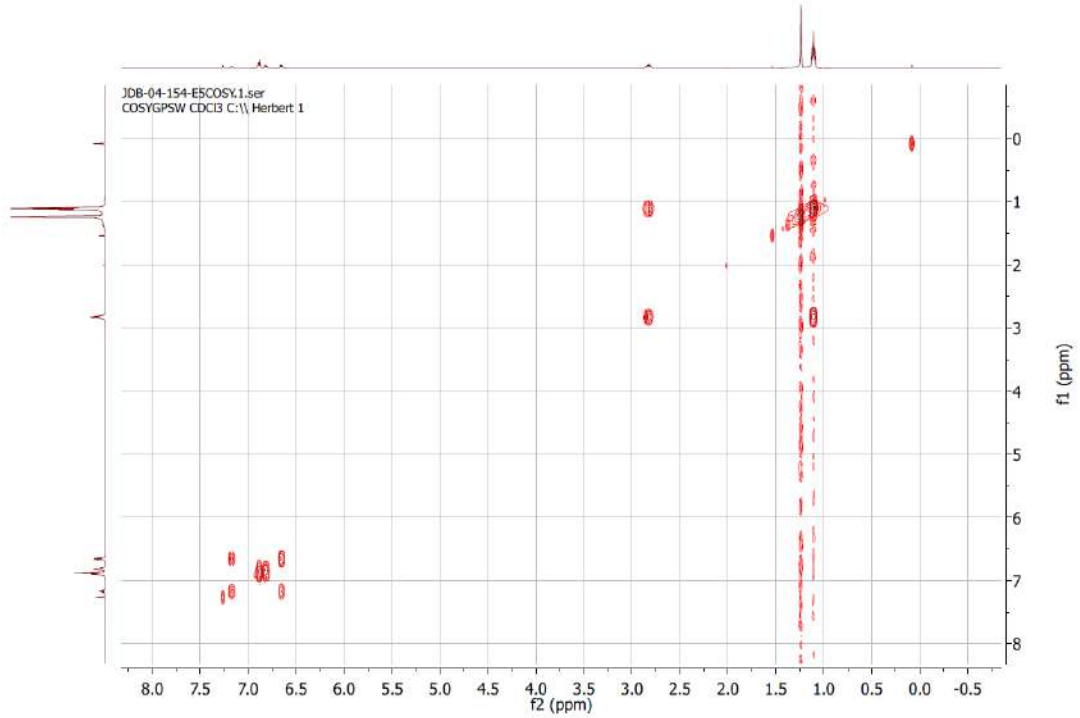

Figure S68. ^{1}H-^{1}H COSY NMR ($CDCl_3$, 500 MHz, 25°C) of ^{dipp}**DIP**$^{t\mathbf{Bu}}$.

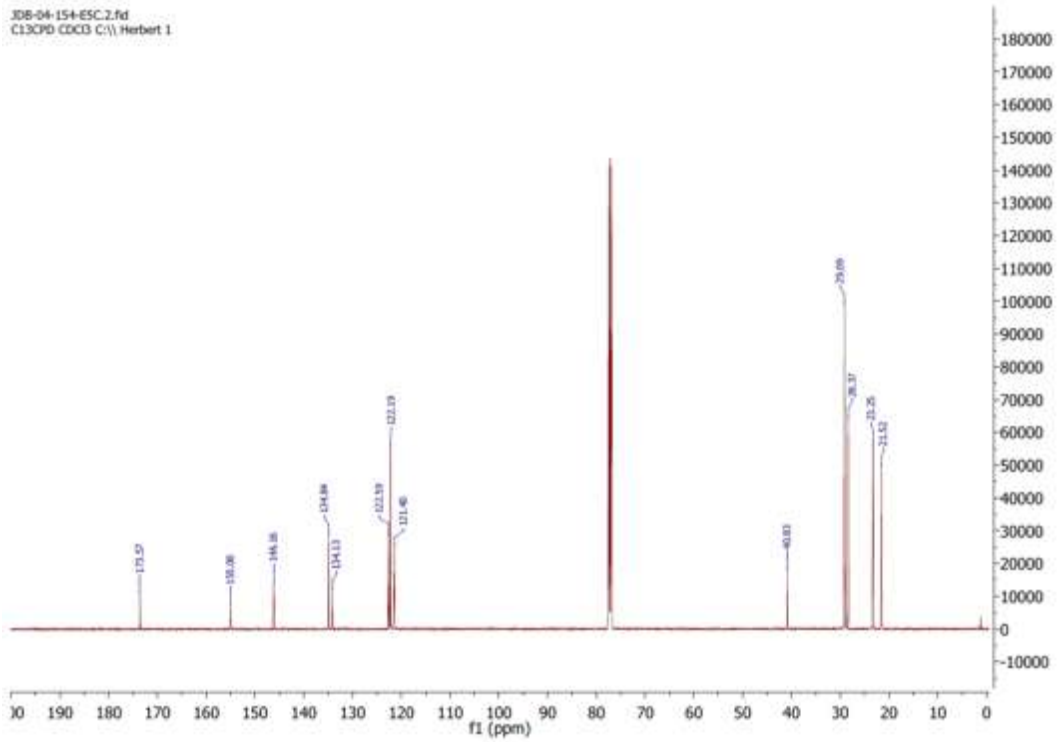

Figure S69. $^{13}C\{^{1}H\}$ NMR ($CDCl_3$, 125 MHz, 25°C) of $^{dipp}DIP^{tBu}$.

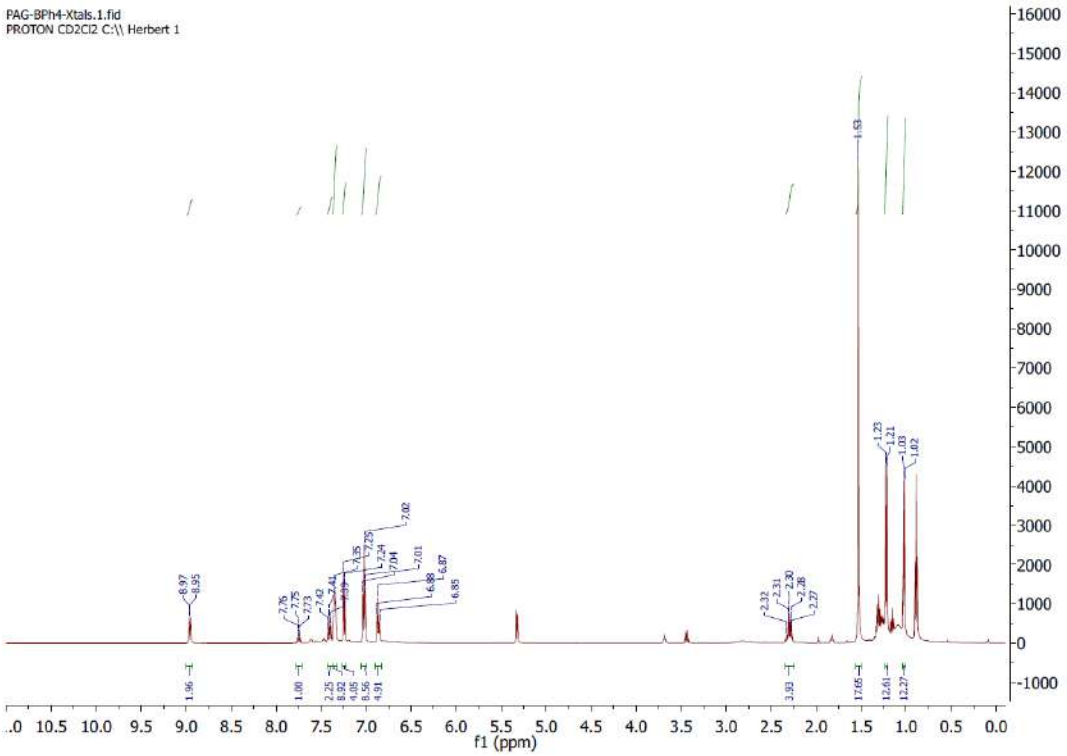

Figure S70. ^{1}H NMR ($CDCl_3$, 500 MHz, 25 °C) of **[($^{dipp}DIP^{tBu}$)P][BPh_4]**.

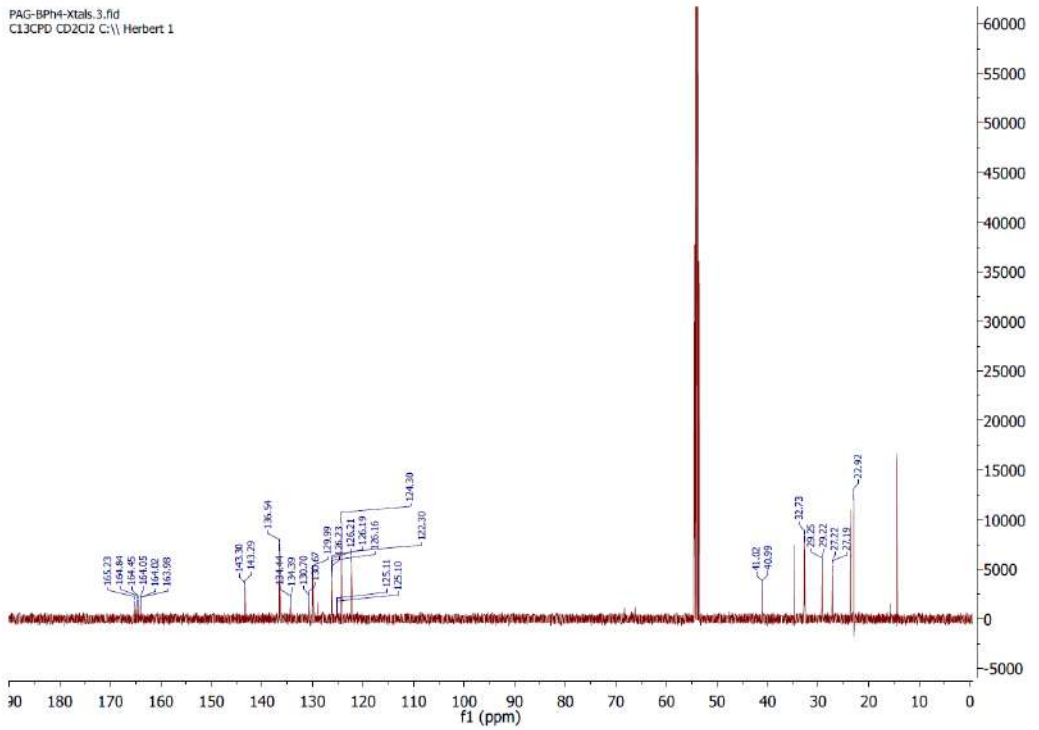

Figure S71. $^{13}C\{^{1}H\}$ NMR ($CDCl_3$, 125 MHz, 25 °C) of **[(dippDIP^{t}Bu)P][BPh$_4$]**.

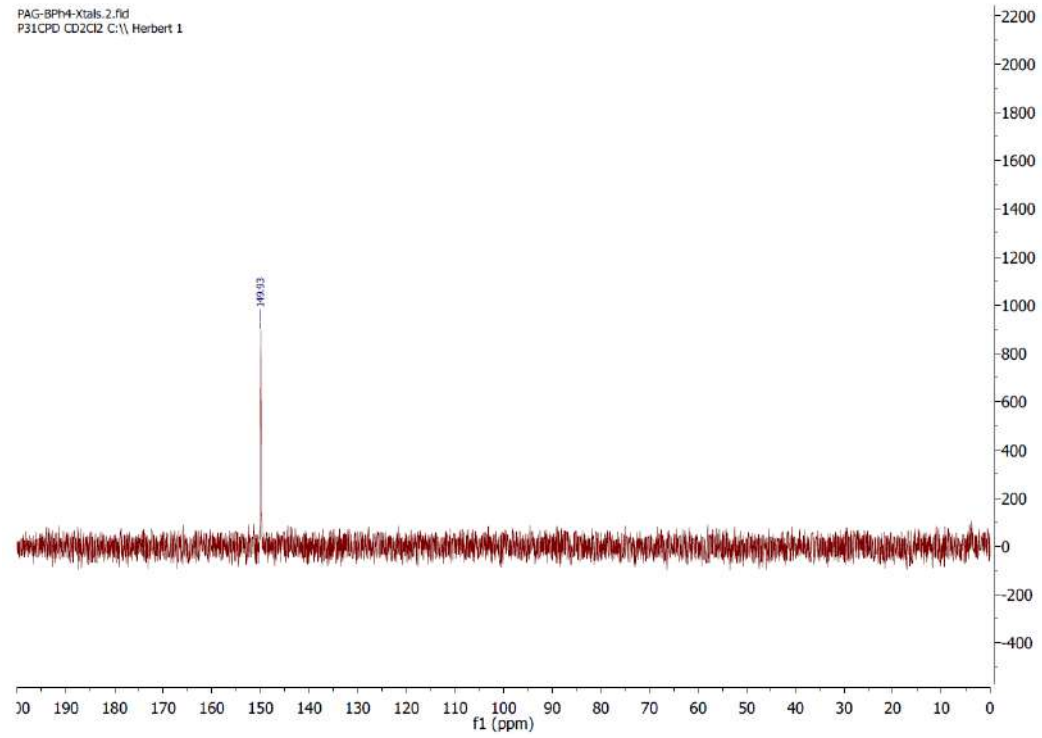

Figure S72. $^{31}P\{^{1}H\}$ NMR ($CDCl_3$, 202 MHz, 25 °C) of **[(dippDIP^{t}Bu)P][BPh$_4$]**.

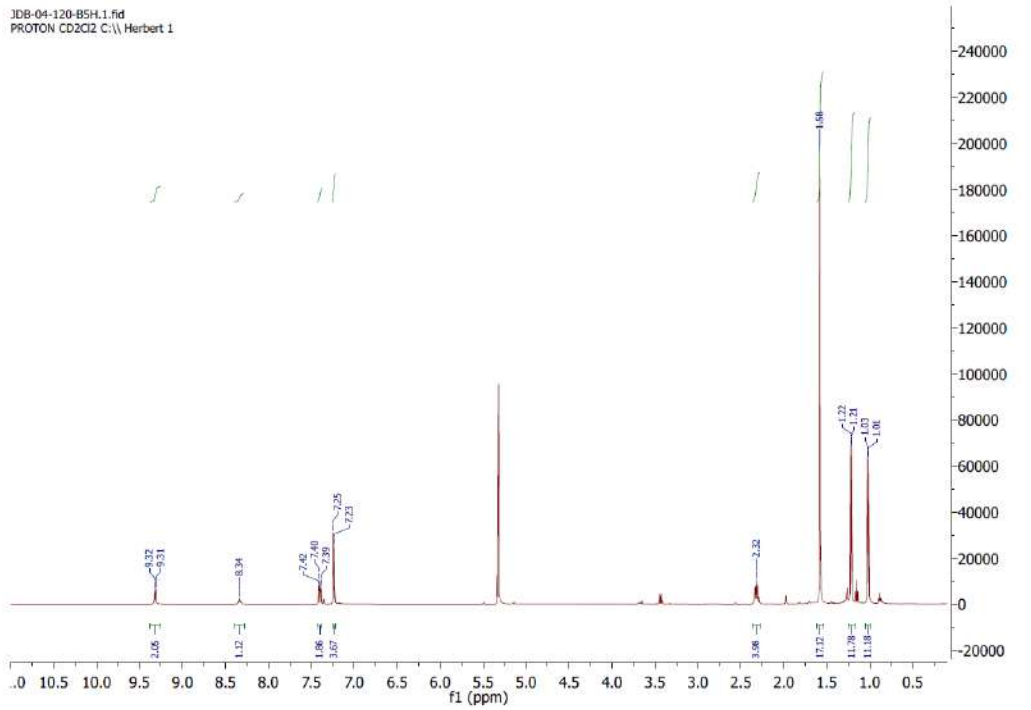

Figure S73. ^{1}H NMR (CD_2Cl_2, 500 MHz, 25 °C) of **[(^dipp^DIP^rBu^)P][OTf]**.

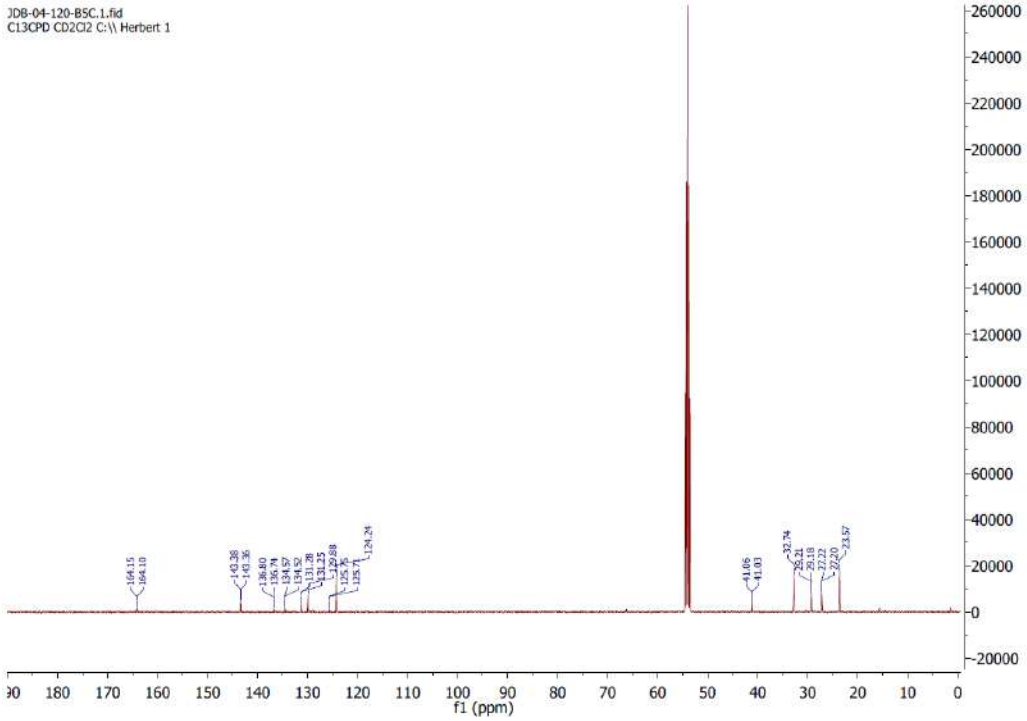

Figure S74. ^{13}C{^{1}H} NMR (CD_2Cl_2, 125 MHz, 25 °C) of **[(^dipp^DIP^rBu^)P][OTf]**.

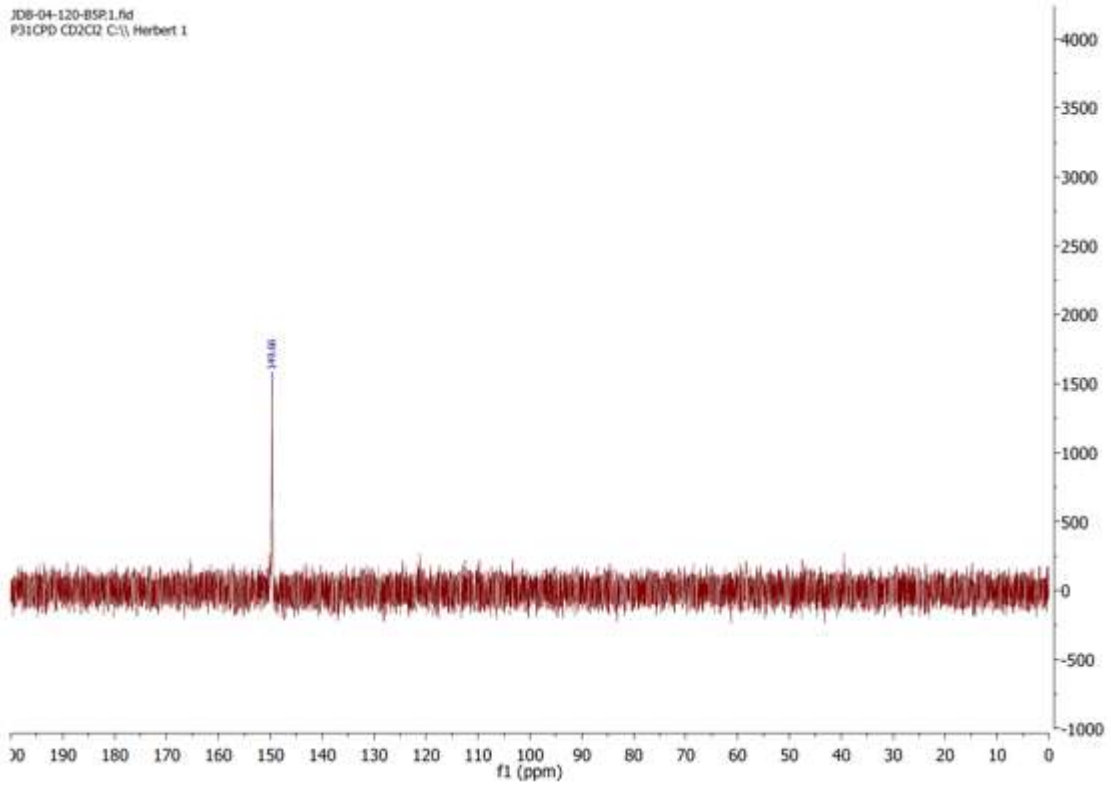

Figure S75. $^{31}P\{^{1}H\}$ NMR (CD_2Cl_2, 202 MHz, 25 °C) of **[(^dippDIP^tBu)P][OTf]**.

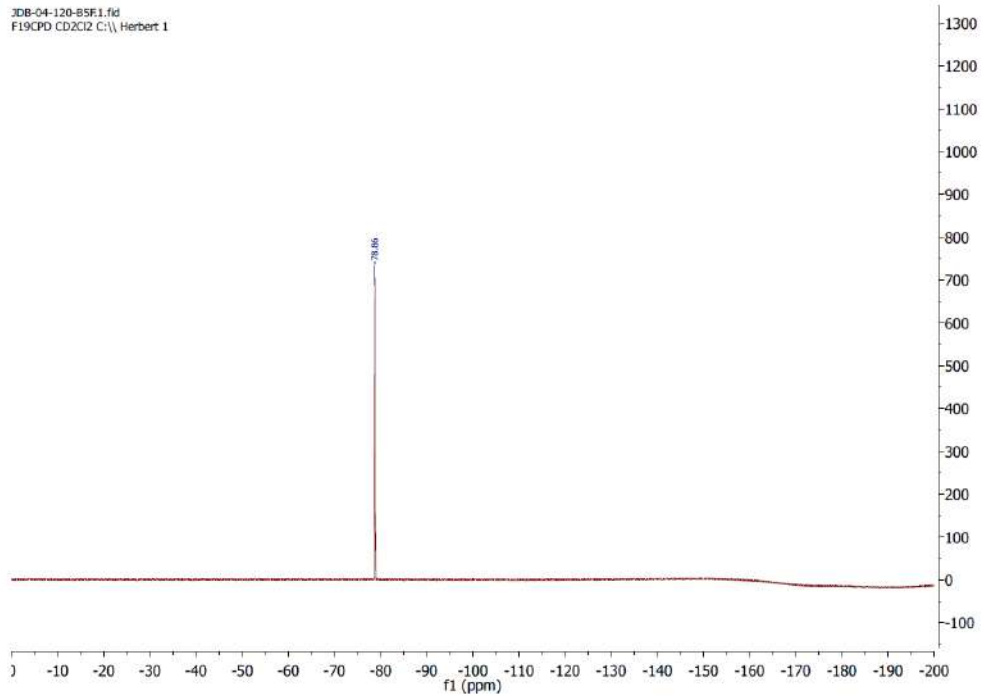

Figure S76. $^{19}F\{^{1}H\}$ NMR (CD_2Cl_2, 471 MHz, 25 °C) of **[(^dippDIP^tBu)P][OTf]**.

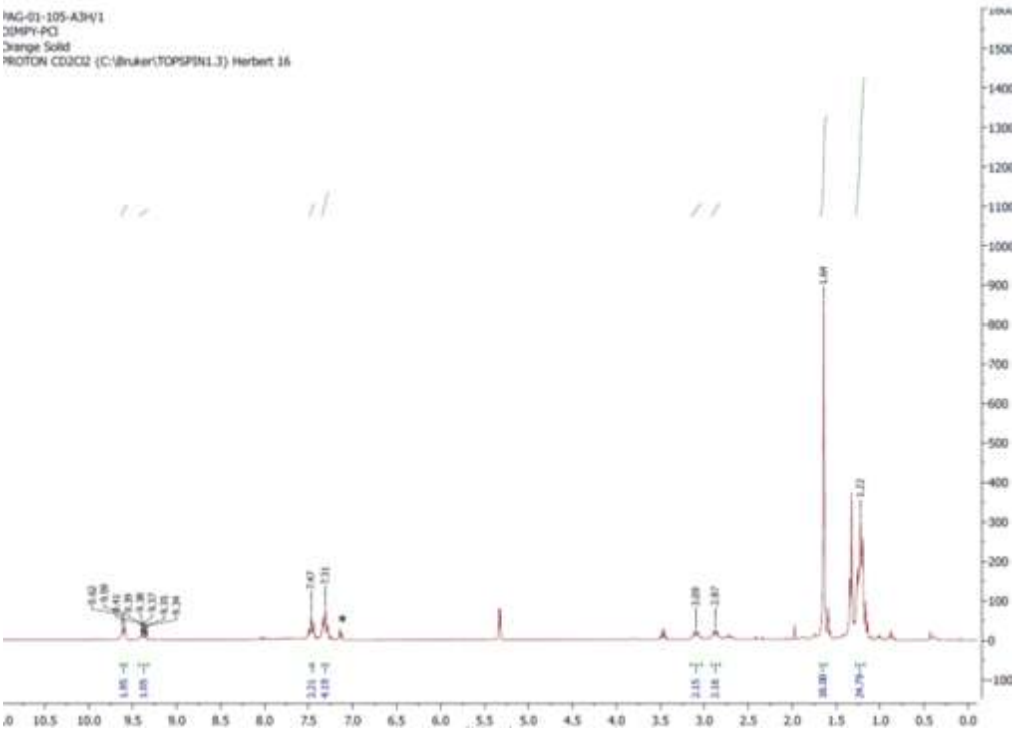

Figure S77. ^{1}H NMR (CD_2Cl_2, 300 MHz, 25 °C) of **[(^{dipp}DIP^{tBu})PCl][OTf]$_2$**.

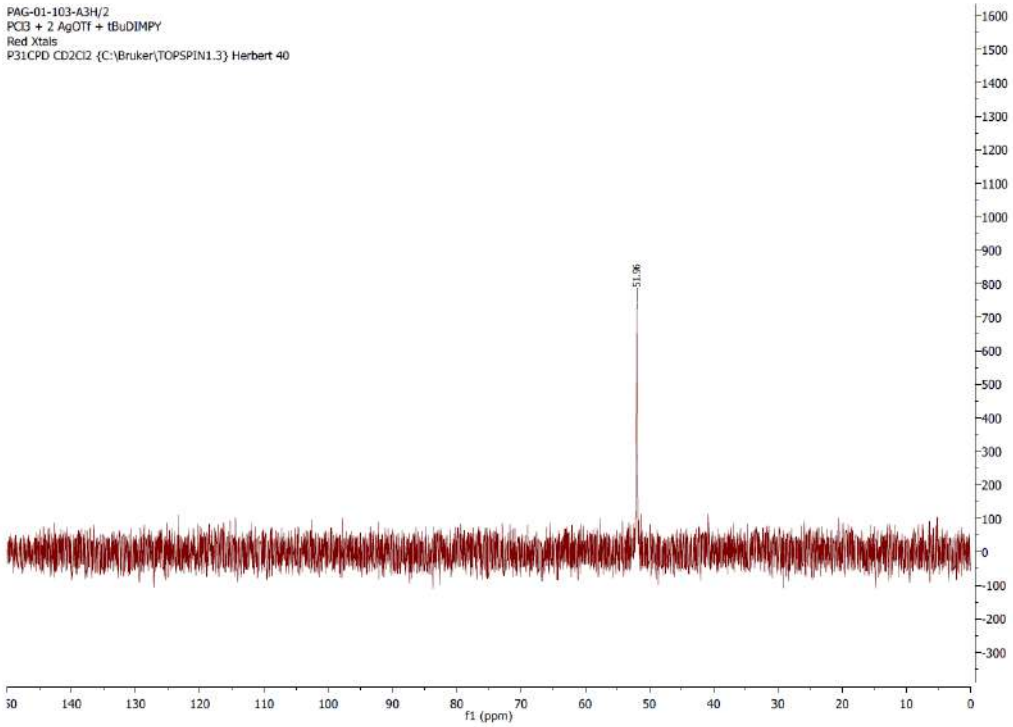

Figure S78. $^{31}P\{^{1}H\}$ NMR (CD_2Cl_2, 121 MHz, 25 °C) of **[(^{dipp}DIP^{tBu})PCl][OTf]$_2$**.

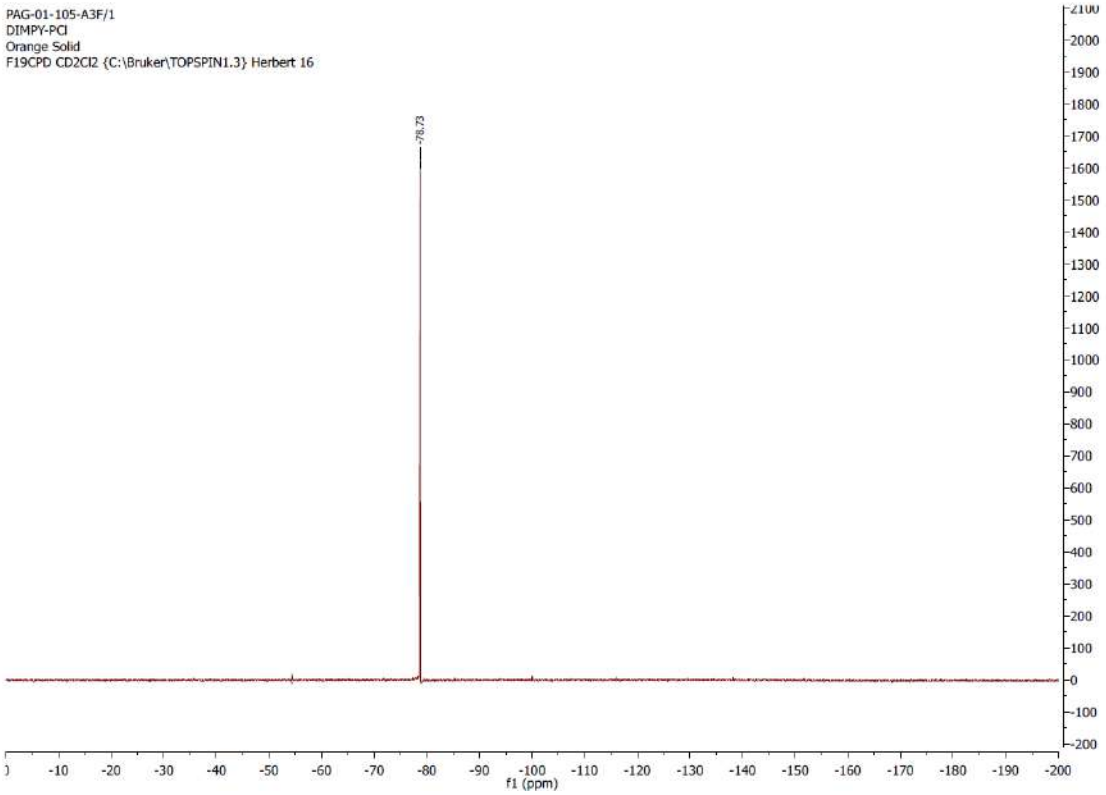

Figure S79. $^{19}F\{^{1}H\}$ NMR (CD_2Cl_2, 282 MHz, 25 °C) of **[(^{dipp}DIP^{tBu})PCl][OTf]$_2$**.

Table S7. ^{31}P NMR Chemical shifts and oxidation states of known (DIP)P(I) and (DIP)P(III) complexes and those reported here.

Compound	Oxidation State	^{31}P NMR Shift (ppm)
[(^{dipp}DIP^{H})P][I$_3$][8]	+1	154
[(^{dipp}DIP^{H})P][B$_{12}$Cl$_{12}$][8]	+1	169
[(^{dipp}DIP^{H})P][B$_{12}$Cl$_{12}$][8]	+1	166
[(^{dipp}DIP^{Ph})P][I$_3$][8]	+1	154
[(^{Fc}DIP^{H})P][I$_3$][9]	+1	124.0
(^{dipp}DIP^{tBu})P[OTf] (this work)	+1	149.7
(^{dipp}DIP^{tBu})P[BPh$_4$] (this work)	+1	149.9
[(^{Mes}DIP^{Me})PPh][OTf]$_2$[10]	+3	33.5
[(^{dipp}DIP^{Me})PPh][OTf]$_2$[10]	+3	61.2
[(^{dipp}DIP^{tBu})PCl][OTf]$_2$ (this work)	+3	52.0

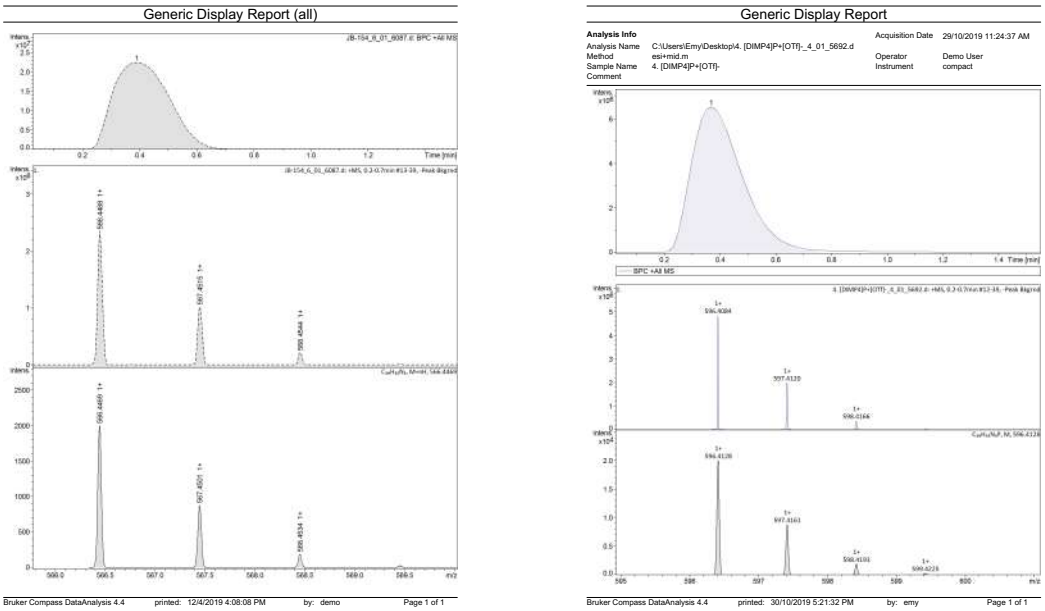

Figure S80. MS (ESI-TOF/MS, m/z) for ^{dipp}**DIP**$^{t\mathbf{Bu}}$ (left) and **[(**^{dipp}**DIP**$^{t\mathbf{Bu}}$**)P][OTf]** (right).

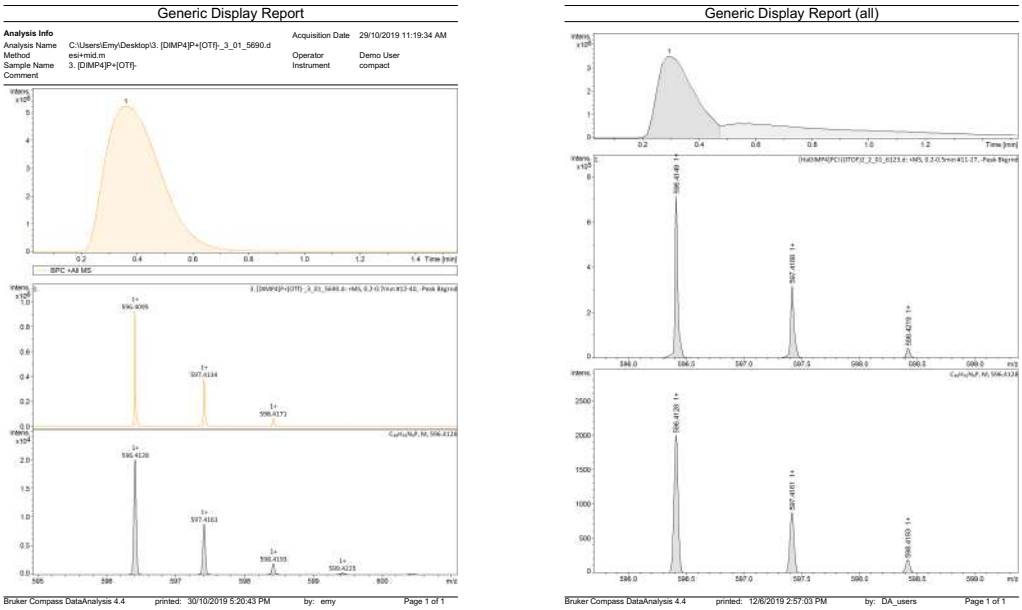

Figure S81. MS (ESI-TOF/MS, m/z) for **[(**^{dipp}**DIP**$^{t\mathbf{Bu}}$**)P][BPh$_4$]** (left) and **[(**^{dipp}**DIP**$^{t\mathbf{Bu}}$**)PCl][OTf]$_2$** (right).

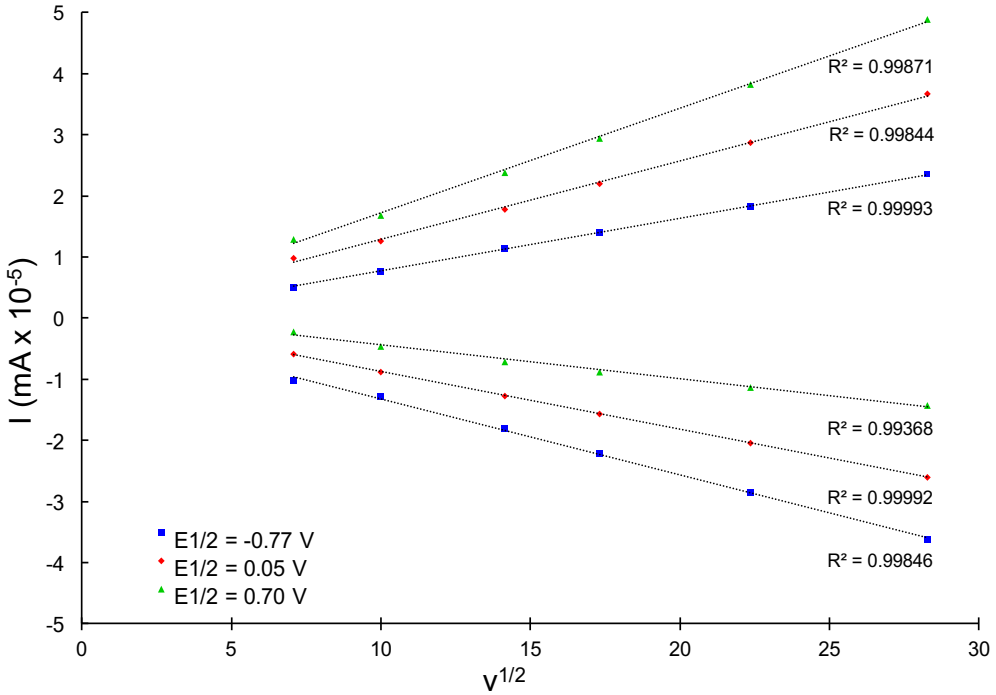

Figure S82. Scan rate dependence (CV) for [**6a**]PF_6.

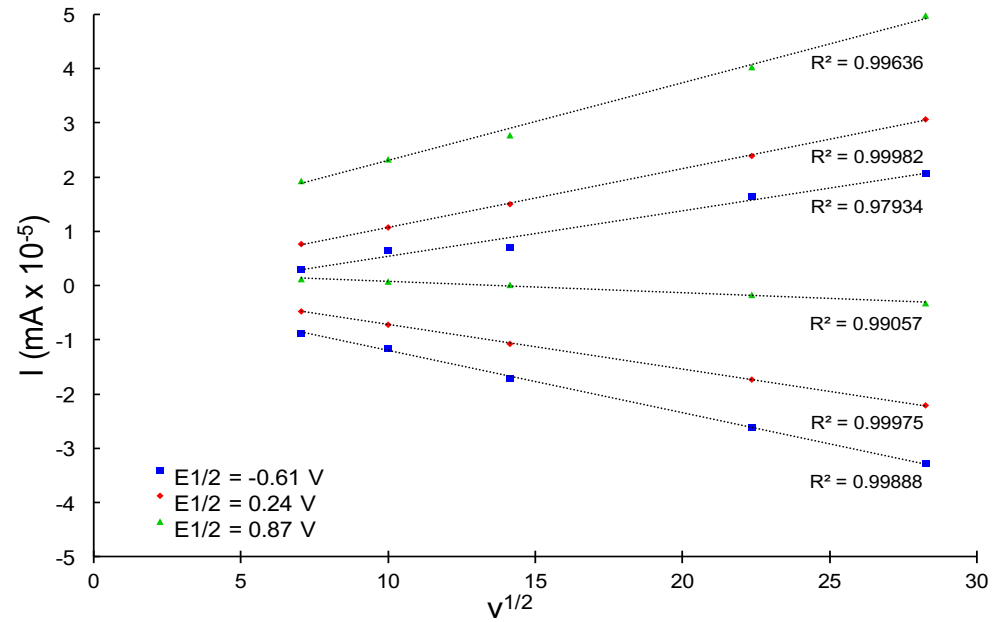

Figure S83. Scan rate dependence (CV) for [**6b**]PF_6.

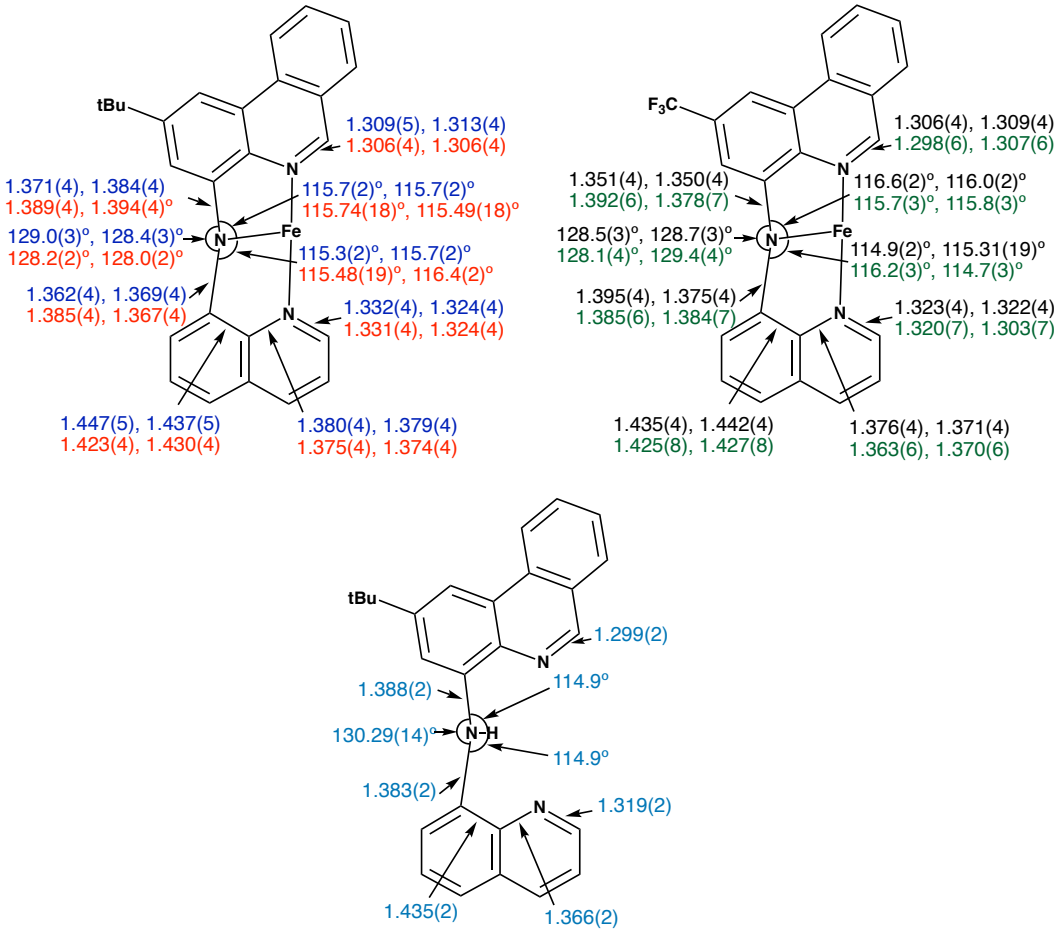

Figure S84. Comparison of bond distances and angles for **5a**, **6a-b** and [**6a-b**]$^{+}$.

MÖSSBAUER AND EPR SPECTROSCOPY

Experimental Details

Mössbauer spectroscopy experiments were performed in zero field in a transmission geometry with a 10 GBq ^{57}Co in Rh source and a WissEl constant acceleration drive. Spectra were collected at 10 K using a Janis SHI-850 closed-cycle refrigerator and were calibrated relative to α-Fe at room temperature. EPR spectra were collected on a Bruker Elexsys 580 FT/CW EPR console at 20 K (X-band; [**6a**]$^{+}$: frequency = 9.469 GHz, power = 2.050 mW; [**6b**]$^{+}$: frequency = 9.472 GHz, power = 2.050 mW). Spectral parameters were simulated using *Easyspin*[10] incorporated in MATLAB.

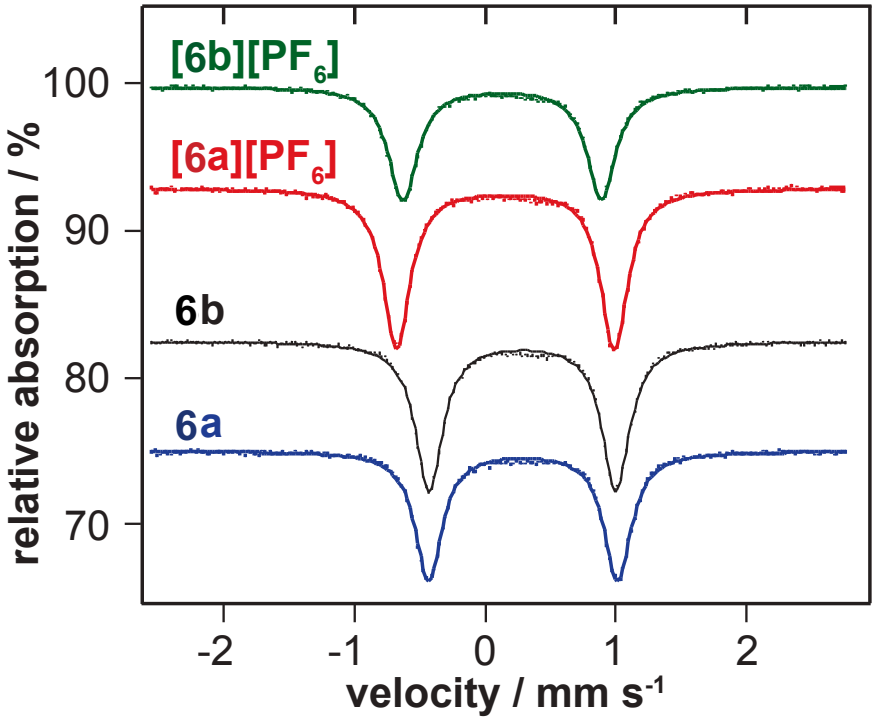

Figure S85. Mössbauer spectra (10 K) of **6a**-b and [**6a**-**b**]PF_6.

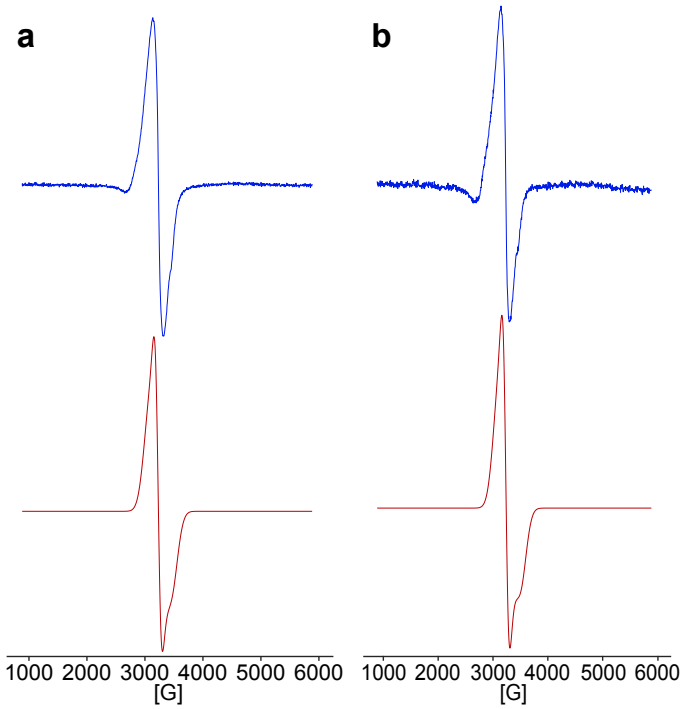

Figure S86. X-band EPR spectrum (top) and simulations (bottom) in frozen CH_2Cl_2 glass at 20 K of (a) [**6a**]PF_6 and (b) [**6b**]PF_6 (ν= 9.469 GHz, power = 2.050 mW; [**6b**]PF_6: ν = 9.472 GHz, power = 2.050 mW). Simulation parameters: [**6a**]PF_6: g = [2.21 2.10 1.95], lw = 10, HStrain = [700 150 600]; [**6b**]PF_6: g = [2.20 2.10 1.93], lw = 10, HStrain [700 150 600].

STEADY-STATE ABSORPTION SPECTROSCOPY AND SPECTROELECTROCHEMISTRY

Experimental Details

Electronic absorption spectra were recorded on an Agilent Technologies Cary 5000 Series UV-Vis-NIR spectrophotometer in dual beam mode (range: 230 – 1600 nm).

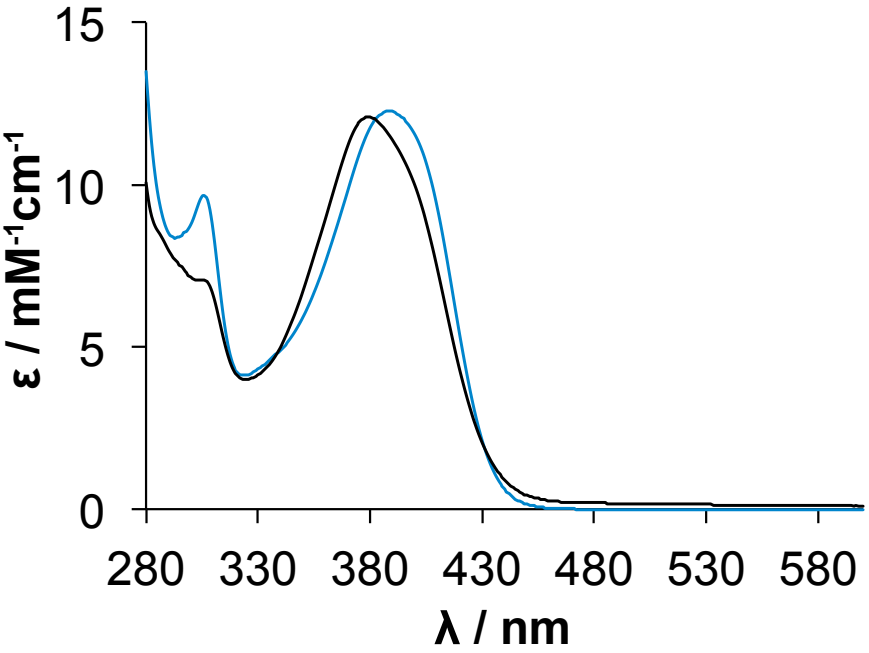

Figure S87. UV-Vis absorption spectra of proligands **5a** (blue) and **5b** (black) in CH_3CN.

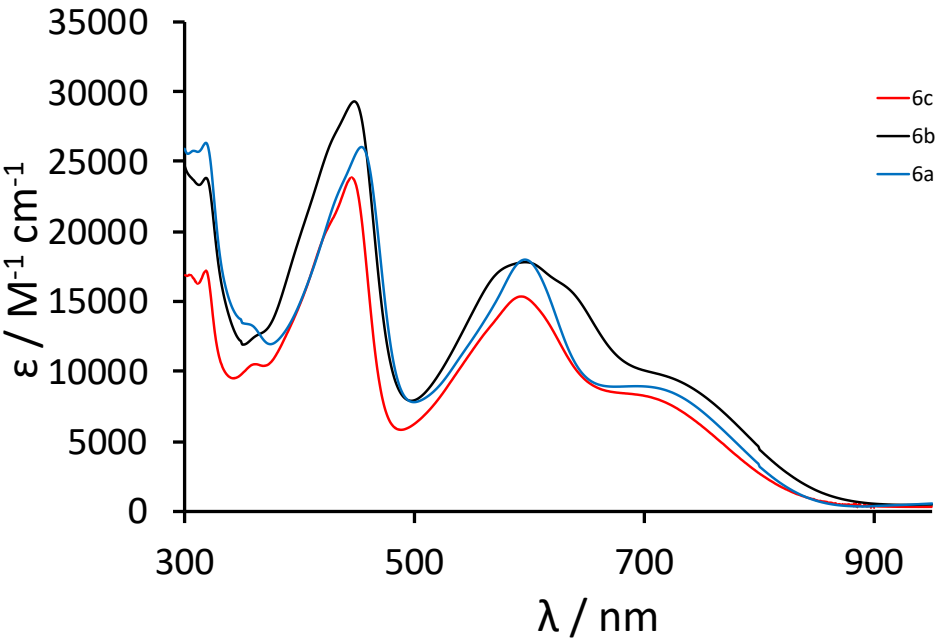

Figure S88. UV-Vis absorption spectra of neutral complexes **6a-c**

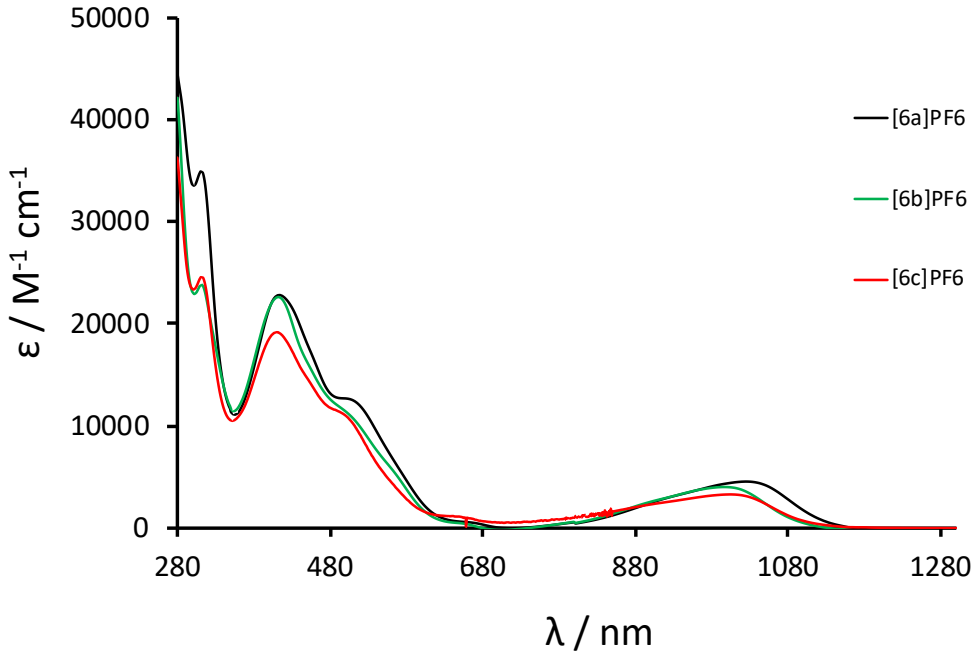

Figure S89. UV-Vis absorption spectra of cationic complexes [**6a-c**]PF_6

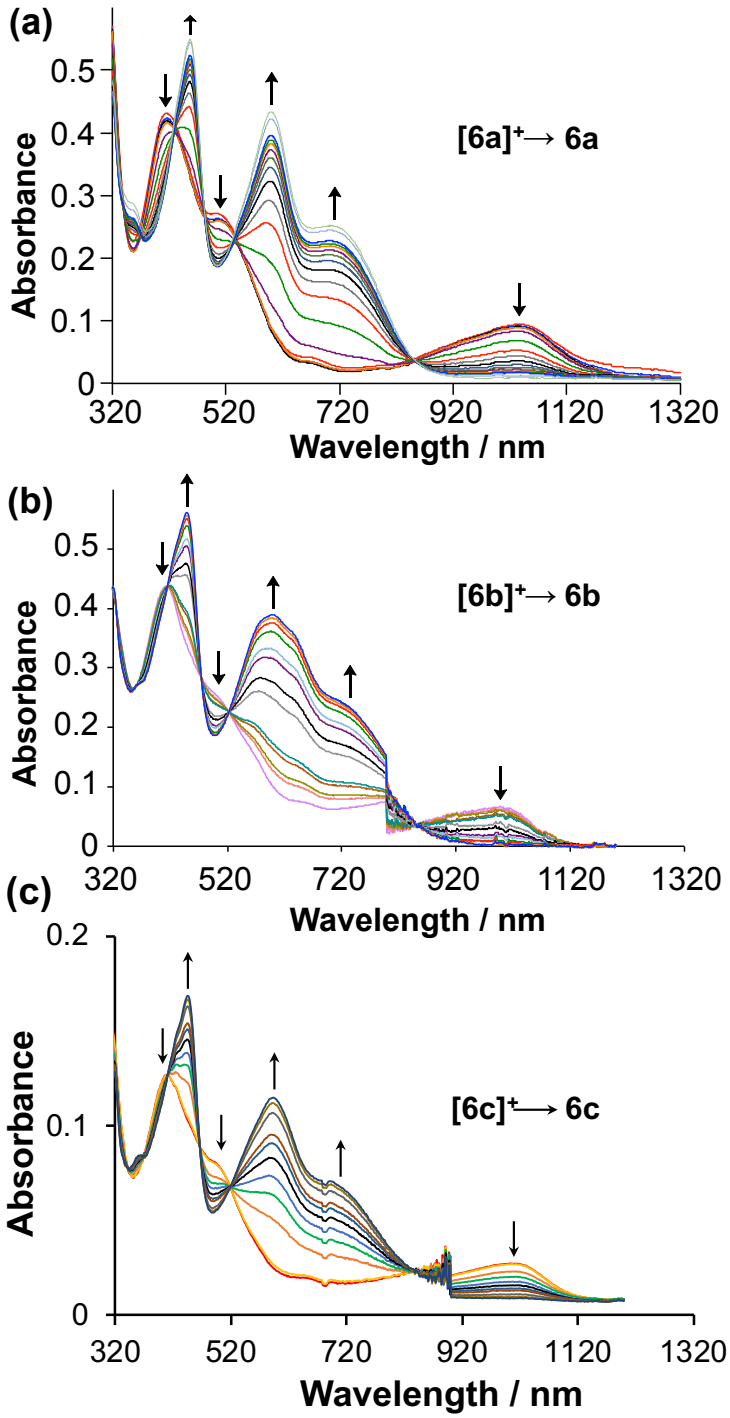

Figure S90. UV-Vis/NIR absorption spectra of (a) [**6a**]PF_6, (b) [**6b**]PF_6 and (c) [**6c**]PF_6 in 0.3 M [^{n}Bu$_4$N]PF_6 CH_3CN solution, with reductive potentials applied from -0.1 to -0.5 V.

DFT AND TD-DFT CALCULATIONS

Computational Details

All calculations were carried out using Gaussian 09, Revision E01.[11] Solvent effects were included using the solvation model based on density (SMD, solvent = CH_3CN).[6] Unless otherwise stated, the restricted KS formalism was used for the singlet ground state electronic configuration while the unrestricted KS formalism was used for open-shell electronic configurations (triplet, quintet, and doublet; *vide infra*). The ground state geometries of the neutral complexes **6a-b** (charge = 0, multiplicity = 1) and cationic complexes [**6a-b**]$^+$ (charge = 1, multiplicity = 2) were optimized using both O3LYP[12] and M06[4] functionals with 6-31+G(d,p) basis set[13–16] on all atoms. Crystal structure coordinates were used as starting inputs for all ground state geometry optimizations. We found O3LYP provided better agreement with the experimental bond lengths and angles; therefore, we used the O3LYP functional for all geometry optimizations. Frequency calculations were performed to confirm all structures were at a minimum.

Single point calculations were performed on the O3LYP optimized structures using three functionals with different HF admixtures, namely, M06L[17] (HF = 0), O3LYP[12] (HF = 12%), and M06[4] (HF = 26%), with 6-31+G(d,p) basis set on all atoms.[13–16] Consistent with previous reports on DFT modelling of the electronic structures of Fe(II) complexes[18–20] hybrid functionals (O3LYP and M06) were found to artificially stabilize the high spin quintet state, while the M06L functional (with zero HF admixture) predicted the same low spin singlet configuration for **6b** as was experimentally observed (see below for extended discussion of different multiplicity states). We therefore used SMD-M06L/6-31+G(d,p) for all single points including TD-DFT. Full TD-DFT approach with non-equilibrium solvation on the neutral and cationic complexes at the O3LYP geometries was carried out for the first 50 states at the SMD-M06L/6-31+G(d,p) level of theory.[17] All spectra were simulated using the GaussSum software.[7] Fragment contributions to the MOs

were calculated using the Hirshfeld partition method[21] available in Multiwfn software.[8,22] Electron density distribution maps (green = electron, blue = hole; for example, Figure **6b** inset) were generated using the same software. Natural transition orbital (NTO; pop=full,nto,savento)[9] calculations were carried out for vertical excitations and are provided in addition to electron density distribution maps where relevant. Where excitations are represented by more than one important particle–hole pair, more than one NTO is included, as described in the literature.[23,24] All structures and MOs were generated using Gaussview 6.0.16.[25]

Table S8. Comparison of experimentally determined bond distances (Å) and angles (°) and optimized structural parameters (S_0; O3LYP/6-31+G(d,p)) for **6a**-**c**.

Bond/Å	6a			6b			6c		
	XRD	**DFT**	**|Δd|**	**XRD**	**DFT**	**|Δd|**	**XRD**	**DFT**	**|Δd|**
$Fe\text{-}N_{amide}$	1.934	1.950	0.016	1.924	1.950	0.026	1.930	1.951	0.021
$Fe\text{-}N_{amide}$	1.936	1.953	0.017	1.932	1.951	0.019	1.941	1.951	0.010
$Fe\text{-}N_{phen}$	1.941	1.967	0.026	1.945	1.966	0.021	1.941	1.969	0.028
$Fe\text{-}N_{phen}$	1.945	1.970	0.025	1.955	1.967	0.022	1.922	1.969	0.047
$Fe\text{-}N_{quin}$	1.943	1.970	0.027	1.946	1.972	0.026	1.956	1.971	0.015
$Fe\text{-}N_{quin}$	1.947	1.970	0.023	1.956	1.970	0.014	1.943	1.971	0.028
Avg (Fe-N)	1.941	1.963	0.022	1.943	1.963	0.021	1.939	1.964	0.025
Angle/°	**XRD**	**DFT**	**|ΔA|**	**XRD**	**DFT**	**Δa**	**XRD**	**DFT**	**|ΔA|**
$N_{amide}\text{-}Fe\text{-}N_{amide}$	179.2	179.8	0.6	179.7	180.0	0.3	178.0	179.9	1.8
$N_{phen}\text{-}Fe\text{-}N_{phen}$	90.5	91.1	0.6	91.8	91.1	0.7	166.0	164.9	0.8
$N_{quin}\text{-}Fe\text{-}N_{quin}$	89.7	91.2	1.5	91.5	90.9	0.6	91.3	90.9	3.1
$N_{quin}\text{-}Fe\text{-}N_{phen}$	165.9	164.9	1.0	166.2	165.0	1.2	93.4	90.8	2.4

Table S9. Comparison of experimentally determined bond distances (Å) and angles (°) and optimized structural parameters (S_0; O3LYP/6-31+G(d,p)) for [**6a**-**b**]$^+$.

Bond/Å	$6a^+$			$6b^+$		
	XRD	**DFT**	**Δd**	**XRD**	**DFT**	**Δd**
$Fe\text{-}N_{amide}$	1.885	1.910	-0.025	1.881	1.908	-0.026
$Fe\text{-}N_{amide}$	1.905	1.909	-0.004	1.906	1.908	-0.019
$Fe\text{-}N_{phen}$	1.946	1.984	-0.038	1.957	1.987	-0.021
$Fe\text{-}N_{phen}$	1.966	1.984	-0.018	1.958	1.988	-0.022
$Fe\text{-}N_{quin}$	1.945	1.987	-0.042	1.959	1.987	-0.026
$Fe\text{-}N_{quin}$	1.964	1.987	-0.023	1.965	1.987	-0.014
Avg (Fe-N)	1.935	1.960	-0.025	1.938	1.961	-0.023
Angle/°	**XRD**	**DFT**	**Δa**	**XRD**	**DFT**	**Δa**
$N_{amide}\text{-}Fe\text{-}N_{amide}$	178.2	180.0	-0.8	179.7	179.9	-0.2
$N_{phen}\text{-}Fe\text{-}N_{phen}$	89.2	89.5	-0.3	89.3	89.5	-0.2
$N_{quin}\text{-}Fe\text{-}N_{quin}$	86.3	89.1	-2.8	88.8	89.3	-0.5
$N_{quin}\text{-}Fe\text{-}N_{phen}$	166.0	164.9	1.1	166.9	164.7	2.2

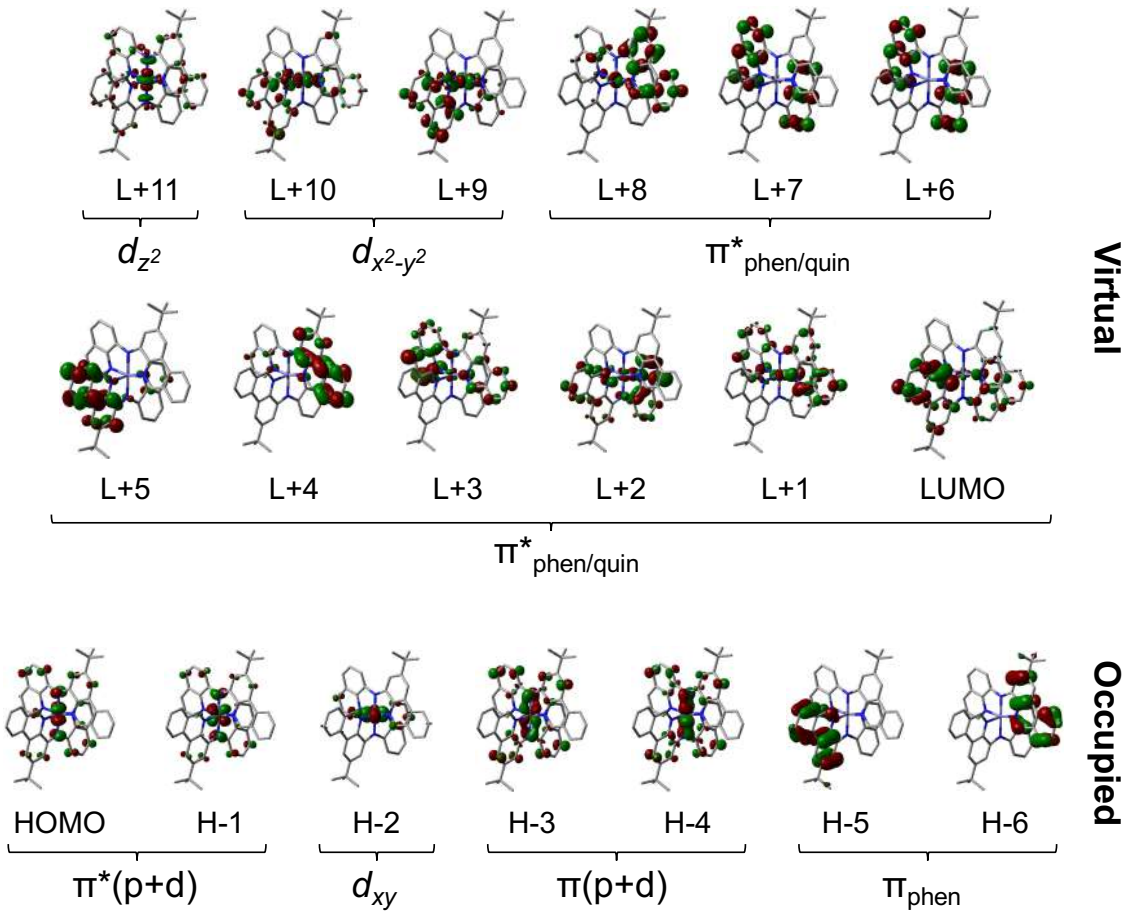

Figure S91. Ground state MOs of **6a** (isosurface = 0.04; SMD-M06L/6-31+G(d,p)//SMD-O3LYP/6-31+G(d,p)).

Table S10. Fragment contributions (%) to the ground state MOs of **6a** using Hirshfeld atomic population method[21] (SMD-M06L/6-31+G(d,p)//SMD-O3LYP/6-31+G(d,p)).

MO	*E*/eV	Fe	N_{amide}		HC=N_{phen}		HC=N_{quin}		Ar_{phen}		Ar_{quin}		^{t}Bu	
L+11	-0.30	35	3	3	3	3	3	2	17	13	10	6	1	1
L+10	-0.65	36	0	0	5	6	3	3	14	26	1	4	1	1
L+9	-0.70	30	0	1	2	7	2	4	1	40	1	10	0	2
L+8	-0.72	9	1	0	7	1	2	1	59	4	10	2	3	0
L+7	-1.07	1	0	0	0	0	9	8	3	3	32	36	0	0
L+6	-1.17	1	0	0	0	0	8	9	1	1	30	42	0	0
L+5	-1.61	1	0	1	0	3	0	2	4	80	1	6	0	0
L+4	-1.62	1	1	0	4	0	2	1	80	4	5	1	1	1
L+3	-2.09	3	2	0	9	2	19	1	25	3	30	0	0	0
L+2	-2.09	4	0	2	1	8	2	19	1	23	2	37	0	0
L+1	-2.19	11	1	0	17	2	6	3	28	5	15	7	1	0
L	-2.20	3	0	1	7	21	1	5	12	37	1	13	0	0
H	-3.63	48	5	5	2	2	2	2	8	7	9	9	0	1
H-1	-3.72	56	5	5	2	2	2	2	6	6	7	7	0	0
H-2	-4.21	67	0	0	4	4	3	3	4	4	4	4	0	0
H-3	-4.61	29	6	6	2	2	1	1	13	13	13	13	0	0
H-4	-4.74	33	5	5	1	2	1	1	12	13	13	12	0	0
H-5	-5.68	1	0	0	0	10	0	0	2	81	0	2	0	4
H-6	-5.70	1	0	0	10	0	0	0	82	1	1	1	4	0

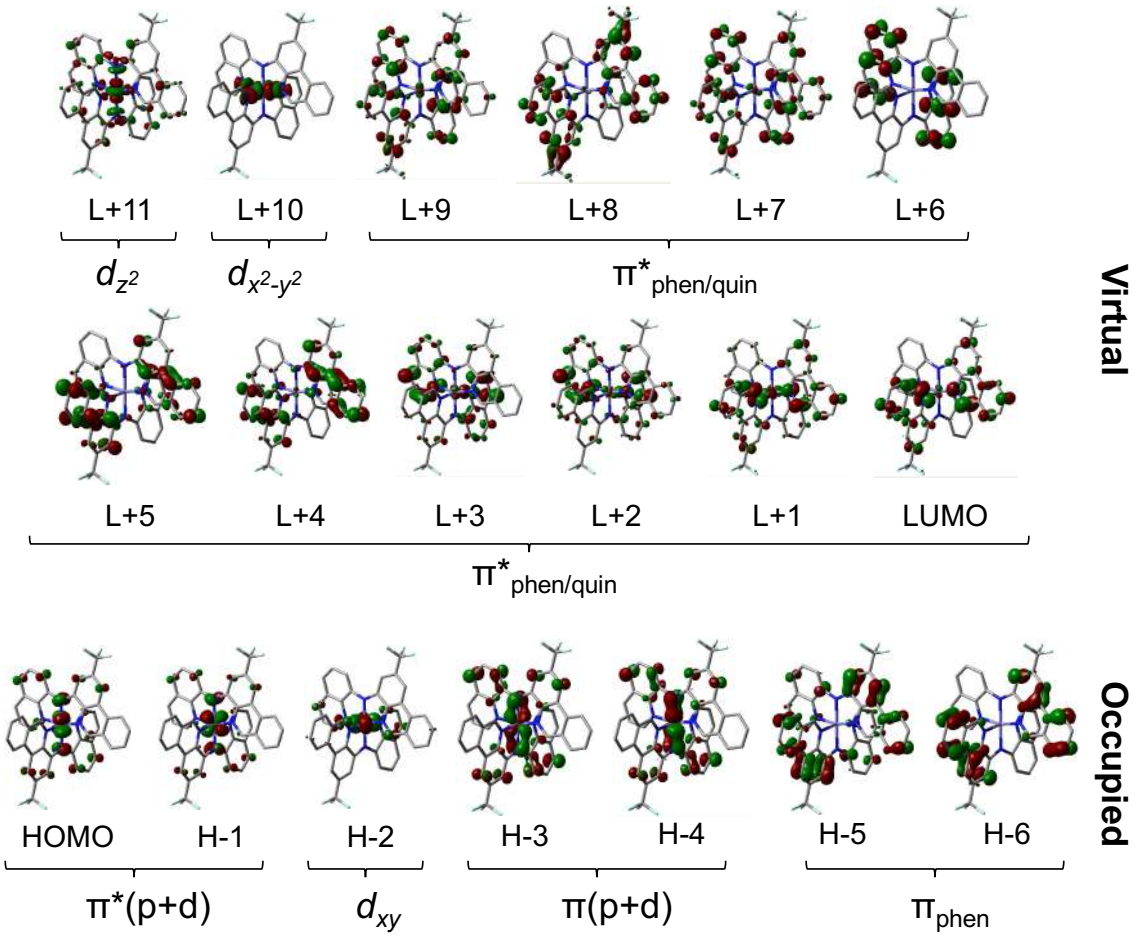

Figure S92. Ground state MOs of **6b** (isosurface = 0.04; SMD-M06L/6-31+G(d,p)//SMD-O3LYP/6-31+G(d,p)).

Table S11. Fragment contributions (%) to the ground state MOs of **6b** using Hirshfeld atomic population method[21] (SMD-M06L/6-31+G(d,p)//SMD-O3LYP/6-31+G(d,p)).

MO	*E*/eV	Fe	N_{amide}		$HC{=}N_{phen}$		$HC{=}N_{quin}$		Ar_{phen}		Ar_{quin}		CF_3	
L+11	-0.46	35	3	3	1	2	3	3	14	13	12	11	1	1
L+10	-0.78	69	0	0	5	5	6	5	2	2	2	2	0	0
L+9	-1.06	2	0	0	2	2	4	4	18	22	21	22	2	2
L+8	-1.09	1	1	0	3	2	1	1	40	35	5	4	3	3
L+7	-1.18	2	0	0	1	1	5	5	20	21	21	20	1	2
L+6	-1.24	1	0	0	0	0	8	8	3	3	37	38	0	0
L+5	-1.77	1	1	1	2	3	1	2	32	48	4	5	0	0
L+4	-1.77	1	1	1	3	2	2	2	48	31	5	3	0	0
L+3	-2.19	3	1	1	1	1	12	13	9	9	24	26	0	0
L+2	-2.20	4	1	1	3	3	11	10	12	11	22	20	0	0
L+1	-2.37	11	1	1	12	13	2	2	22	23	6	6	1	1
L	-2.40	2	1	1	16	15	1	1	28	27	4	4	1	1
H	-3.78	50	5	5	3	2	2	2	8	8	8	8	0	0
H-1	-3.86	57	5	5	2	2	2	2	6	6	7	7	0	0
H-2	-4.32	67	0	0	4	4	3	3	4	4	4	4	0	0
H-3	-4.79	27	6	6	0	1	1	1	12	12	15	15	0	0
H-4	-4.91	32	6	6	1	1	2	2	11	11	15	15	0	0
H-5	-5.92	0	1	1	1	1	2	2	36	34	11	11	0	0
H-6	-5.94	0	0	0	2	2	0	0	44	45	2	2	0	0

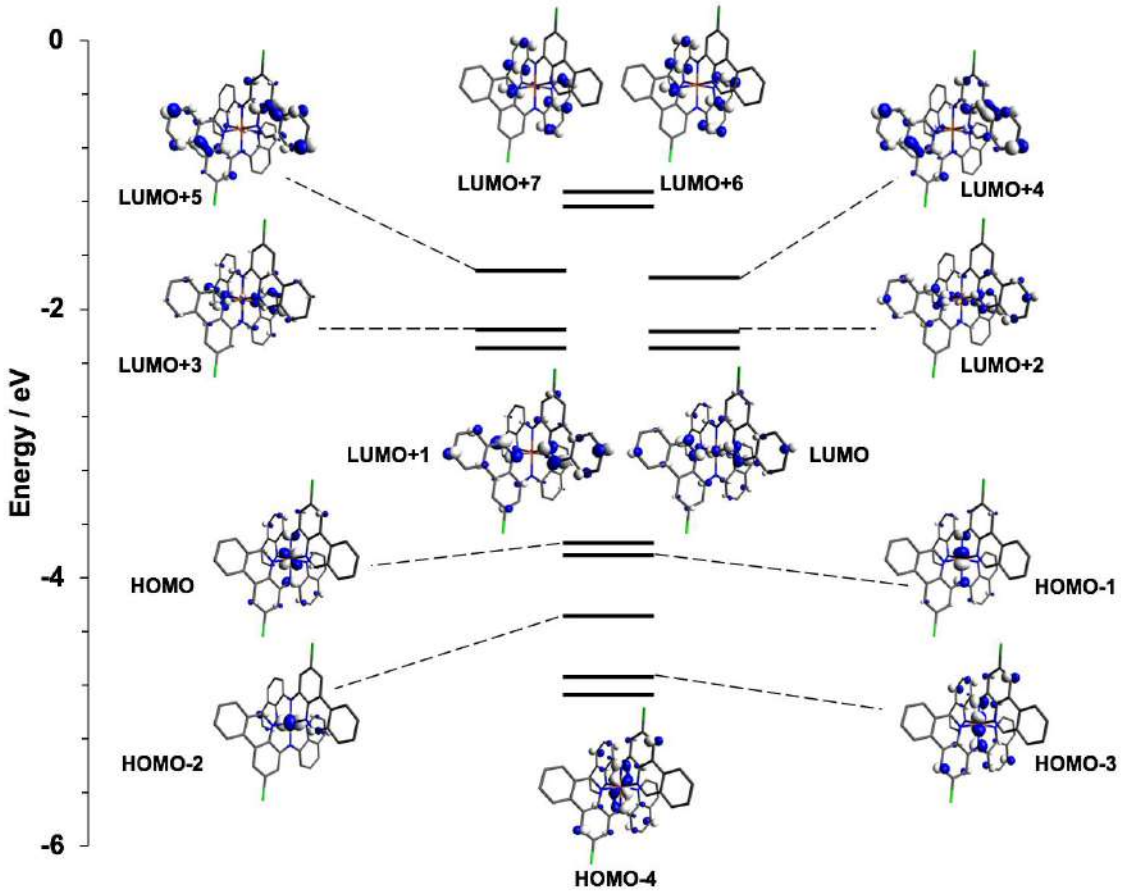

Figure S93. Selected molecular orbitals and diagrams for **6c** (SMD-M06L/6-31+G(d,p); isosurface value = 0.05).

Table S12. Fragment contributions (%) to the ground state MOs of **6c** using Hirshfeld atomic population method[21] (SMD-M06L/6-31+G(d,p)//SMD-O3LYP/6-31+G(d,p)).

MOs	Fe	N^{amide}	$HC{=}N^{phen}$	HCN^{quin}	Ar^{phen}	Ar^{quin}	Cl
H-4	31	11	3	3	24	27	1
H-3	26	12	3	3	25	29	1
H-2	67	1	8	6	9	8	0
H-1	58	9	4	4	12	13	0
HOMO	51	9	5	4	15	16	0
LUMO	12	1	18	9	34	25	1
L+1	1	1	27	6	48	16	1
L+2	5	2	14	16	34	28	0
L+3	2	2	7	21	25	43	0
L+4	1	2	4	4	81	8	0
L+5	1	2	4	4	80	9	0
L+6	1	0	0	18	2	79	0
L+7	1	0	1	16	9	73	0

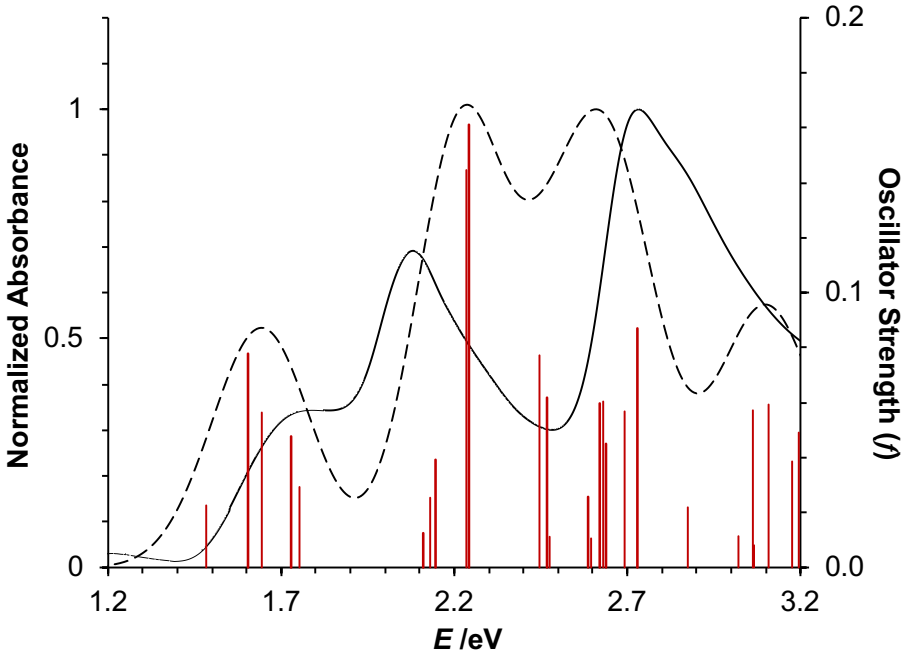

Figure S94. TD-DFT simulated spectrum (---) and vertical excitation energies (red) superimposed on the experimental spectrum (−) of **6a** in CH_3CN (SMD-M06L/6-31+G(d,p)//SMD-O3LYP/6-31+G(d,p); FWHM = 2250 cm^{-1}; $f > 0.01$).

Table S13. TD-DFT predicted vertical excitation energies, oscillator strengths (f > 0.01) and MO contributions (> 10%) for **6a**.

No.	E / eV	f	MO contribution
1	1.48	0.023	H-1→L+1 (10%), HOMO→LUMO (79%)
5	1.60	0.078	H-1→LUMO (47%), HOMO→L+1 (30%)
6	1.64	0.056	H-1→L+1 (49%), H-1→L+3 (16%)
7	1.73	0.048	H-1→L+2 (51%), H-1→L+3 (20%)
8	1.75	0.029	H-1→L+2 (12%), H-1→L+3 (36%), HOMO→L+2 (19%), HOMO→L+3 (16%)
11	2.11	0.013	H-2→LUMO (50%), H-1→L+4 (34%)
12	2.13	0.025	H-2→LUMO (21%), H-1→L+4 (48%), H-1→L+5 (22%)
13	2.15	0.039	H-2→LUMO (11%), H-1→L+5 (67%)
14	2.24	0.145	H-2→L+2 (78%)
15	2.24	0.161	H-2→L+3 (81%)
16	2.45	0.077	H-3→LUMO (84%)
17	2.47	0.062	H-3→L+1 (76%)
18	2.48	0.011	H-2→L+1 (31%), HOMO→L+6 (40%)
23	2.59	0.026	H-4→LUMO (49%), H-2→L+4 (17%), H-2→L+5 (13%)
24	2.60	0.011	H-4→LUMO (11%), H-4→L+1 (14%), H-2→L+4 (29%), H-2→L+5 (12%), H-1→L+6 (11%), HOMO→L+7 (20%)
25	2.62	0.060	H-4→L+1 (45%), H-1→L+6 (10%), HOMO→L+7 (17%)
26	2.63	0.060	H-2→L+4 (42%), H-1→L+7 (10%), HOMO→L+7 (13%)
27	2.64	0.045	H-2→L+5 (56%), H-1→L+7 (11%), HOMO→L+7 (10%)
28	2.69	0.057	H-4→L+2 (15%), H-1→L+7 (57%)
29	2.73	0.087	H-4→L+2 (27%), H-4→L+3 (45%), H-3→L+2 (10%)
32	2.88	0.022	H-1→L+9 (13%), HOMO→L+8 (37%), HOMO→L+9 (11%), HOMO→L+11 (14%)
35	3.02	0.011	H-3→L+4 (79%)
37	3.06	0.057	H-2→L+6 (23%), H-1→L+8 (29%), H-1→L+9 (11%), H-1→L+10 (24%)
38	3.07	0.008	H-2→L+6 (70%), H-1→L+8 (11%)
40	3.11	0.059	H-1→L+8 (22%), H-1→L+9 (34%), HOMO→L+9 (12%)
42	3.18	0.039	H-4→L+4 (83%)
43	3.20	0.049	H-4→L+5 (81%)

Transition	Natural Transition Orbitals			Electron Density Distribution Map
1	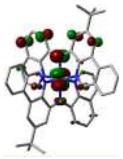	87%	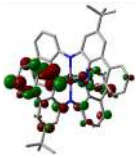	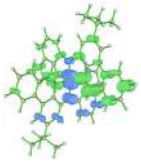
5		55%	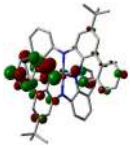	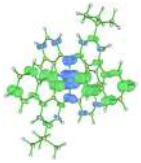
	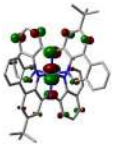	39%	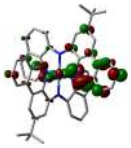	
6	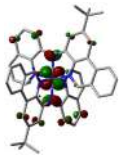	81%	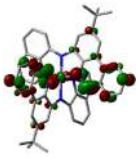	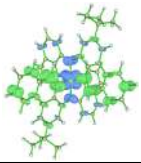
7	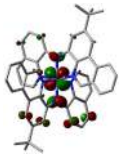	72%	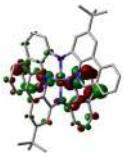	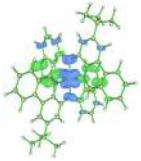
8	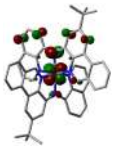	58%	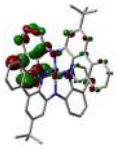	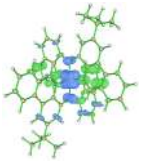
		32%	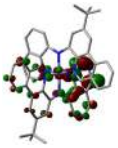	

Figure S95. Natural transition orbitals[9] (NTOs; isosurface = 0.04), and TD-DFT calculated electron density gain (green) and depletion (blue) distribution maps (isosurface = 0.002) for the five lowest energy transitions in **6a** (SMD-M06L/6-31+G(d,p)//SMD-O3LYP/6-31+G(d,p)). Where excitations are represented by more than one important particle–hole pair, more than one NTO is included.

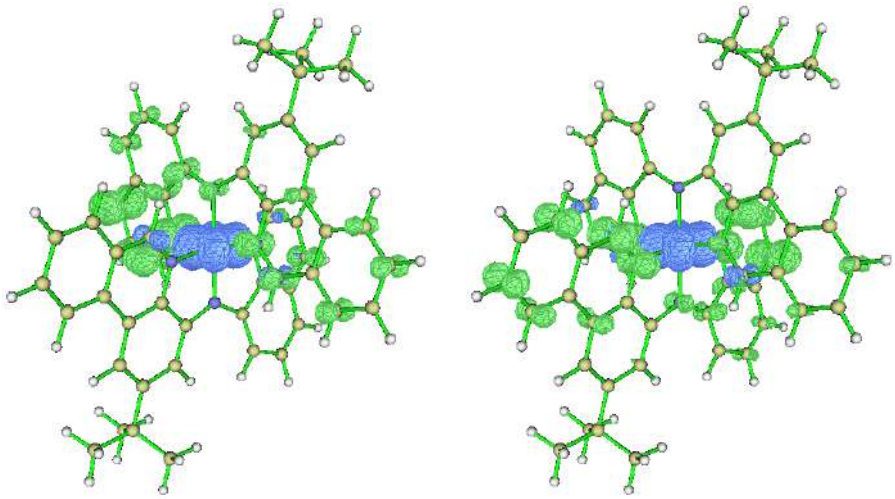

Figure S96. TD-DFT calculated electron density gain (green) and depletion (blue) distribution maps (isosurface = 0.002) for MLCT-type transitions 14 (HOMO-2→LUMO+2) and 15 (HOMO-2→LUMO+3) of **6a** (SMD-M06L/6-31+G(d,p)//SMD-O3LYP/6-31+G(d,p)).

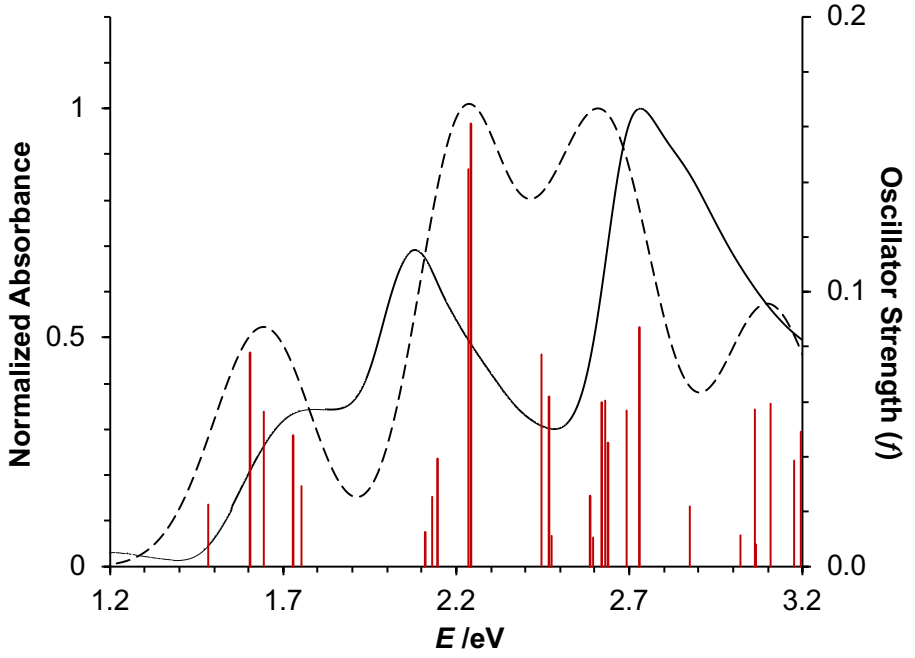

Figure S97. TD-DFT simulated spectrum (---) and vertical excitation energies (red) superimposed on the experimental spectrum (−) of **6b** in CH_3CN (SMD-M06L/6-31+G(d,p)//SMD-O3LYP/6-31+G(d,p); FWHM = 2250 cm^{-1}; $f > 0.01$).

Table S14. TD-DFT predicted vertical excitation energies, oscillator strengths (f > 0.01) and MO contributions (> 10%) for **6b**.

No.	E / eV	f	MO contribution
1	1.44	0.018	H-1→L+1 (18%), HOMO→LUMO (80%)
3	1.56	0.069	H-1→LUMO (43%), HOMO→L+1 (48%)
4	1.60	0.046	H-1→L+1 (75%), HOMO→LUMO (16%)
7	1.77	0.054	H-1→L+3 (71%), HOMO→L+2 (21%)
8	1.79	0.041	H-1→L+2 (53%), HOMO→L+3 (34%)
9	2.02	0.014	H-2→LUMO (41%), HOMO→L+5 (54%)
11	2.04	0.048	H-2→LUMO (47%), H-1→L+4 (16%), HOMO→L+5 (33%)
13	2.12	0.039	H-1→L+4 (78%), HOMO→L+5 (11%)
14	2.22	0.164	H-2→L+1 (10%), H-2→L+2 (81%)
15	2.23	0.099	H-2→L+3 (88%)
16	2.41	0.021	H-4→LUMO (13%), H-2→L+1 (53%)
17	2.43	0.063	H-3→LUMO (88%)
18	2.46	0.031	H-4→LUMO (18%), H-3→L+1 (78%)
21	2.57	0.019	H-2→L+4 (82%)
22	2.59	0.077	H-4→L+1 (63%), HOMO→L+7 (13%)
24	2.62	0.052	H-4→LUMO (32%), H-3→L+2 (15%), H-2→L+5 (13%), H-1→L+7 (13%)
25	2.63	0.047	H-4→L+3 (10%), H-3→L+2 (68%)
26	2.65	0.051	H-4→L+2 (22%), H-3→L+3 (61%)
30	2.75	0.022	H-4→L+3 (25%), H-1→L+7 (42%), HOMO→L+8 (19%)
33	2.83	0.171	H-4→L+2 (38%), H-3→L+3 (15%), H-1→L+8 (27%), HOMO→L+9 (10%)
34	2.88	0.056	H-4→L+3 (49%)
36	2.96	0.026	H-1→L+9 (15%), H-1→L+11 (23%), HOMO→L+10 (37%)
37	3.05	0.025	H-4→L+5 (11%), H-3→L+4 (86%)
38	3.05	0.010	H-4→L+4 (11%), H-3→L+5 (86%)
41	3.19	0.019	H-4→L+4 (59%), H-2→L+7 (24%)
42	3.20	0.041	H-4→L+5 (82%)

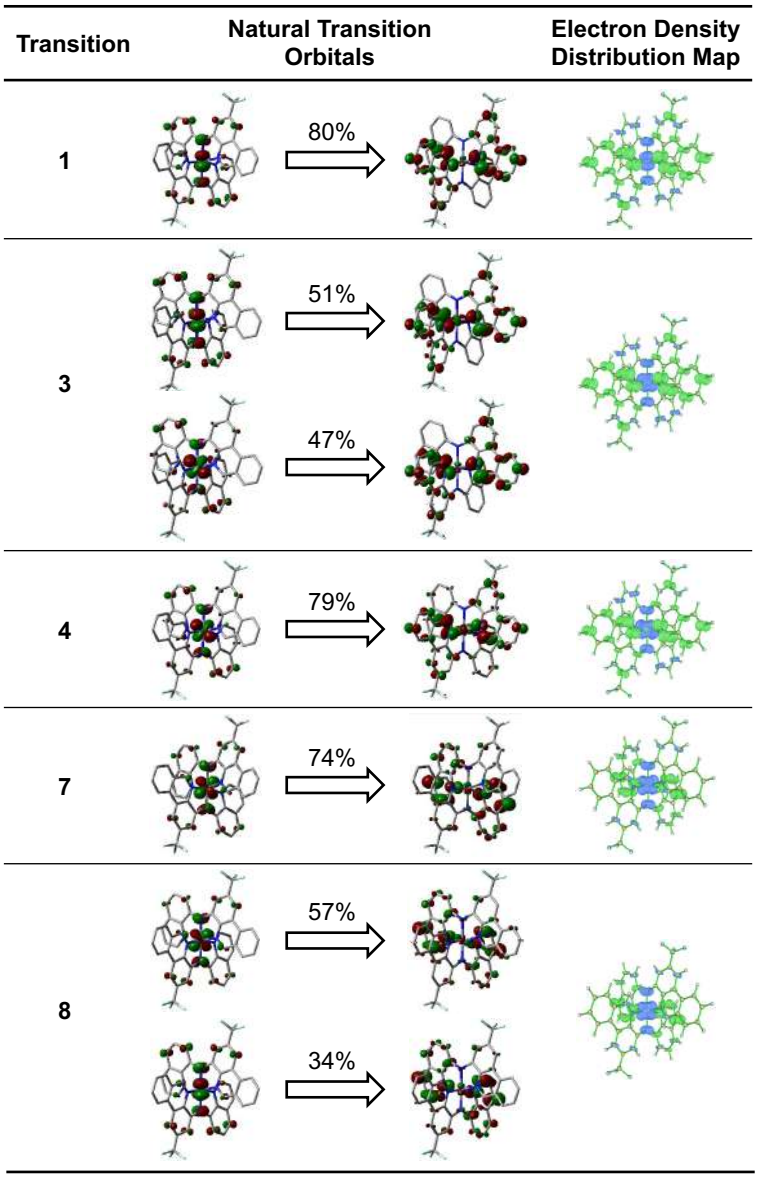

Figure S98. Natural transition orbitals[9] (NTOs; isosurface = 0.04), and TD-DFT calculated electron density gain (green) and depletion (blue) distribution maps (isosurface = 0.002) for the five lowest energy transitions in **6b** (SMD-M06L/6-31+G(d,p)//SMD-O3LYP/6-31+G(d,p)).

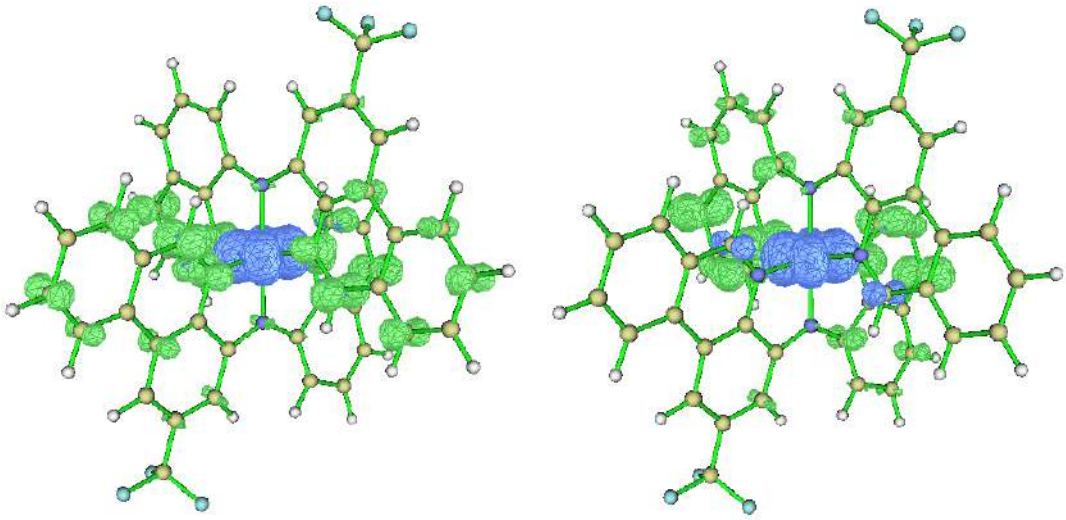

Figure S99. TD-DFT calculated electron density gain (green) and depletion (blue) distribution maps (isosurface = 0.002) for MLCT-type transitions 14 (HOMO-2→LUMO+2) and 15 (HOMO-2→LUMO+3) of **6b** (SMD-M06L/6-31+G(d,p)//SMD-O3LYP/6-31+G(d,p)).

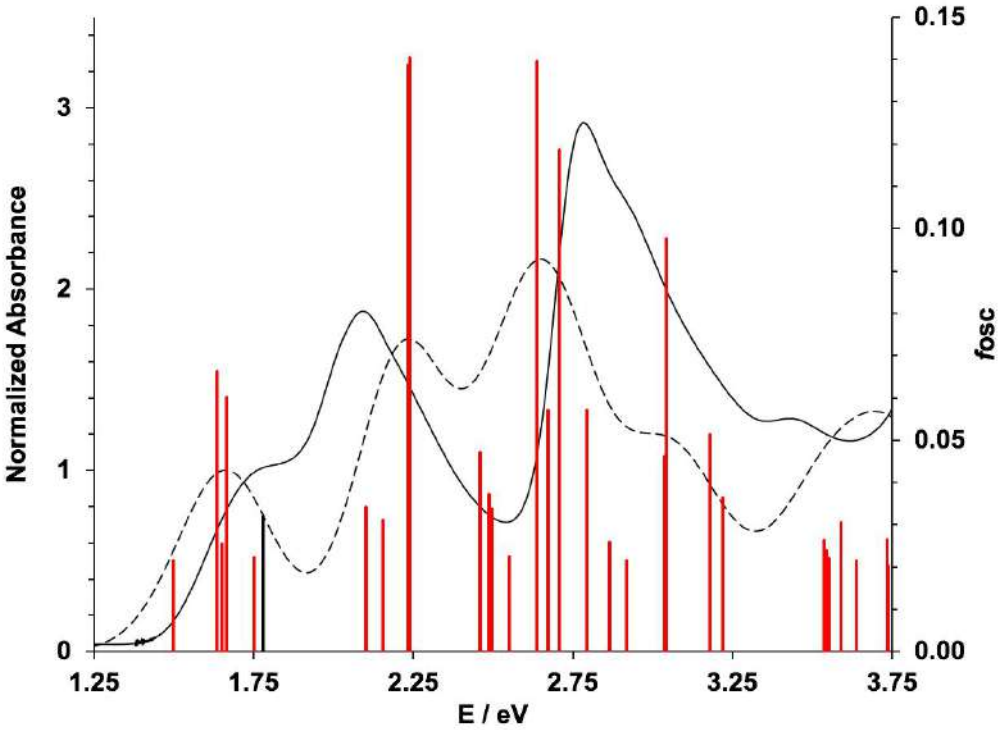

Figure S100. TD-DFT simulated spectrum (---) and vertical excitation energies (red) superimposed on the experimental spectrum (−) of **6c** in CH_3CN (TD-SMD-M06L/6-31+G(d,p); FWHM = 2500 cm^{-1}; f_{osc} > 0.02).

Table S15. TD-DFT predicted vertical excitation energies, oscillator strengths (f > 0.02) for **6c**.

State	E / eV	f_{osc}	Major contributions
1	1.50	0.02	H-1→LUMO (16%), HOMO→L+1 (83%)
4	1.64	0.07	H-1→L+1 (41%), H-1→L+3 (16%), HOMO→LUMO (25%), HOMO→L+2 (14%)
5	1.65	0.03	H-1→L+1 (16%), H-1→L+3 (17%), HOMO→LUMO (10%), HOMO→L+2 (54%)
6	1.67	0.06	H-1→LUMO (51%), H-1→L+2 (24%), HOMO→L+1 (12%)
7	1.75	0.02	H-1→L+2 (62%), HOMO→L+3 (26%)
8	1.78	0.03	H-1→L+3 (62%), HOMO→L+2 (25%)
11	2.10	0.03	H-2→L+1 (82%), H-1→L+5 (10%)
13	2.15	0.03	H-1→L+5 (86%)
14	2.23	0.14	H-2→L+3 (88%)
15	2.24	0.14	H-2→L+2 (88%)
16	2.46	0.05	H-2→LUMO (59%)
17	2.49	0.04	H-3→L+1 (83%)
18	2.50	0.03	H-4→L+1 (11%), H-3→LUMO (77%)
20	2.55	0.02	H-2→L+4 (48%), HOMO→L+6 (43%)
25	2.64	0.14	H-4→L+1 (77%), H-3→LUMO (12%)
26	2.67	0.06	H-4→LUMO (35%), H-4→L+2 (12%), H-3→L+3 (13%), HOMO→L+7 (22%)
27	2.71	0.12	H-4→LUMO (15%), H-2→L+5 (14%), H-1→L+6 (13%), HOMO→L+7 (26%)
29	2.79	0.06	H-4→L+3 (79%), H-3→L+2 (11%)
32	2.86	0.03	H-4→L+2 (25%), H-1→L+9 (20%), HOMO→L+8 (25%)
33	2.92	0.02	HOMO→L+9 (59%), HOMO→L+10 (26%)
36	3.04	0.05	H-1→L+8 (59%), H-1→L+11 (16%), HOMO→L+10 (12%)
37	3.04	0.10	H-3→L+4 (34%), H-1→L+9 (39%)
41	3.18	0.05	H-4→L+4 (75%), H-3→L+5 (18%)
43	3.22	0.04	H-4→L+5 (88%)
51	3.54	0.03	H-6→L+1 (24%), H-5→LUMO (49%), H-1→L+13 (20%)
52	3.54	0.02	H-6→L+1 (23%), H-1→L+11 (10%), H-1→L+13 (53%)
53	3.55	0.02	H-6→LUMO (32%), H-5→L+1 (28%)
55	3.59	0.03	HOMO→L+14 (61%)
59	3.64	0.02	H-7→LUMO (30%), H-6→L+1 (10%), H-5→L+2 (50%)
64	3.73	0.03	H-4→L+6 (33%), H-3→L+7 (25%), HOMO→L+15 (29%)
65	3.74	0.02	H-4→L+6 (14%), H-3→L+7 (11%), HOMO→L+15 (69%)

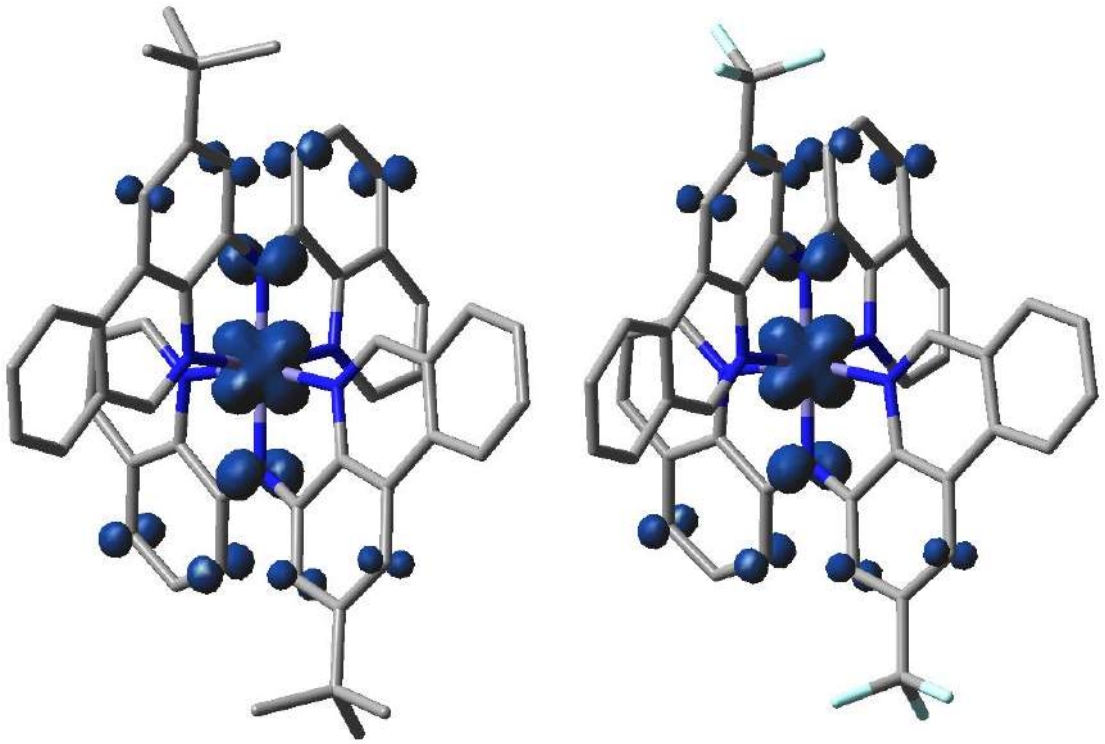

[3a]$^+$ [3b]$^+$

Element	Spin density	
	[3a]$^+$	[3b]$^+$
Fe	0.55	0.59
$N_{amide,1}$	0.074	0.068
$N_{amide,2}$	0.074	0.068

Figure S101. Spin density map (isosurface = 0.004) of [**6a**-**b**]$^+$ (SMD-M06L/6-31+G(d,p)//SMD-O3LYP/6-31+G(d,p)).

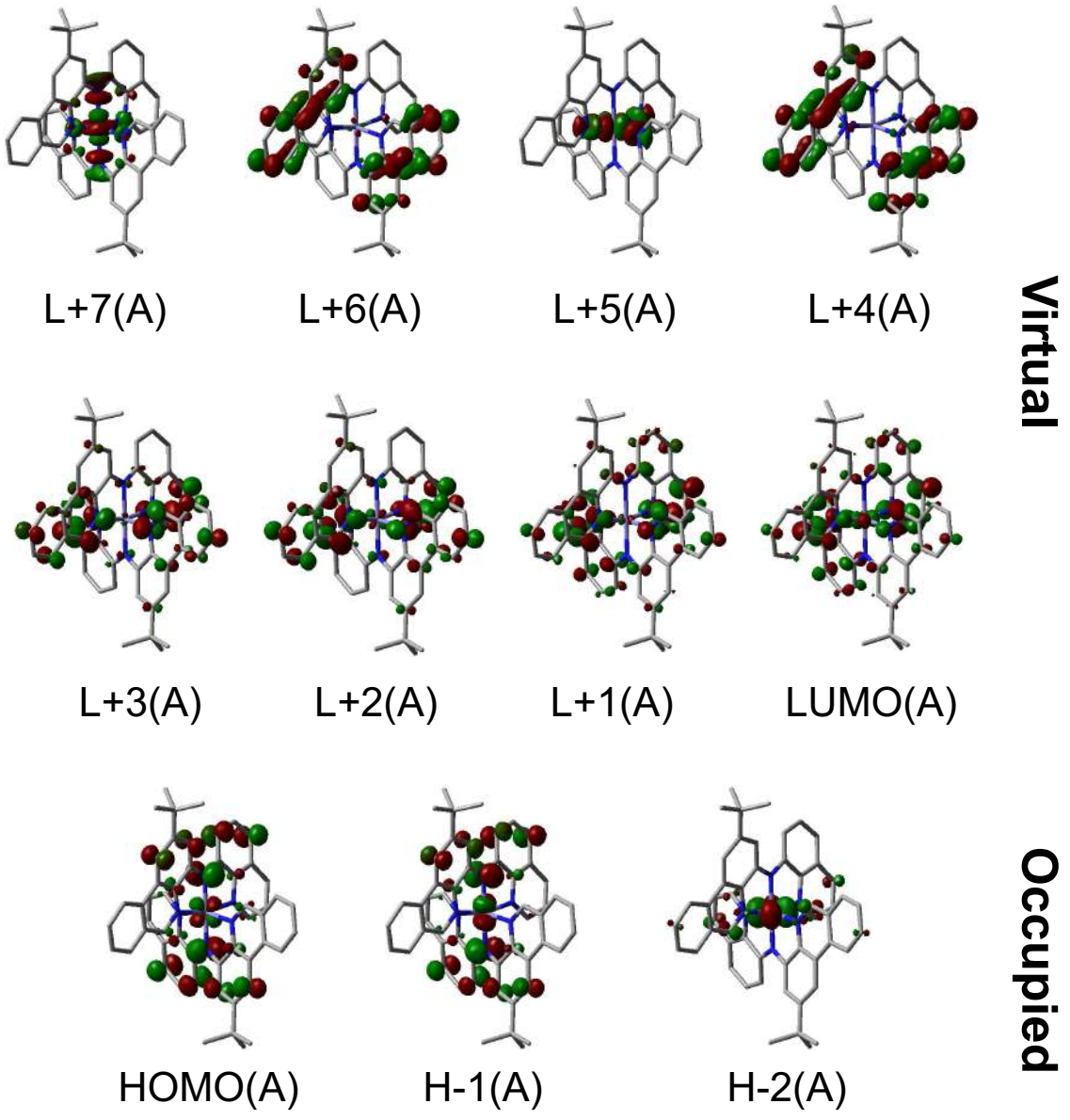

Figure S102. Ground state α-MOs of [**6a**]$^{+}$ (isosurface = 0.04; SMD-M06L/6-31+G(d,p)//SMD-O3LYP/6-31+G(d,p)).

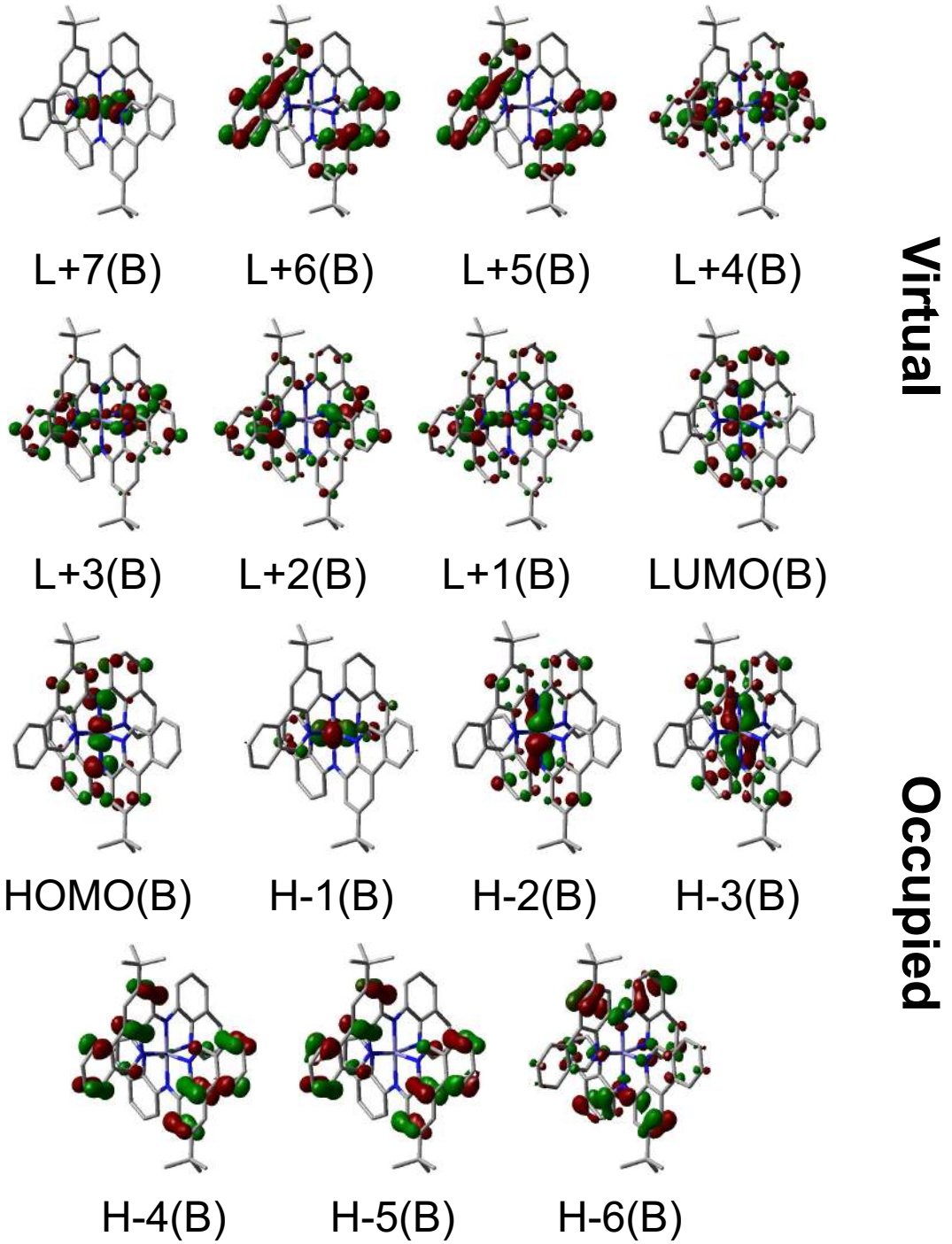

Figure S103. Ground state β-MOs of [**6a**]$^{+}$ (isosurface = 0.04; SMD-M06L/6-31+G(d,p)//SMD-O3LYP/6-31+G(d,p)).

Table S16. Fragment contribution (%) to the ground state MOs of [**6a**]$^{+}$ using Hirshfeld atomic population method[21] (SMD-M06L/6-31+G(d,p)//SMD-O3LYP/6-31+G(d,p)).

α-MO	*E*/eV	Fe	N_{amide}		$HC{=}N_{phen}$		$HC{=}N_{quin}$		Ar_{phen}		Ar_{quin}		^{t}Bu	
L+7	-1.56	56	6	6	2	3	3	3	5	5	5	5	0	0
L+6	-1.86	1	1	1	2	2	1	1	43	43	3	3	1	1
L+5	-1.91	67	0	0	6	6	6	6	2	2	2	2	0	0
L+4	-1.92	0	1	1	2	2	1	1	43	44	2	2	1	1
L+3	-2.40	2	1	1	10	10	6	6	19	19	12	12	0	0
L+2	-2.48	3	1	1	11	12	6	6	19	19	10	10	0	0
L+1	-2.49	2	1	1	8	8	8	8	14	14	19	19	0	0
L	-2.60	6	1	1	7	7	8	9	12	12	19	19	0	0
H	-4.51	15	9	9	2	2	2	2	14	14	16	15	0	0
H-1	-4.61	21	9	9	2	2	2	2	13	13	14	14	0	0
H-2	-5.29	64	0	0	4	4	3	3	6	6	5	5	0	0
β-MO	***E*/eV**	**Fe**	**N_{amide}**		**$HC{=}N_{phen}$**		**$HC{=}N_{quin}$**		**Ar_{phen}**		**Ar_{quin}**		**^{t}Bu**	
L+7	-1.53	69	0	0	6	6	6	6	2	2	2	2	0	0
L+6	-1.82	1	1	1	2	2	1	1	43	43	3	3	1	1
L+5	-1.88	0	1	1	2	2	1	1	43	44	2	2	1	1
L+4	-2.38	2	1	1	7	7	9	9	14	14	18	17	0	0
L+3	-2.42	6	1	1	9	9	7	8	16	17	12	12	0	0
L+2	-2.47	1	0	0	11	11	6	6	19	18	14	13	1	1
L+1	-2.53	9	0	0	8	8	7	7	14	14	15	16	0	0
L	-3.88	41	6	6	2	2	2	2	9	9	10	10	0	0
H	-4.26	38	8	8	2	2	2	2	9	9	10	10	0	0
H-1	-4.82	69	0	0	4	4	3	3	4	4	4	4	0	0
H-2	-5.08	47	4	4	1	1	1	1	10	10	10	10	0	0
H-3	-5.24	38	5	5	1	1	1	1	12	12	11	11	0	0
H-4	-5.92	1	0	0	4	4	0	0	44	43	0	0	2	2
H-5	-5.95	0	0	0	4	4	0	0	43	44	0	0	2	2
H-6	-6.04	1	2	2	3	3	2	2	23	22	19	19	1	1

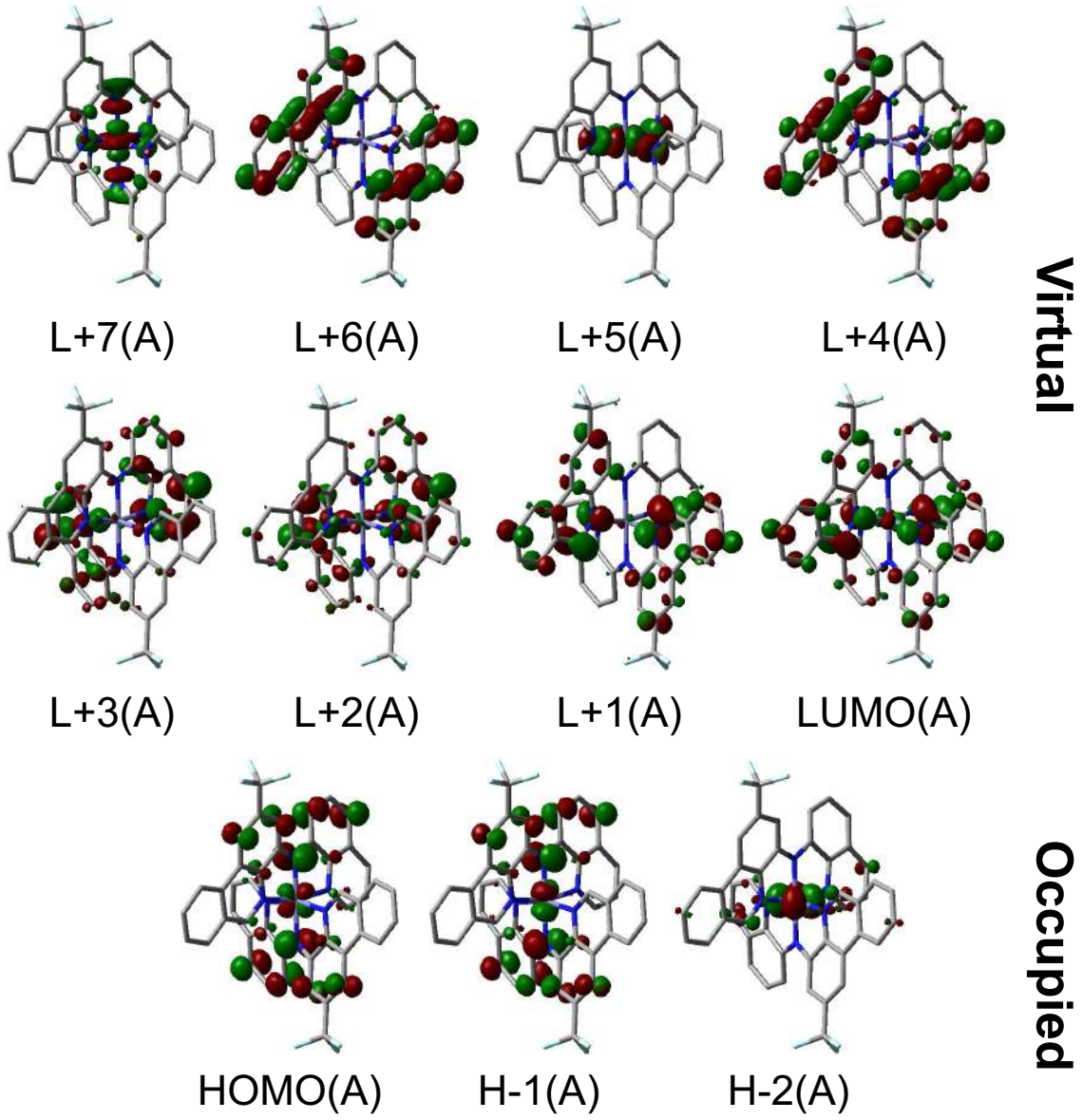

Figure S104. Ground state α-MOs of [**6b**]$^{+}$ (isosurface = 0.04; SMD-M06L/6-31+G(d,p)//SMD-O3LYP/6-31+G(d,p)).

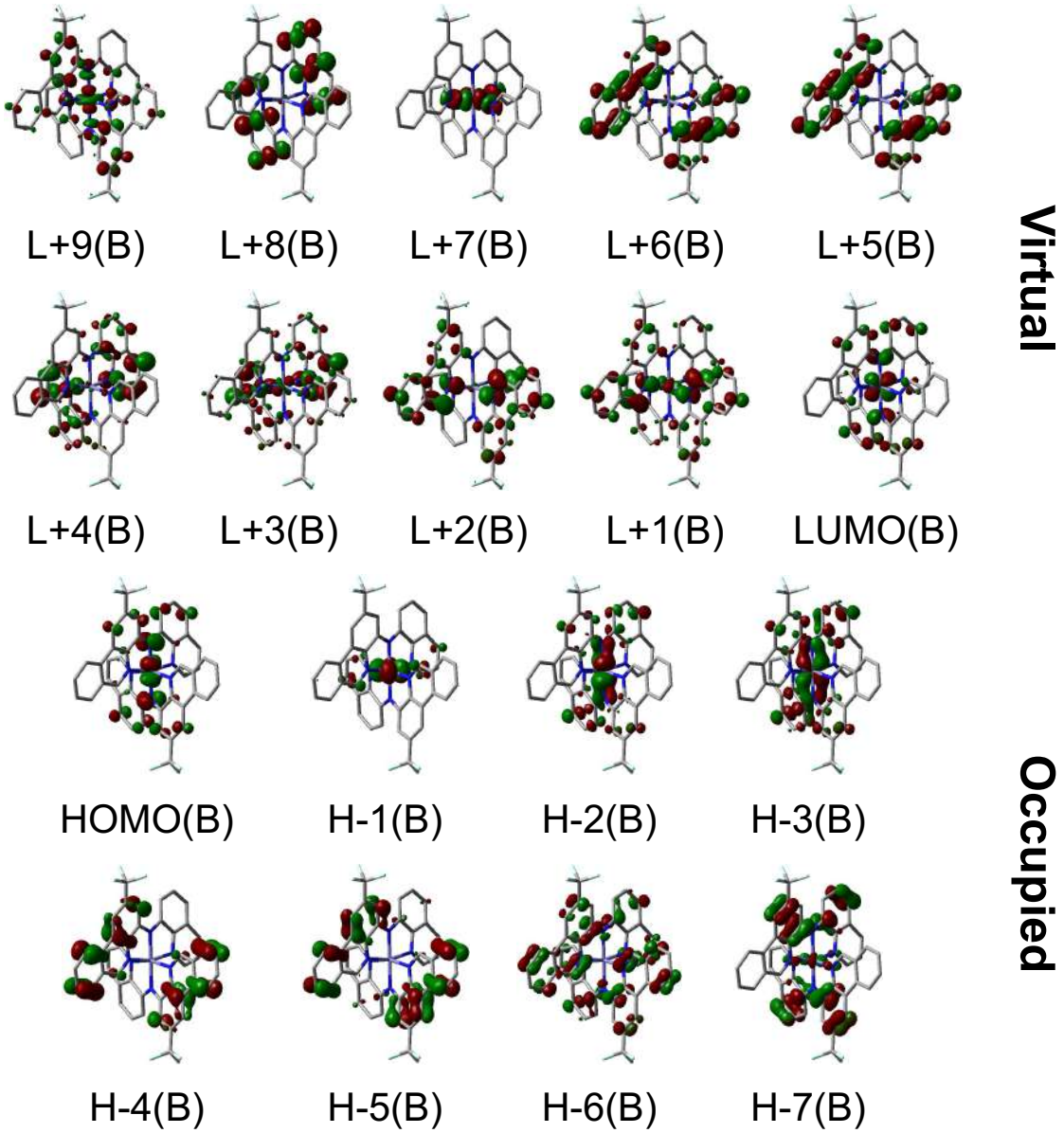

Figure S105. Ground state β-MOs of [**6b**]$^{+}$ (isosurface = 0.04; SMD-M06L/6-31+G(d,p)//SMD-O3LYP/6-31+G(d,p)).

Table S17. Fragment contribution to the ground state MOs of [**6b**]$^{+}$ using Hirshfeld atomic population method[21] (SMD-M06L/6-31+G(d,p)//SMD-O3LYP/6-31+G(d,p)).

α-MO	*E*/eV	Fe	N_{amide}		HC=N_{phen}		HC=N_{quin}		Ar_{phen}		Ar_{quin}		CF_3	
L+7	-1.75	54	6	6	3	3	2	2	8	8	4	4	0	0
L+6	-2.03	1	1	1	2	2	1	1	42	42	3	3	0	0
L+5	-2.08	66	0	0	6	6	6	6	3	3	2	2	0	0
L+4	-2.10	1	1	1	2	2	2	2	41	41	3	3	0	0
L+3	-2.52	2	1	1	2	2	12	12	8	8	26	26	0	0
L+2	-2.61	3	1	1	4	4	12	12	10	10	21	21	0	0
L+1	-2.69	1	0	0	15	15	2	2	26	26	5	5	1	1
L	-2.78	6	0	0	14	14	3	3	22	22	8	8	1	1
H	-4.68	15	9	9	2	2	2	2	14	14	16	16	0	0
H-1	-4.78	21	9	9	2	2	2	2	12	12	15	14	0	0
H-2	-5.44	65	0	0	4	4	3	3	5	5	5	5	0	0

α-MO	*E*/eV	Fe	N_{amide}		HC=N_{phen}		HC=N_{quin}		Ar_{phen}		Ar_{quin}		CF_3	
L+9	-1.49	31	3	3	3	3	2	2	20	20	6	6	1	1
L+8	-1.54	1	0	0	0	0	9	9	1	1	39	39	0	0
L+7	-1.68	68	0	0	5	5	5	5	3	3	2	2	0	0
L+6	-1.99	1	1	1	2	2	1	1	41	42	3	3	0	0
L+5	-2.06	1	1	1	3	3	1	1	42	42	3	3	0	0
L+4	-2.49	2	1	1	2	2	13	13	7	7	27	27	0	0
L+3	-2.54	6	1	1	3	3	12	12	10	10	21	21	0	0
L+2	-2.68	1	0	0	16	16	1	1	27	27	4	4	1	1
L+1	-2.71	9	1	1	13	13	2	2	22	22	7	7	1	1
L	-4.04	43	6	6	2	2	2	2	9	9	10	10	0	0
H	-4.43	40	7	7	2	2	2	2	9	9	10	10	0	0
H-1	-4.95	69	0	0	4	4	3	3	4	4	4	4	0	0
H-2	-5.25	45	4	4	1	1	1	1	8	8	12	12	0	0
H-3	-5.42	37	5	5	1	1	1	1	10	10	14	14	0	0
H-4	-6.17	0	0	0	2	3	0	0	44	47	1	1	0	0
H-5	-6.17	0	0	0	1	1	1	1	44	40	5	5	0	0
H-6	-6.28	1	1	1	6	6	2	2	26	26	14	14	1	1
H-7	-6.45	7	1	1	2	2	2	2	22	22	19	19	1	1

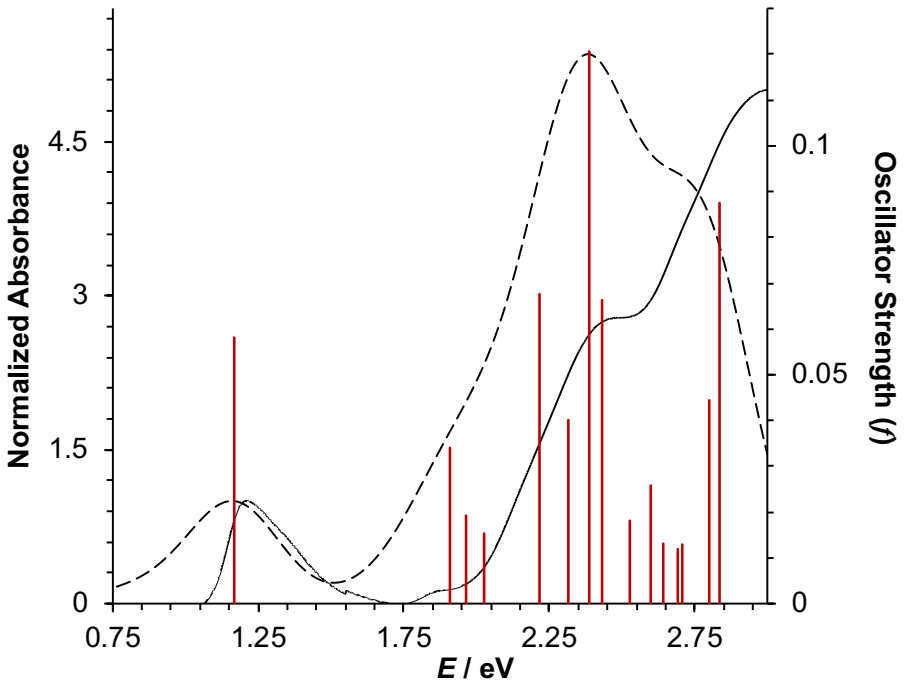

Figure S106. TD-DFT simulated spectrum (---) and vertical excitation energies (red) superimposed on the experimental spectrum (−) of [**6a**]$^{+}$ in CH_3CN (SMD-M06L/6-31+G(d,p)//SMD-O3LYP/6-31+G(d,p); FWHM = 3000 cm^{-1}; $f > 0.01$).

Table S18. TD-DFT predicted vertical excitation energies, oscillator strengths ($f > 0.01$) and MO contributions (> 10%) for [**6a**]$^+$.

No.	E / eV	f	MO contributions
3	1.17	0.058	H-2(B)→LUMO(B) (96%)
9	1.91	0.034	HOMO(A) →LUMO(A) (60%), HOMO(B) →L+2(B) (10%), HOMO(B) →L+4(B) (11%)
10	1.96	0.019	H-1(A) →LUMO(A) (28%), HOMO(A) →L+1(A) (29%), H-6(B) →LUMO(B) (21%), HOMO(B) →L+1(B) (12%)
13	2.03	0.015	H-1(A) →L+5(A) (17%), HOMO(B) →L+7(B) (32%)
21	2.22	0.068	H-6(B) →LUMO(B) (71%)
24	2.32	0.040	H-7(B) →LUMO(B) (65%), H-1(B) →L+3(B) (15%)
27	2.39	0.121	H-1(B) →L+3(B) (71%)
29	2.43	0.066	H-1(B) →L+4(B) (83%)
31	2.53	0.018	HOMO(A) →L+5(A) (32%), H-2(B) →L+1(B) (48%)
33	2.60	0.026	HOMO(A) →L+4(A) (79%)
35	2.64	0.013	H-2(B) →L+3(B) (90%)
38	2.69	0.012	H-1(A) →L+4(A) (35%), HOMO(A) →L+7(A) (10%), H-2(B) →L+4(B) (14%)
39	2.71	0.013	H-1(A) →L+4(A) (18%), HOMO(A) →L+7(A) (30%), H-3(B) →L+1(B) (21%)
47	2.80	0.044	H-2(A) →L+2(A) (36%), H-1(A) →L+5(A) (18%), HOMO(A) →L+7(A) (16%)
48	2.84	0.088	H-2(A) →L+2(A) (33%), H-1(A) →L+5(A) (25%), HOMO(A) →L+7(A) (16%)

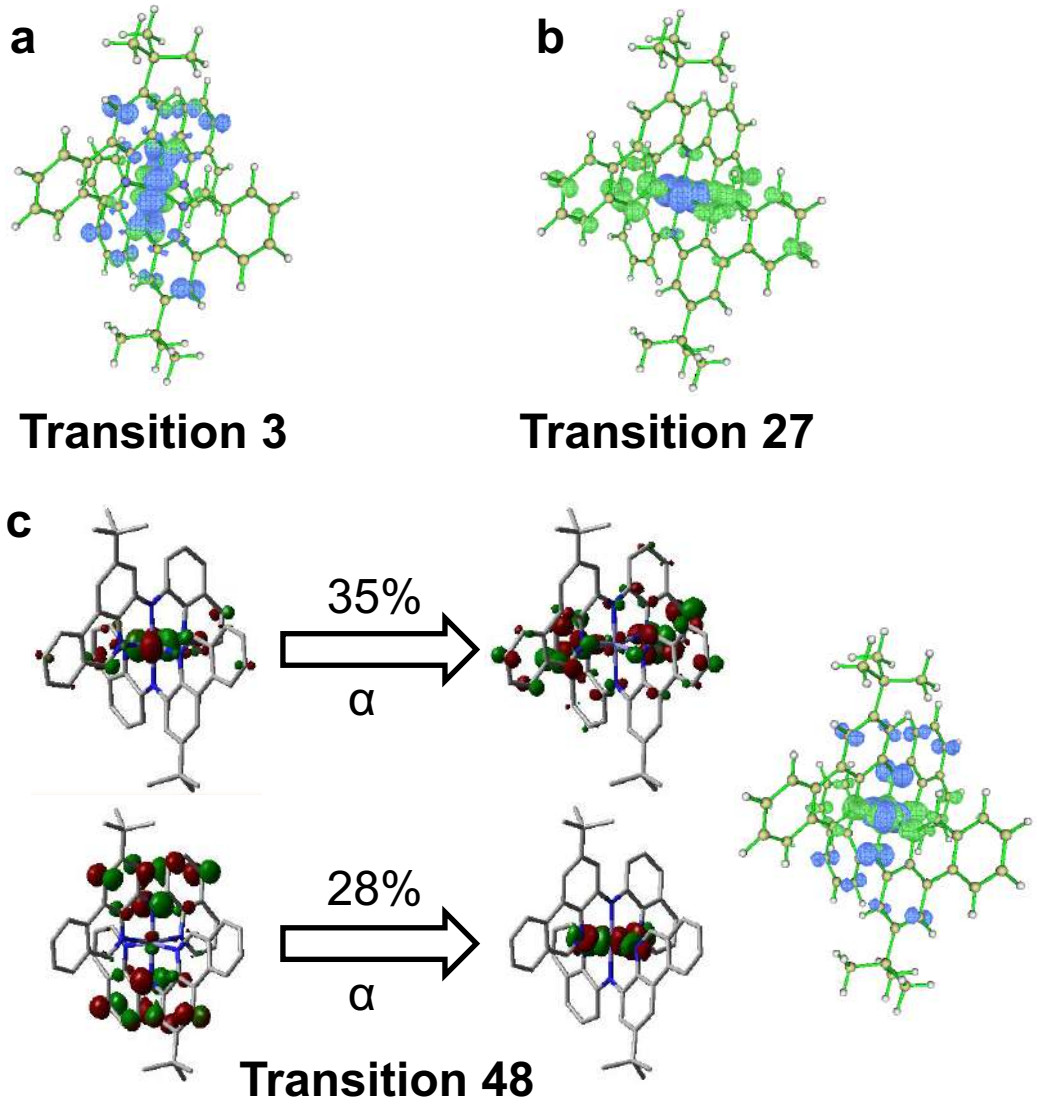

Figure S107. TD-DFT calculated NTOs and electron density gain (green) and depletion (blue) distribution maps (isosurface = 0.004) for transitions (a) 3 (β-HOMO-2→β-LUMO), (b) 27 (β-HOMO-1→β-LUMO+3); and (c) 48 of [**6a**]$^{+}$ (SMD-M06L/6-31+G(d,p)//SMD-O3LYP/6-31+G(d,p)).

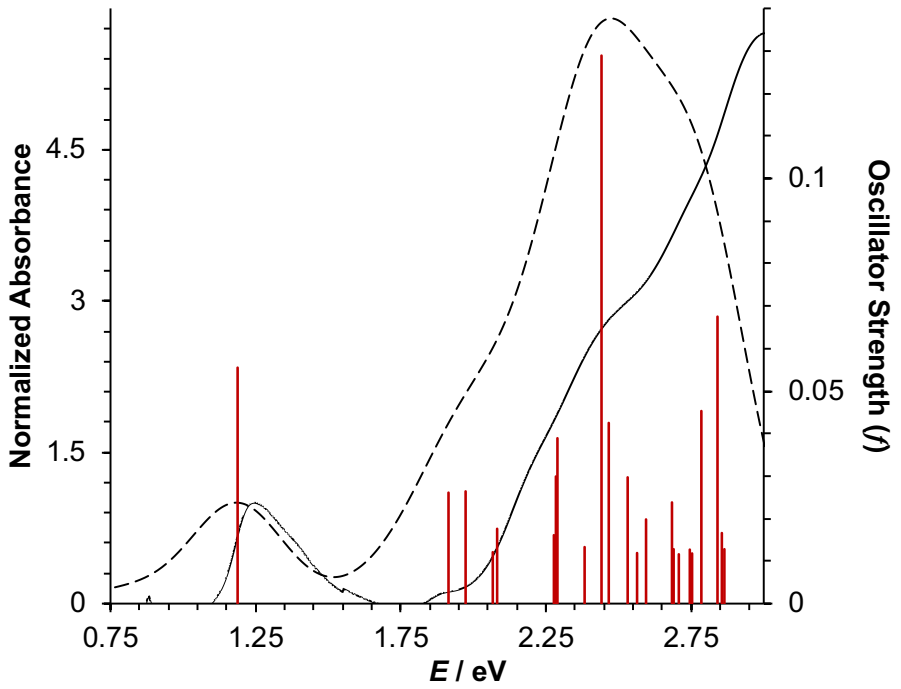

Figure S108. TD-DFT simulated spectrum (---) and vertical excitation energies (red) superimposed on the experimental spectrum (−) of $[\mathbf{6b}]^+$ in CH_3CN (SMD-M06L/6-31+G(d,p)//SMD-O3LYP/6-31+G(d,p); FWHM = 3000 cm^{-1}; $f > 0.01$).

Table S19. TD-DFT predicted vertical excitation energies, oscillator strengths ($f > 0.01$) and MO contributions (> 10%) for [**6b**]$^+$.

No.	E / eV	f	MO contributions
3	1.19	0.056	H-2(B) →LUMO(B) (96%)
9	1.91	0.026	HOMO(A) →LUMO(A) (55%), HOMO(B) →L+4(B) (20%)
10	1.97	0.026	HOMO(A) →L+1(A) (66%)
13	2.07	0.012	HOMO(A) →L+2(A) (22%), H-1(B) →L+1(B) (17%), HOMO(B) →L+4(B) (18%), HOMO(B) →L+7(B) (11%)
15	2.08	0.018	H-1(A) →L+1(A) (70%)
22	2.28	0.016	H-3(A) →L+7(A) (10%), H-1(A) →L+7(A) (17%), HOMO(A→L+5(A) (10%), H-6(B) →LUMO(B) (18%), HOMO(B) →L+9(B) (18%)
23	2.28	0.030	H-6(B) →LUMO(B) (47%)
24	2.29	0.039	H-1(B) →L+2(B) (72%)
26	2.38	0.013	H-7(B) →LUMO(B) (20%), H-1(B) →L+3(B) (70%)
28	2.44	0.129	H-7(B) →LUMO(B) (64%), H-1(B) →L+3(B) (11%)
29	2.47	0.043	H-1(B) →L+4(B) (80%)
31	2.53	0.030	HOMO(A) →L+5(A) (34%), H-2(B) →L+1(B) (42%)
32	2.56	0.012	H-2(B) →L+2(B) (91%)
33	2.60	0.020	HOMO(A) →L+4(A) (78%), HOMO(B) →L+6(B) (10%)
37	2.68	0.024	H-2(A) →L+1(A) (17%), H-2(B) →L+3(B) (68%)
38	2.69	0.013	H-1(A) →L+4(A) (37%), HOMO(A) →L+7(A) (11%), H-3(B) →L+1(B) (18%)
40	2.71	0.012	HOMO(A) →L+7(A) (42%), H-3(B) →L+1(B) (20%), HOMO(B) →L+7(B) (13%)
43	2.75	0.013	H-1(A) →L+6(A) (61%), H-3(B) →L+2(B) (20%)
44	2.75	0.012	H-2(A) →L+1(A) (36%), H-1(A) →L+6(A) (26%), H-3(B) →L+2(B) (17%), H-2(B) →L+3(B) (12%)
45	2.79	0.045	H-2(A) →LUMO(A) (26%), H-2(A) →L+2(A) (13%), HOMO(A) →L+7(A) (10%)
47	2.84	0.068	H-2(A) →L+2(A) (19%), H-1(A) →L+5(A) (20%), HOMO(B) →L+8(B) (20%)
48	2.86	0.017	H-3(B) →L+3(B) (52%), HOMO(B) →L+8(B) (34%)
49	2.86	0.013	H-2(A) →L+3(A) (21%), H-1(B) →L+5(B) (61%)

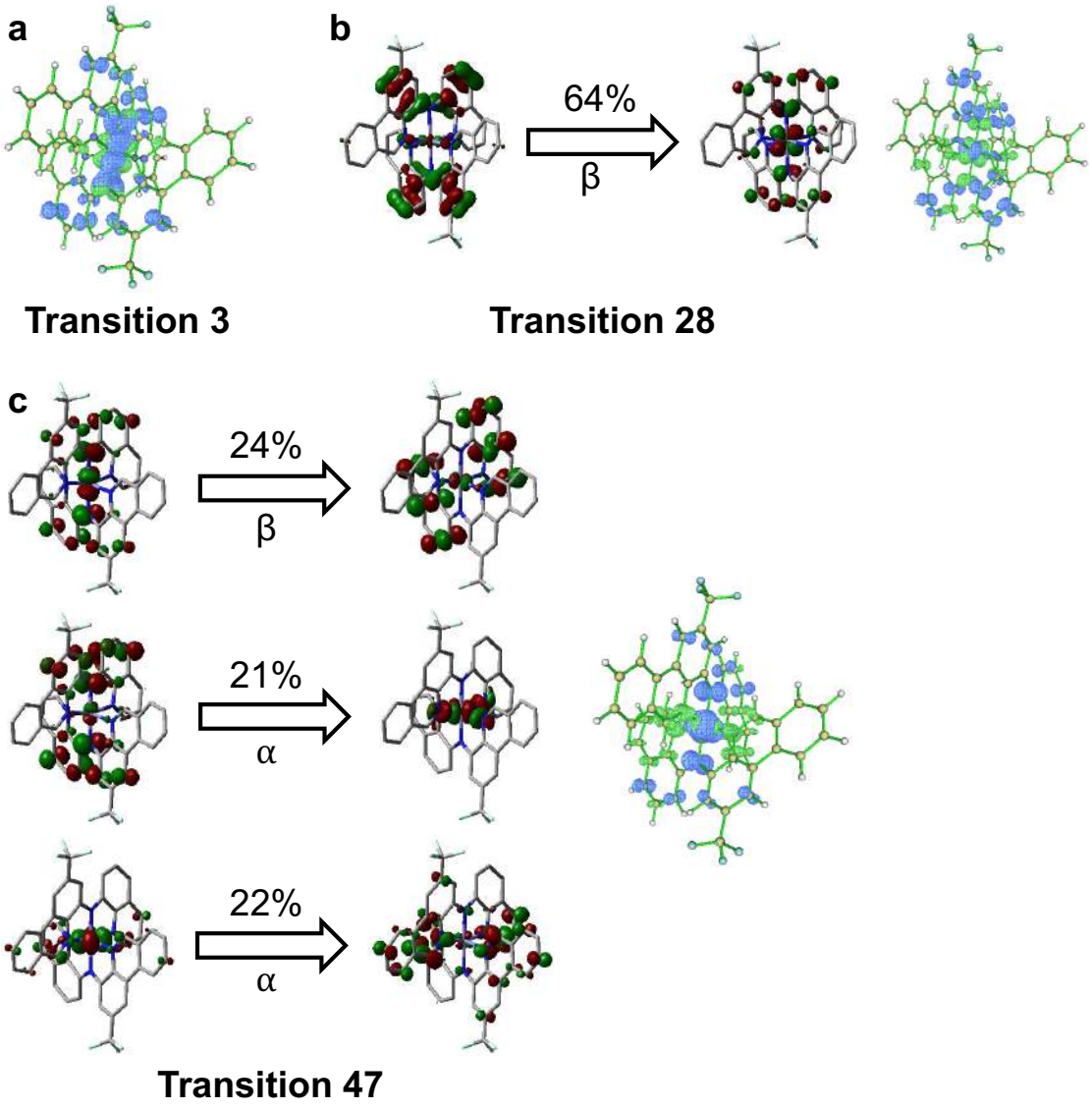

Figure S109. TD-DFT calculated NTOs and electron density gain (green) and depletion (blue) distribution maps (isosurface = 0.004) for transitions (a) 3 (β-HOMO-2→β-LUMO), (b) 28; and (c) 47 of [**6b**]$^{+}$ (SMD-M06L/6-31+G(d,p)//SMD-O3LYP/6-31+G(d,p)).

Theoretical Calculations: Higher Multiplicity States

As described above, unconstrained geometry optimizations of **6b** were carried out using Gaussian09[11] employing the O3LYP[12] functional, 6-31+G(d,p) basis set[13–16] on all atoms, and the solvation model based on density[6] (SMD, solvent = CH_3CN). Beyond the ground state, unrestricted DFT (uDFT) calculations were also performed on a set of different states given by different multiplicities, including the lowest excited triplet (charge = 0, multiplicity = 3) state and quintet (charge = 0, multiplicity = 5) state, with the optimized singlet ground state geometry as starting input. Frequency calculations were performed to confirm these structures were at a minimum. Subsequently, single-point calculations of the different states given by different multiplicities were carried out using M06L[17] (SMD-M06L/6-31+G(d,p)) at the minimum geometry of each state. As discussed above, this computational approach was selected to be compatible with the experimentally determined ground state of **6b** (*vide supra*), in light of recent reports on the use of DFT for investigating the electronic structures of pseudo-octahedral iron complexes.[20,26]

Quantum chemical calculations indicate the origin of the increased excited state lifetime is due to suppressed non-radiative decay of the ^{3}MLCT-type state (here, ^{3}PABLCT) via MC states. Figure 4.11 shows the density functional theory (DFT) calculated ground state and excited state potential energy minima of **6b** (open triangles) and sketches the potential energy surfaces (lines) through the energy of each state at the minimum geometry of the other states (open circles). The lowest-lying state of triplet multiplicity was found to have considerable CT character (see spin density at Fe, Table S20).

Table S20. Quantum chemically calculated properties of **6b**. Calculated properties include relative total energies (E_{rel}) in eV, average Fe-N bond distances in Å (Avg. Fe-N), and Mulliken Spin Densities on iron (SD(Fe)).

Geometry	State	E_{rel} / eV	Avg. Fe-N / Å	SD(Fe)
^{1}6b (ground state)	^{1}**6b**	0.00	1.963	-
	^{3}**6b**	1.25		0.82
	^{5}**6b**	1.56		3.87
^{3}6b (triplet, ^{3}T)	^{1}**6b**	0.75	2.083	-
	^{3}**6b**	0.80		2.08
	^{5}**6b**	0.84		3.78
^{5}6b (quintet, ^{5}Q)	^{1}**6b**	1.44	2.185	-
	^{3}**6b**	1.63		2.22
	^{5}**6b**	0.41		4.21

PUMP-PROBE SPECTROSCOPY

Experimental Details

All samples were handled and prepared in a glovebox under Ar atmosphere. During spectroscopic measurements, solutions were also kept under Ar to prevent oxidation from exposure to air. UV-Vis spectra of solutions of **6a-c** measured before and after the transient absorption laser experiments did not indicate any spectral changes, verifying the samples did not degrade during the time-resolved laser measurements. The pump-probe measurements were made using a Clark MXR CPA-2001 Ti:Sapphire laser system generating 150 fs laser pulses of 780 nm wavelength fundamental output with 1 kHz repetition rate, 50 μW power. The 780 nm fundamental wavelength was used to pump all samples. The probe beam was a white light continuum spanning 450-780 nm, generated by focusing 5% of the fundamental laser output into a sapphire crystal. A motorized delay stage controlled the relative time differentials between pump and probe pulses from time zero, when pump and probe pulse traverse the sample simultaneously, to 3 ns. The differential spectra were averaged over 3 seconds for each delay time point recorded and chirp corrected.

Analysis of TA Spectra of **6c**

The transient spectral features of **6c** (Figure S112 and S113) are similar to that of **6a-b** (Figure 4.10), with rapid formation of a long-lived ESA at 472 nm within the first picosecond in toluene. This accompanies formation of a transient bleaching that reaches maximum intensity at 0.78 ps delay time. This is attributed to formation of a triplet state charge-transfer state (^{3}MLCT-like, here PALCT in character) from an initially formed ^{1}MLCT one, consistent with a fast rate of intersystem crossing (ISC) as is typically observed for iron polypyridyl complexes.[27,28] Both the ESA and GSB then decay with lifetimes of 3.3 and 3.0 ns, respectively (Figure S112, Table 4.3). Principle component analysis illustrates these spectral changes, with Component 1 showing the initial excited state evolving to the long-lived PALCT state represented by Component 2. The principle component features of **6a-c** are similar suggesting similar processes occur for all iron complexes. The most prominent features in the long-lived spectra observed by TA for **6c** again match those of the singly oxidized [**6c**]$^+$.

TA Spectra in Different Solvents

Transient differential pump-probe spectra were collected for **6a-b** in additional solvents to investigate any solvent dependence to the charge-transfer lifetimes. Acetonitrile and tetrahydrofuran (THF) solutions were excited into the lower energy end of the broad charge-transfer manifold ($\lambda_{excitation}$ = 780 nm) and probed with broadband white light. Similar transient spectral features are observed for both complexes, in all solvents (see Figure Ss 32-35), with the most prominent features in the long-lived spectra observed by TA matching those of the singly oxidized complexes in their respective solvents. For **6a**, the bleach lifetimes are all very similar, regardless of solvent (Table S 15). For **6b**, there is a little more variance, but all of them are still

very similar. Solvent polarity does not appear to play a role in how the compounds relax. As can be seen in the calculated electron-hole maps and NTOs (Figure Ss 15 and 18), the symmetry of **6a-b** means charge-transfer does not reorganize electron density in a strictly linear fashion. Accordingly, large changes in dipole moments are not expected and there is little solvent dependence of the CT lifetimes.

Table S21. Time constants obtained from fitting kinetics traces at indicated wavelengths with single exponential decay functions.

Compound	Solvent	λ_{obs} (nm)	τ_{decay} (ps)
6a	Toluene	486	2041 ± 23
		600	2625 ± 35
	Acetonitrile	485	1866 ± 33
		600	2614 ± 47
	THF	489	2499 ± 20
		600	2695 ± 42
6b	Toluene	485	2454 ± 13
		600	2669 ± 41
	Acetonitrile	483	2221 ± 14
		600	2562 ± 38
	THF	483	2717 ± 23
		600	2801 ± 41
6c	Toluene	472	3280 ± 118
		602	2965 ± 110
	Acetonitrile	472	2793 ± 127
		596	2907 ± 114
	THF	475	3204 ± 70
		600	2802 ± 98

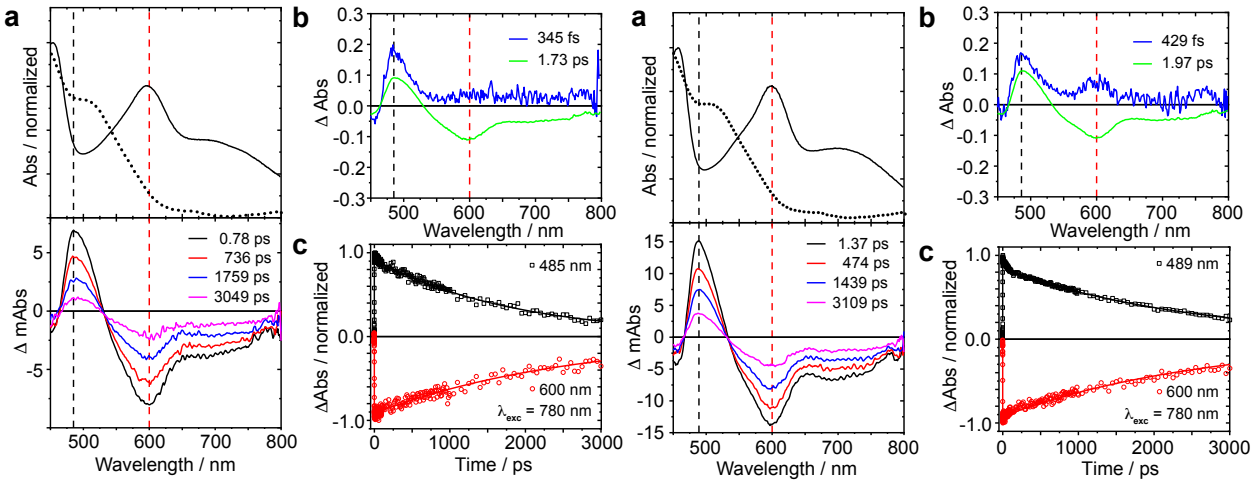

Figure S110. (a) Steady-state absorption spectrum of [**6a**]$^{0/+}$ (top) and transient absorption spectra (bottom) of **6a** in CH_3CN (left) and THF (right) at indicated time delays. (b) Global fit analysis principle components constructed from TA data. The two shown components model the main spectral changes: a red shift of the initial ESA and formation of the transient bleaching. (c) Kinetic traces at indicated wavelengths (see legend) and exponential fits (solid lines, fitting results are summarized in Table S21.

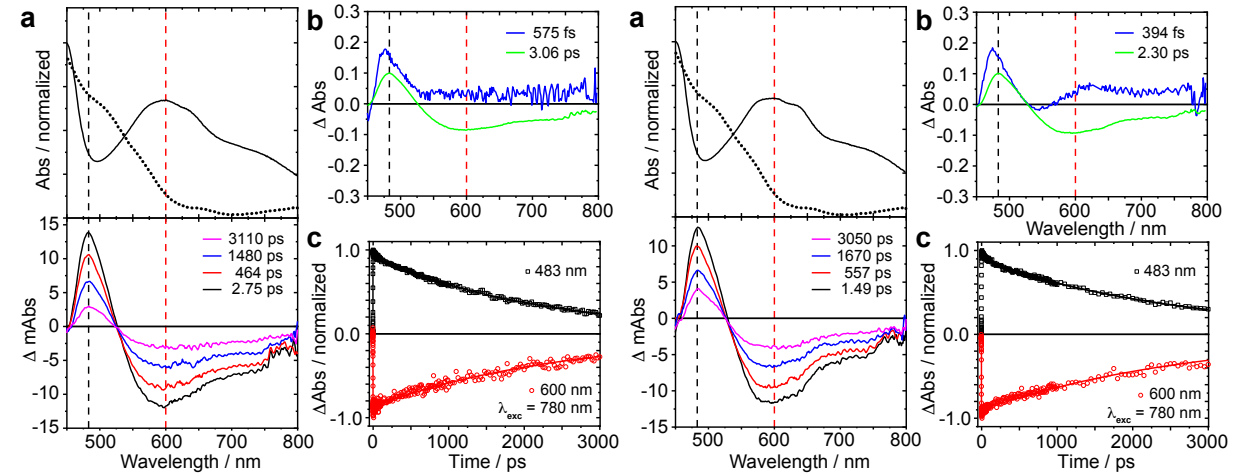

Figure S111. (a) Steady-state absorption spectrum of [**6b**]$^{0/+}$ (top) and transient absorption spectra (bottom) of **6b** in CH_3CN (left) and THF (right) at indicated time delays. (b) Global fit analysis principle components constructed from TA data. The two shown components model the main spectral changes: a red shift of the initial ESA and formation of the transient bleaching. (c) Kinetic traces at indicated wavelengths (see legend) and exponential fits (solid lines, fitting results are summarized in Table S21.

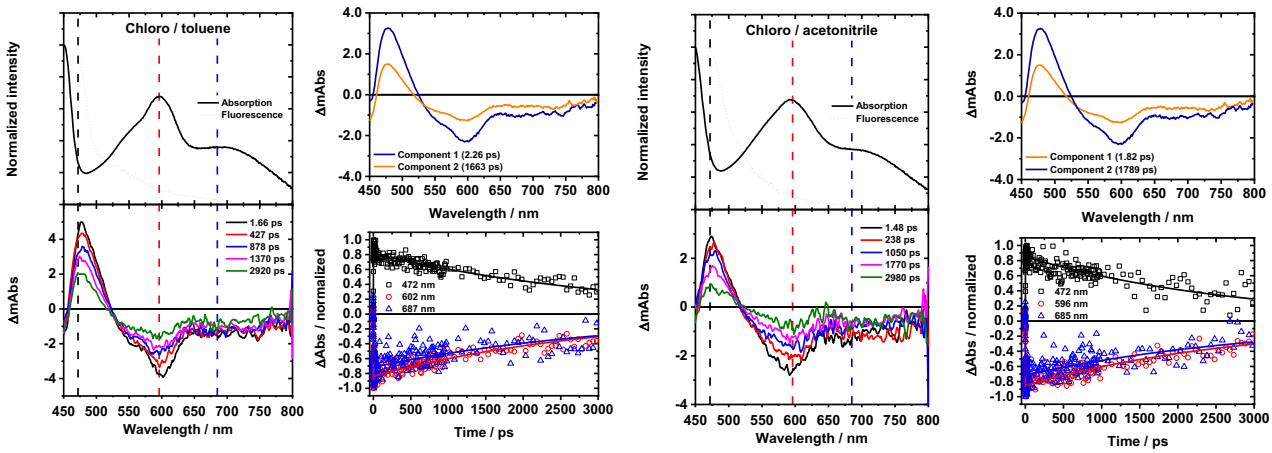

Figure S112. (a) Steady-state absorption spectrum of $[\mathbf{6c}]^{0/+}$ (top) and transient absorption spectra (bottom) of **6c** in toluene (left) and CH_3CN (right) at indicated time delays. (b) Global fit analysis principle components constructed from TA data. The two shown components model the main spectral changes: a red shift of the initial ESA and formation of the transient bleaching. (c) Kinetic traces at indicated wavelengths (see legend) and exponential fits (solid lines, fitting results are summarized in Table S21.

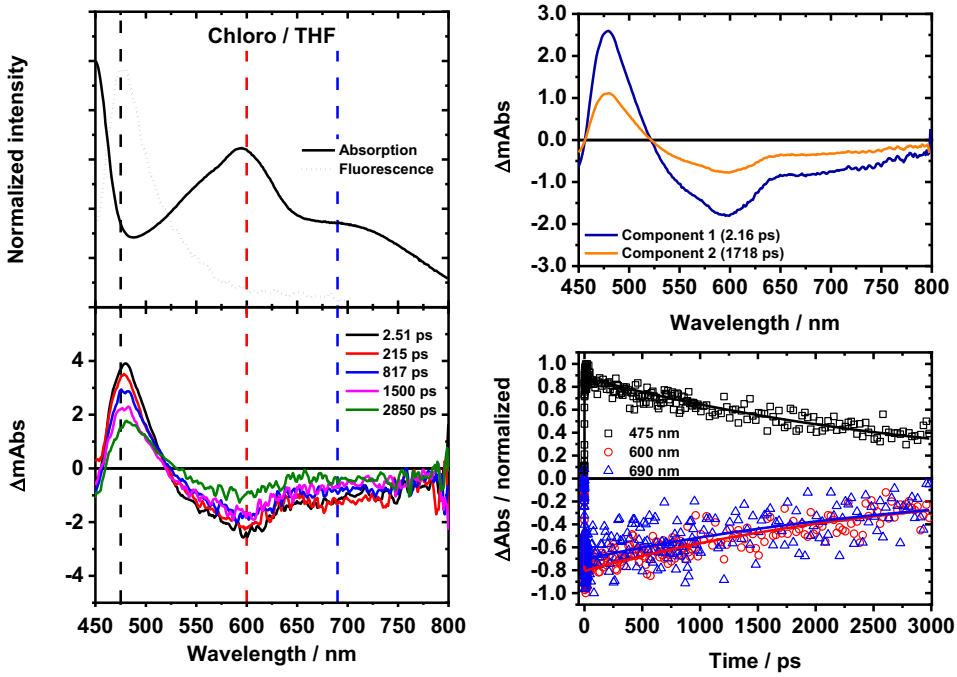

Figure S113. (a) Steady-state absorption spectrum of $[\mathbf{6c}]^{0/+}$ (top) and transient absorption spectra (bottom) of **6c** in THF at indicated time delays. (b) Global fit analysis principle components constructed from TA data. The two shown components model the main spectral changes: a red shift of the initial ESA and formation of the transient bleaching. (c) Kinetic traces at indicated wavelengths (see legend) and exponential fits (solid lines, fitting results are summarized in Table S21.

NMR SPECTRA

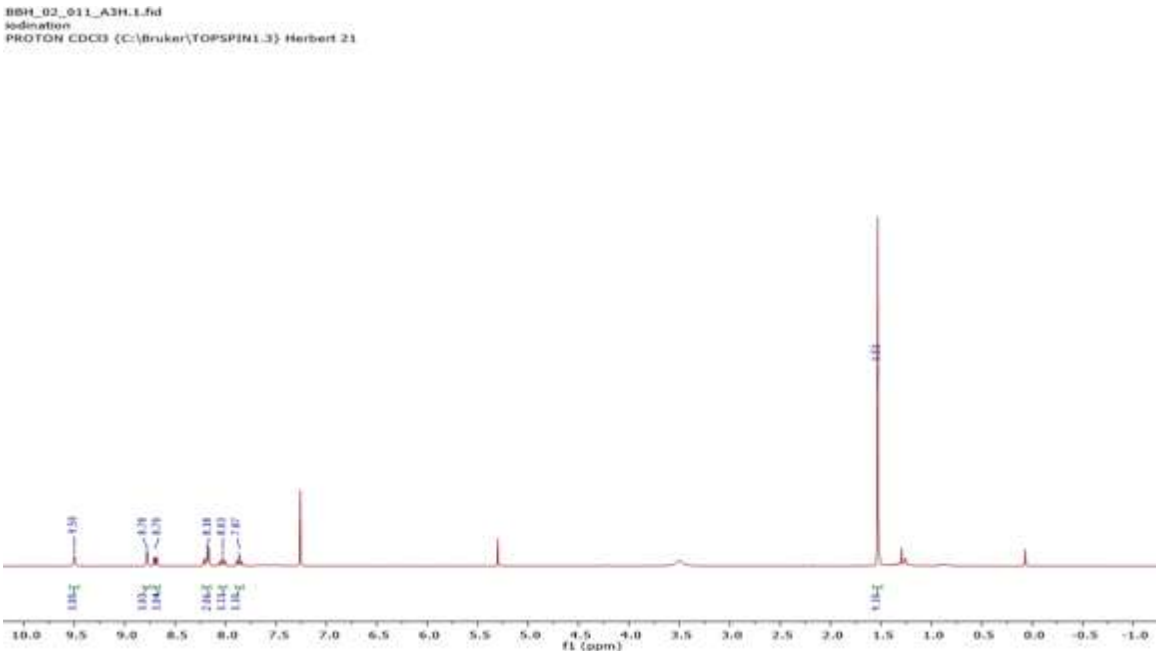

Figure S114. ^{1}H NMR (300 MHz, $CDCl_3$, 25 °C) of 4-nitro-2-tert-butylphenanthridine (**4a**).

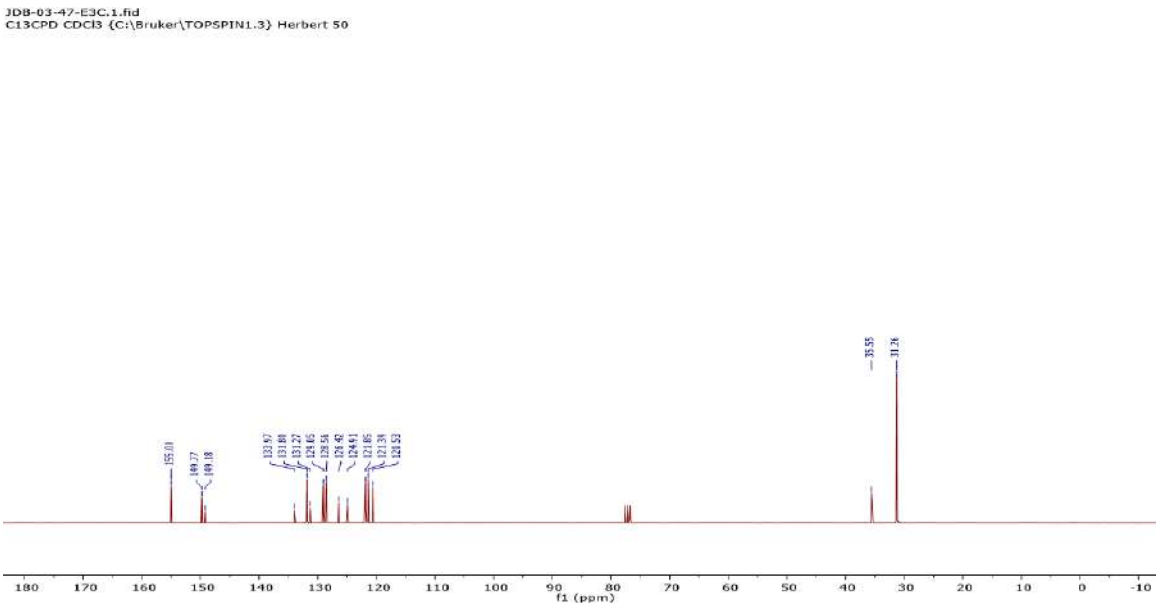

Figure S115. $^{13}C\{^{1}H\}$ NMR (75 MHz, $CDCl_3$, 25°C) of 4-nitro-2-tert-butylphenanthridine (**4a**).

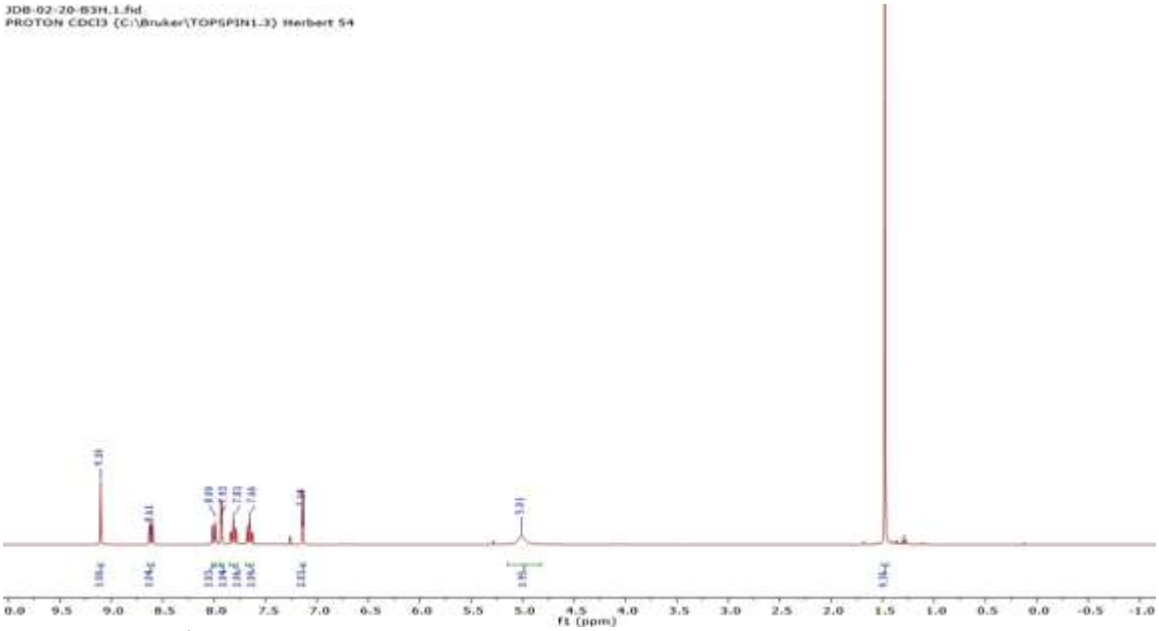

Figure S116. ^{1}H NMR (300 MHz, $CDCl_3$, 25°C) of 4-amino-2-*t*Bu-phenanthridine (**4d**).

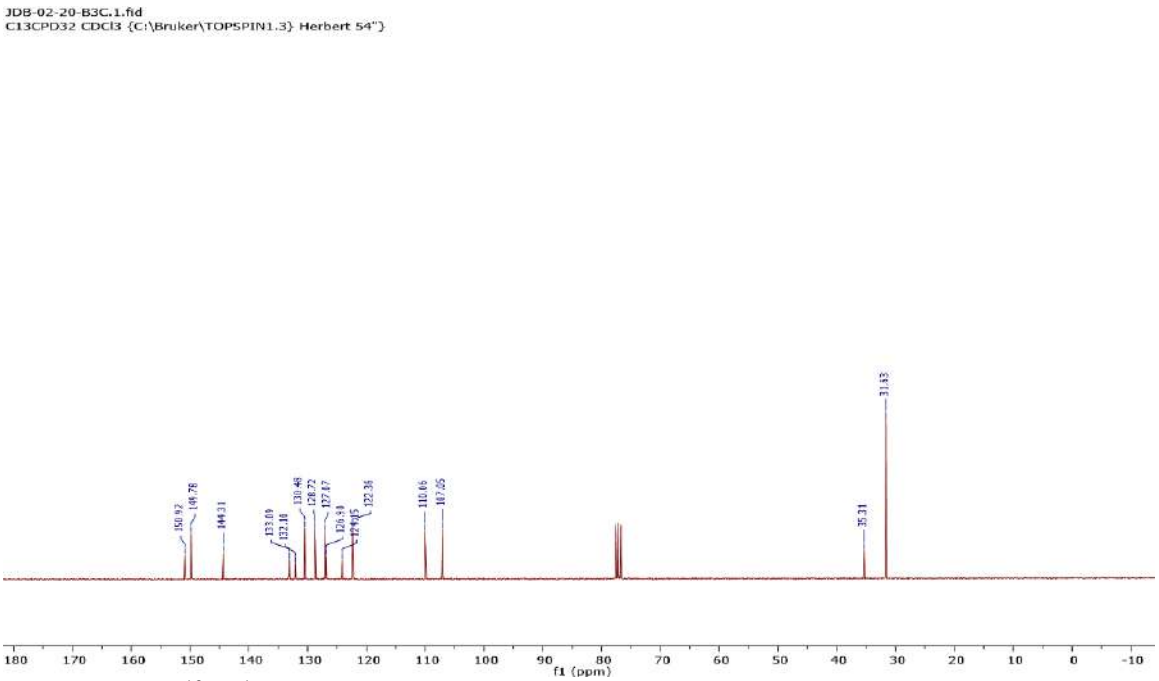

Figure S117. $^{13}C\{^{1}H\}$ NMR (75 MHz, $CDCl_3$, 25°C) of 4-amino-2-*t*Bu-phenanthridine (**4d**).

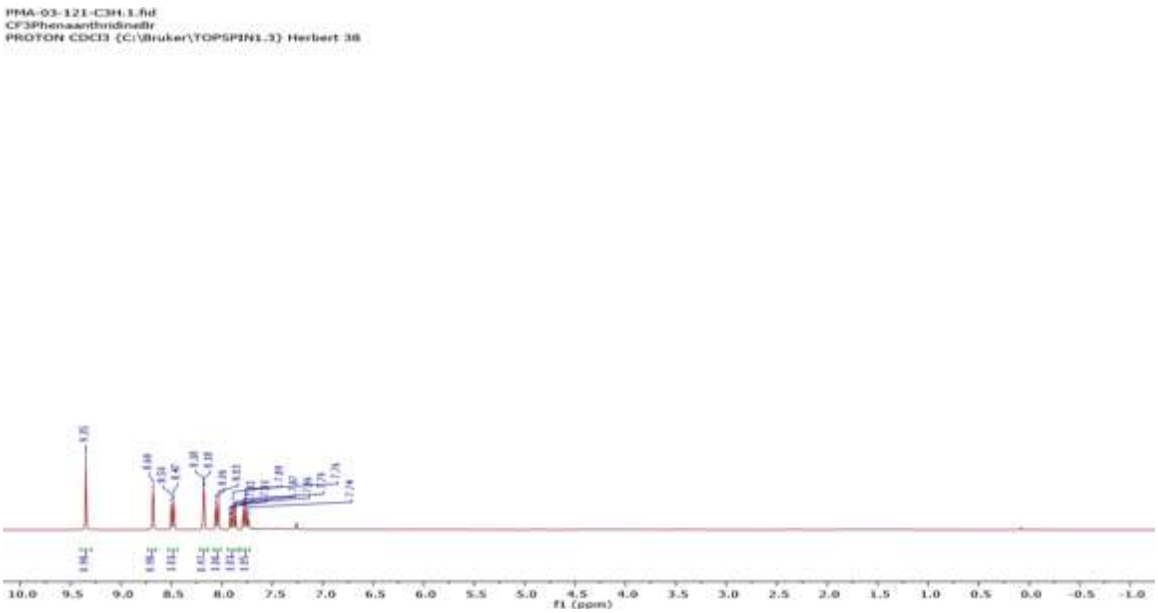

Figure S118. ^{1}H NMR (300 MHz, $CDCl_3$, 25°C) of 4-bromo-2-trifluoromethylphenanthridine (**4b**).

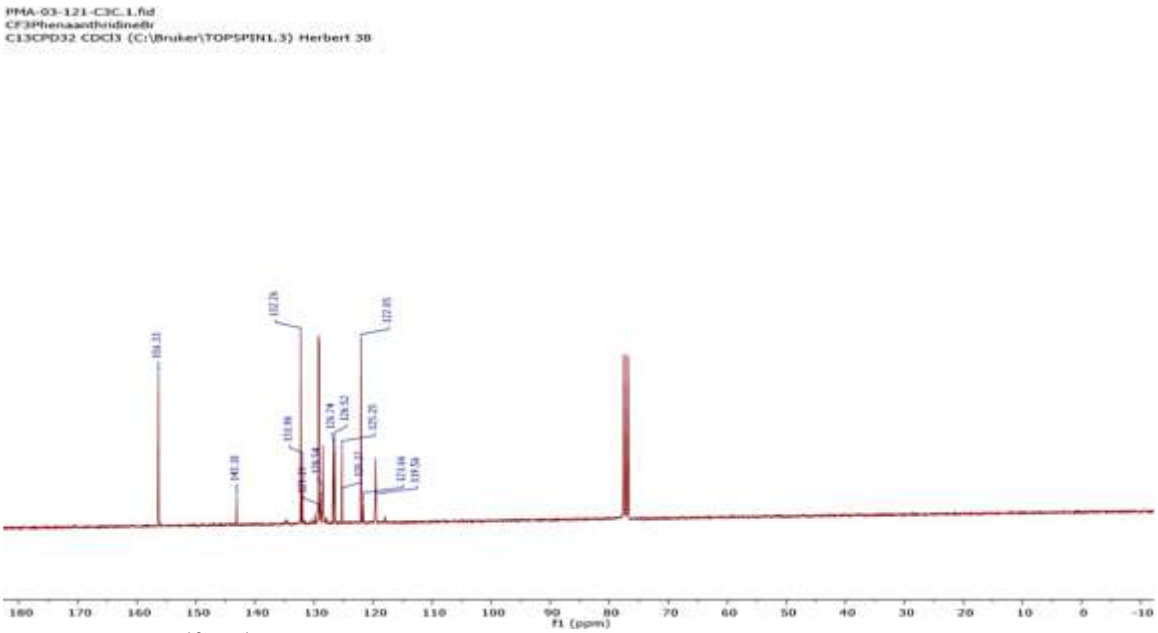

Figure S119. $^{13}C\{^{1}H\}$ NMR (75 MHz, $CDCl_3$, 25°C) of 4-bromo-2-CF_3-phenanthridine (**4b**).

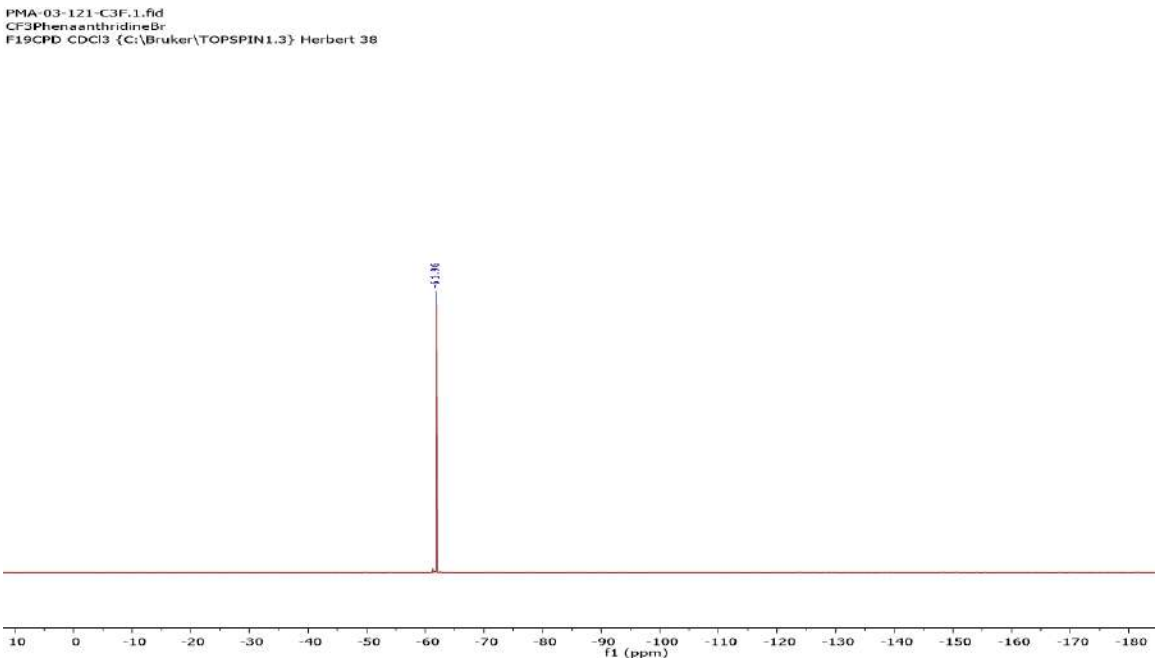

Figure S120. ^{19}F NMR (470 MHz, $CDCl_3$, 25°C) of 4-bromo-2-trifluoromethylphenanthridine (**4b**).

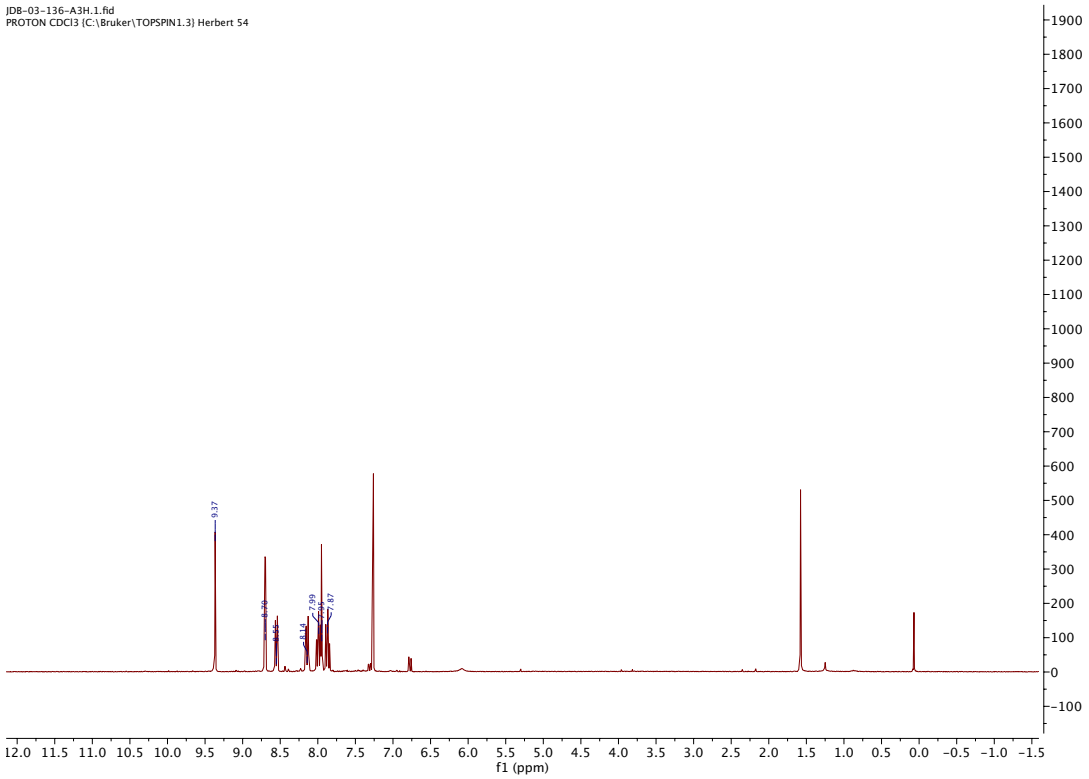

Figure S121. ^{1}H NMR (300 MHz, $CDCl_3$, 25°C) of 4-nitro-2-chlorophenanthridine (**4c**).

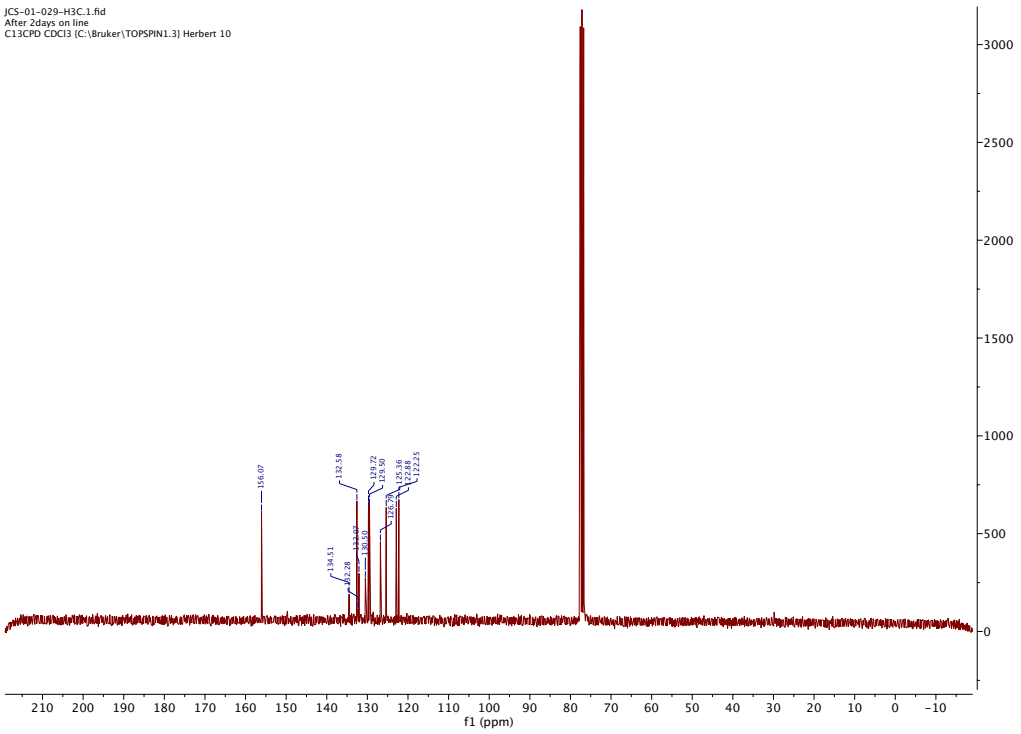

Figure S122. ^{13}C NMR (300 MHz, $CDCl_3$, 25°C) of 4-nitro-2-chlorophenanthridine (**4c**).

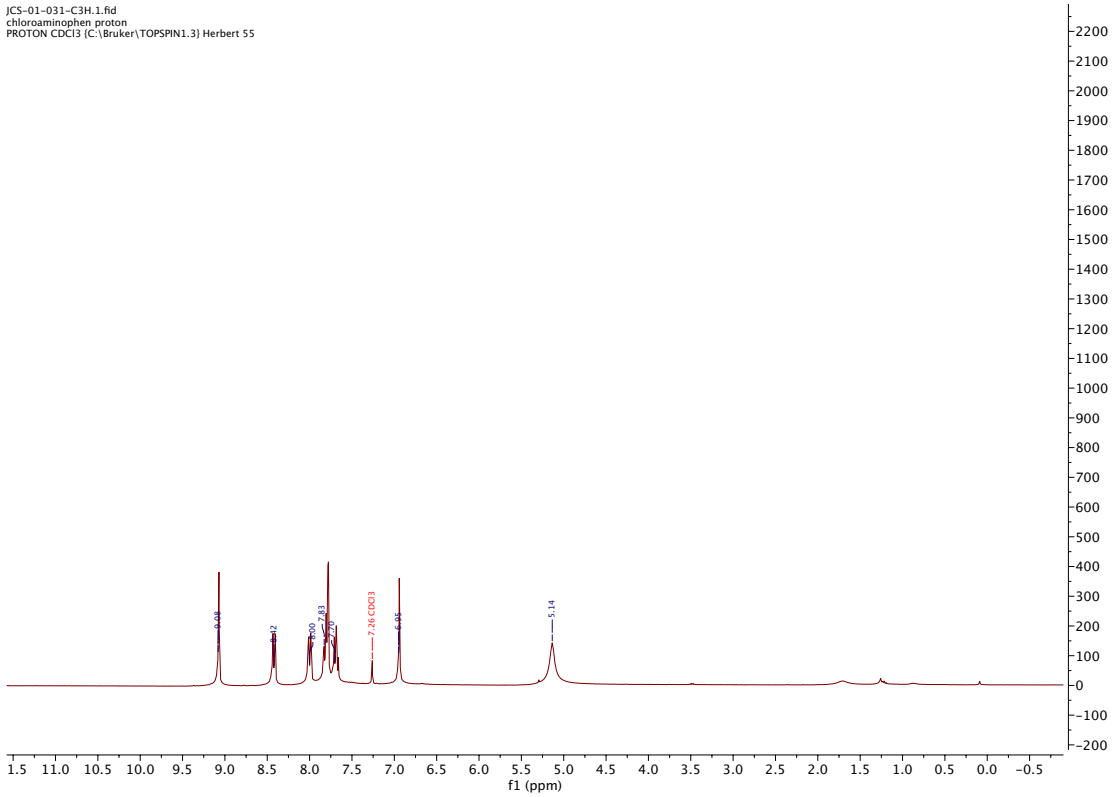

Figure S123. ^{1}H NMR (300 MHz, $CDCl_3$, 25°C) of 4-amino-2-chlorophenanthridine (**4e**).

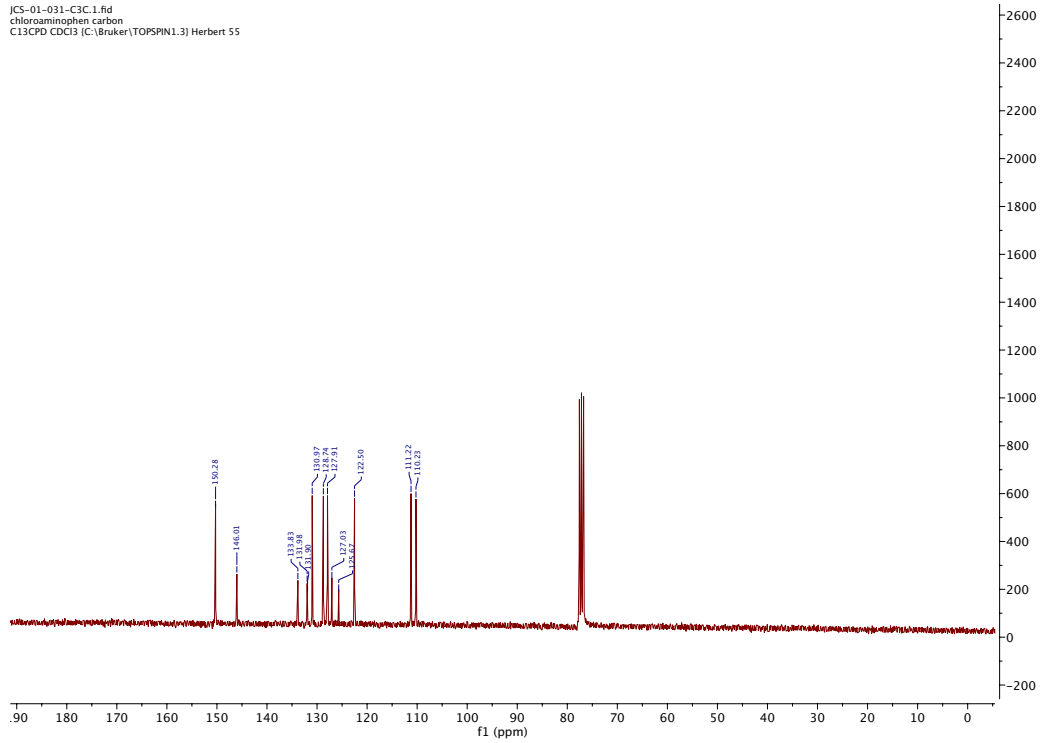

Figure S124. ^{1}H NMR (300 MHz, $CDCl_3$, 25°C) of 4-amino-2-chlorophenanthridine (**4e**).

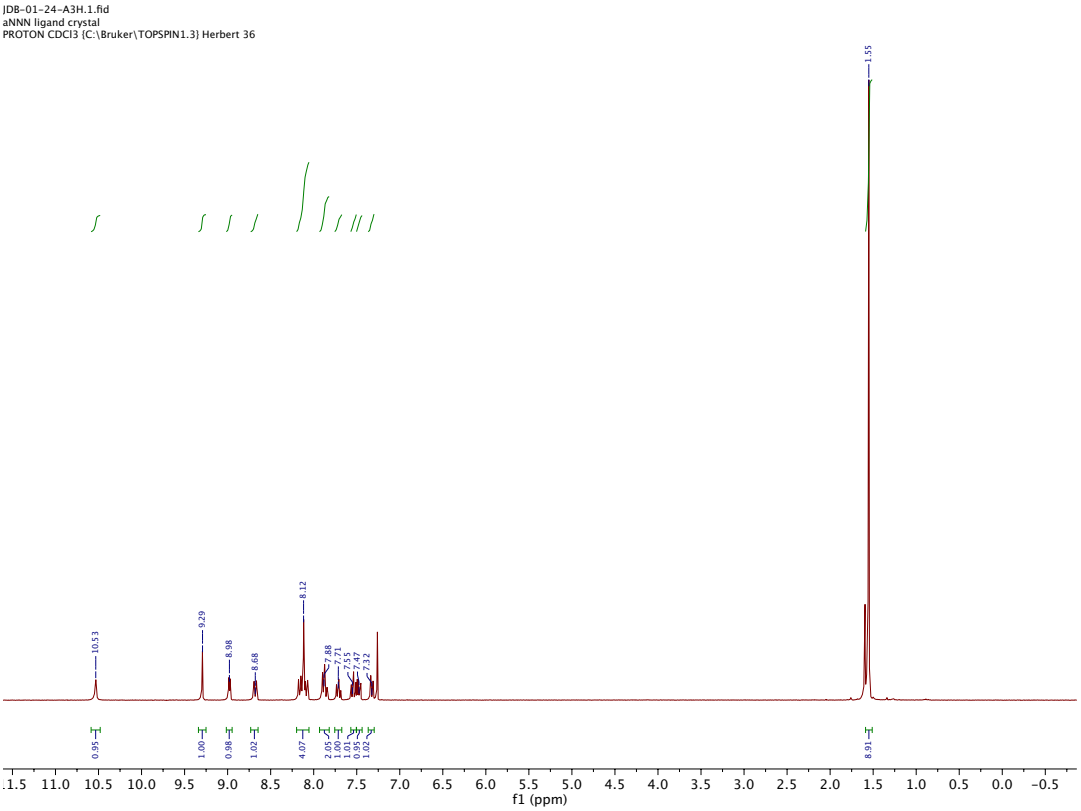

Figure S125. ^{1}H NMR (300 MHz, $CDCl_3$, 25°C) of ^{t}Bu-PhenNN(H)N^{Quin} (**5a**).

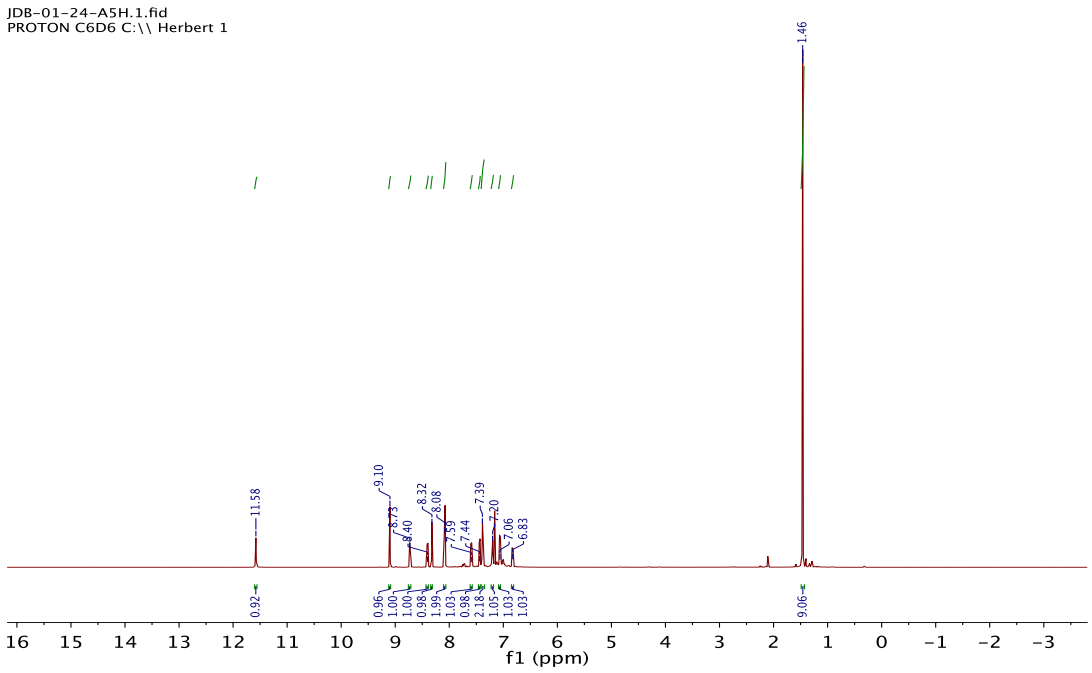

Figure S126. ^{1}H NMR (300 MHz, C_6D_6, 25°C) of $^{t\text{Bu-Phen}}$NN(H)N$^{\text{Quin}}$ (**5a**).

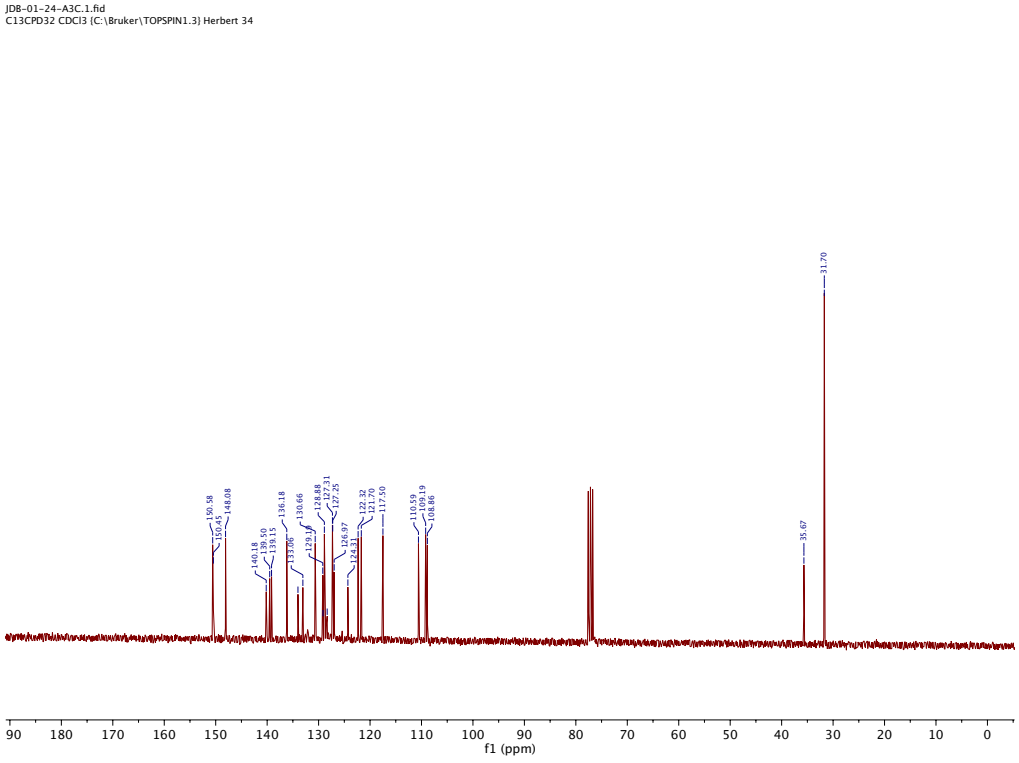

Figure S127. ^{13}C{^{1}H} NMR (125 MHz, $CDCl_3$, 25°C) of tBu-phenNN(H)NQuin (**5a**).

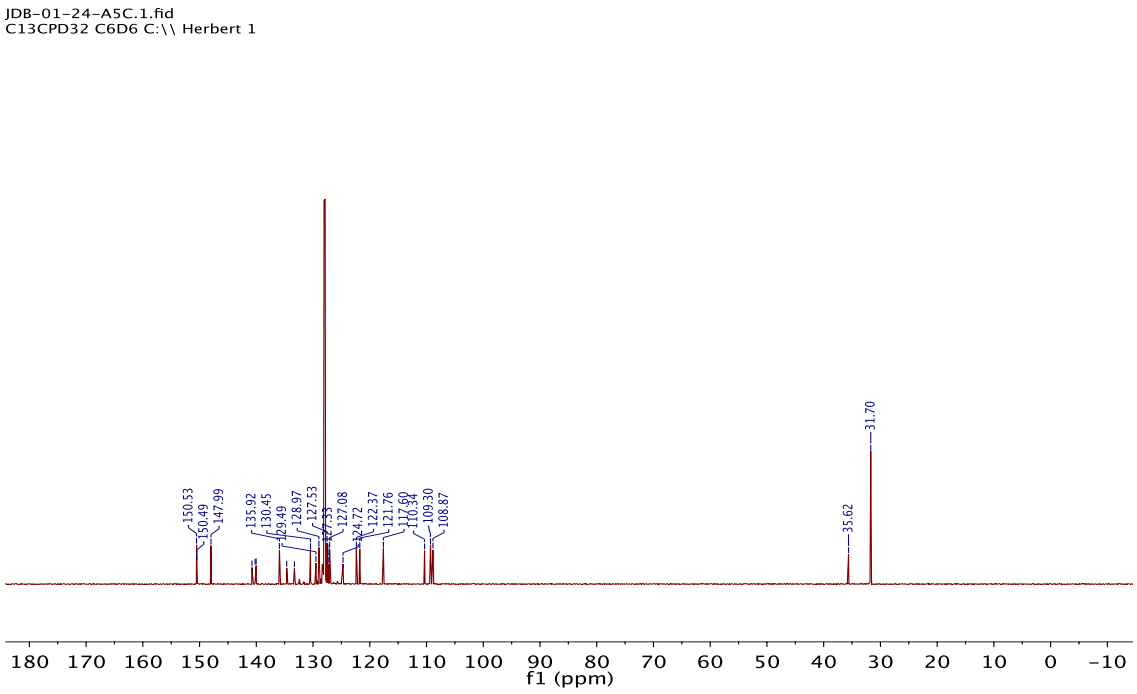

Figure S128. $^{13}C\{^{1}H\}$ NMR (125 MHz, C_6D_6, 25°C) of ^{t}Bu-Phen$NN(H)N^{Quin}$ (**5a**).

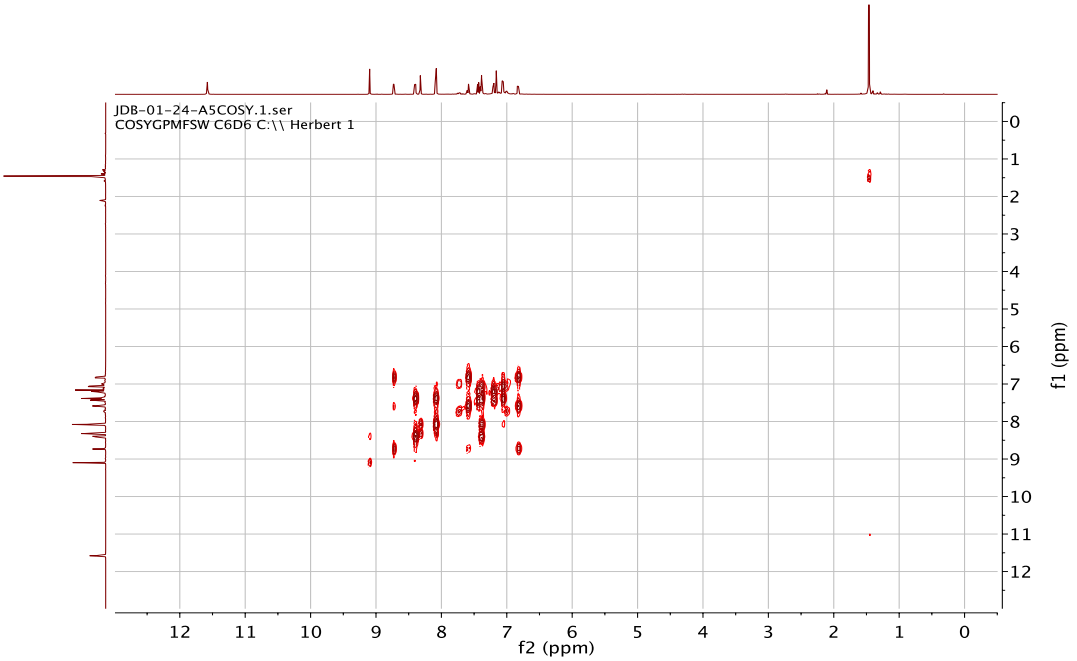

Figure S129. ^{1}H-^{1}H COSY NMR (500 MHz, C_6D_6, 25°C) of ^{t}Bu-Phen$NN(H)N^{Quin}$ (**5a**).

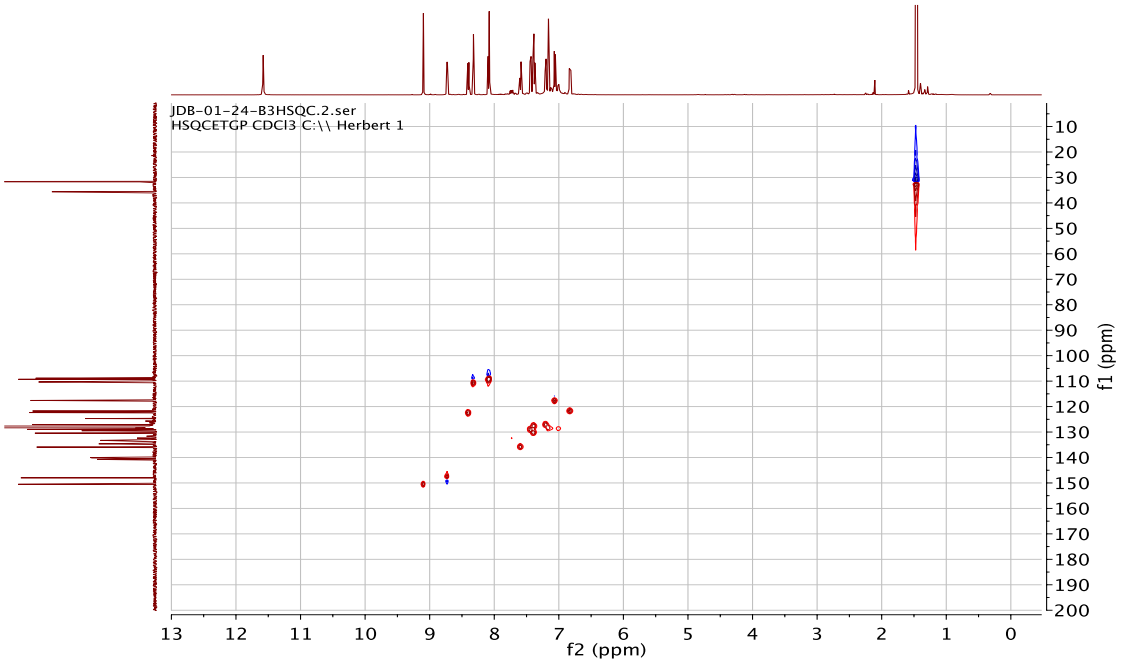

Figure S130. HSQC NMR (500/125 MHz, C_6D_6, 25°C) of $^{tBu\text{-}Phen}NN(H)N^{Quin}$ (**5a**).

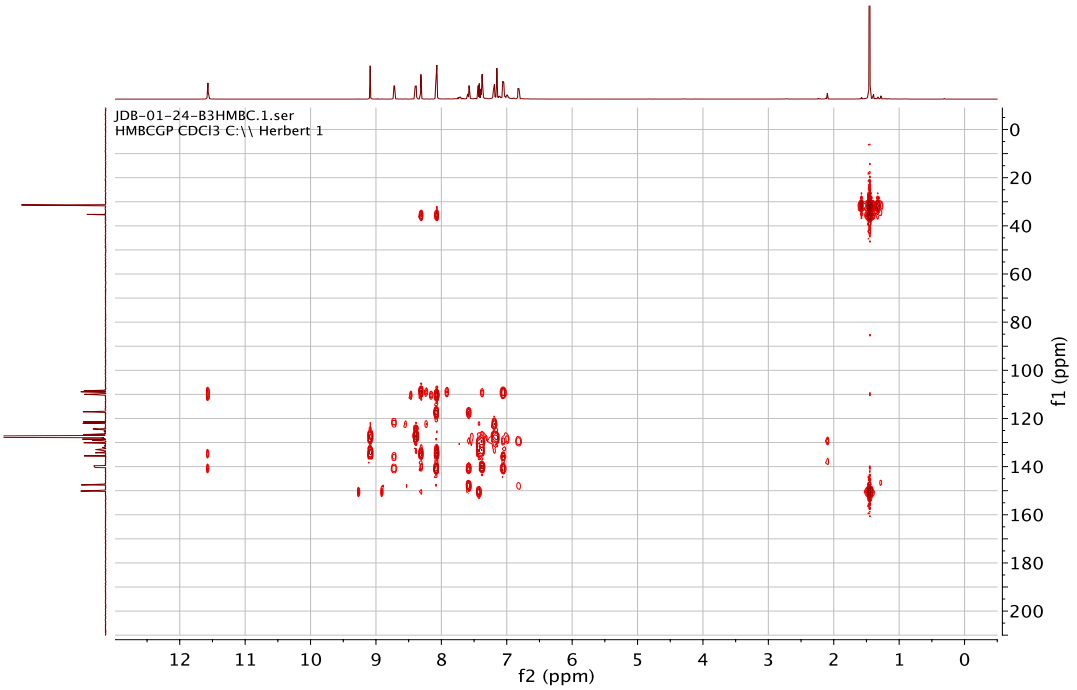

Figure S131. HMBC NMR (500/125 MHz, C_6D_6, 25°C) of $^{t\text{Bu-Phen}}NN(H)N^{Quin}$ (**5a**).

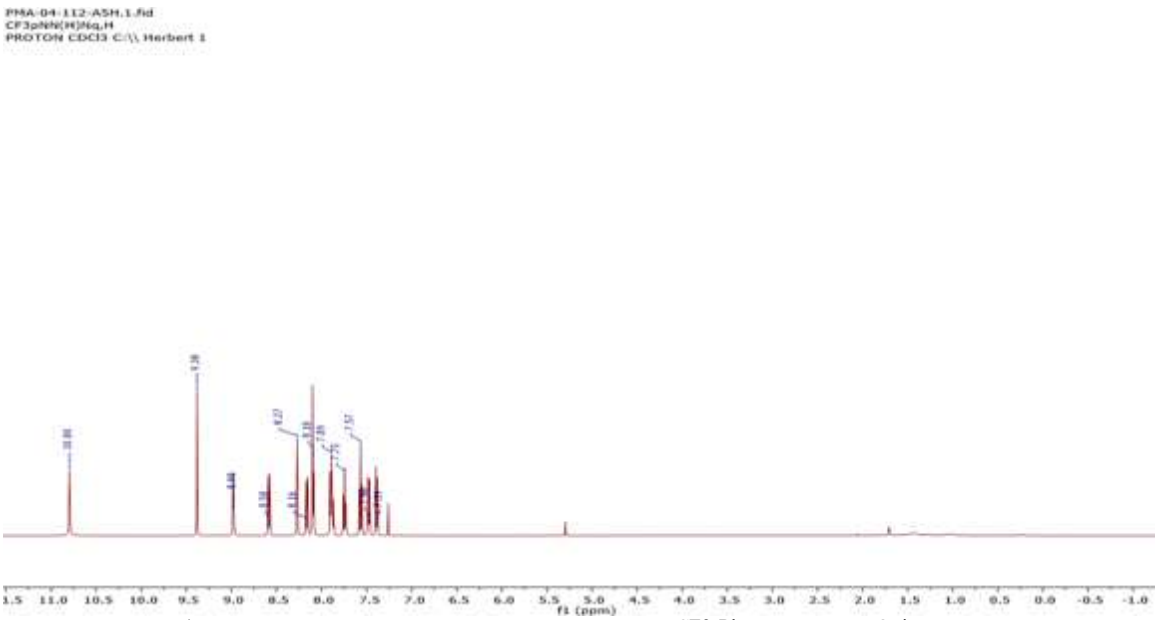

Figure S132. ^{1}H NMR (300 MHz, $CDCl_3$, 25°C) of $^{CF3\text{-}Phen}NN(H)N^{Quin}$ (**5b**).

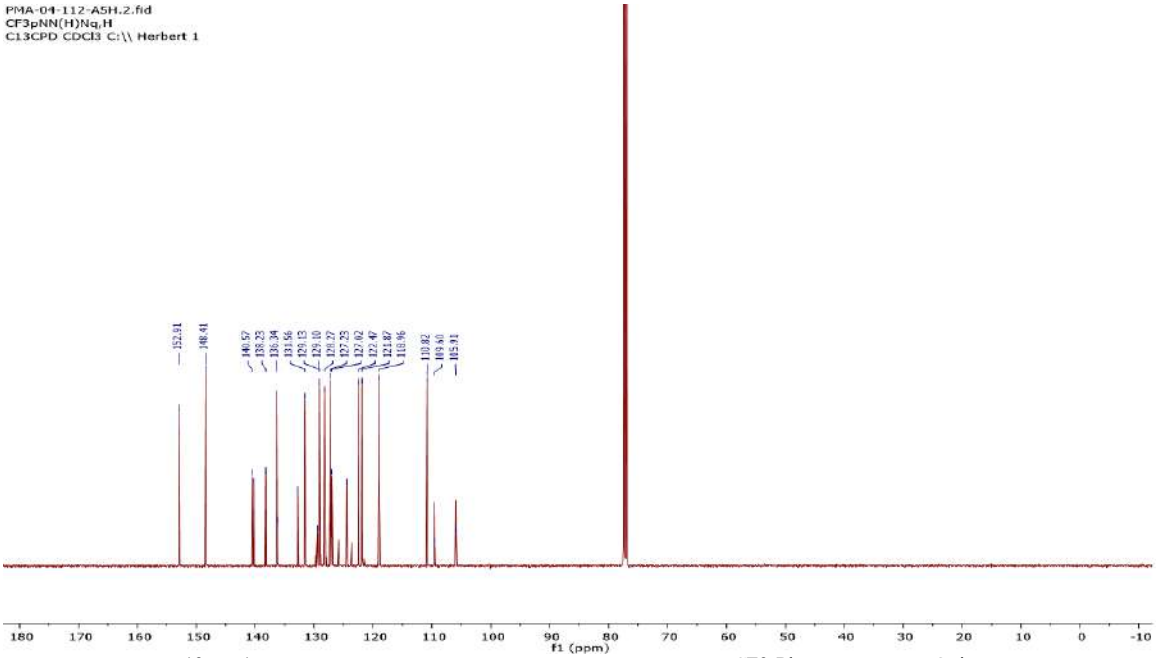

Figure S133. $^{13}C\{^{1}H\}$ NMR (75 MHz, $CDCl_3$, 25°C) of $^{CF3\text{-}Phen}NN(H)N^{Quin}$ (**5b**).

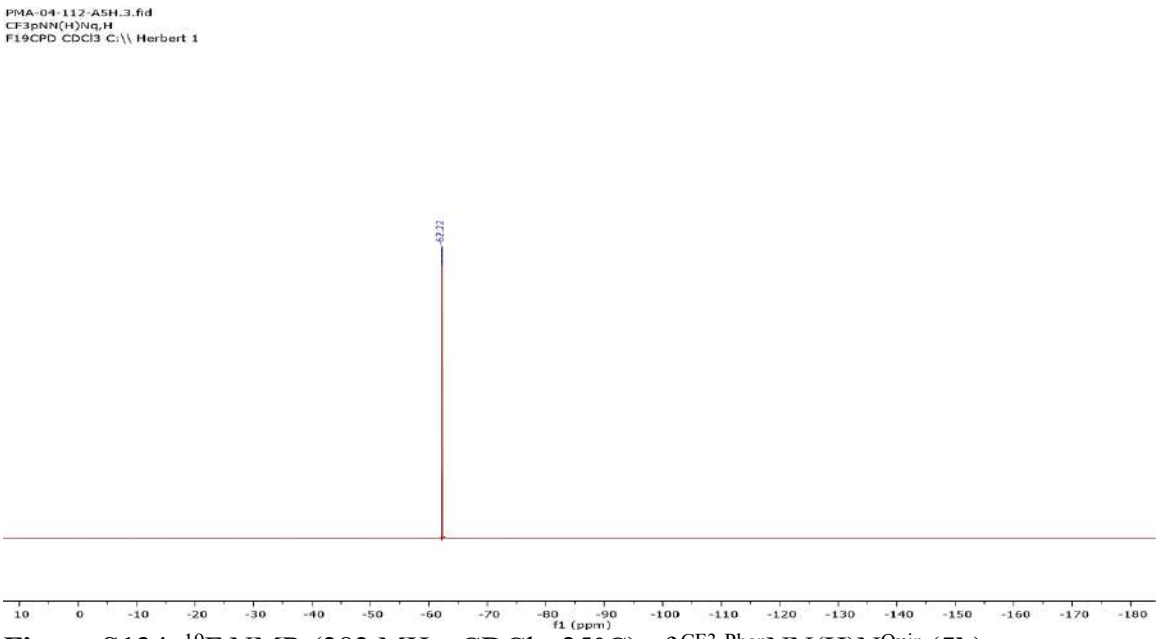

Figure S134. ^{19}F NMR (282 MHz, $CDCl_3$, 25°C) of $^{CF3\text{-}Phen}NN(H)N^{Quin}$ (**5b**).

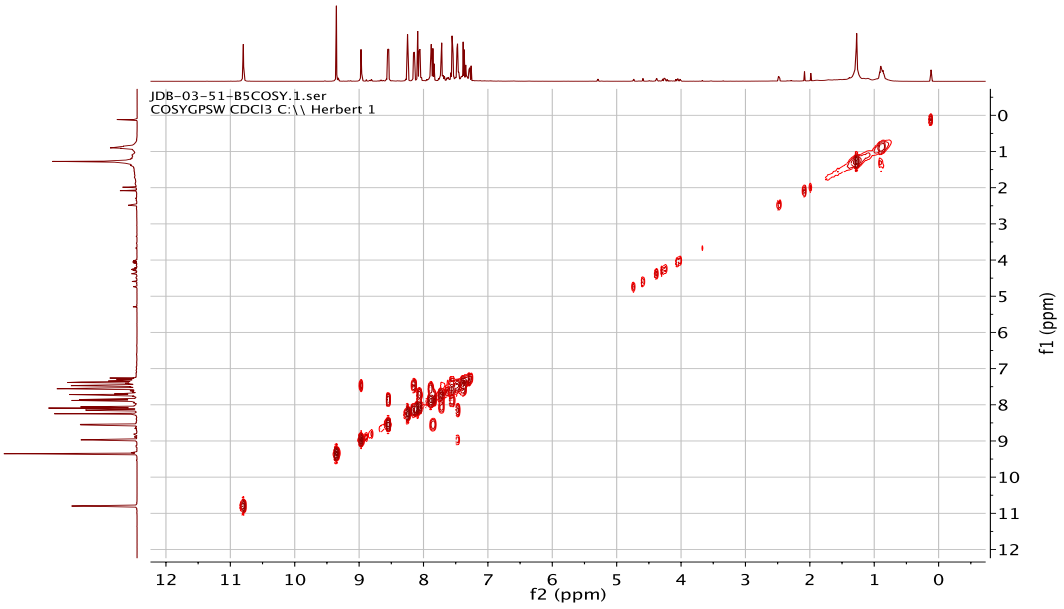

Figure S135. ^{1}H-^{1}H COSY NMR (500 MHz, $CDCl_3$, 25°C) of $^{CF3\text{-}Phen}NN(H)N^{Quin}$ (**5b**).

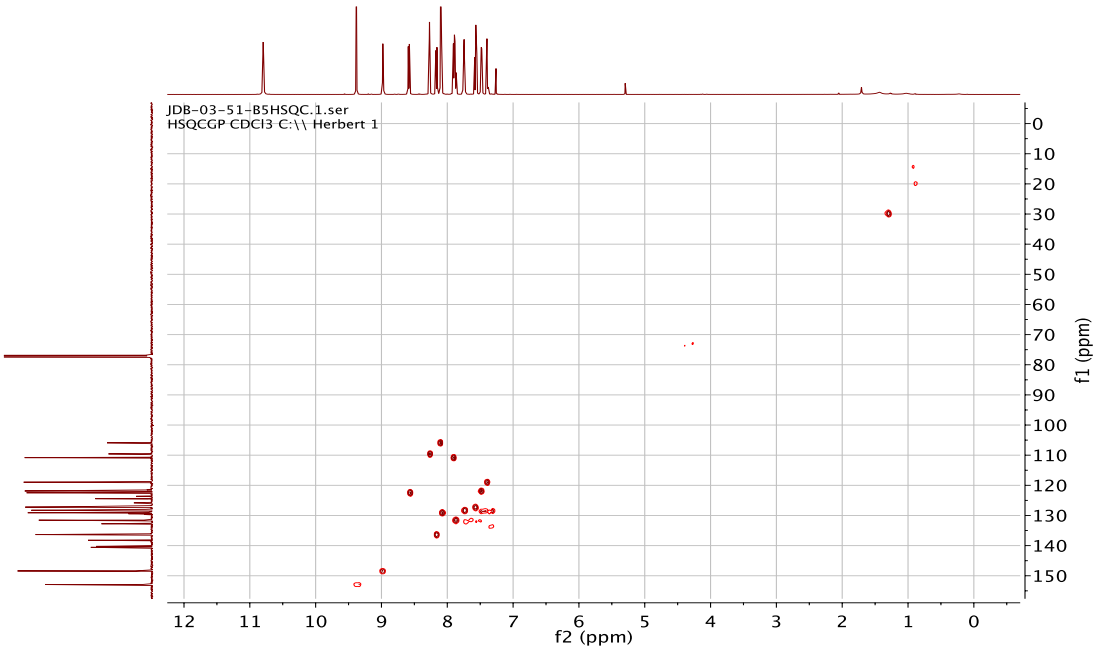

Figure S136. HSQC NMR (500/125 MHz, CDCl3, 25°C) of $^{CF3\text{-}Phen}NN(H)N^{Quin}$ (**5b**).

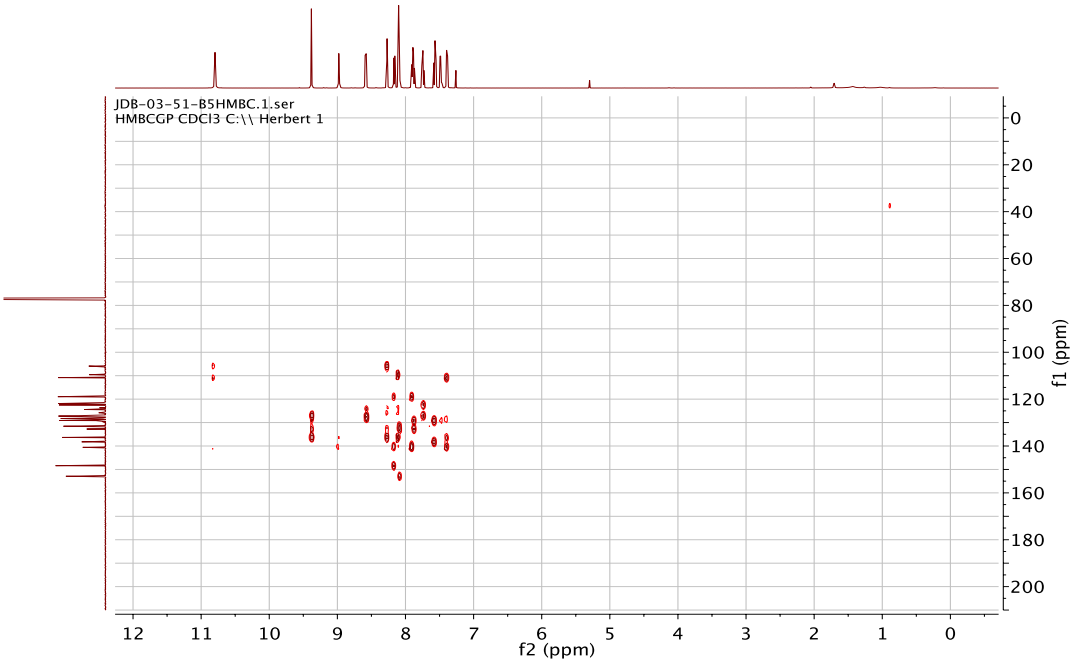

Figure S137. HMBC NMR (500/125 MHz, $CDCl_3$, 25°C) of $^{CF3\text{-}Phen}NN(H)N^{Quin}$ (**5b**).

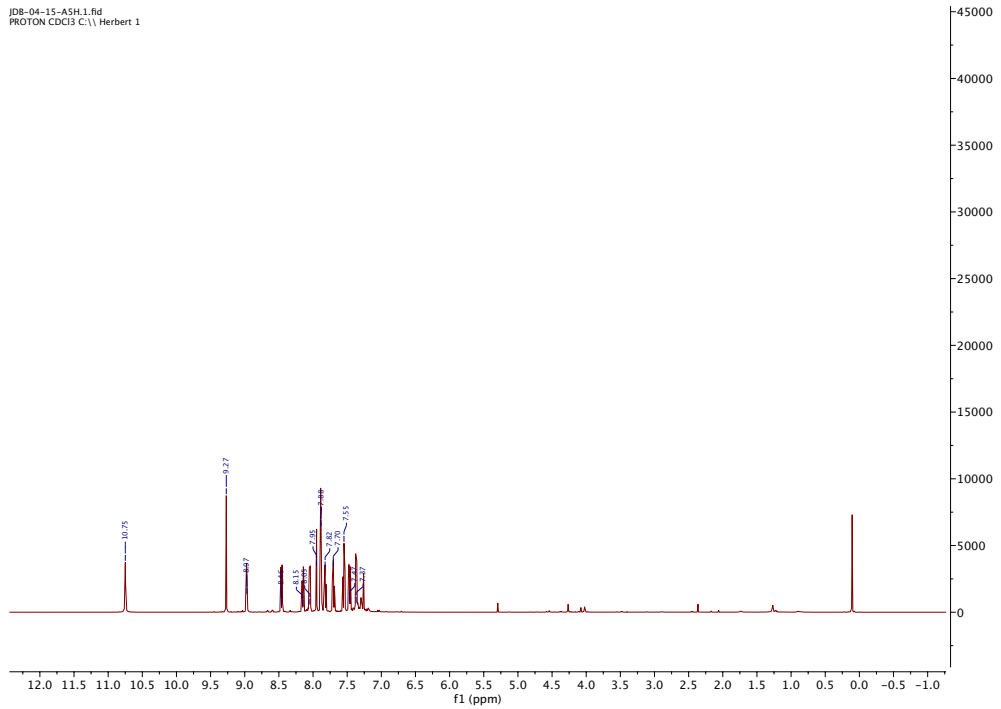

Figure S138. ^{1}H NMR (500 MHz, $CDCl_3$, 25°C) of $^{Cl\text{-}Phen}NN(H)N^{Quin}$ (**5c**).

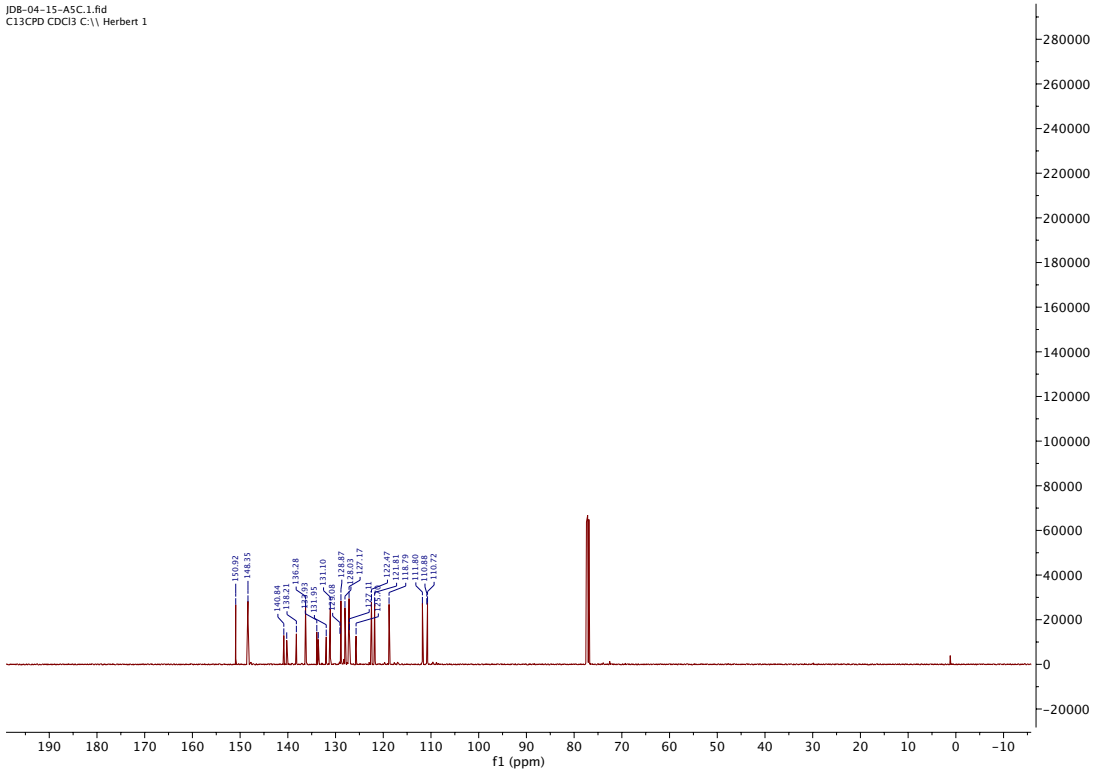

Figure S139. ^{13}C NMR (125 MHz, $CDCl_3$, 25°C) of $^{Cl\text{-}Phen}NN(H)N^{Quin}$ (**5c**).

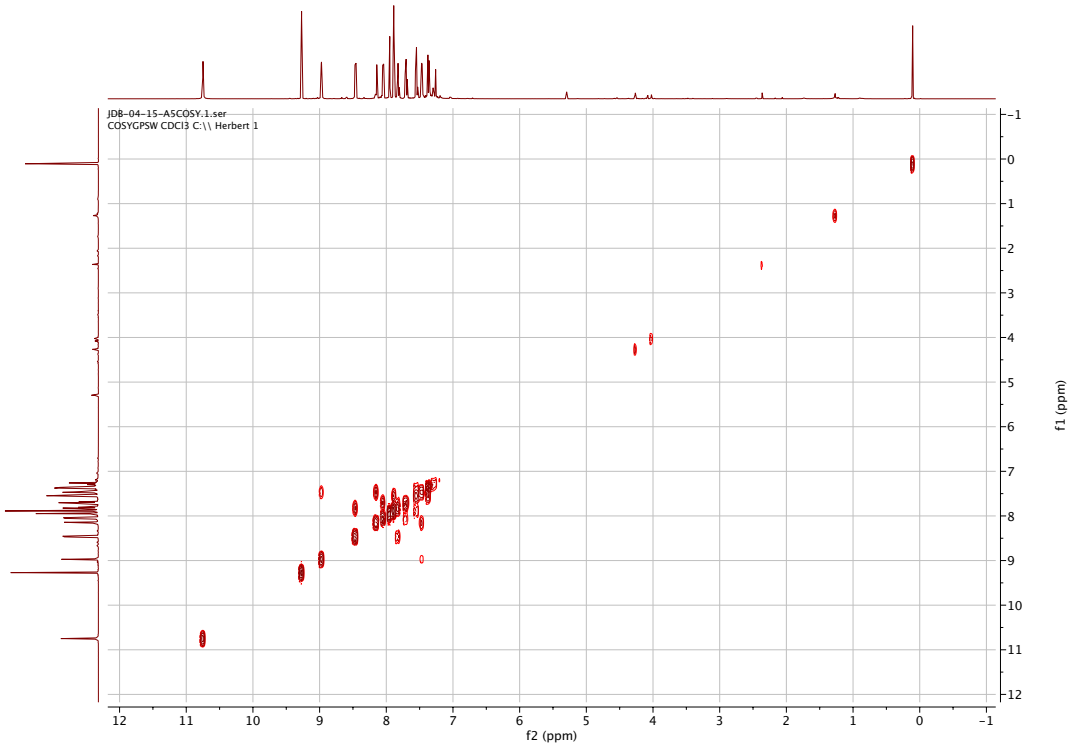

Figure S140. ^{1}H-^{1}H COSY NMR (500 MHz, $CDCl_3$, 25°C) of $^{Cl\text{-}Phen}NN(H)N^{Quin}$ (**5c**).

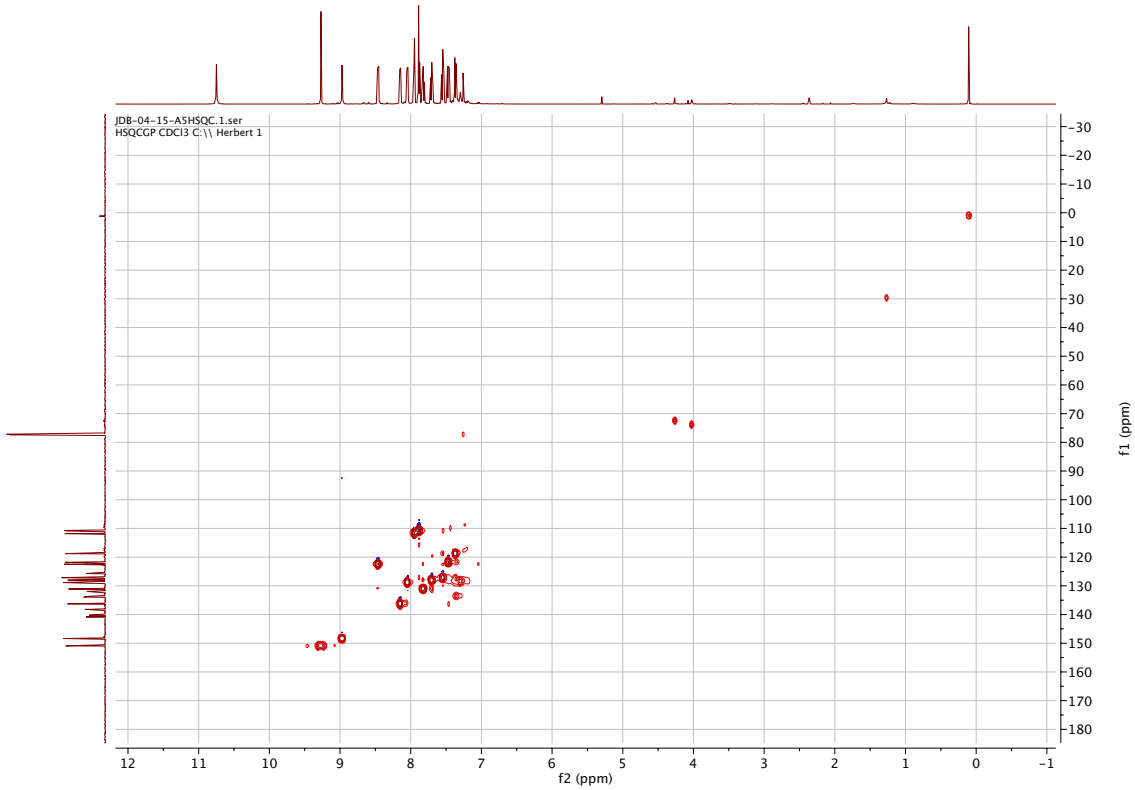

Figure S141. HSQC NMR (500/125 MHz, $CDCl_3$, 25°C) of $^{Cl\text{-}Phen}NN(H)N^{Quin}$ (**5c**).

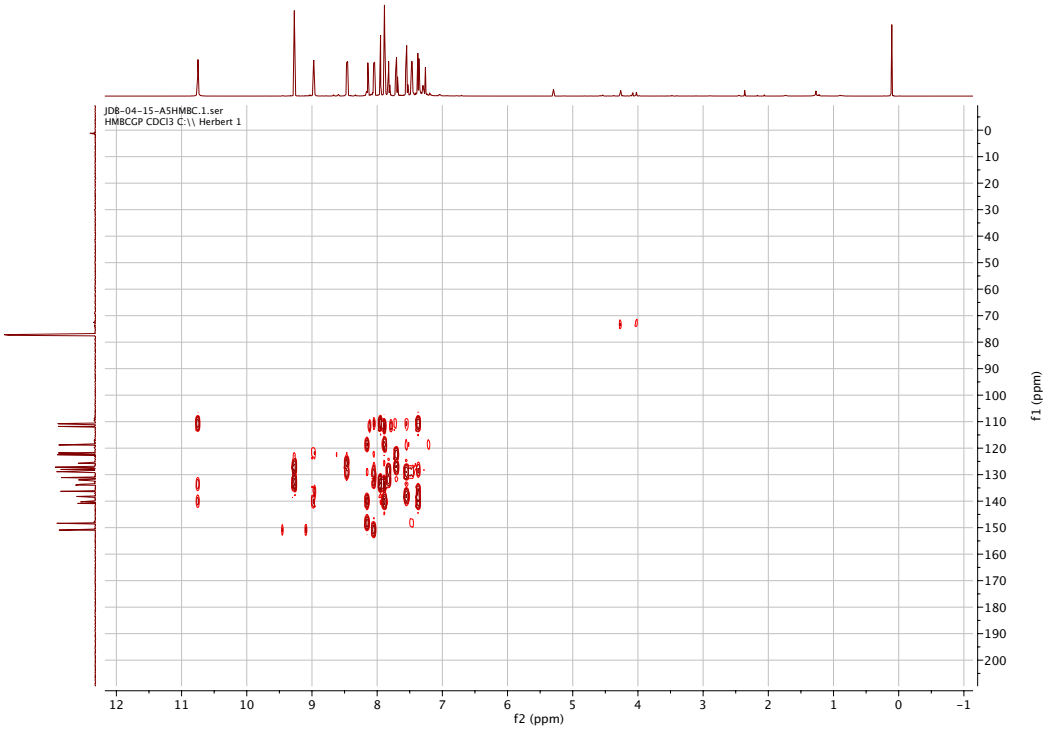

Figure S142. HMBC NMR (500/125 MHz, $CDCl_3$, 25°C) of $^{Cl\text{-}Phen}NN(H)N^{Quin}$ (**5c**).

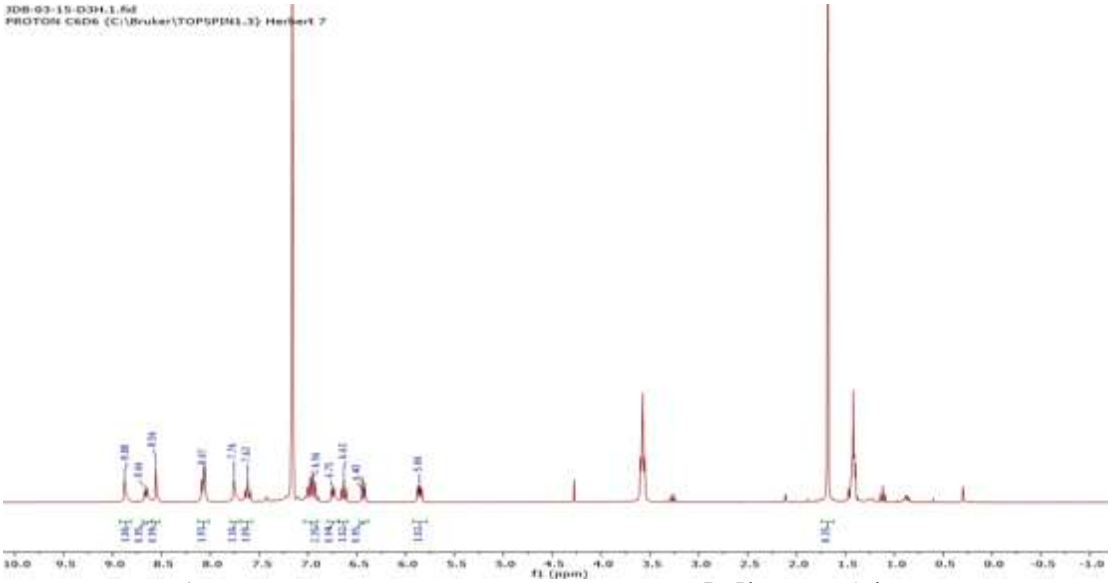

Figure S143. ^1H NMR (500 MHz, C_6D_6, 25°C) of $Fe(^{t\text{Bu-Phen}}NNN^{Quin})_2$ (**6a**).

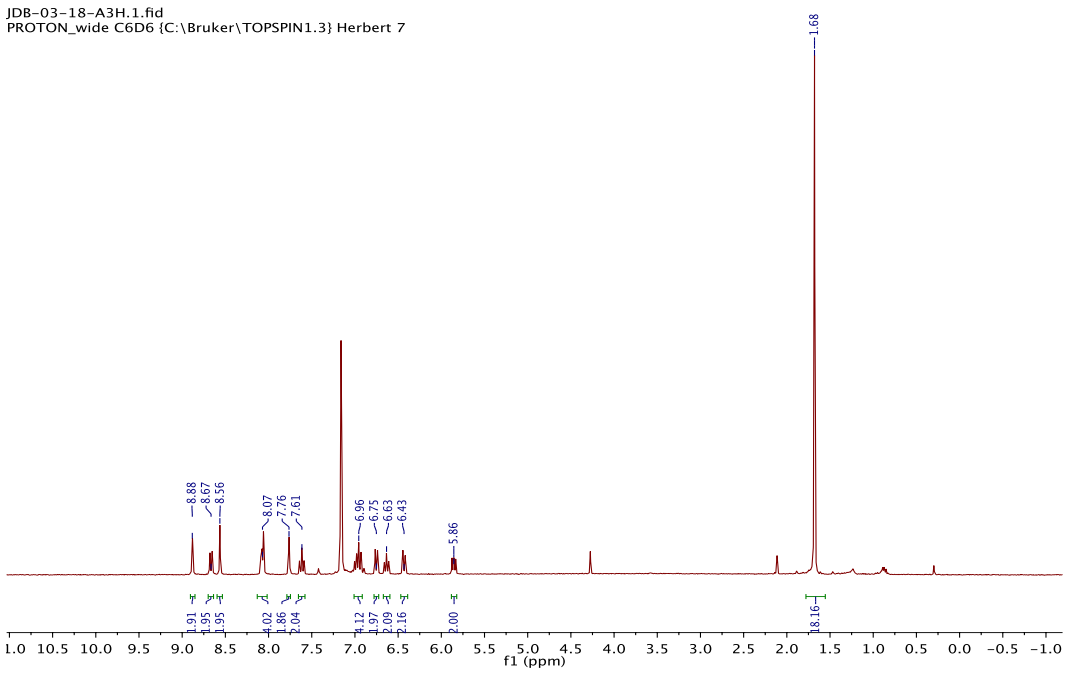

Figure S144. ^{1}H NMR (500 MHz, C_6D_6, 25°C) of **6a** by reduction of [**6a**]$^{+}$ with cobaltocene.

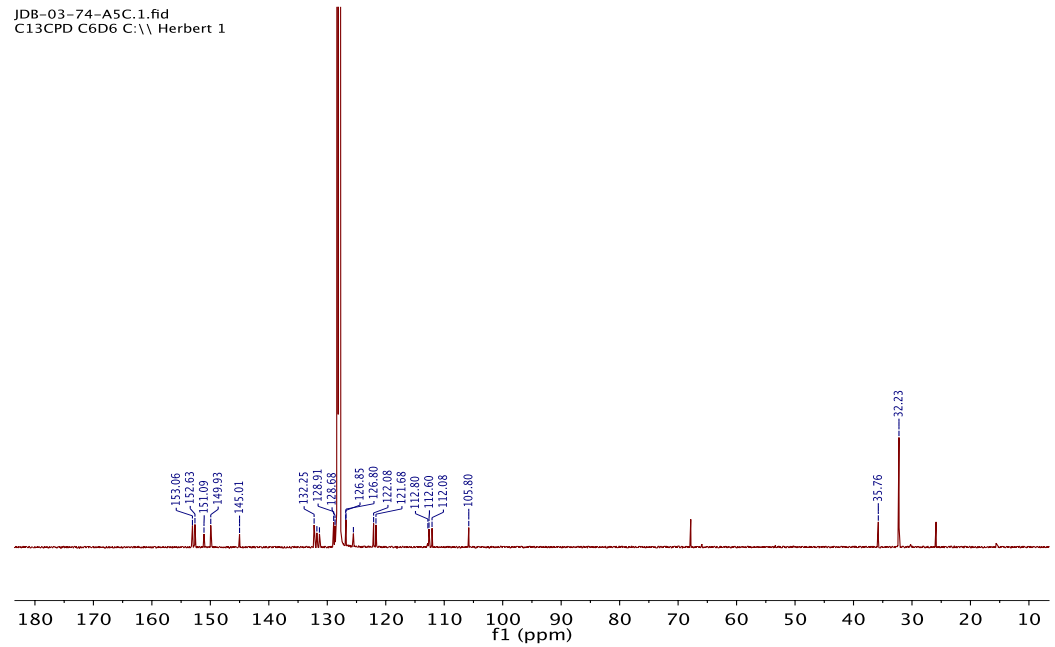

Figure S145. ^{13}C{^{1}H} NMR (125 MHz, C_6D_6, 25°C) of Fe($^{t\text{Bu-Phen}}$NNN$^{\text{Quin}}$)$_2$ (**6a**).

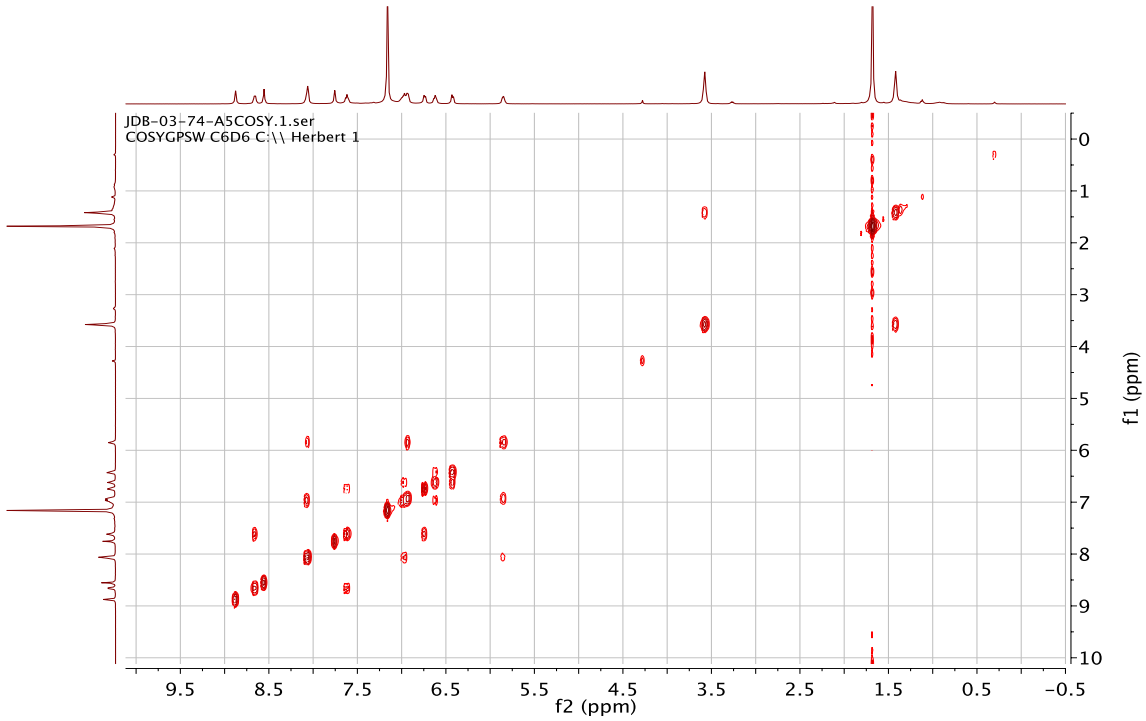

Figure S146. ^{1}H-^{1}H COSY NMR (500 MHz, C_6D_6, 25°C) of Fe($^{t\text{Bu-Phen}}$NNN$^{\text{Quin}}$)$_2$ (**6a**).

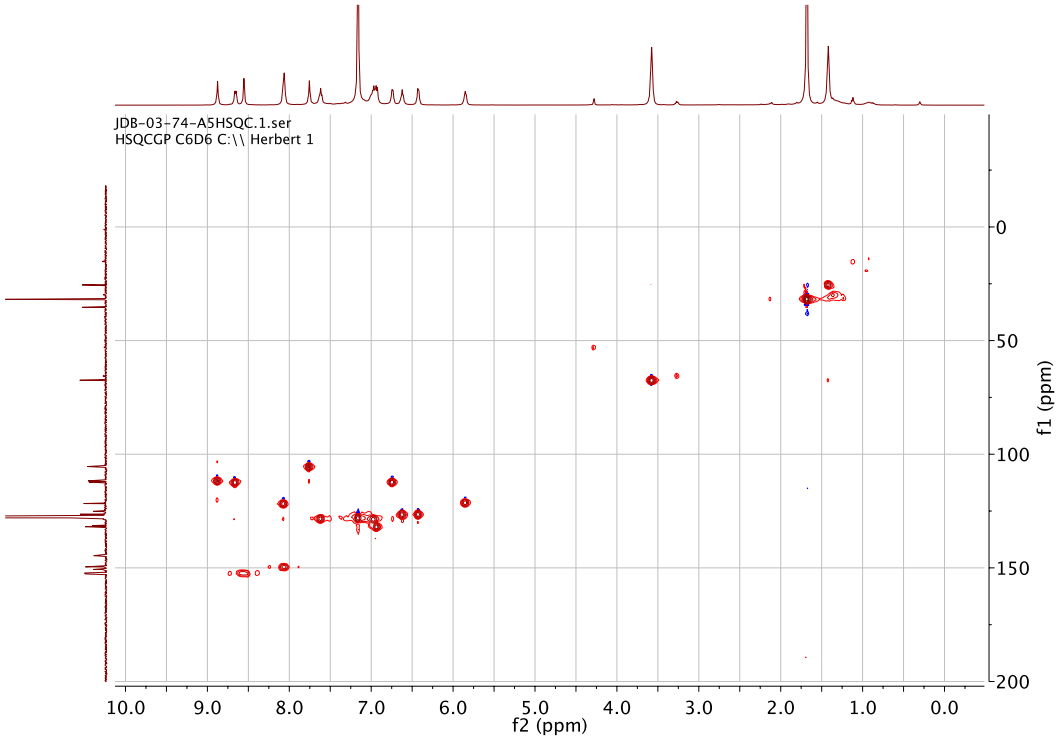

Figure S147. HSQC NMR (500/125 MHz, C_6D_6, 25°C) of Fe($^{\text{tBu-Phen}}$NNN$^{\text{Quin}}$)$_2$ (**6a**).

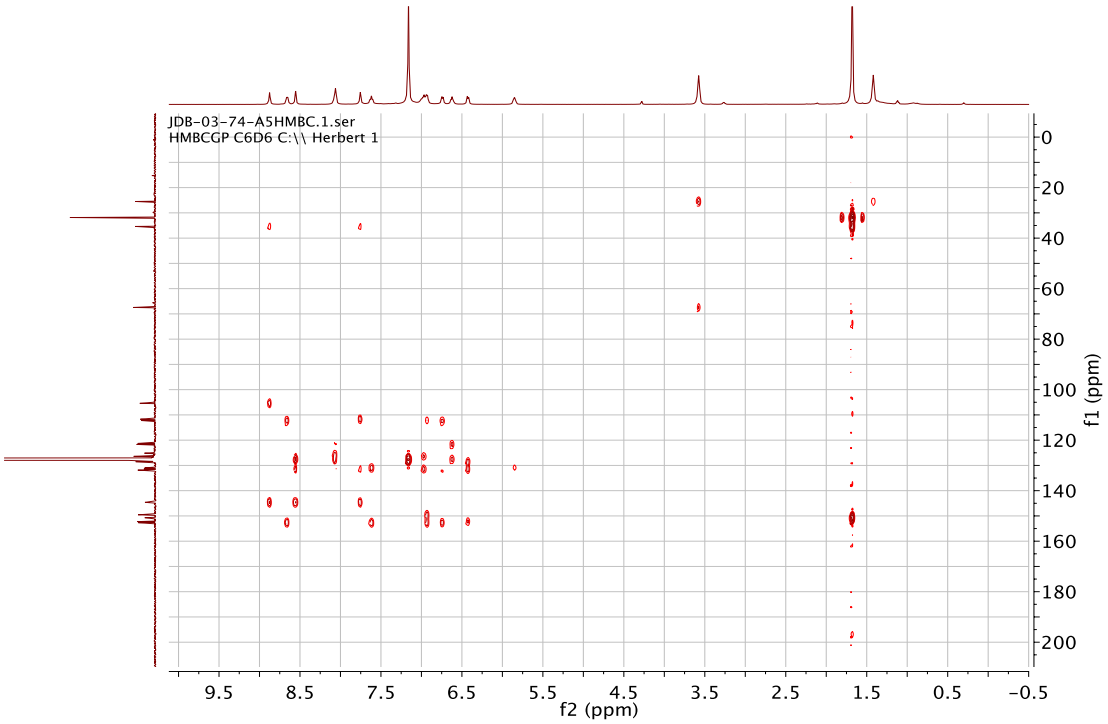

Figure S148. HMBC NMR (500/125 MHz, C_6D_6, 25°C) of Fe($^{t\text{Bu-Phen}}$NNN$^{\text{Quin}}$)$_2$ (6a).

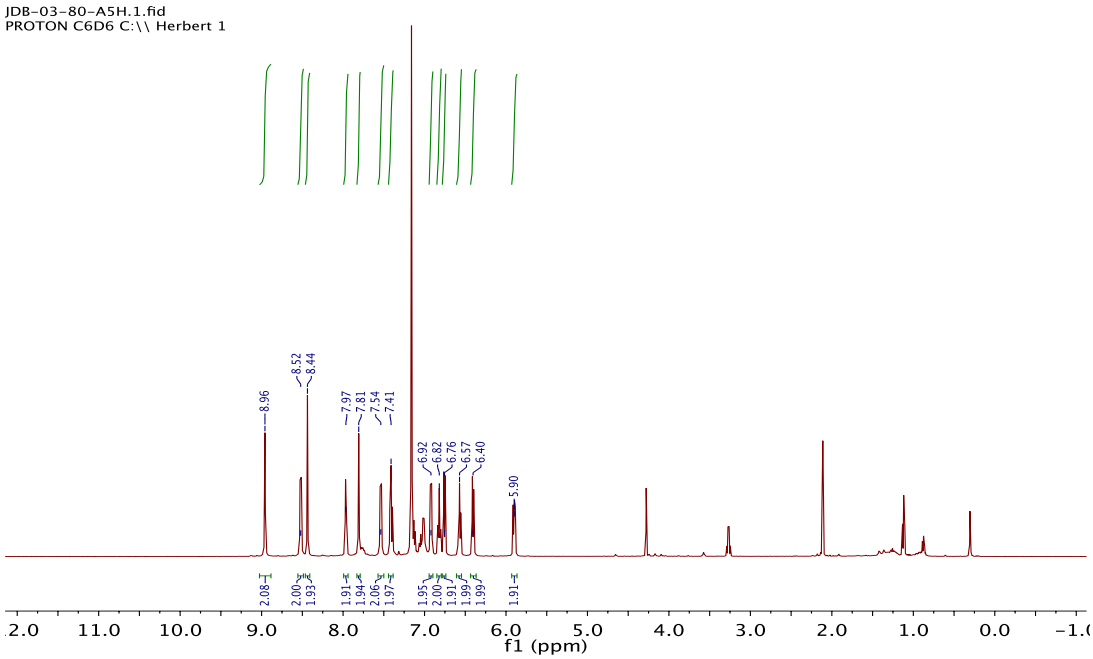

Figure S149. ^{1}H NMR (500 MHz, C_6D_6, 25°C) of Fe($^{\text{CF3-Phen}}$NNN$^{\text{Quin}}$)$_2$ (**6b**).

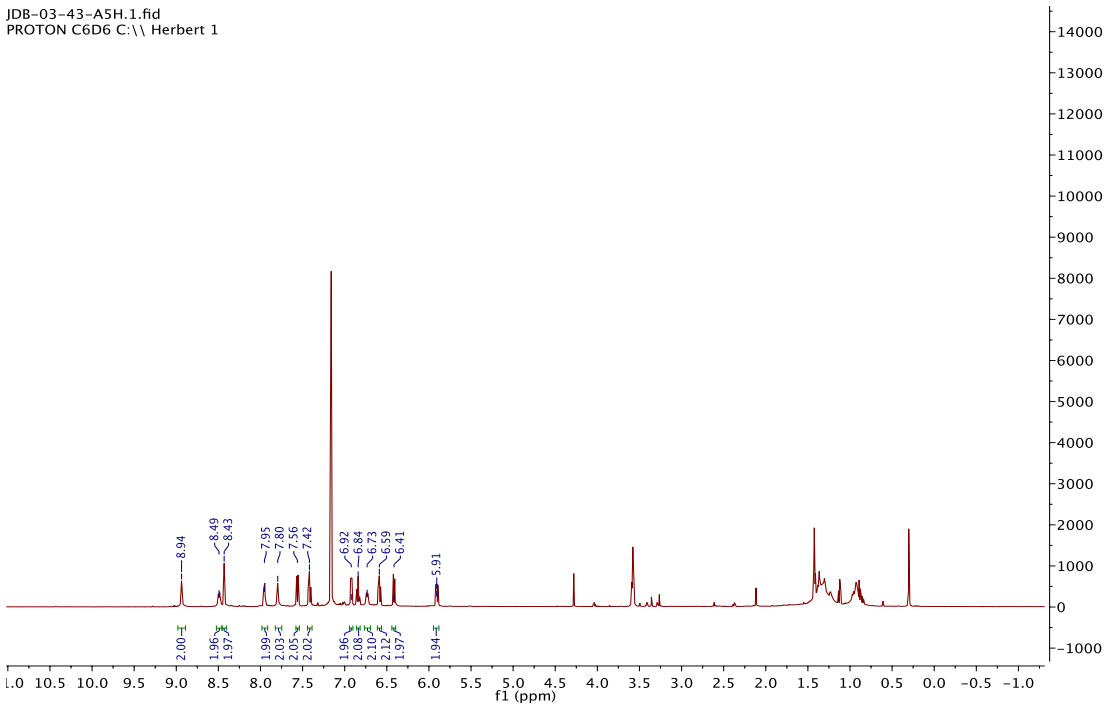

Figure S150. ^{1}H NMR (500 MHz, C_6D_6, 25°C) of **6b** by reduction of [**6b**]$^{+}$ with cobaltocene.

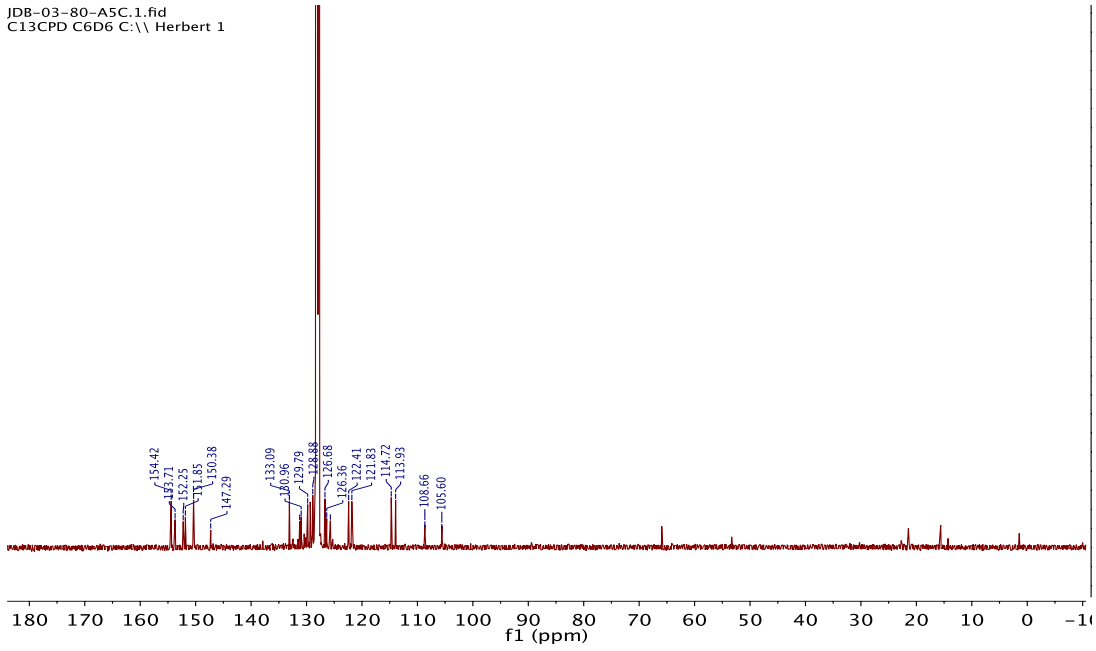

Figure S151. $^{13}C\{^{1}H\}$ NMR (125 MHz, C_6D_6, 25°C) of Fe($^{CF3\text{-}Phen}NNN^{Quin}$)$_2$ (**6b**).

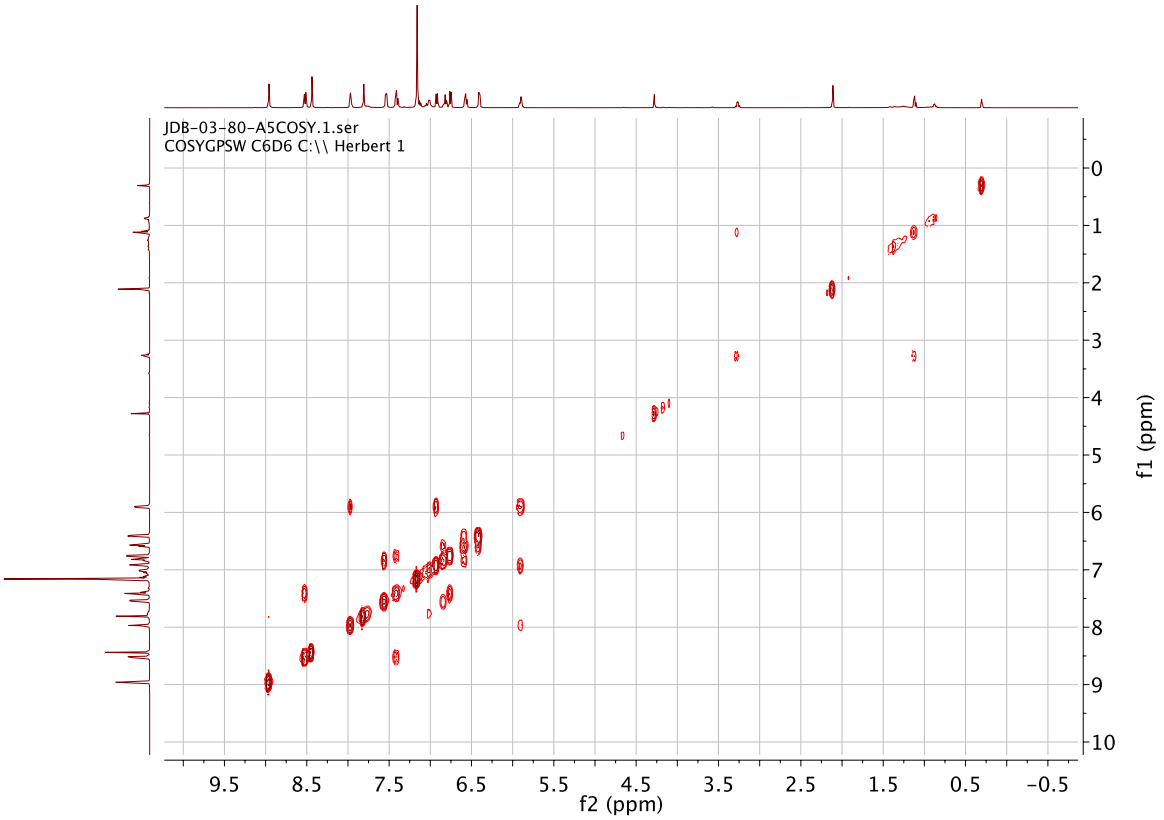

Figure S152. ^{1}H-^{1}H COSY NMR (500 MHz, C_6D_6, 25°C) of Fe($^{CF3\text{-}Phen}NNN^{Quin}$)$_2$ (**6b**).

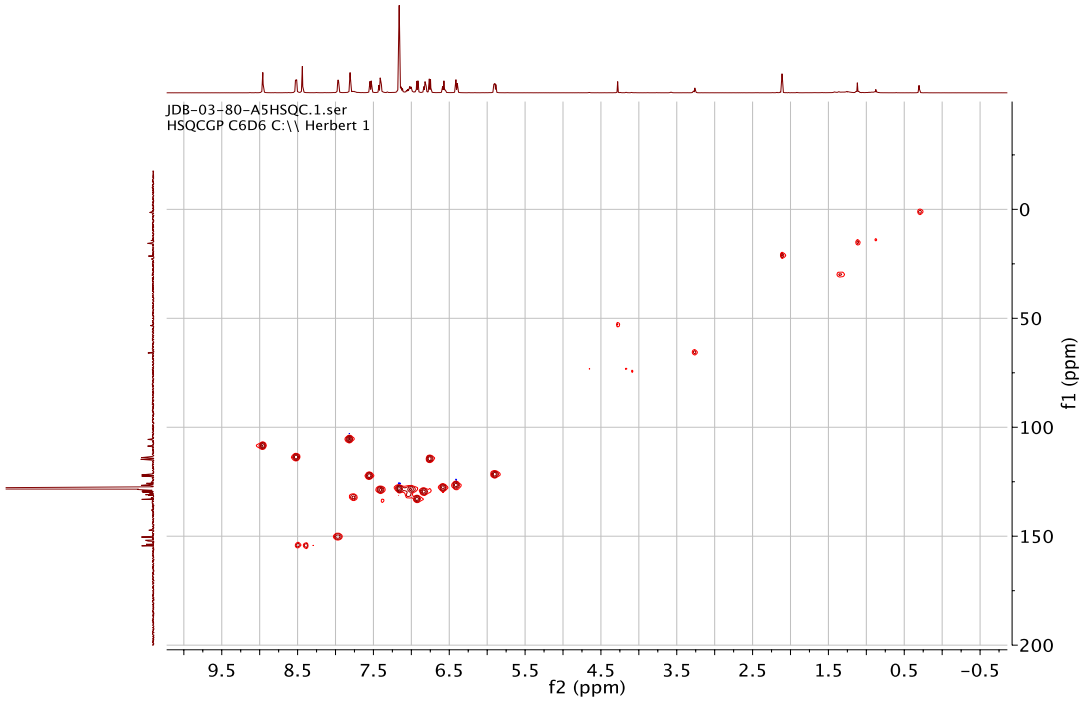

Figure S153. HSQC NMR (500/125 MHz, C_6D_6, 25°C) of Fe($^{CF3\text{-}Phen}NNN^{Quin}$)$_2$ (**6b**).

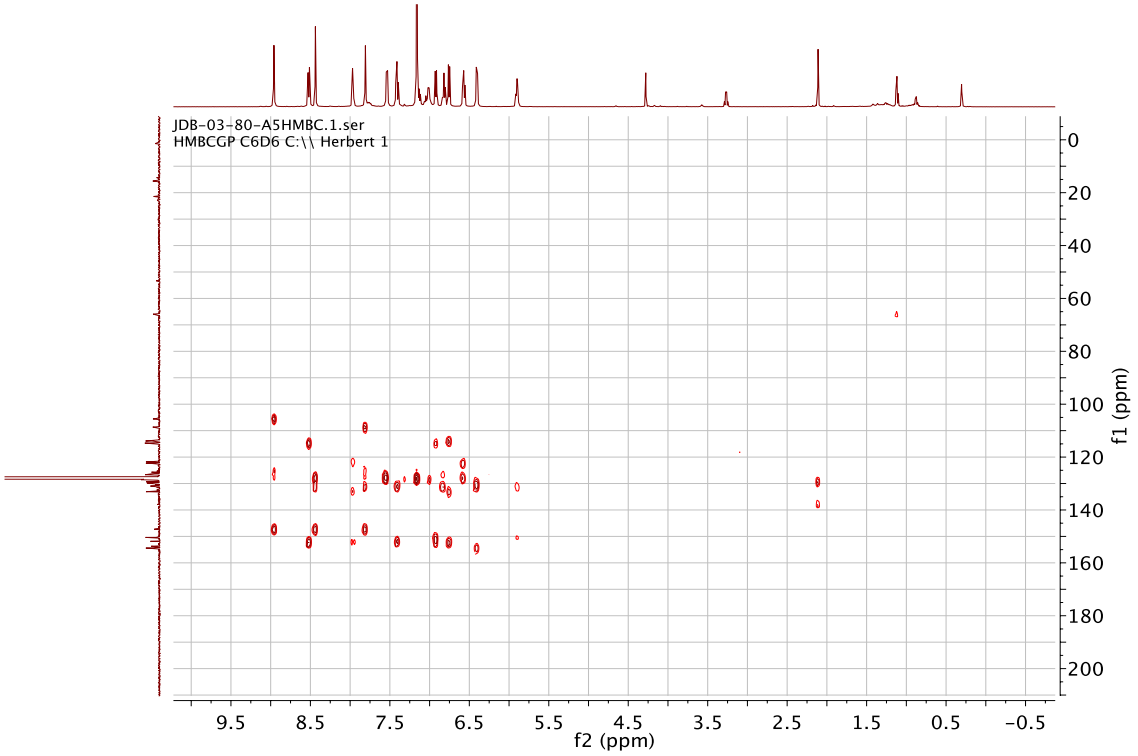

Figure S154. HMBC NMR (500/125 MHz, C_6D_6, 25°C) of Fe($^{CF3\text{-}Phen}NNN^{Quin}$)$_2$ (**6b**).

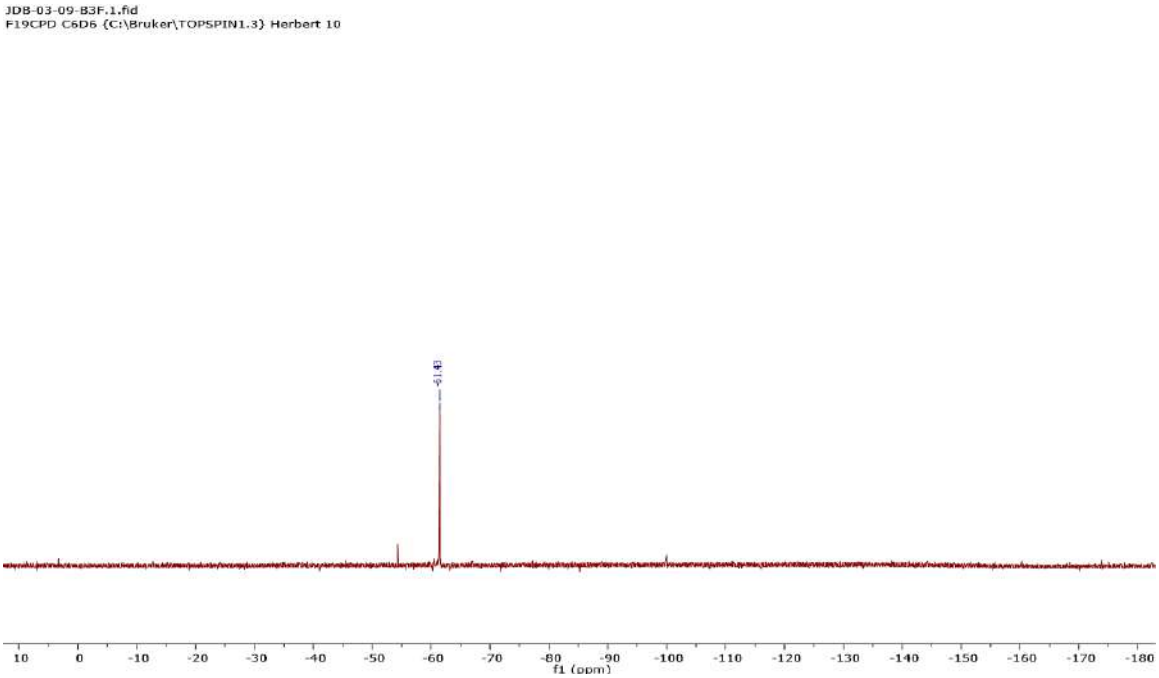

Figure S155. ^{19}F NMR (282 MHz, C_6D_6, 25°C) of Fe($^{CF3\text{-}Phen}NNN^{Quin}$)$_2$ (**6b**).

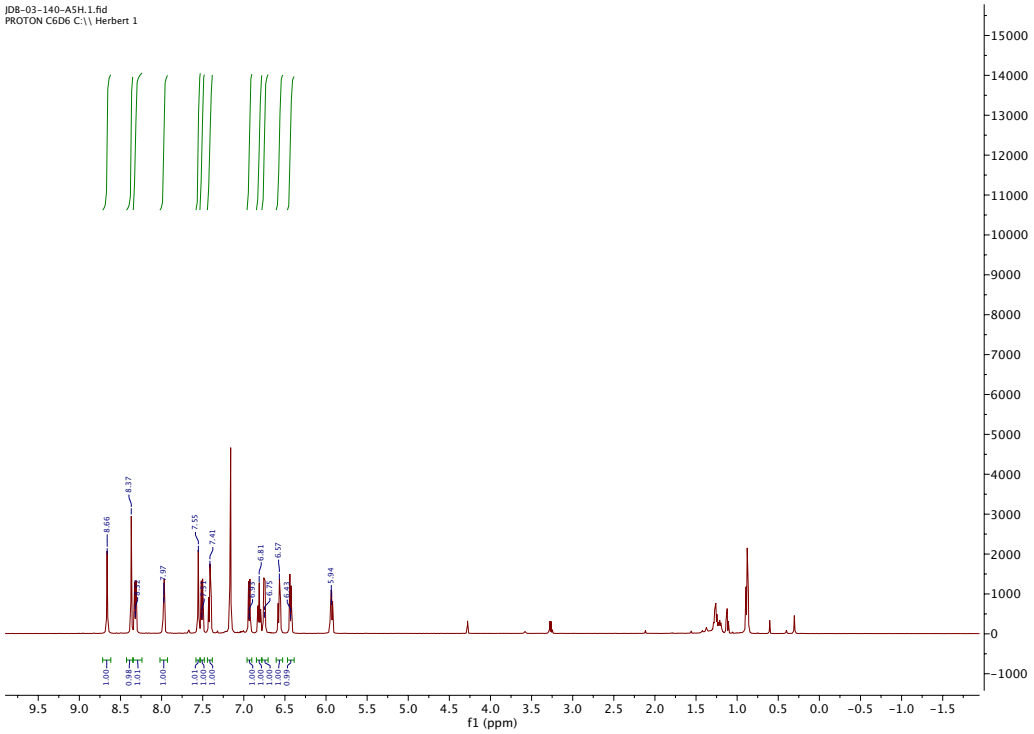

Figure S156. ^{1}H NMR (500 MHz, C_6D_6, 25°C) of Fe($^{Cl\text{-}Phen}NNN^{Quin}$)$_2$ (**6c**).

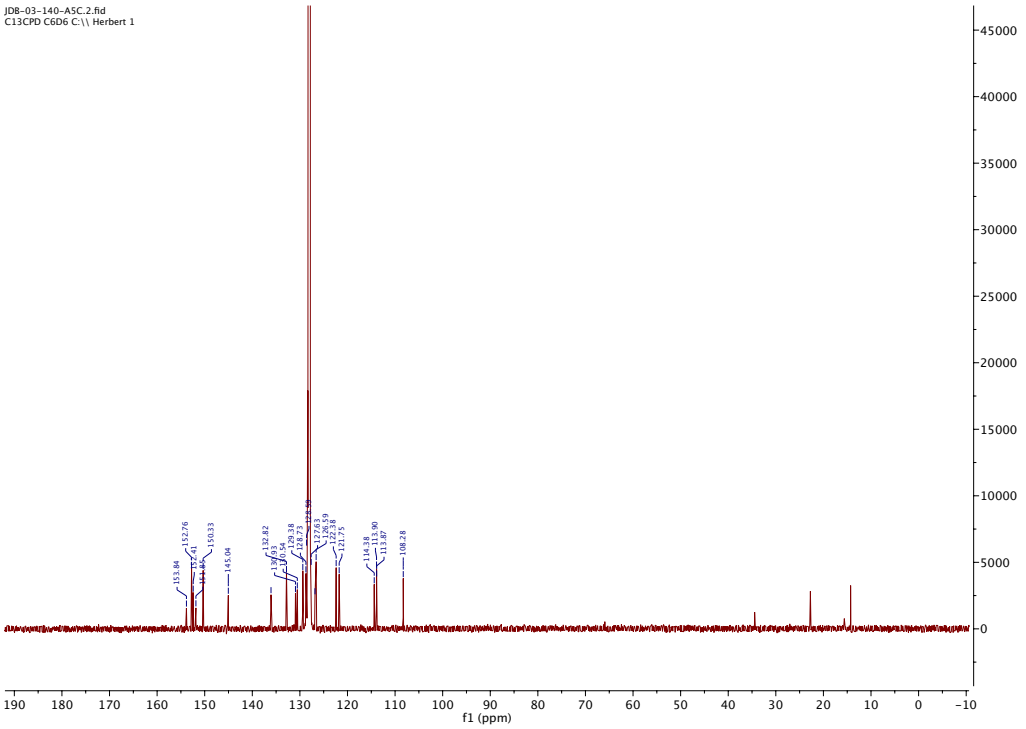

Figure S157. ^{13}C{^{1}H} NMR (125 MHz, C_6D_6, 25°C) of Fe($^{Cl\text{-}Phen}NNN^{Quin}$)$_2$ (**6c**).

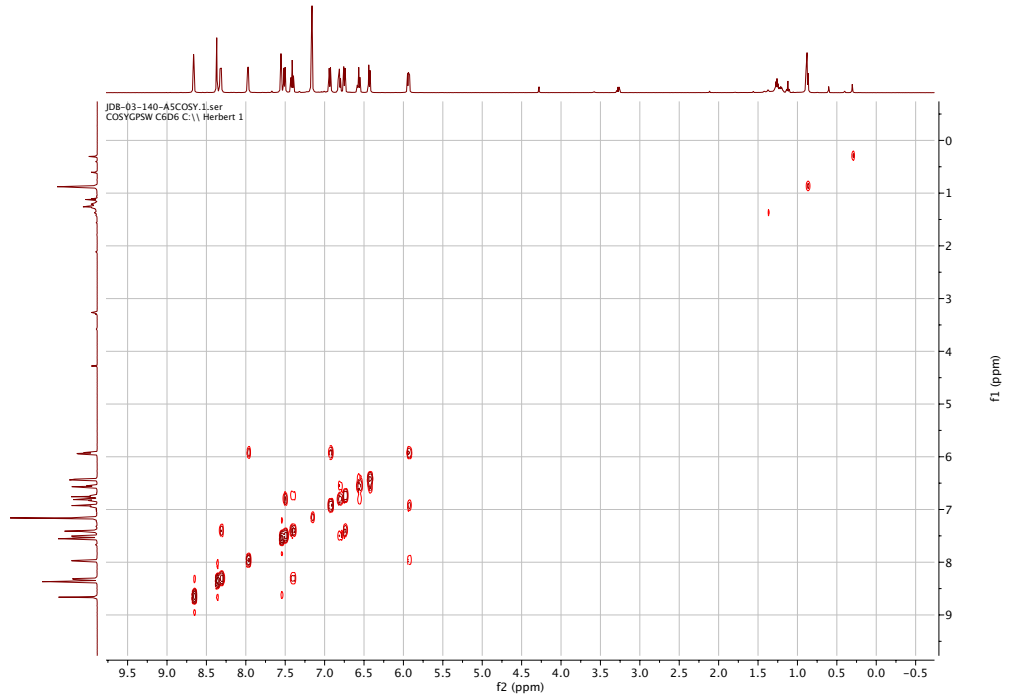

Figure S158. ^{1}H-^{1}H COSY NMR (500 MHz, C_6D_6, 25°C) of Fe($^{Cl\text{-}Phen}NNN^{Quin}$)$_2$ (**6c**).

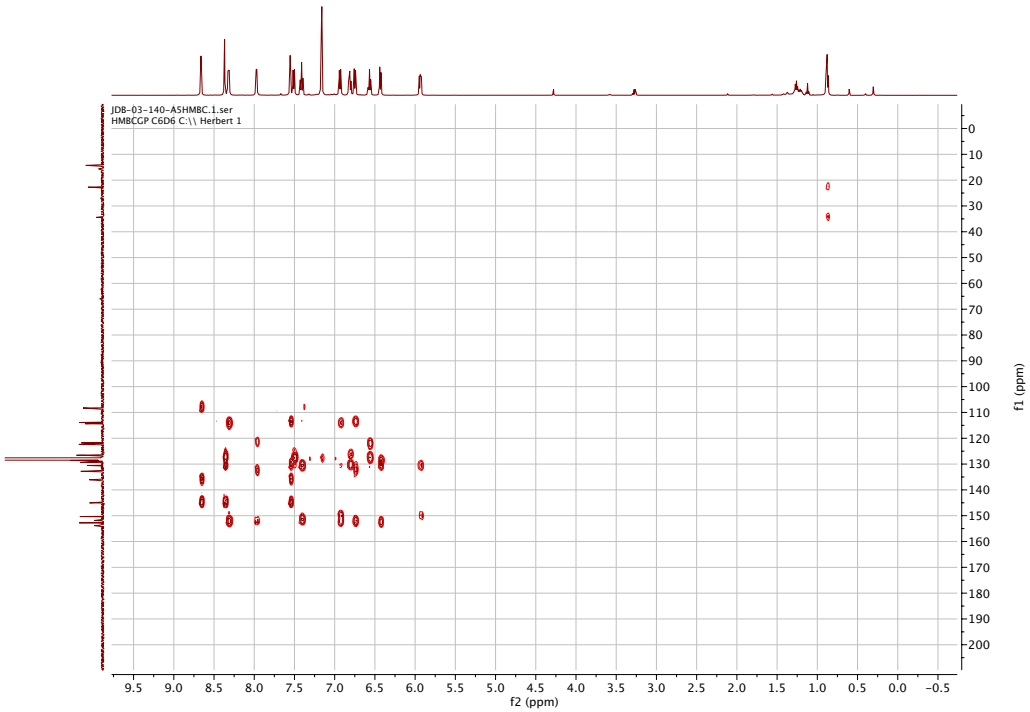

Figure S159. HMBC NMR (500/125 MHz, C_6D_6, 25°C) of Fe($^{Cl\text{-}Phen}NNN^{Quin}$)$_2$ (**6c**).

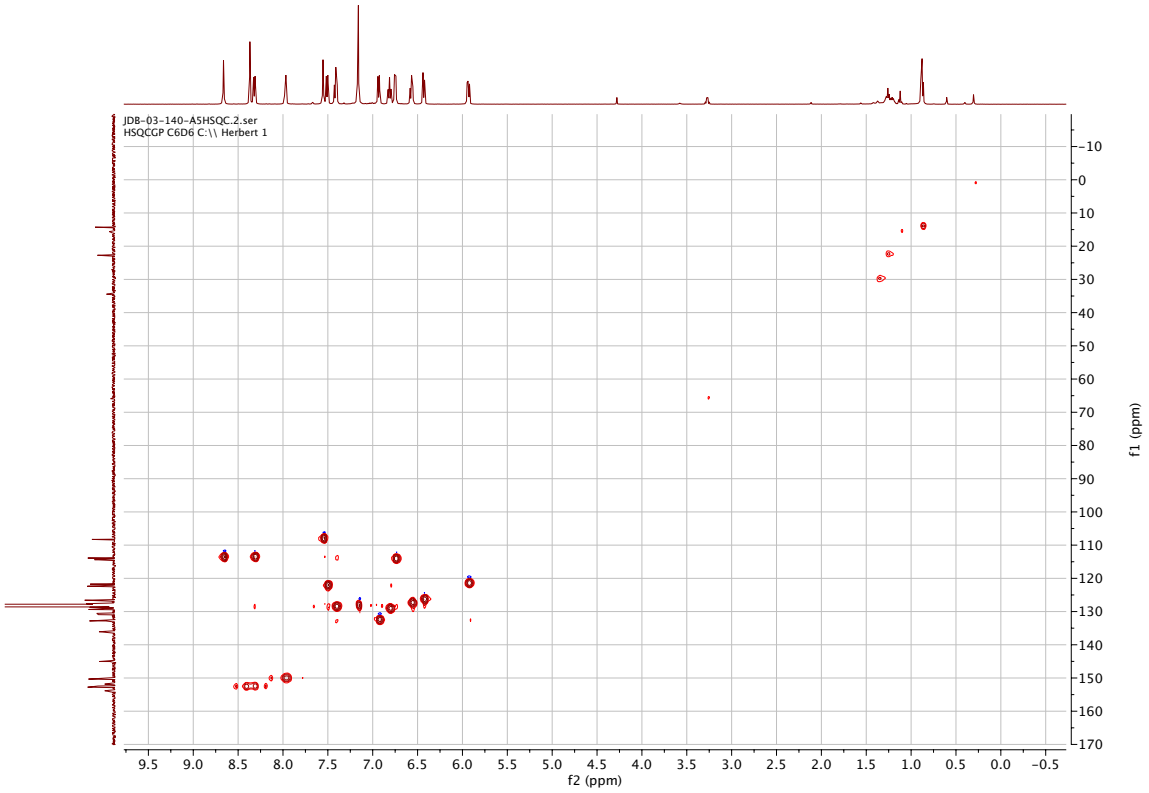

Figure S160. HSQC NMR (500/125 MHz, C_6D_6, 25°C) of Fe($^{Cl\text{-}Phen}NNN^{Quin}$)$_2$ (**6c**).

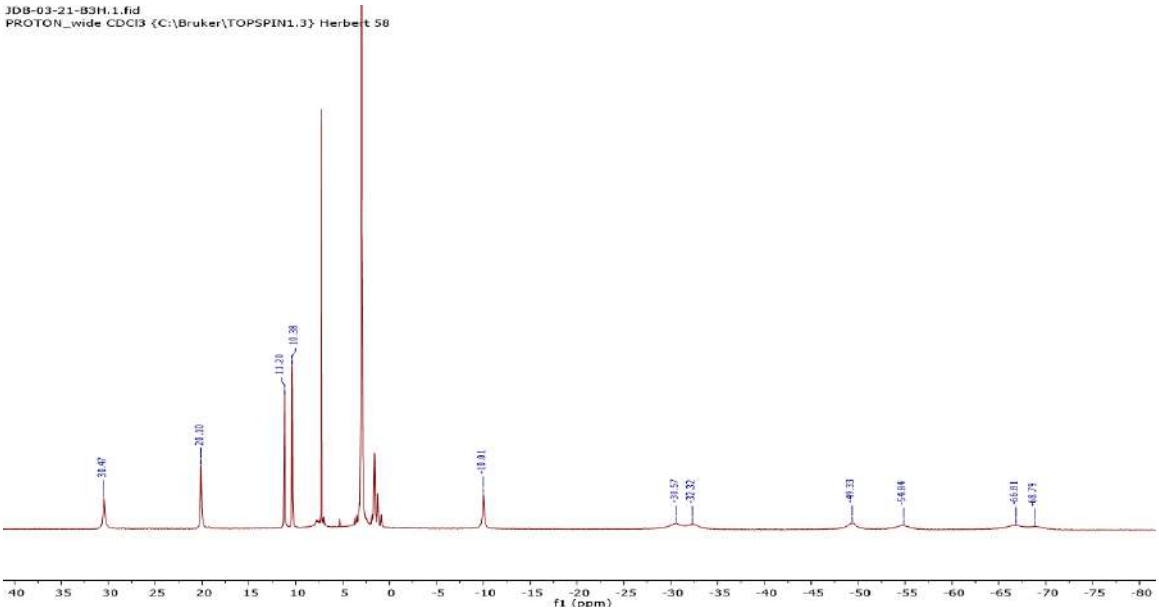

Figure S161. ^{1}H NMR (300 MHz, $CDCl_3$, 25°C) of [Fe($^{t\text{Bu-}Phen}NNN^{Quin}$)$_2$]$PF_6$ ([**6a**]PF_6).

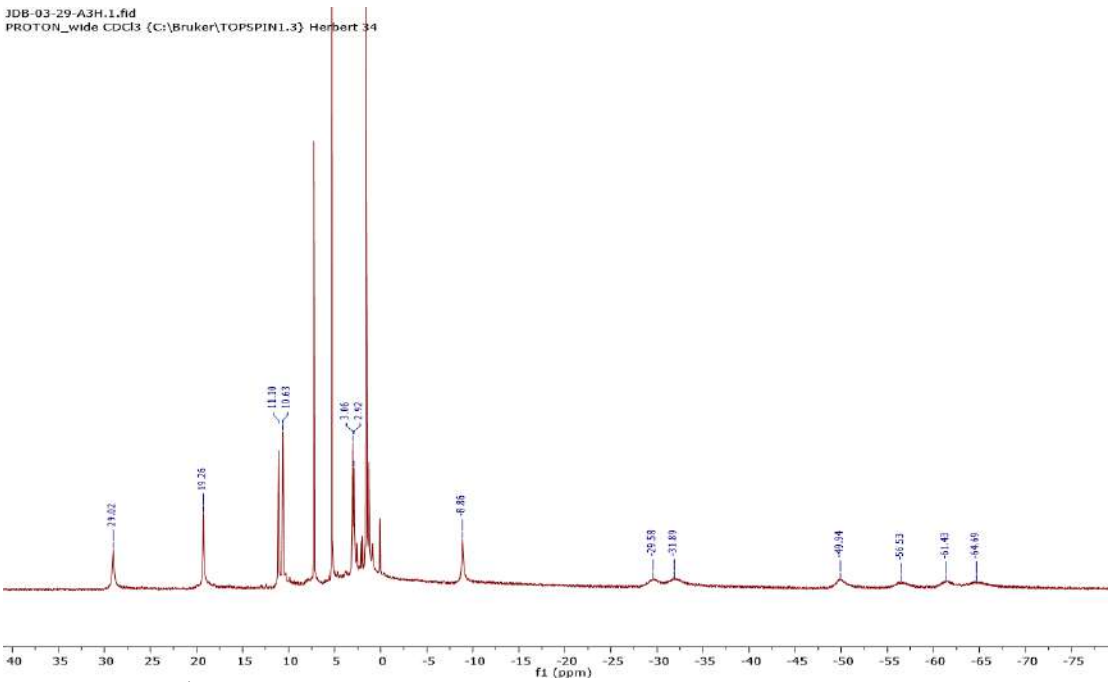

Figure S162. ^{1}H NMR (300 MHz, $CDCl_3$, 25°C) of [Fe(CF3-PhenNNNQuin)2]PF6 ([**6b**]PF6).

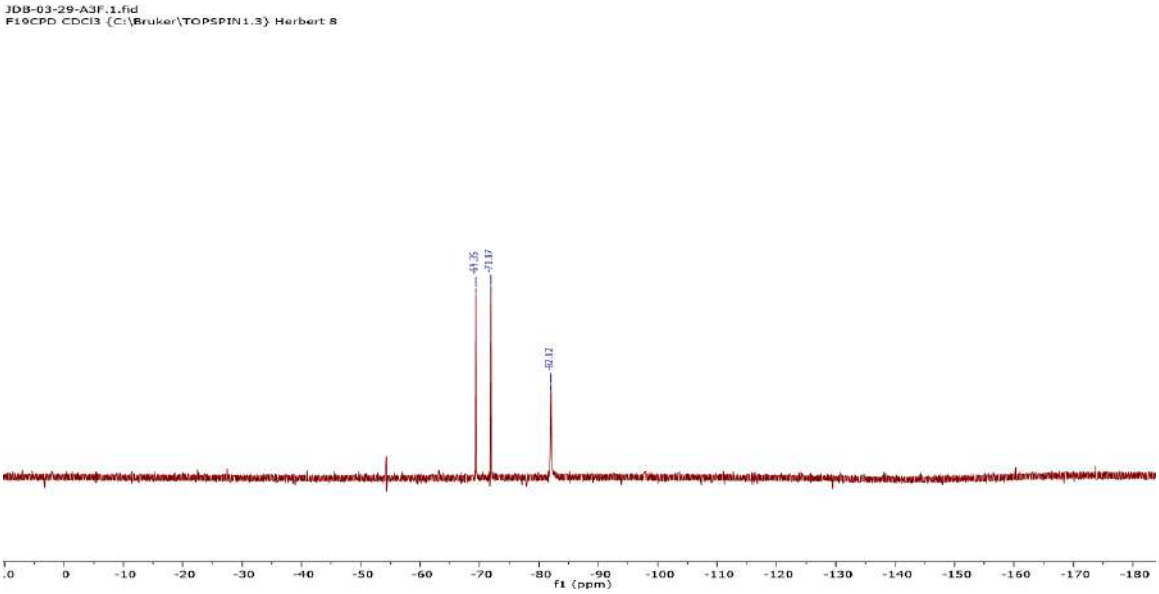

Figure S163. ^{19}F NMR (282 MHz, $CDCl_3$, 25°C) of [Fe(CF3-PhenNNNQuin)2]PF6 ([**6b**]PF6).

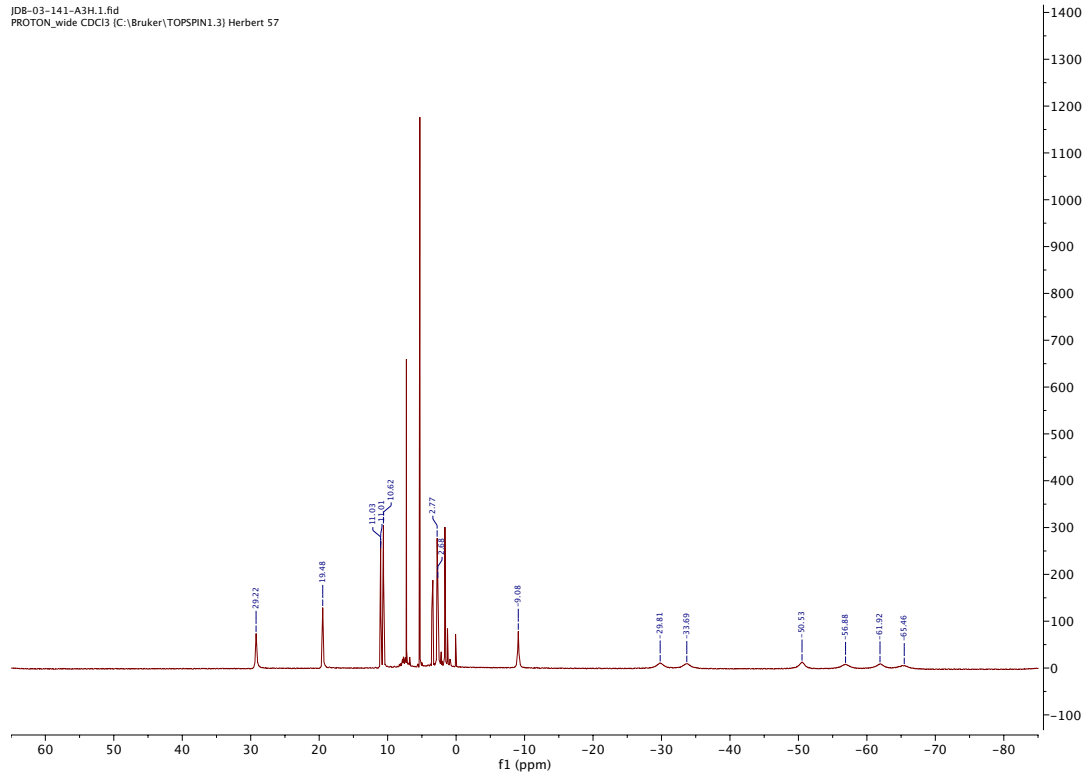

Figure S164. ^{1}H NMR (300 MHz, $CDCl_3$, 25°C) of [Fe(Cl-PhenNNNQuin)2]PF6 ([**6c**]PF6).

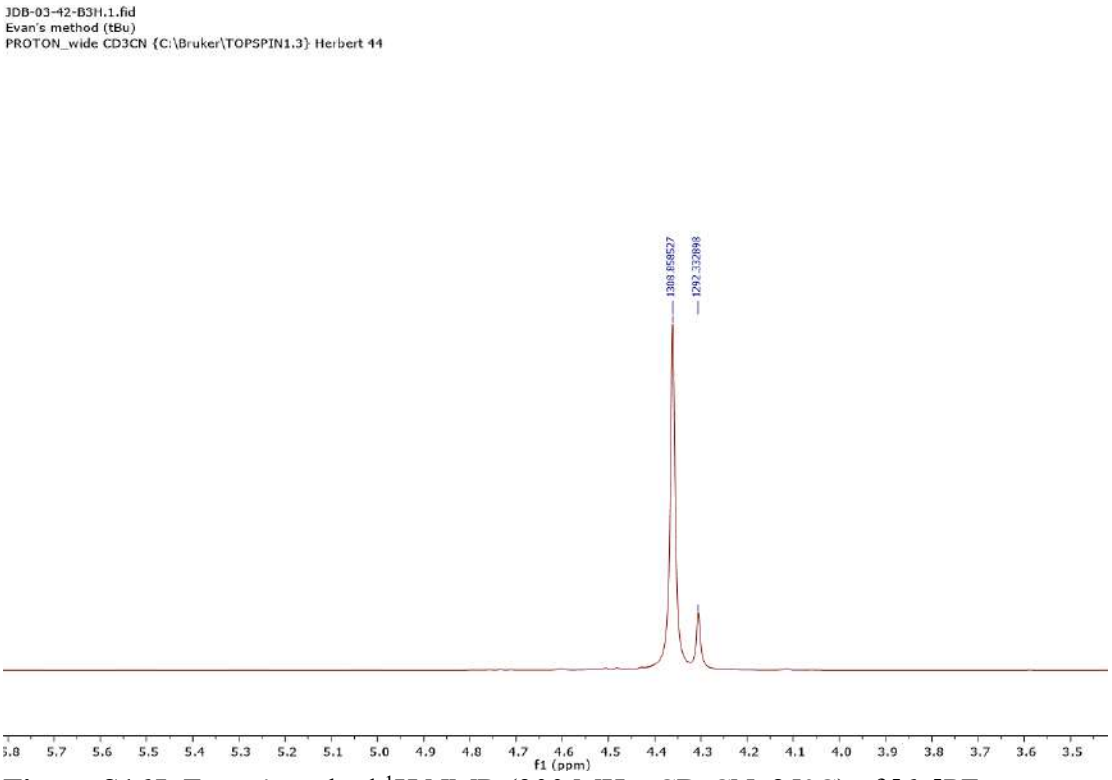

Figure S165. Evans' method ^{1}H NMR (300 MHz, CD_3CN, 25°C) of [**6a**]PF_6.

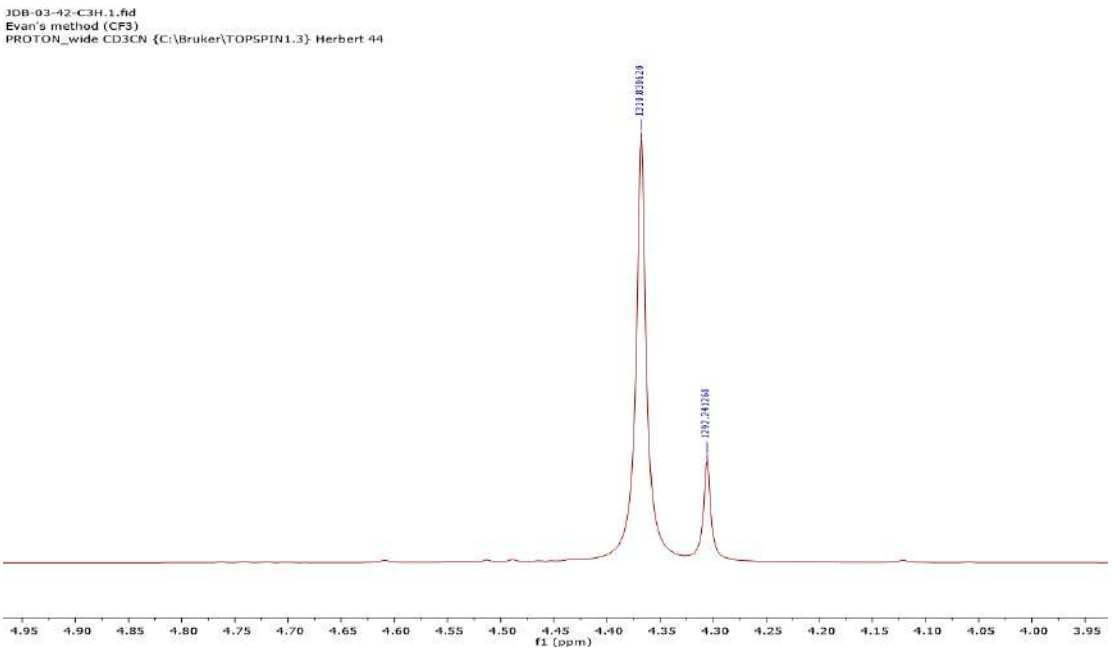

Figure S166. Evans' method ^{1}H NMR (300 MHz, CD_3CN, 25°C) of [**6b**]PF6.

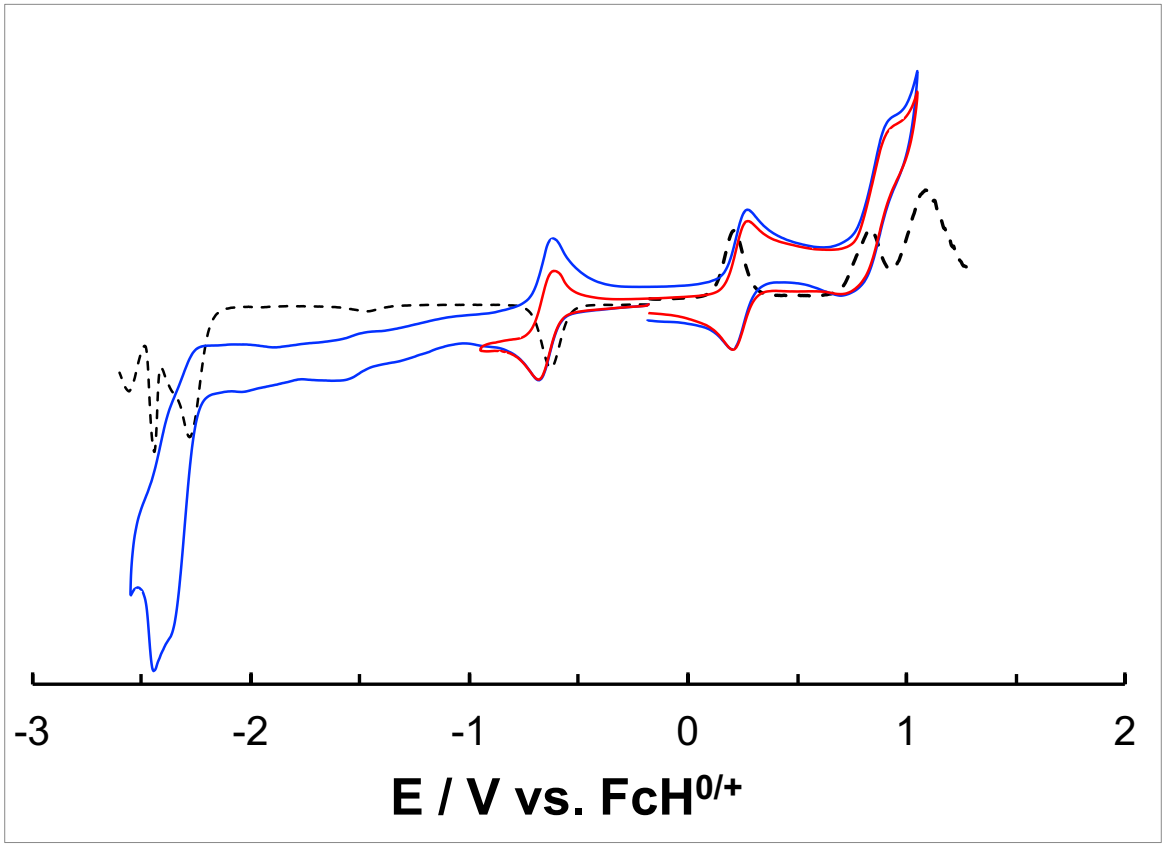

Figure S167. Cyclic voltammograms (—) and differential pulse voltammograms (---) of [**6c**]PF_6 in CH_3CN with 0.10 M [nBu_4N]PF_6 as the supporting electrolyte.

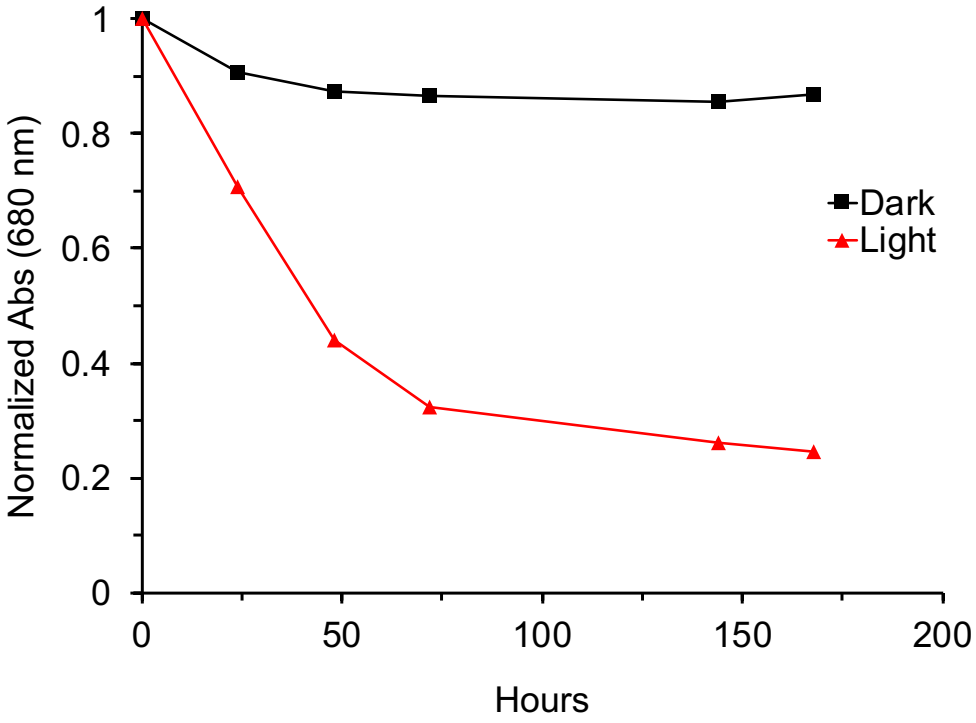

Figure S168. Plot of peak absorbance at 680 nm over time for **6c** in wet toluene in the dark and light.

Chapter 5

Table S22. Selected bond distances (Å) and angles (°) for [**6a**]PF_6, [**7a**]PF_6, **8a** and [**10a**]PF_6

	[**6a**]PF_6	[**7a**]PF_6	**8a**	[**10a**]PF_6
M – N$_{phen}$				
M1 – N1	1.946(2)	1.908(3)	2.0707(13)	2.074(3)
M1 – N4	1.966(2)	1.908(3)	2.0783(13)	2.074(3)
M – N$_{amido}$				
M1 – N2	1.885(2)	1.897(2)	2.0167(12)	1.958(3)
M1 – N5	1.905(2)	1.897(2)	2.0160(13)	1.958(3)
M – N$_{quin}$				
M1 – N3	1.945(2)	1.915(3)	2.0761(13)	2.074(3)
M1 – N6	1.964(2)	1.915(3)	2.0720(13)	2.074(3)
N$_{phen}$ – C27				
N1 – C1	1.306(4)	1.298(4)	1.310(2)	1.301(4)
N4 – C27	1.306(3)	1.298(4)	1.3050(19)	1.301(4)
Intraligand angles				
N1 – M1 – N3	167.08(10)	169.50(11)	159.76(5)	161.66(10)
N1 – M1 – N2	83.80(10)	85.07(11)	80.09(5)	80.75(11)
N2 – M1 – N3	83.41(10)	84.43(11)	79.73(5)	80.98(10)
N4 – M1 – N6	164.87(10)	169.50(11)	160.25(5)	161.66(10)
N4 – M1 – N5	82.58(10)	85.07(11)	79.97(5)	80.75(11)
N5 – M1 – N6	82.33(10)	84.43(11)	80.29(5)	80.98(10)
Interligand angles				
N2 – M1 – N5	178.16(11)	178.10(17)	178.23(5)	178.89(15)
N1 – M1 – N6	93.24(10)	91.08(11)	91.84(5)	92.47(14)
N2 – M1 – N4	98.72(10)	96.28(11)	98.37(5)	100.05(11)
N2 – M1 – N6	96.39(10)	94.22(11)	101.37(5)	98.24(10)
N1 – M1 – N5	94.93(10)	96.28(11)	100.50(5)	100.05(11)
N3 – M1 – N5	97.81(10)	94.22(11)	99.72(5)	98.24(10)
N3 – M1 – N4	94.57(10)	91.08(11)	93.45(5)	92.47(14)

Table S23. Redox potentials and electronic absorption spectral data for [(**6-10**)**a**]$^{n+}$

Compound	$E_{1/2}$/V	λ/nm (ε/M^{-1}cm^{-1})
6a /**[6a]**PF_6	-2.59 -2.43 -0.77 0.05 0.70	**6a**: 319 (26 310), 454 (26 030), 596 (17 990), 724 (8 510) **[6a]**PF_6: 311 (34 950), 414, (22 810), 512 (12 430), 1024 (4 560)
[7a]PF_6	-2.23 -1.30 0.31 0.50	**[7a]**PF_6: 308 (41 880), 390 (9 670), 510 (23 310)
8a	-2.55 -2.42 -0.23 -0.04 0.48	**8a**: 289 (51 330), 318 (32 190), 405 (10 280), 519 (28 370)
9a	-2.49 -2.38 -0.20 -0.07 0.47	**[9a]**: 314 (33 000), 393 (19 880), 503 (24 040)
[10a]PF_6	-2.45 -2.13 -1.85 0.42 0.59	**[10a]**PF_6: 280 (42 710), 324 (20 510), 472 (17 220)

Computational Methods:

All density functional theory (DFT) calculations was carried out using Gaussian 16, rev. B01. All complexes were optimized using the O3LYP[29] functional in combination with the 6-31+G(d,p) basis set on all atoms.[13–16,30] We also include implicit solvation using the solvation model based on density (SMD; solvent=acetonitrile)[6] as implemented in Gaussian. We have previously shown that SMD-O3LYP/6-31+G(d,p) provides a better agreement with X-ray structures for the neutral **[6a]** and a similar neutral iron complex bearing CF_3-substituents at the C_2-position of the phenanthridine fragments.[31] Unless otherwise mentioned, the restricted and unrestricted Kohn-Sham (KS) formalisms were used for closed shell singlets and open-shell species (i.e. triplets, open-shell singlets, and doublets), respectively. Time-dependent DFT (TD-DFT) was carried out on the optimized geometries with different functionals to match the experimental UV-Vis-NIR spectra closely. The second oxidation of the complex could result in the formation of a complex with two possible multiplicities, that is a triplet or an open-shell singlet. We therefore carried out broken-symmetry DFT calculations on **[6a]**$^{2+}$ in the gas phase. A geometry optimization of the complex in its triplet electronic configuration (HS) was first carried

out with O3LYP/6-31+G(d,p). Single point calculations in gas phase (energies and wavefunction stability calculations) were carried out using M06L[17] in combination with different basis set sizes (i.e. 6-31+G(d,p), 6-311G(d,p),[32] and 6-311+G(d,p);[15,32] to determine any basis set effects on the calculated single point energies at the optimized geometry of the triplet electronic configuration. We previously found that M06L, without any HF admixture, worked well for these iron systems in line with findings from Jakubikova and co-workers.[20] The single point calculation on the open-shell singlet at the optimized triplet geometry was carried out using the fragment guess job feature available in Gaussview. The unpaired electrons are essentially placed in each of the ligands, and the α spin and the other β spin. The iron centre is left at its +2 oxidation state and with all its electrons paired. The gas phase magnetic coupling constant for the complex at the optimized triplet geometry is estimated using the Yamaguchi formula:[33,34]

$$J_{AB} = -\frac{(E_{HS}-E_{BS})}{\langle S^2\rangle_{HS}-\langle S^2\rangle_{BS}} \qquad (1)$$

All orbitals (MOs, NTOs, and spin density maps) were generated using Gaussview 6. TDDFT spectra were generated using the Gausssum software,[7] and electronic excitation analyses (electron-hole density map) and fragment contributions to the molecular orbitals were generated using Multiwfn 3.6.[35] For **8a**, TDDFT using unrestricted KS at the SMD-PBE0/6-31+G(d,p) level of theory was first carried out. We then subsequently carried out a single point calculation at the same level of theory using restricted-open shell (RO) formalism to generate canonical closed-shell orbitals enabling us to compare the molecular orbitals of **[6a]**, **[7a]**$^+$, and **[10a]**$^+$, as shown in Figure 4, calculated using restricted KS formalism.

Results and Discussion

Structural parameters of the optimized triplet geometries of **[6a]**$^{2+}$ in gas phase and solution are shown in **Table S14**. Consistent with further removal of electron in a $d\pi^*$ orbital, the Fe – N_{amide} bond length further contracts compared to the neutral and one electron-oxidized species with average Fe – N_{amide} lengths of 1.952 Å and 1.910 Å, respectively.[31] Moreover, inclusion of implicit solvation does not modify the structure of the complex. BS-DFT on the gas phase optimized triplet geometry (**Table S15**) suggests that the triplet electronic configuration of **[6a]**$^{2+}$ is more stable than the open-shell singlet. The basis set dependence of the single point energies and the estimated magnetic coupling constants between the N_{amide} unpaired electrons was explored (**Table S15**). In general, there is an increase in value of these parameters as the basis set size is increased from a double zeta quality to triple zeta quality basis sets. This is more obvious on going from the 6-31+G(d,p) to 6-311G(d,p) basis set.

Optimized ground state geometric parameters of the Co, Ni, and Ga analogues are in good agreement with the X-ray structures (**Table S3**). Compared to the neutral **6a**, the **[7a]**$^+$ and **[10a]**$^+$ have shorter M – N_{amide} bond lengths consistent with increased Coulombic attraction between the N_{amido} donors and the positive metal centre, while the neutral **8a** has longer M – N_{amide} bond. Oxidation of **[7a]**$^+$ results in a minor contraction of the Co – N_{amide} bond due to the weak π-bonding between the Co *d*-orbitals and the N_{amido} lone pairs. TDDFT on the oxidized species proved to be sensitive with the amount of Hartree-Fock (HF) exchange admixture (**Figure S12**). This was particularly problematic with the IVCT band at ~0.6 eV. Full TDDFT treatment with the PBE0 functional severely underestimates the IVCT vertical excitation energy and intensity. Tamm-Dancoff approximation (TDA) with PBE0 shifts the energy closer to the experimental and increases the intensity of the absorption band. Increasing the HF admixture (i.e. M062X and CAM-B3LYP), even with TDA, results with unphysical (i.e. imaginary) vertical excitation energies

indicating instability in the reference ground state.[36,37] Global hybrids with low amounts of HF admixture (i.e. O3LYP) and GGA or meta-GGA (i.e. M06L) in conjunction with TDA provide a more accurate vertical excitation energies and intensities. Due to the difference in ordering of the α- and β-orbitals in open-shell systems, restricted open-shell DFT was carried out on the neutral **8a**. This facilitates a more straightforward comparison of the MOs of **8a** with the three closed-shell complexes. Both UKS and ROKS solutions for **8a** indicate metal based SOMOs (**Figure S2**).

Table S24. Crystal structure and optimized (SMD-O3LYP/6-31+G(d,p)) ground state geometric parameters for **[($^{t\mathrm{Bu}}$L)$_2$M]**$^{n+}$.

	M = Co			M = Ni		M = Ga	
Bond / Å	XRD n = 1	DFT n = 1	DFT n = 2[a]	XRD n = 0	DFT n = 0	XRD n = 1	DFT n = 1
M-$N_{amide,1}$	1.897	1.918	1.902	2.017	2.043	1.958	1.996
M-$N_{amide,2}$	1.897	1.918	1.902	2.016	2.043	1.958	1.996
M-$N_{phen,1}$	1.908	1.942	1.950	2.071	2.130	2.074	2.065
M-$N_{phen,2}$	1.908	1.942	1.950	2.078	2.131	2.074	2.065
M-$N_{quin,1}$	1.915	1.943	1.953	2.076	2.135	2.074	2.073
M-$N_{quin,2}$	1.915	1.943	1.953	2.072	2.134	2.074	2.073
Angle / °							
$N_{amide,1}$-M-$N_{amide,2}$	178.1	180.0	179.9	178.2	179.8	178.9	179.9
$N_{phen,1}$-M-$N_{phen,2}$	89.8	90.6	90.4	91.0	91.0	89.2	91.7
$N_{quin,1}$-M-$N_{quin,2}$	89.9	90.7	90.3	90.6	90.6	91.7	91.4
N_{phen}-M-N_{quin}	169.5	168.1	167.4	160.1	160.0	161.7	161.6

[a] Optimized with unrestricted DFT.

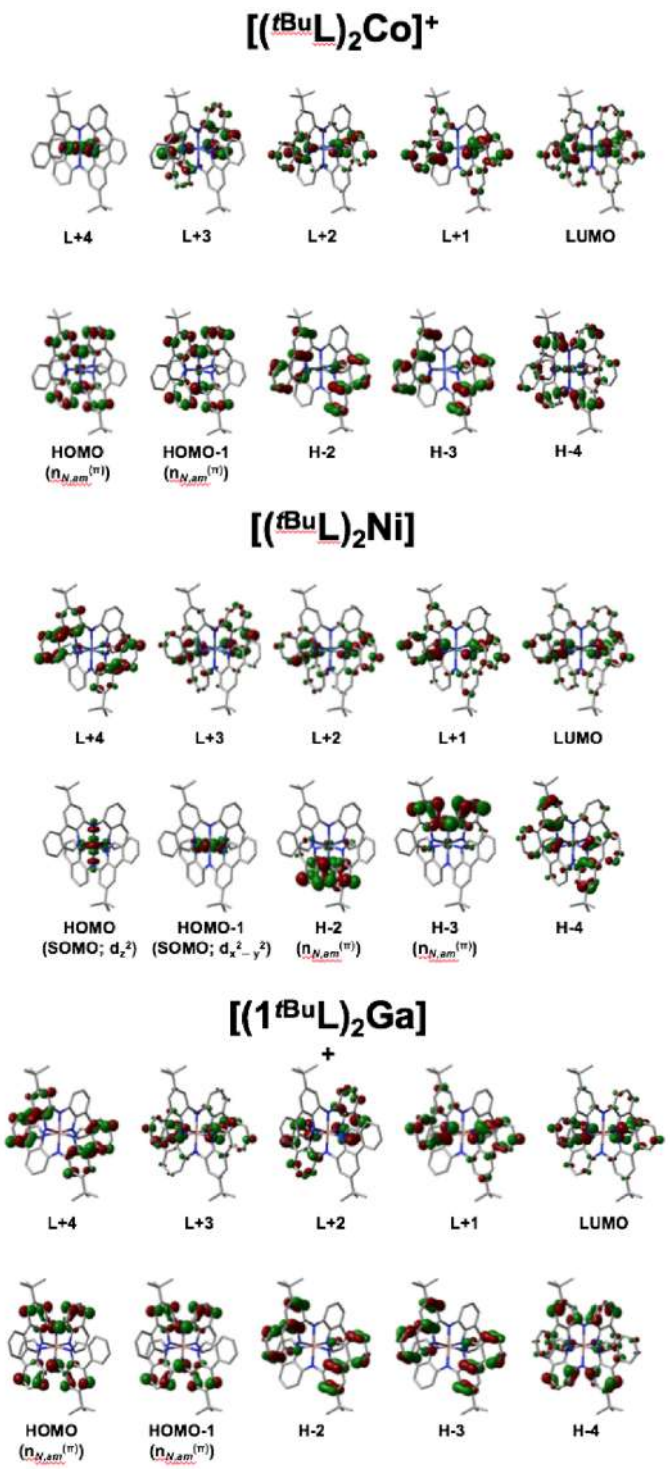

Figure S169. Frontier molecular orbitals surfaces for **[7a]**$^{+}$, **8a**, and **[10a]**$^{+}$ (Co and Ga: SMD-rPBE0/6-31+G(d,p)//SDM-rO3LYP/6-31+G(d,p); Ni: SMD-roPBE0/6-31+G(d,p)//SDM-uO3LYP/6-31+G(d,p); isosurface = 0.04).

Table S25. Fragment contributions (%) to selected ground state MOs of **[7a]**$^{+}$ using Hirshfeld atomic population method (SMD-PBE0/6-31+G(d,p)//SMD-O3LYP/6-31+G(d,p)).

MO	Co	N_{amide}	$HC{=}N_{phen}$	$HC{=}N_{quin}$	Ar_{phen}	Ar_{quin}	*t*Bu
L+3	1	2	3	27	10	57	0
L+2	2	2	18	17	32	29	1
L+1	1	1	33	2	56	6	2
L	3	1	19	14	31	31	1
H	3	19	4	3	34	36	1
H-1	3	20	4	3	34	36	1

Table S26. Fragment contributions (%) to selected ground state α- and β-MOs **8a** using Hirshfeld atomic population method (SMD-uPBE0/6-31+G(d,p)//SMD-uO3LYP/6-31+G(d,p)).

α-MO	Ni	N_{amide}	$HC{=}N_{phen}$	$HC{=}N_{quin}$	Ar_{phen}	Ar_{quin}	*t*Bu
L+5	0	1	3	3	81	8	1
L+4	0	1	3	4	81	7	1
L+3	1	2	6	21	23	47	1
L+2	1	2	12	17	34	33	1
L+1	1	1	22	4	51	13	1
L	2	1	18	10	39	26	1
H	2	20	6	3	33	37	1
H-1	2	20	3	3	33	37	1
β-MO	**Ni**	N_{amide}	$HC{=}N_{phen}$	$HC{=}N_{quin}$	Ar_{phen}	Ar_{quin}	*t*Bu
L+11	58	1	6	7	19	6	2
L+4	1	2	3	4	80	8	1
L+3	1	2	6	20	26	43	1
L+2	1	2	12	16	36	32	1
L+1	1	1	22	5	50	15	1
L	2	1	18	10	38	26	1
H	3	20	6	3	33	36	1
H-1	3	20	3	3	33	36	1
H-9	53	2	3	8	11	20	1

Table S27. Fragment contributions (%) to selected ground state α- and β-MOs **[10a]**$^{+}$ using Hirshfeld atomic population method (SMD-rPBE0/6-31+G(d,p)//SMD-rO3LYP/6-31+G(d,p)).

MO	Ga	N_{amide}	$HC{=}N_{phen}$	$HC{=}N_{quin}$	Ar_{phen}	Ar_{quin}	*t*Bu
L+3	1	2	16	18	30	32	1
L+2	1	2	1	29	6	62	0
L+1	1	1	36	1	58	1	2
L	1	1	21	13	34	29	1
H	1	19	3	3	35	37	1
H-1	1	19	3	3	35	37	1

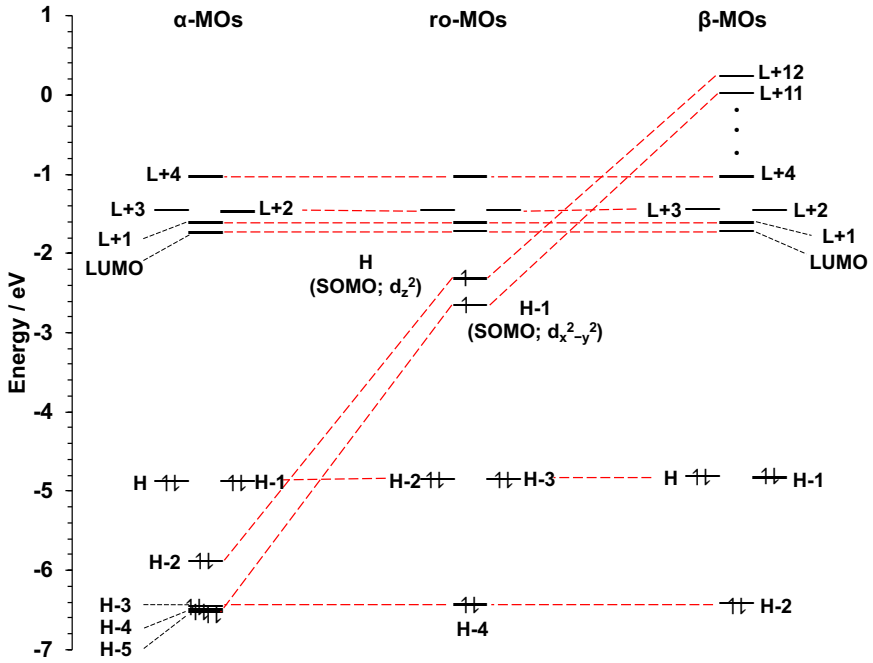

Figure S170. Molecular orbital diagrams for **8a** showing correlation between UKS (α-MOs, left; β-MOs, right; SMD-uPBE0/6-31+G(d,p)//SMD-uO3LYP/6-31+G(d,p)) and ROKS (middle; roPBE0/6-31+G(d,p)//uO3LYP/6-31+G(d,p)) solutions. The unpaired electrons are largely localized at Ni d_z^2 and $d_{x^2-y^2}$ orbitals.

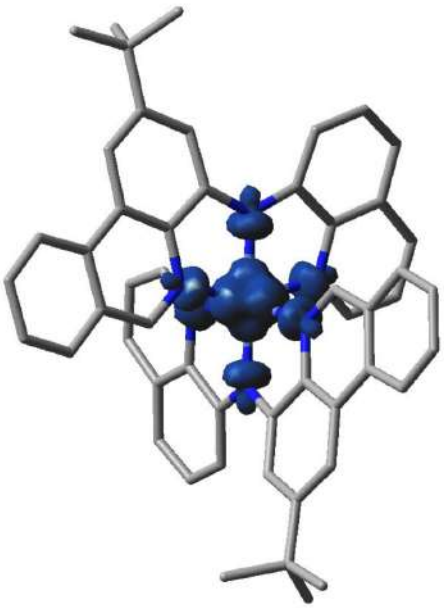

Fragment	Spin Density
Ni	1.74

Figure S171. Spin density map of **8a** (SMD-uPBE0/6-31+G(d,p)//SMD-uO3LYP/6-31+G(d,p); isosurface = 0.004).

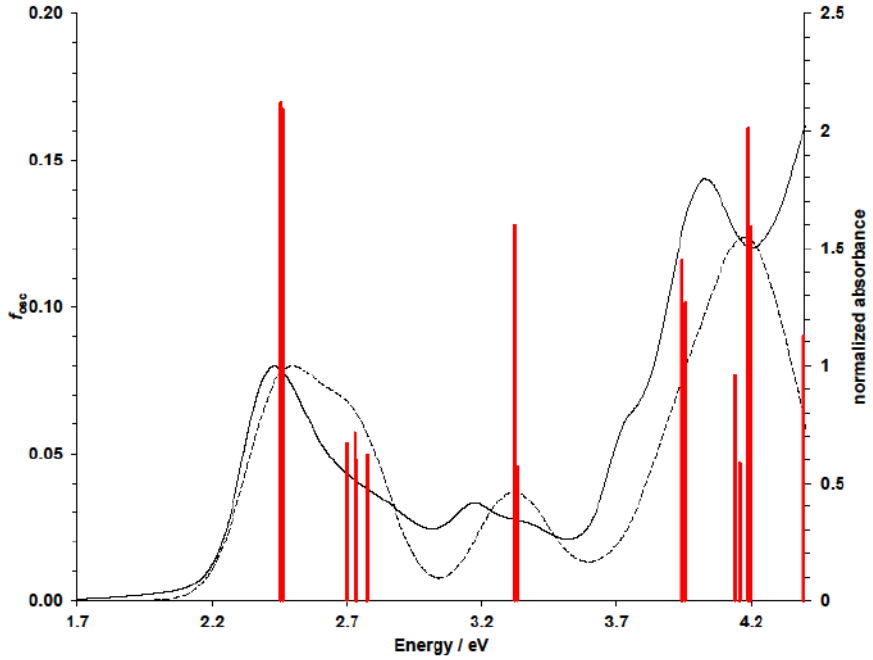

Figure S172. TD-DFT simulated spectrum (---) and vertical excitation energies (red) superimposed on the experimental spectrum (-) of **[7a]**$^+$ in CH_3CN (SMD-rPBE0/6-31+G(d,P)//SMD-rO3LYP/6-31+G(d,p); FWHM = 2500 cm^{-1}; $f > 0.05$).

Table S28. TDDFT predicted vertical excitation energies, oscillator strengths (f_{osc} > 0.05), and MO contributions (> 10%) **[7a]**$^+$ (SMD-rPBE0/6-31+G(d,p)//SMD-rO3LYP/6-31+G(d,p)).

No.	E / eV	f_{osc}	Major MO contribs
3	2.45	0.17	HOMO→LUMO (98%)
4	2.46	0.17	H-1→LUMO (97%)
8	2.70	0.05	HOMO→L+1 (89%)
10	2.73	0.06	H-1→L+2 (58%), HOMO→L+3 (31%)
11	2.74	0.05	H-1→L+1 (10%), HOMO→L+2 (79%)
13	2.77	0.05	H-1→L+3 (87%), HOMO→L+2 (12%)
14	3.32	0.13	H-1→L+7 (30%), HOMO→L+5 (60%)
15	3.33	0.05	H-1→L+5 (54%), HOMO→L+7 (35%)
26	3.94	0.12	H-14→L+4 (10%), H-3→LUMO (38%)
28	3.96	0.10	H-14→L+4 (13%), H-3→LUMO (30%)
31	4.14	0.08	H-3->LUMO (16%), H-2->L+1 (65%)
32	4.16	0.05	H-4→LUMO (11%), H-3→L+1 (37%), H-2→L+2 (16%), HOMO→L+10 (14%)
33	4.19	0.16	H-1→L+10 (51%), HOMO→L+11 (29%)
34	4.19	0.13	H-3→L+1 (15%), H-1→L+11 (20%), HOMO→L+10 (47%)
44	4.39	0.09	H-5→L+2 (25%), H-4→L+3 (28%), H-2→L+3 (13%), HOMO→L+11 (13%)

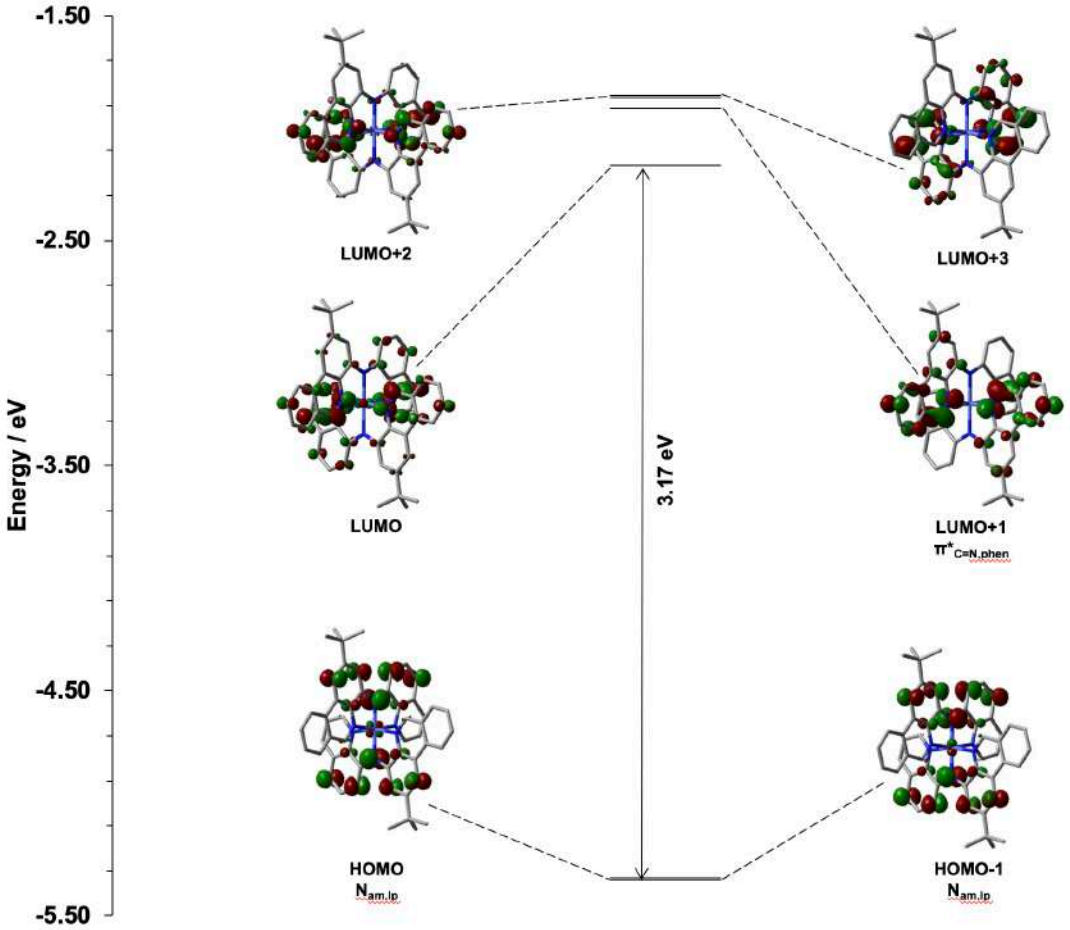

Figure S173. MO energies and diagrams dominating the visible region of the UV-Vis absorbance spectrum of **[7a]**$^{+}$ (SMD-rPBE0/6-31+G(d,p)//SMD-rO3LYP/6-31+G(d,p); isosurface = 0.04).

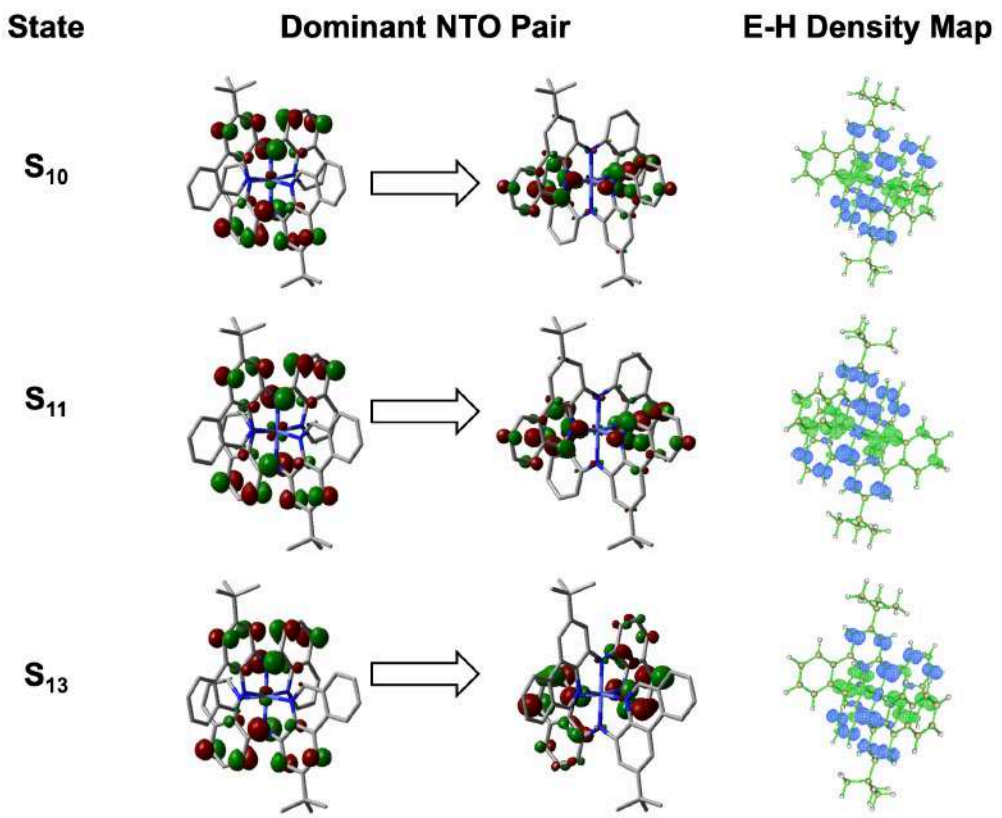

Figure S174. Natural transition orbitals (isosurface = 0.04) and TDDFT calculated electron density gain (green) and depletion (blue) maps (isosurface = 0.002) of the dominant excited states in the visible region of **[7a]**$^{+}$ (SMD-rPBE0/6-31+G(d,p)//SMD-rO3LYP/6-31+G(d,p)). NTOs are calculated only for states with more than one MO pair contribution.

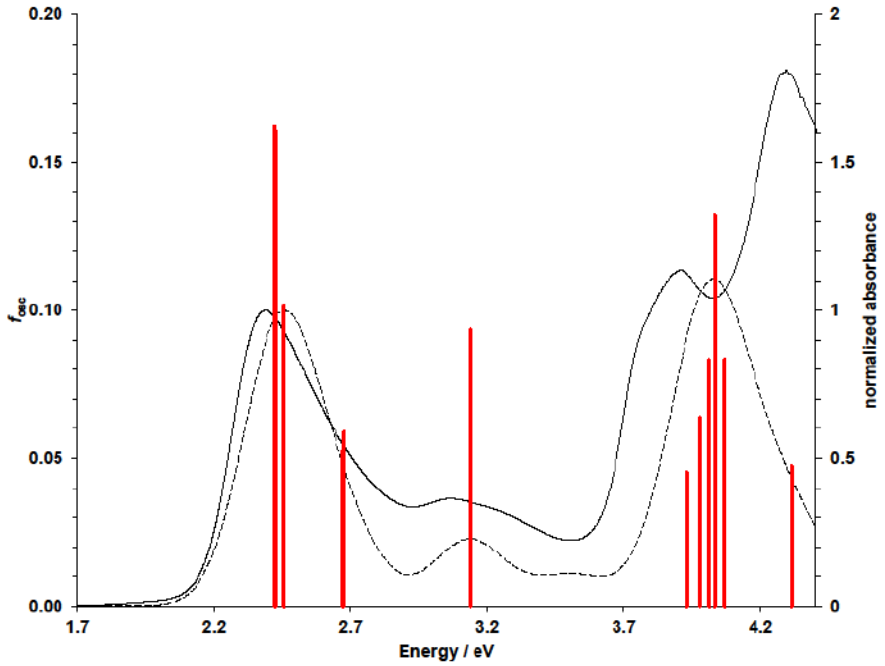

Figure S175. TD-DFT simulated spectrum (---) and vertical excitation energies (red) superimposed on the experimental spectrum (-) of **8a** in CH_3CN (TD-SMD-uPBE0/6-31+G(d,p)//SMD-uO3LYP/6-31+G(d,p); FWHM = 2500 cm^{-1}; $f > 0.05$).

Table S29. TDDFT predicted vertical excitation energies, oscillator strengths ($f_{osc} > 0.05$), and MO contributions (> 10%) **8a** (SMD-uPBE0/6-31+G(d,p)//SMD-uO3LYP/6-31+G(d,p)).

No.	E /eV	f_{osc}	Major MO contribs
8	2.42	0.16	H-1(A)→LUMO(A) (10%), HOMO(A)→LUMO(A) (19%), H-1(B)→LUMO(B) (14%), HOMO(B)→LUMO(B) (33%)
9	2.42	0.16	H-1(A)→LUMO(A) (17%), HOMO(A)→LUMO(A) (10%), H-1(B) →LUMO(B) (33%), HOMO(B) →LUMO(B) (14%)
10	2.46	0.09	H-1(A)→LUMO(A) (11%)
11	2.46	0.10	HOMO(A)→LUMO(A) (12%), H-9(B)→L+11(B) (10%)
18	2.67	0.05	HOMO(A)→L+2(A) (31%), HOMO(A)→L+3(A) (18%), HOMO(B)→L+2(B) (32%)
19	2.68	0.06	H-1(A) →L+2(A) (23%), H-1(A) →L+3(A) (27%), H-1(B) →L+2(B) (17%), H-1(B)→L+3(B) (21%)
29	3.14	0.09	H-1(A)→L+4(A) (17%), H-1(A)→L+5(A) (11%), HOMO(A)→L+4(A) (12%), HOMO(A)→L+5(A) (11%), H-1(B)→L+4(B) (15%), HOMO(B)→L+4(B) (10%)
58	3.93	0.05	HOMO(B)→L+9(B) (24%), HOMO(B)→L+11(B) (12%)
62	3.98	0.06	H-1(A)→L+8(A) (10%), H-1(B)→L+8(B) (18%), H-1(B) →L+9(B) (12%), H-1(B)→L+11(B) (21%)
65	4.01	0.08	H-3(A)→LUMO(A) (14%), H-2(B)→LUMO(B) (13%)
66	4.03	0.13	H-4(A)→LUMO(A) (13%), H-2(A)→L+5(A) (16%)
70	4.07	0.08	H-2(A)→L+5(A) (51%)
92	4.31	0.05	H-7(A)→LUMO(A) (16%), H-3(A)→L+3(A) (12%), H-4(B)→L+1(B) (15%), H-2(B)→L+3(B) (17%)

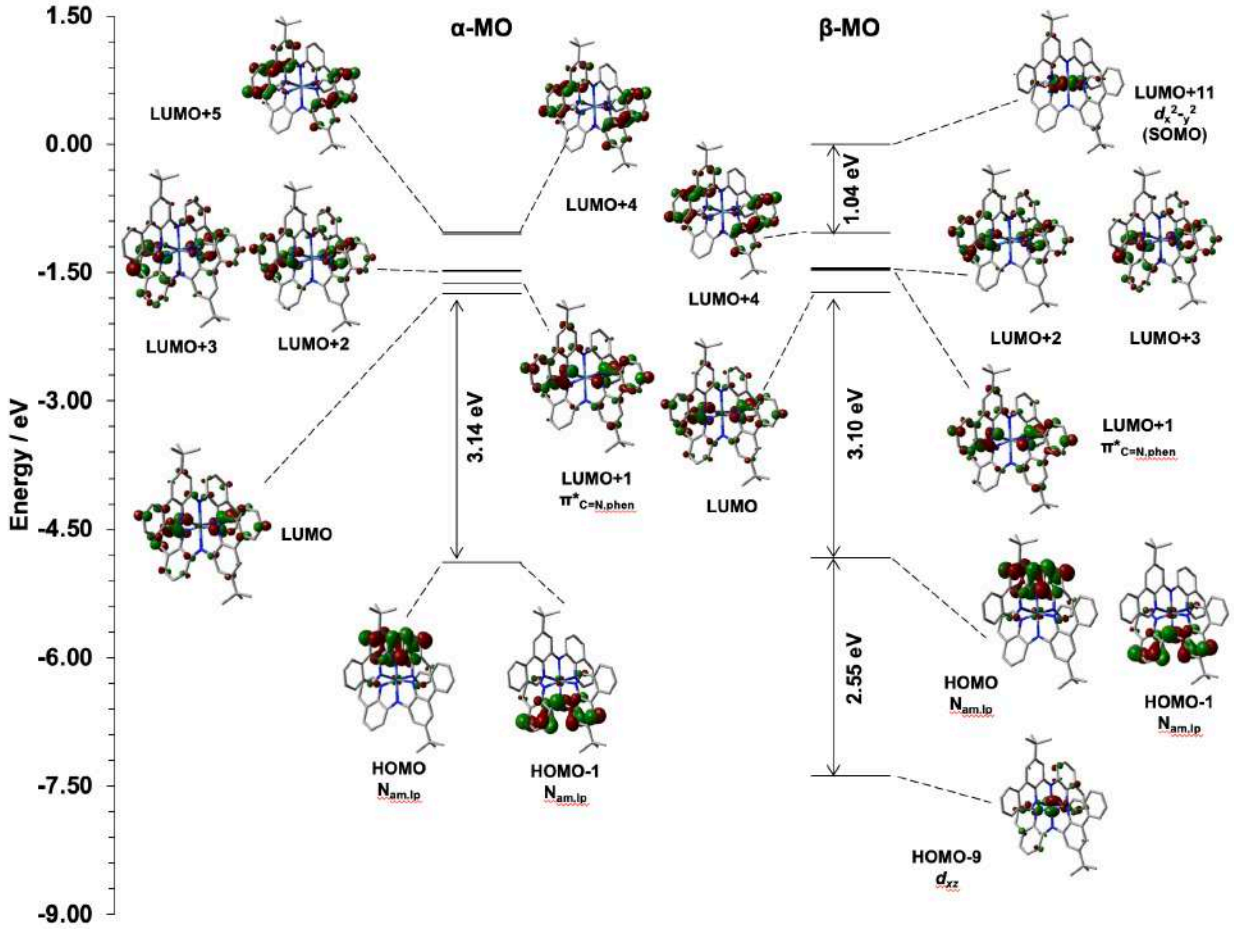

Figure S176. MO energies and diagrams dominating the visible region of the UV-Vis absorbance spectrum of **8a** (SMD-uPBE0/6-31+G(d,p)//SMD-uO3LYP/6-31+G(d,p); isosurface = 0.04).

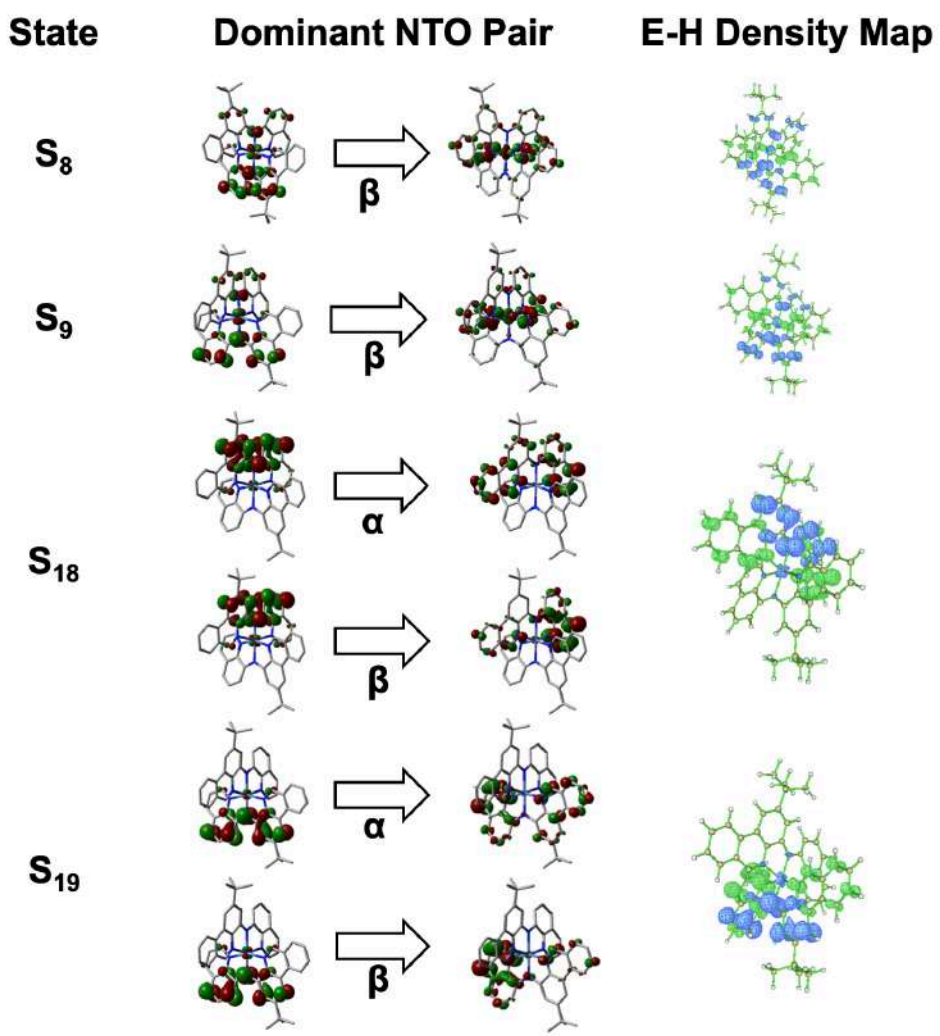

Figure S177. Natural transition orbitals (isosurface = 0.04) and TDDFT calculated electron density gain (green) and depletion (blue) maps (isosurface = 0.002) of the dominant excited states in the visible region of **8a**. NTOs are calculated only for states with more than one MO pair contribution.

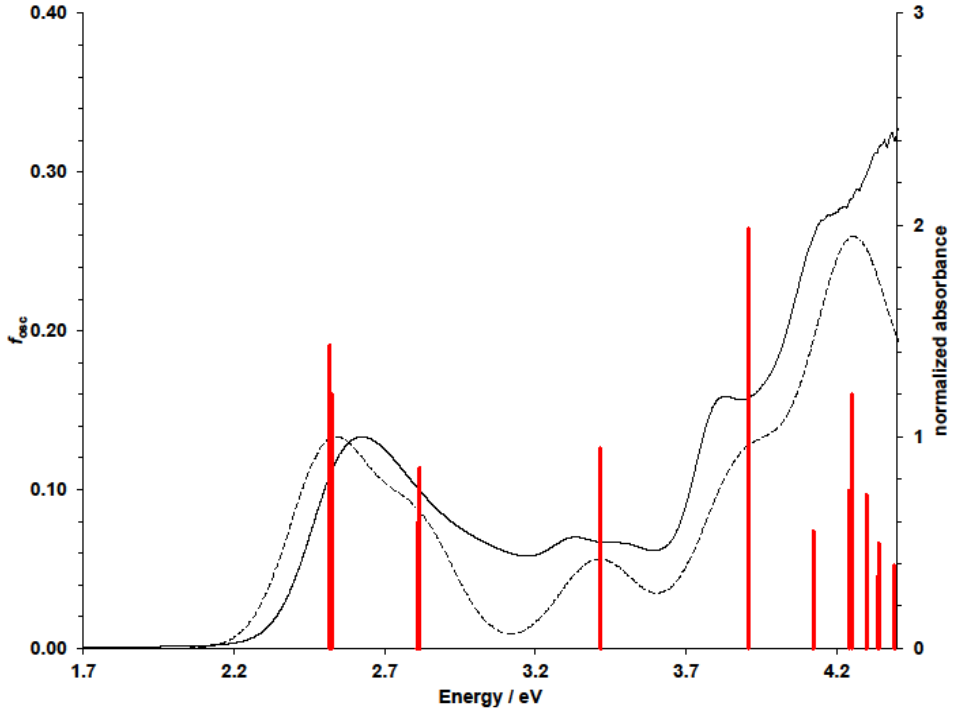

Figure S178. TD-DFT simulated spectrum (---) and vertical excitation energies (red) superimposed on the experimental spectrum (−) of **[10a]**$^+$ in CH_3CN (TD-SMD-rPBE0/6-31+G(d,p)//SMD-rO3LYP/6-31+G(d,p); FWHM = 2500 cm^{-1}; $f > 0.05$).

Table S30. TDDFT predicted vertical excitation energies, oscillator strengths ($f_{osc} > 0.05$), and MO contributions (> 10%) **[10a]**$^+$ (SMD-rPBE0/6-31+G(d,p)//SMD-rO3LYP/6-31+G(d,p)).

No.	E / eV	f_{osc}	Major MO contribs
1	2.52	0.19	HOMO→LUMO (97%)
2	2.52	0.16	H-1→LUMO (96%)
5	2.81	0.08	H-1→L+3 (13%), HOMO→L+2 (80%)
6	2.82	0.11	H-1→L+2 (71%), HOMO→L+3 (20%)
9	3.42	0.13	H-1→L+4 (44%), HOMO→L+5 (47%)
16	3.91	0.26	H-3→LUMO (70%)
21	4.12	0.07	H-3→LUMO (16%), H-2→L+1 (71%)
24	4.24	0.10	H-2→L+2 (48%), H-1→L+9 (11%), HOMO→L+8 (27%)
25	4.25	0.16	H-5→L+1 (26%), H-1→L+9 (11%), HOMO→L+8 (27%)
26	4.25	0.12	H-4→L+1 (11%), H-3→L+2 (38%), H-1→L+8 (27%), HOMO→L+9 (12%)
28	4.30	0.10	H-5→L+1 (25%), H-3→L+3 (48%)
29	4.34	0.05	H-5→L+1 (18%), H-3→L+3 (32%), H-2→L+2 (28%)
30	4.34	0.07	H-4→L+1 (15%), H-3→L+2 (34%), H-2→L+3 (26%)
32	4.39	0.05	H-5→L+2 (54%), H-4→L+3 (19%)

39	4.65	0.10	H-6→LUMO (60%)
40	4.67	0.27	H-7→LUMO (41%)
41	4.72	0.28	H-3→L+4 (27%), H-2→L+5 (24%)
42	4.74	0.30	H-7→LUMO (19%), H-3→L+5 (21%), H-2→L+4 (27%)
43	4.76	0.13	H-7→LUMO (10%), H-1→L+15 (14%), HOMO→L+12 (38%), HOMO→L+14 (12%)
49	4.90	0.08	H-7→LUMO (18%), H-7→L+3 (10%), H-6→L+2 (49%)

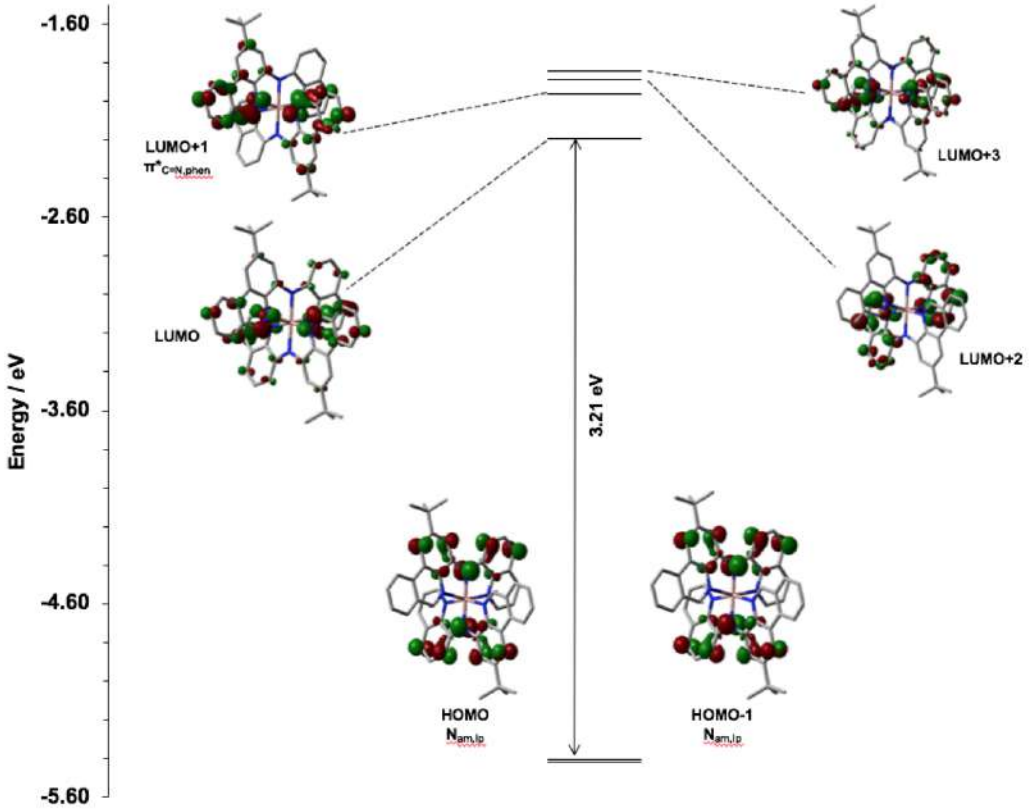

Figure S179. MO energies and diagrams dominating the visible region of the UV-Vis absorbance spectrum of **[10a]**$^{+}$ (SMD-rPBE0/6-31+G(d,p)//SMD-rO3LYP/6-31+G(d,p); isosurface = 0.04).

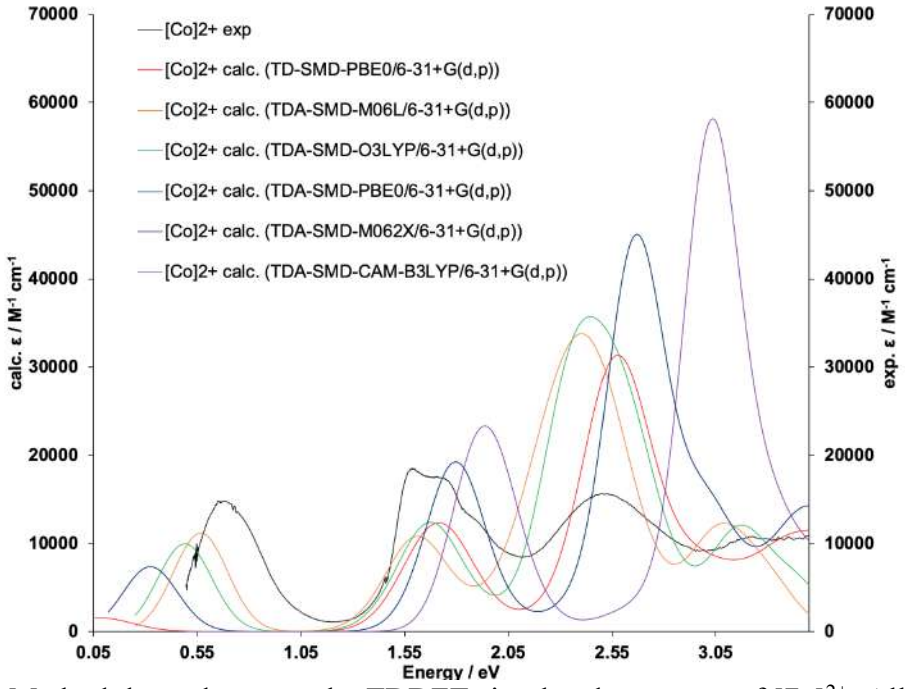

Figure S180. Method dependence on the TDDFT simulated spectrum of **[7a]**$^{2+}$. All methods use unrestricted KS formalism.

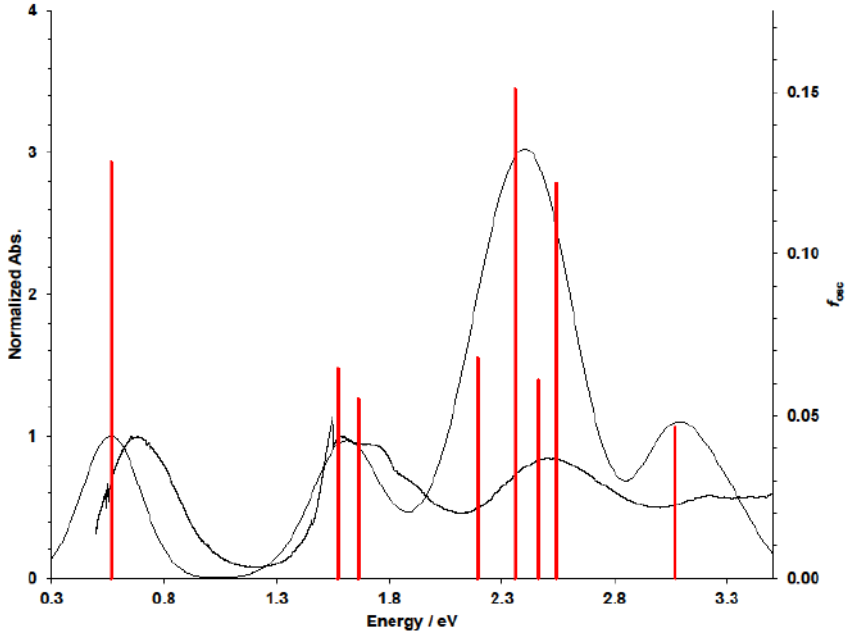

Figure S181. TD-DFT simulated spectrum (---) and vertical excitation energies (red) superimposed on the experimental spectrum (-) of **[7a]**$^{2+}$ in CH_3CN (TDA-SMD-uM06L/6-31+G(d,p)//SMD-uO3LYP/6-31+G(d,p); FWHM = 2500 cm^{-1}; f > 0.05).

Table S31. TDDFT predicted vertical excitation energies, oscillator strengths (f_{osc} > 0.05), and MO contributions (> 10%) **[7a]**$^{2+}$ (TDA-SMD-uM06L/6-31+G(d,p)//SMD-uO3LYP/6-31+G(d,p)).

No.	E / eV	f_{osc}	Major MO contribs
1	0.57	0.13	HOMO(B)→LUMO(B) (95%)
5	1.57	0.06	H-3(B)→LUMO(B) (82%)
6	1.66	0.06	H-4(B)→LUMO(B) (90%)
18	2.19	0.07	H-1(A)→L+3(A) (11%), HOMO(A)→L+2(A) (13%), H-6(B)→LUMO(B) (31%), H-5(B)→LUMO(B) (18%), HOMO(B)→L+4(B) (14%)
25	2.36	0.15	HOMO(A)→L+3(A) (38%), H-10(B)→LUMO(B) (10%), H-8(B)→LUMO(B) (11%)
29	2.46	0.06	H-1(A)→L+5(A) (80%)
30	2.54	0.12	H-1(A)→L+3(A) (25%), H-9(B)→LUMO(B) (37%)
51	3.07	0.05	H-5(A)→LUMO(A) (15%), H-1(A)→L+6(A) (36%), H-1(B)→L+2(B) (10%)

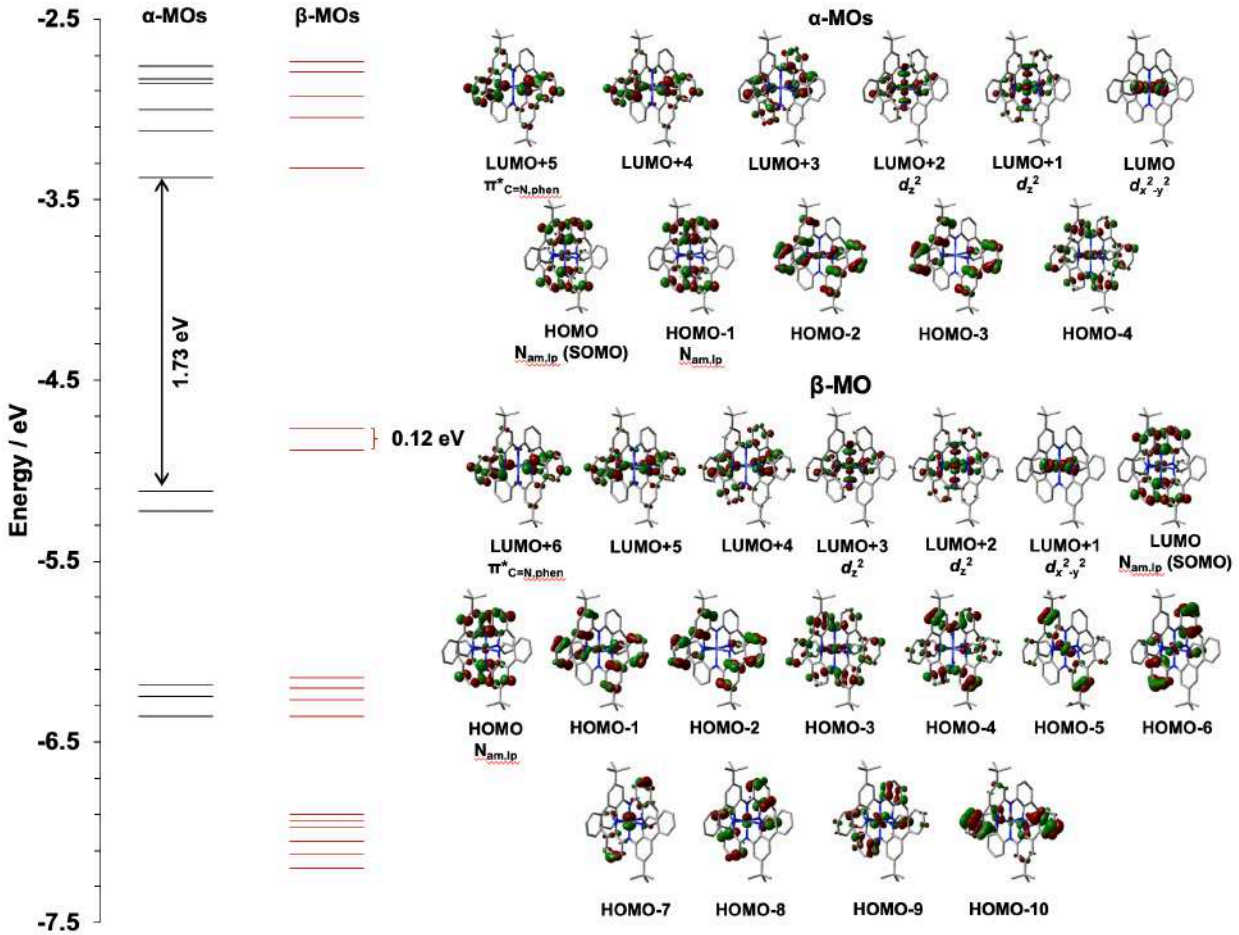

Figure S182. MO energies and diagrams dominating the visible region of the UV-Vis absorbance spectrum of **[7a]**$^{2+}$ (SMD-uM06L/6-31+G(d,p)//SMD-uO3LYP/6-31+G(d,p)).

Table S32. Fragment contributions (%) to selected ground state α- and β-MOs **[7a]**$^{2+}$ using Hirshfeld atomic population method (TDA-SMD-uM06L/6-31+G(d,p)//SMD-uO3LYP/6-31+G(d,p)).

α-MO	**Co**	**N_{amide}**	**$HC{=}N_{phen}$**	**$HC{=}N_{quin}$**	**Ar_{phen}**	**Ar_{quin}**	***t*Bu**
L+5	1	1	34	4	51	7	1
L+4	2	2	27	11	39	18	1
L+3	1	2	4	26	11	57	0
L+2	33	9	8	14	11	24	0
L+1	32	8	9	11	15	24	0
L	62	0	15	15	4	4	0
H	7	17	4	3	33	35	1
H-1	4	18	3	3	35	36	1
H-2	5	0	11	1	74	4	4
H-3	0	0	9	0	87	0	3
H-4	12	1	3	5	53	26	0
β-MO	**Co**	**N_{amide}**	**$HC{=}N_{phen}$**	**$HC{=}N_{quin}$**	**Ar_{phen}**	**Ar_{quin}**	***t*Bu**
L+6	1	2	27	10	42	17	1
L+5	2	2	23	14	35	23	1
L+4	1	1	10	21	20	46	1
L+3	36	10	10	12	12	19	0
L+2	28	7	11	11	18	23	1
L+1	62	0	15	14	4	4	0
L	7	19	3	3	32	35	1
H	4	20	3	3	34	35	1
H-1	5	0	11	1	73	4	5
H-2	0	0	8	0	88	1	3
H-3	11	1	3	4	54	26	0
H-4	1	3	6	4	48	35	3
H-5	41	2	3	2	43	3	7
H-6	14	1	1	11	4	70	0
H-7	45	3	1	6	10	33	1
H-8	12	2	1	14	9	62	1
H-9	30	2	3	9	16	40	0
H-10	2	1	12	1	77	4	4

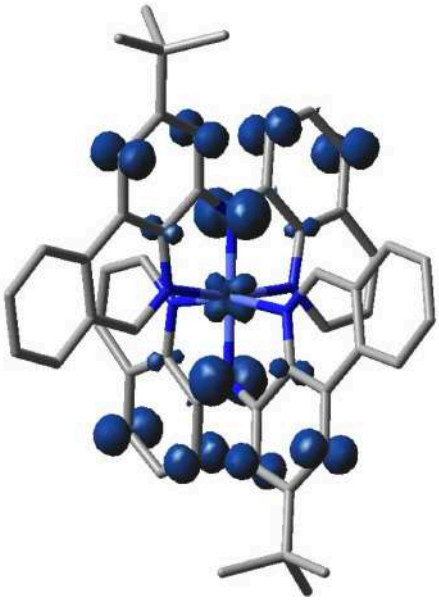

Fragment	Spin Density
N_{amide}	0.30
Ar_{phen}	0.30
Ar_{quin}	0.38

Figure S183. Spin density map of **[7a]**$^{2+}$ (SMD-uM06L/6-31+G(d,p)//SMD-uO3LYP/6-31+G(d,p); isosurface = 0.004).

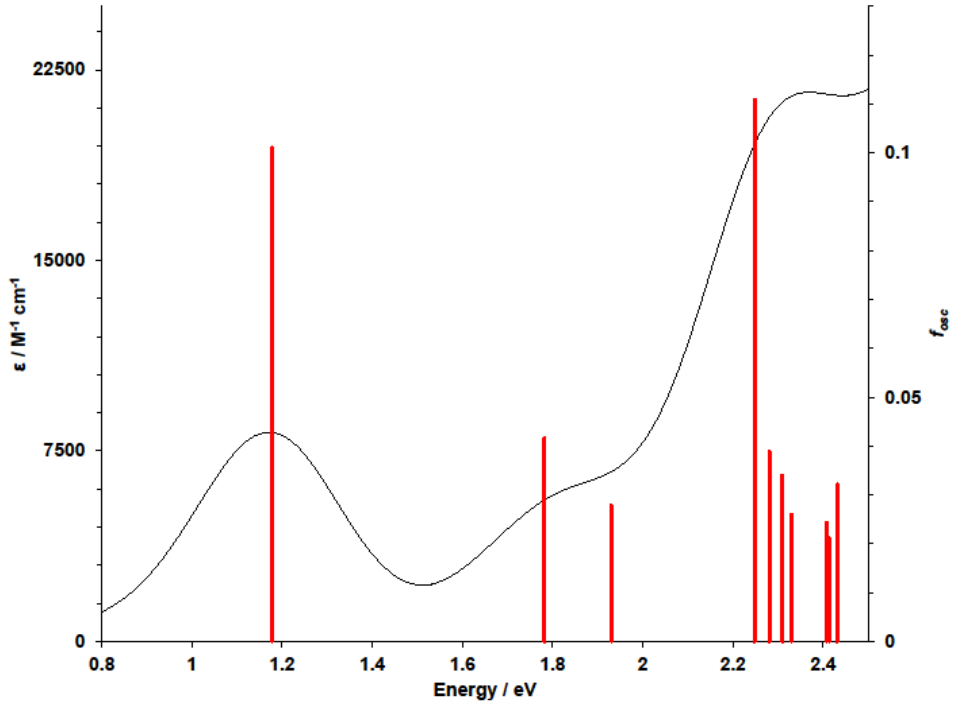

Figure S184. TDDFT (SMD-uM06L/6-31+G(d,p)//SMD-uO3LYP/6-31+G(d,p); $f_{osc} > 0.02$; FWHM = 3000 cm^{-1}) simulated UV-Vis spectrum of **[6a]**$^{2+}$.

Table S33. TDDFT predicted vertical excitation energies, oscillator strengths (f_{osc} > 0.02), and MO contributions (> 10%) **[6a]**$^{2+}$ (SMD-uM06L/6-31+G(d,p)//SMD-uO3LYP/6-31+G(d,p)).

State	*E* / eV	f_{osc}	Major MO contribs.
4	1.18	0.101	H-2(B)→LUMO(B) (26%), H-1(B) →L+1(B) (73%)
9	1.78	0.042	H-5(B) →LUMO(B) (90%)
12	1.93	0.028	H-6(B) →LUMO(B) (81%)
16	2.25	0.111	HOMO(A) →LUMO(A) (49%), H-6(B) →L+1(B) (40%)
17	2.28	0.039	HOMO(A) →L+1(A) (59%), HOMO(B) →L+2(B) (14%)
18	2.31	0.034	H-1(A) →LUMO(A) (77%)
19	2.33	0.026	HOMO(A) →L+2(A) (52%), HOMO(B) →L+2(B) (14%)
22	2.41	0.024	H-1(A) →L+1(A) (24%), HOMO(A) →L+3(A) (13%), H-8(B) →LUMO(B) (53%)
23	2.41	0.021	HOMO(A) →L+4(A) (67%)
24	2.43	0.032	H-1(A) →L+1(A) (41%), H-8(B) →LUMO(B) (40%)

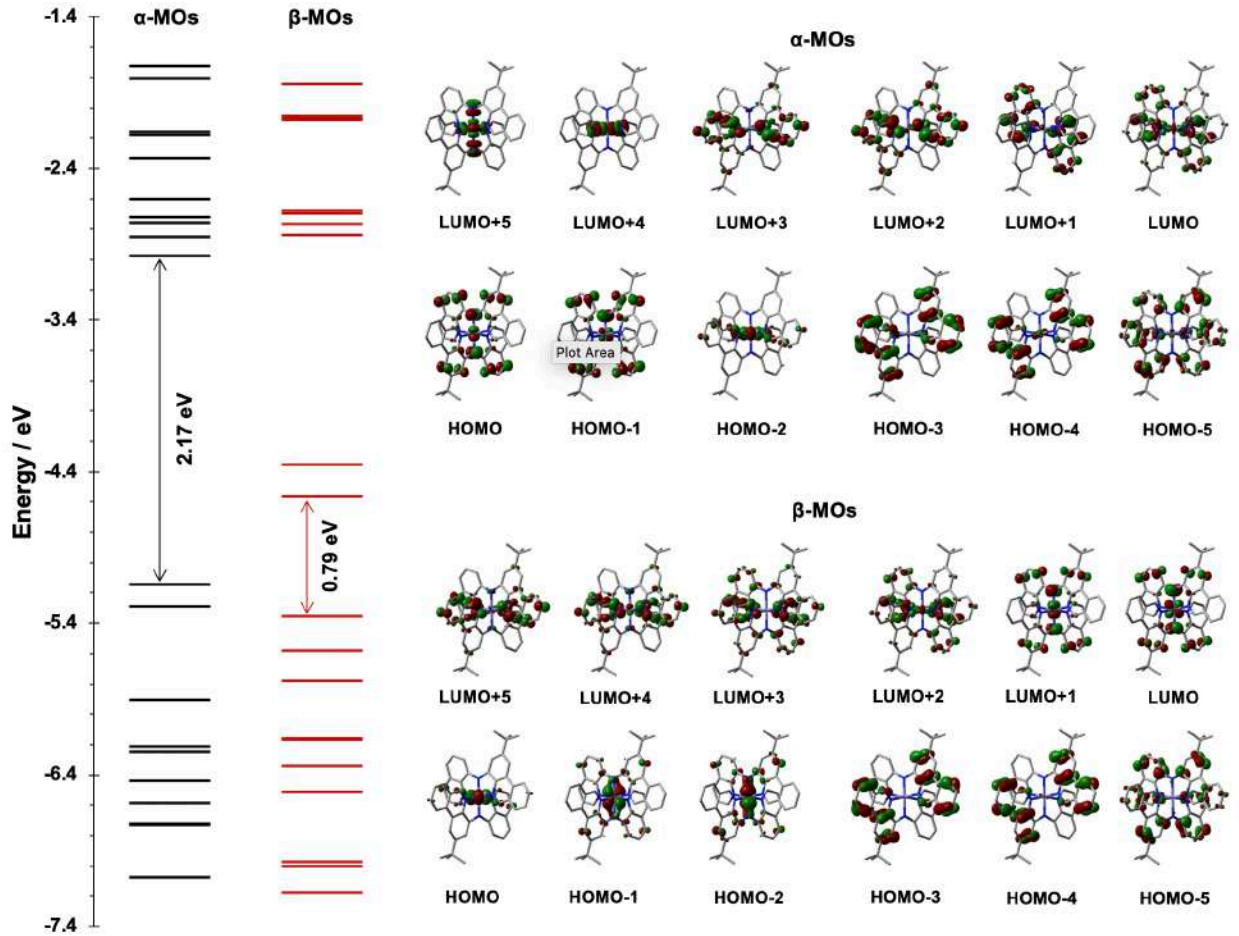

Figure S185. Selected ground state orbital energies, and α- and β-orbital diagrams of **[6a]**$^{2+}$ (SMD-uM06L/6-31+G(d,p)//SMD-uO3LYP/6-31+G(d,p); isosurface = 0.04).

Table S34. Fragment contribution to the ground state MOs of **[6a]**$^{2+}$ using Hirshfeld atomic population method (SMD-uM06L/6-31+G(d,p)//SMD-uO3LYP/6-31+G(d,p)).

α-MOs	**Fe**	**N_{amide}**	**$HC{=}N_{phen}$**	**$HC{=}N_{quin}$**	**Ar_{phen}**	**Ar_{quin}**	***t*Bu**
L+5	61	14	5	6	7	7	0
L+4	65	1	13	13	5	4	0
L+3	2	2	28	9	43	16	1
L+2	3	1	36	2	53	3	1
L+1	2	2	2	27	8	58	0
L	5	1	9	20	18	46	1
H	14	16	4	4	30	32	1
H-1	9	17	4	3	33	33	1
H-2	52	1	9	6	20	12	1
H-3	1	0	10	0	85	0	3
H-4	5	0	5	1	84	3	3
H-5	1	2	5	5	54	31	2
β-MOs	**Fe**	**N_{amide}**	**$HC{=}N_{phen}$**	**$HC{=}N_{quin}$**	**Ar_{phen}**	**Ar_{quin}**	***t*Bu**
L+5	2	2	25	12	39	20	1
L+4	4	3	20	14	34	24	1
L+3	1	1	17	16	29	36	1
L+2	7	1	12	18	22	40	1
L+1	30	15	4	4	22	25	0
L	28	17	3	3	22	25	0
H	67	1	8	6	10	8	0
H-1	56	6	3	3	17	15	1
H-2	49	7	3	3	21	17	1
H-3	0	0	8	0	88	0	3
H-4	1	0	7	0	88	1	3
H-5	1	3	6	5	45	39	2

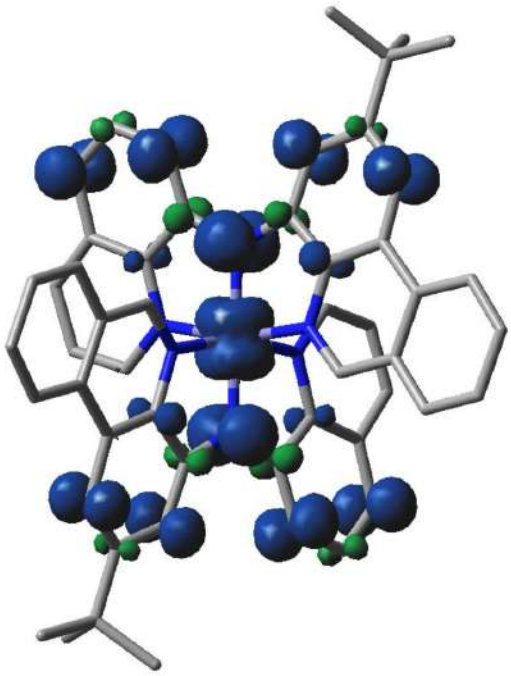

Fragment	Spin Density
Fe	0.73
N_{amide}	0.46

Figure S186. Spin density map of **[6a]**$^{2+}$ (SMD-uM06L/6-31+G(d,p)//SMD-uO3LYP/6-31+G(d,p); isosurface = 0.004).

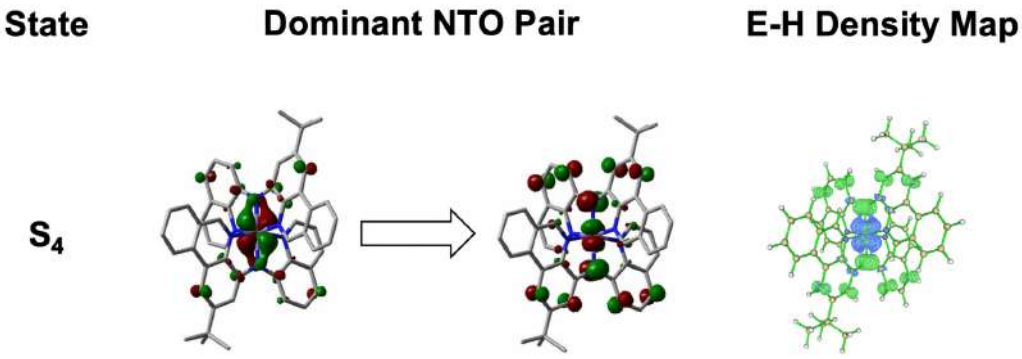

Figure S187. Natural transition orbitals (isosurface = 0.04) and TDDFT calculated electron density gain (green) and depletion (blue) map (isosurface = 0.002) of the dominant excited state (state 4) in the lowest energy band of **[6a]**$^{2+}$.

Table S35. Optimized gas phase (uO3LYP/6-31+G(d,p)) and solution phase (SMD-uO3LYP/6-31+G(d,p); solvent = CH_3CN) triplet state geometric parameters of **[6a]**$^{2+}$.

	[**6a**]$^{2+}$	
Bond / Å	Gas	Solution
Fe-$N_{amide,1}$	1.898	1.895
Fe-$N_{amide,2}$	1.898	1.895
Fe-$N_{phen,1}$	1.985	1.981
Fe-$N_{phen,2}$	1.985	1.981
Fe-$N_{quin,1}$	1.991	1.984
Fe-$N_{quin,2}$	1.991	1.984
Angle / °	Gas	Solution
$N_{amide,1}$-Fe-$N_{amide,2}$	179.8	180.0
$N_{phen,1}$-Fe-$N_{phen,2}$	90.6	90.0
$N_{quin,1}$-Fe-$N_{quin,2}$	91.0	90.6
$[N_{phen}$-Fe-$N_{quin}]_{average}$	165.1	165.4

Table S36. Gas phase single-point energies and $<S^2>$ of triplet and broken-symmetry states at the gas phase optimized triplet geometry (uO3LYP/6-31+G(d,p)) and uM06L/*basis* level of theory, and estimated gas phase magnetic coupling constant (J_{AB}) for **[6a]**$^{2+}$.

$[Fe]^{2+}$	6-31+G(d,p)	6-311G(d,p)	6-311+G(d,p)	$<S^2>$
$\boldsymbol{E_{HS}}$ **/ a.u.**	-3599.73664020	-3600.21424068	-3600.23426220	2.0337
$\boldsymbol{E_{BS}}$ **/ a.u.**	-3599.73479875	-3600.21213016	-3600.23233224	0.9336
$\boldsymbol{J_{AB}}$ **/ cm^{-1}**	367.3	420.6	385.5	

Equations.

$$E_{OP} = \lambda \quad (1)$$

$$H_{ab}\ (cm^{-1}) = [(4.2 \times 10^{-4})\varepsilon_{max}\ \Delta\nu_{1/2} E_{OP}]^{1/2} / d \quad (2)$$

$$\Delta G^*\ (cm^{-1}) = (\lambda - 2H_{ab})^2 / 4\lambda \quad (3)$$

$$k_{et} = (2H_{ab}^2 / h)[\pi^3 / \lambda k_B T]^{1/2} \exp - (\Delta G^* / k_B T) \quad (4)$$

Table S37. Summary of electrochemical data pertaining to IVCT of [(**6-10**)**a**]$^{n+}$ complexes.

	E°/V vs. $FcH^{0/+}$			
	$E°_{ox1}$	$E°_{ox2}$	$^{a}\Delta E°_{1}$	$^{b}K_{com}$
[6a]$^{+}$	-0.77	0.05	0.82	1.13×10^{14}
[7a]$^{+}$	0.31	0.50	0.19	1.76×10^{3}
8a	-0.23	-0.04	0.19	1.76×10^{3}
[10a]$^{+}$	0.42	0.59	0.17	802

[a] $E°_{ox2} - E°_{ox1}$
[b] $K_{com} = e^{(\Delta EF/RT)}$, T = 295 K

Table S38. Summary of IVCT analysis

	[7a]$^{2+}$	**[8a]$^{+}$**	**[10a]$^{2+}$**
$E_{OP} = \lambda$ (cm^{-1})	5482	5549	6002
ε_{max} ($M^{-1}cm^{-1}$)	14801	15743	3531
$\Delta\nu_{1/2}$ (cm^{-1})	2927	3051	3032
$\Delta\nu_{1/2}$ HTL (cm^{-1})	3559	3580	3724
$\theta = \Delta\nu_{1/2}/\Delta\nu_{1/2}$ (HTL)	0.822	0.852	0.814
d **(Å)**	3.804[a]	4.055[a]	4.047[a]
H_{ab} (cm^{-1})	2625	2609	1284
$\alpha = 2H_{ab}/\lambda$	0.958	0.940	0.428
ΔG^* (cm^{-1})	2.454	4.936	491.2
k_{et} (s^{-1})	2.129×10^{15}	2.065×10^{15}	9.806×10^{14}
	Class II-III limit	Class IIB	Class IIA

[a] average values from DFT-optimized structures.
$k_B = 0.695\ cm^{-1}\ K^{-1}$
$h = 3.36 \times 10^{-11}\ cm^{-1} \cdot s$
T = 295 K

NMR SPECTRA

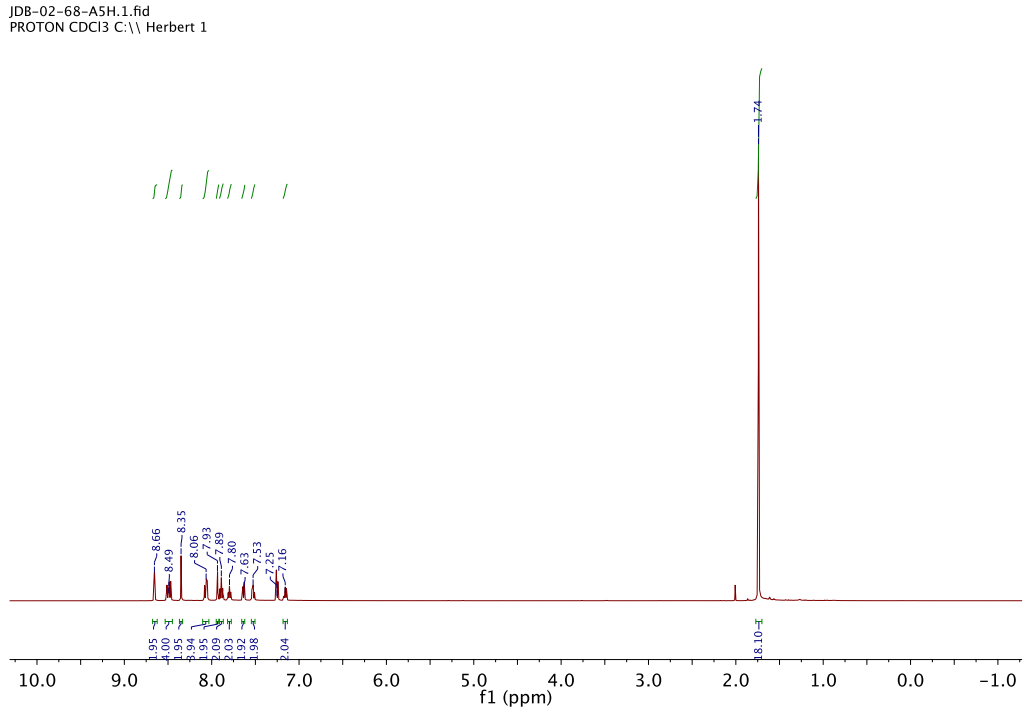

Figure S188. ^{1}H NMR (500 MHz, $CDCl_3$, 25°C) of **[7a]**PF_6.

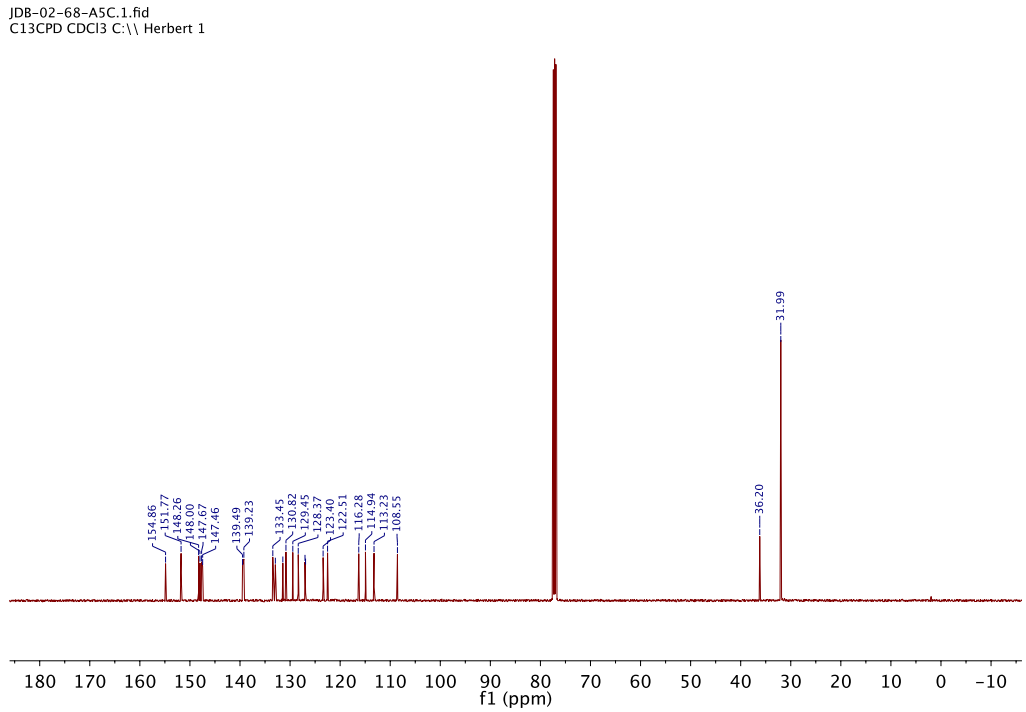

Figure S189. ^{13}C NMR (125 MHz, $CDCl_3$, 25°C) of **[7a]**PF_6.

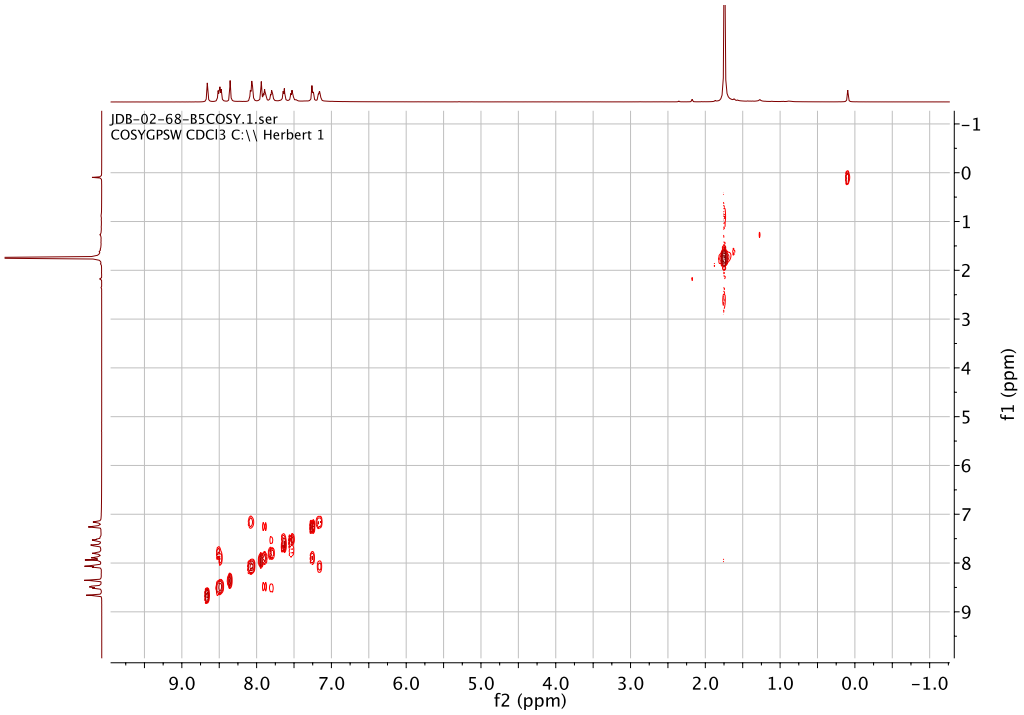

Figure S190. ^{1}H-^{1}H COSY NMR (500 MHz, $CDCl_3$, 25°C) of **[7a]**PF_6.

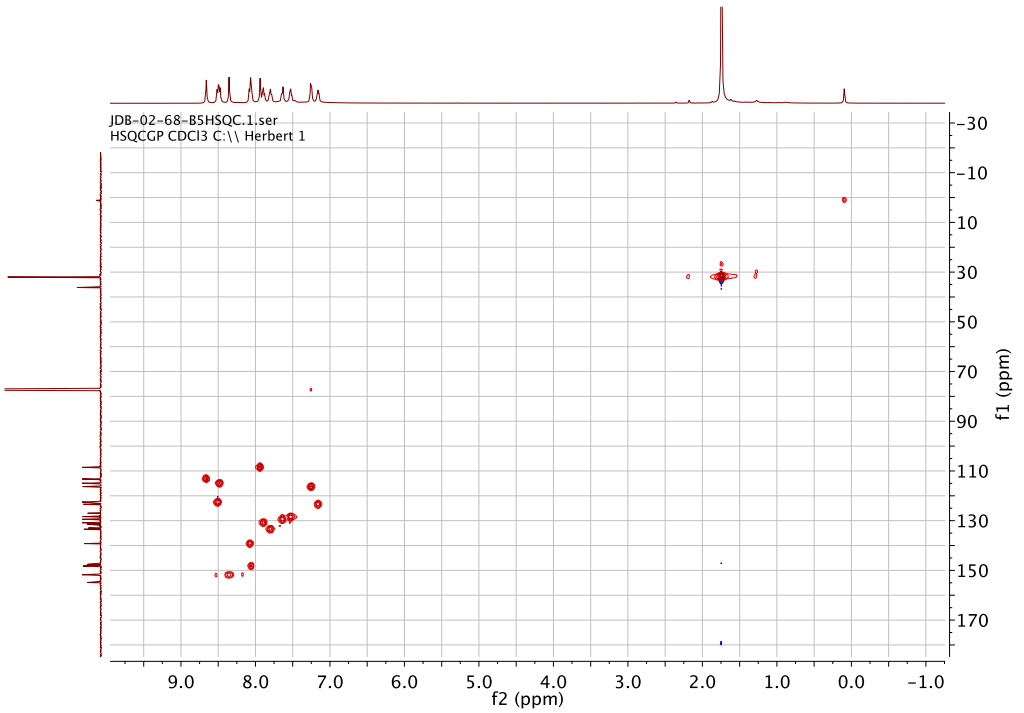

Figure S191. HSQC NMR (500/125 MHz, $CDCl_3$, 25°C) of **[7a]**PF_6.

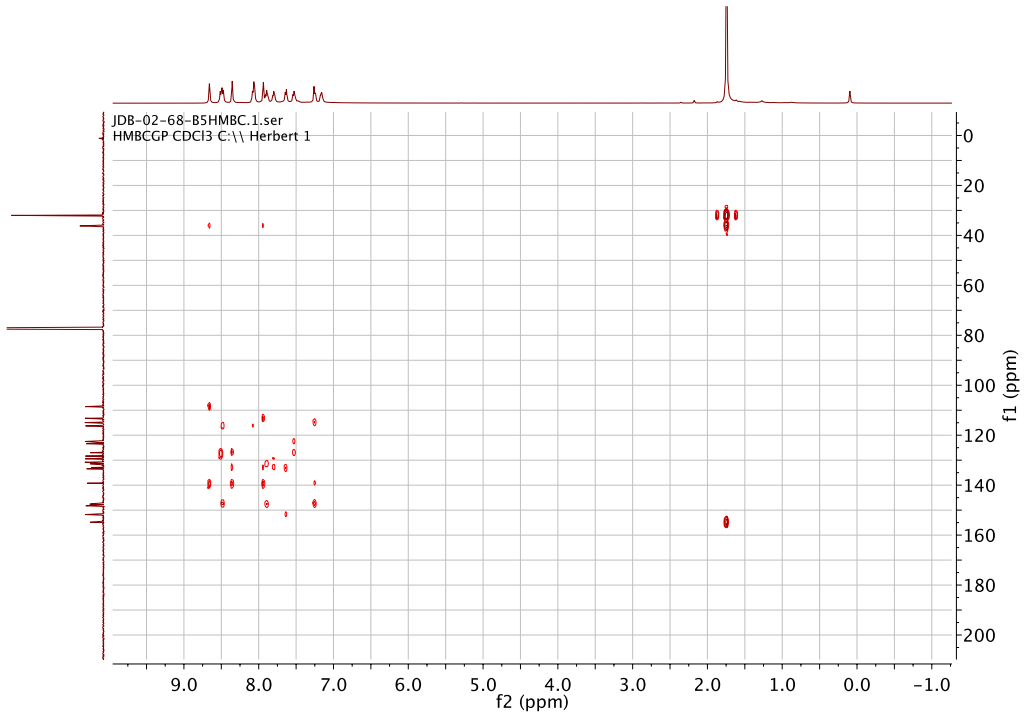

Figure S192. HMBC NMR (500/125 MHz, $CDCl_3$, 25°C) of **[7a]**PF_6.

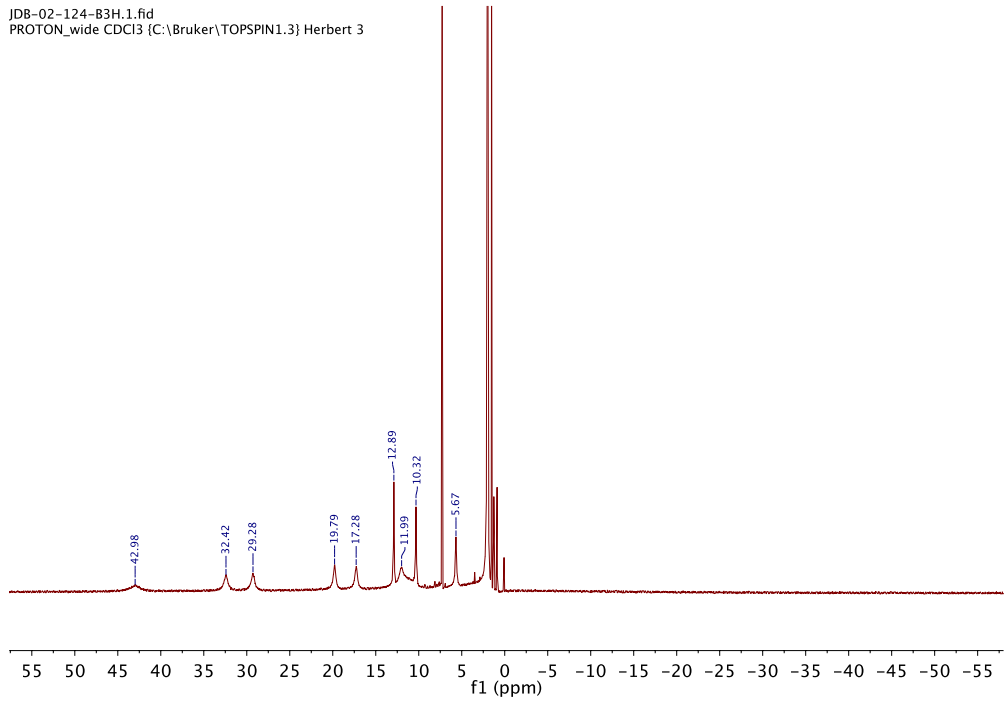

Figure S193. ^1H NMR (300 MHz, $CDCl_3$, 25°C) of **8a**.

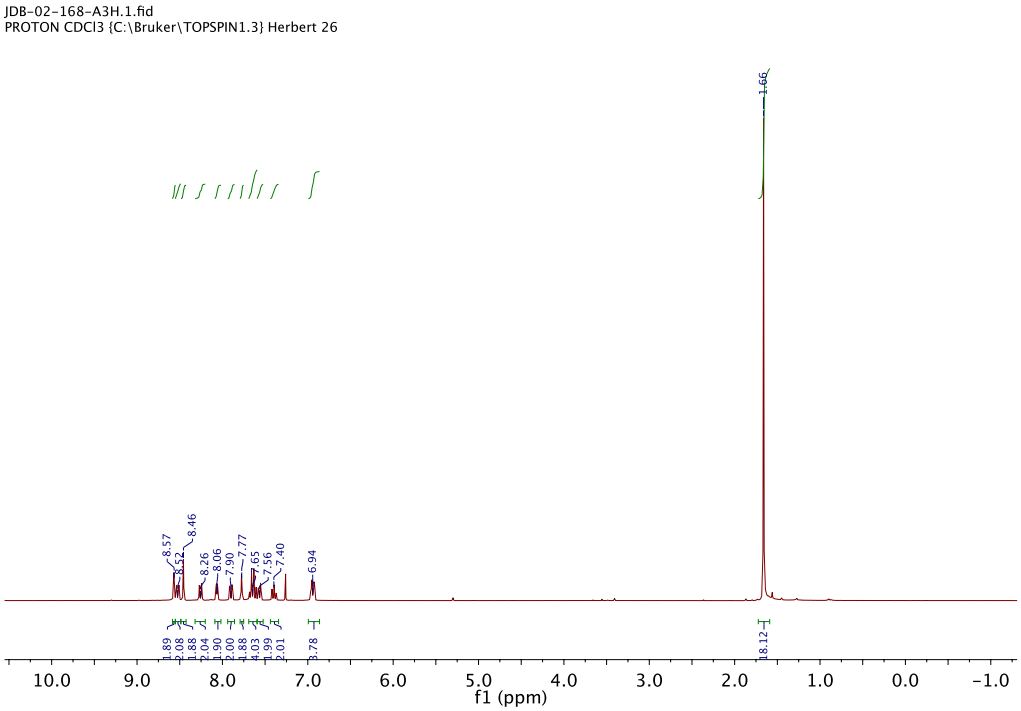

Figure S194. ^{1}H NMR (300 MHz, $CDCl_3$, 25°C) of **9a**.

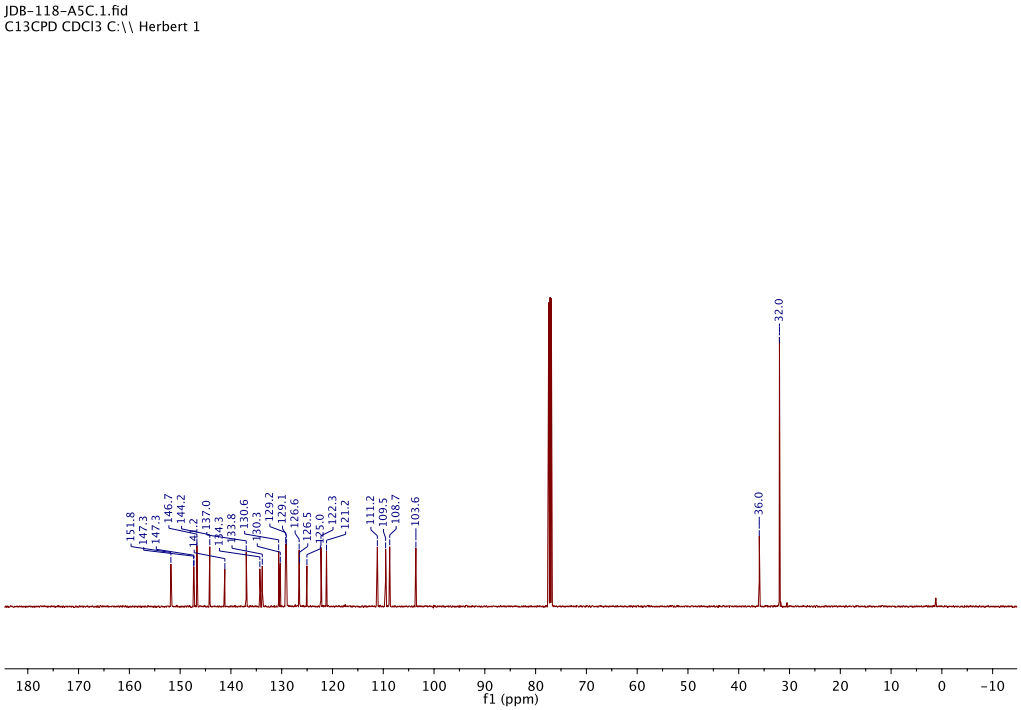

Figure S195. ^{13}C NMR (500 MHz, $CDCl_3$, 25°C) of **9a**.

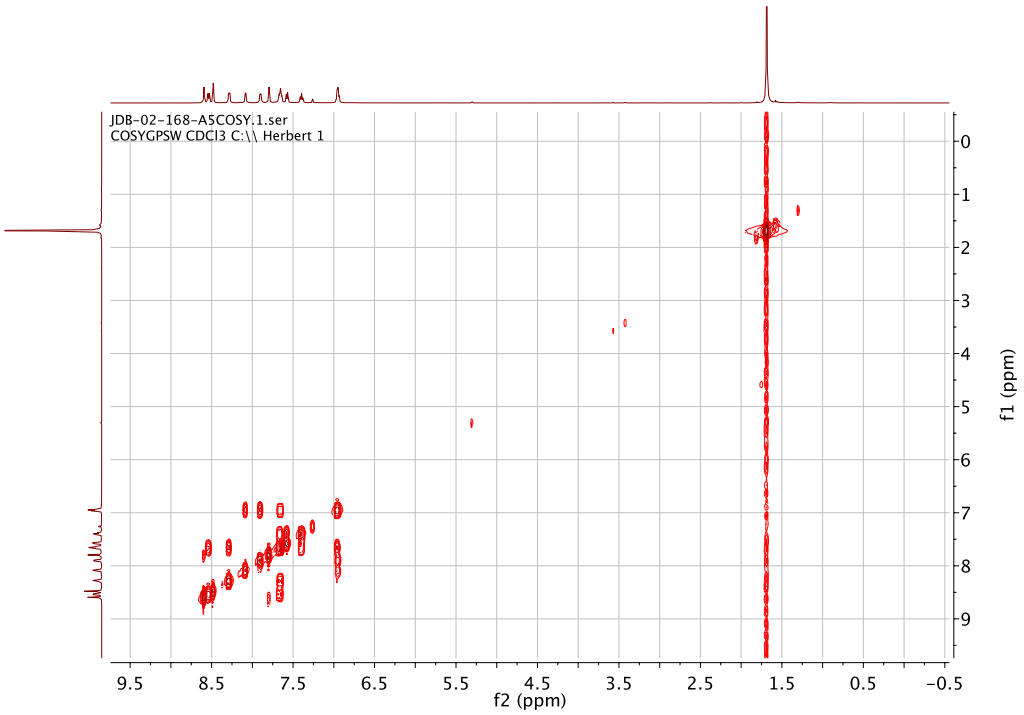

Figure S196. ^{1}H-^{1}H COSY NMR (500 MHz, $CDCl_3$, 25°C) of **9a**.

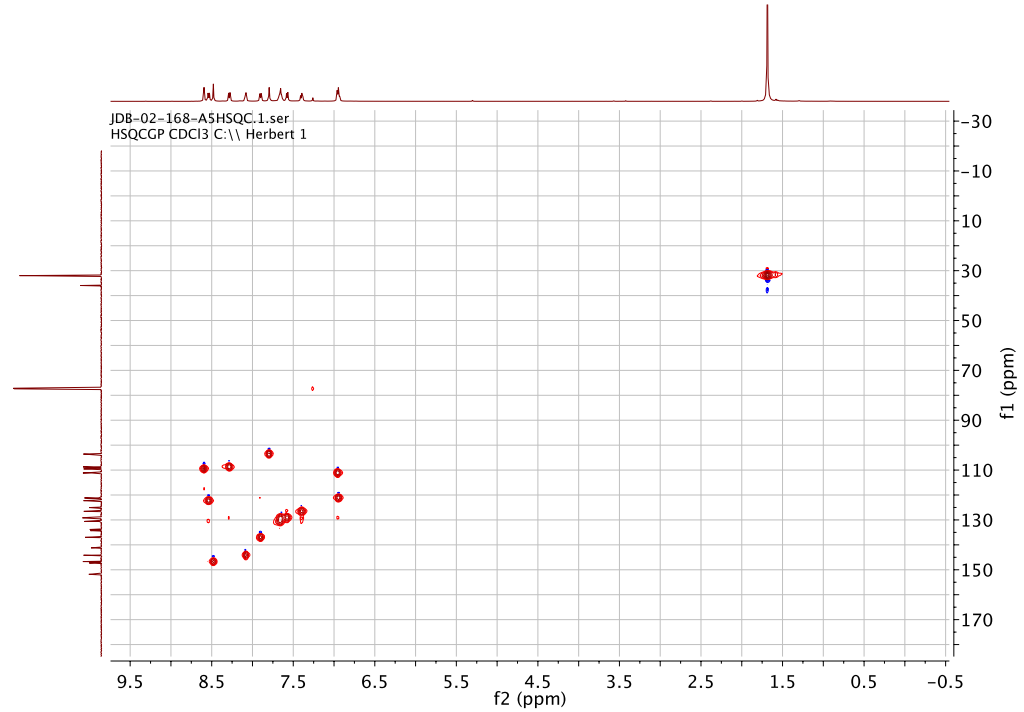

Figure S197. HSQC NMR (500/125 MHz, $CDCl_3$, 25°C) of **9a**.

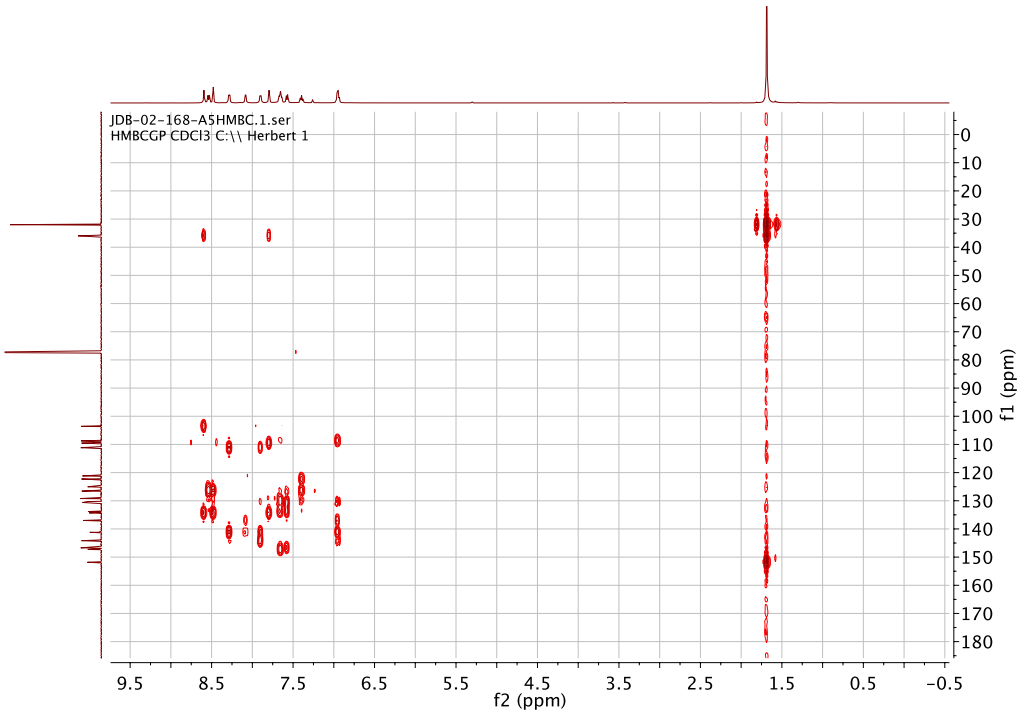

Figure S198. HMBC NMR (500/125 MHz, $CDCl_3$, 25°C) of **9a**.

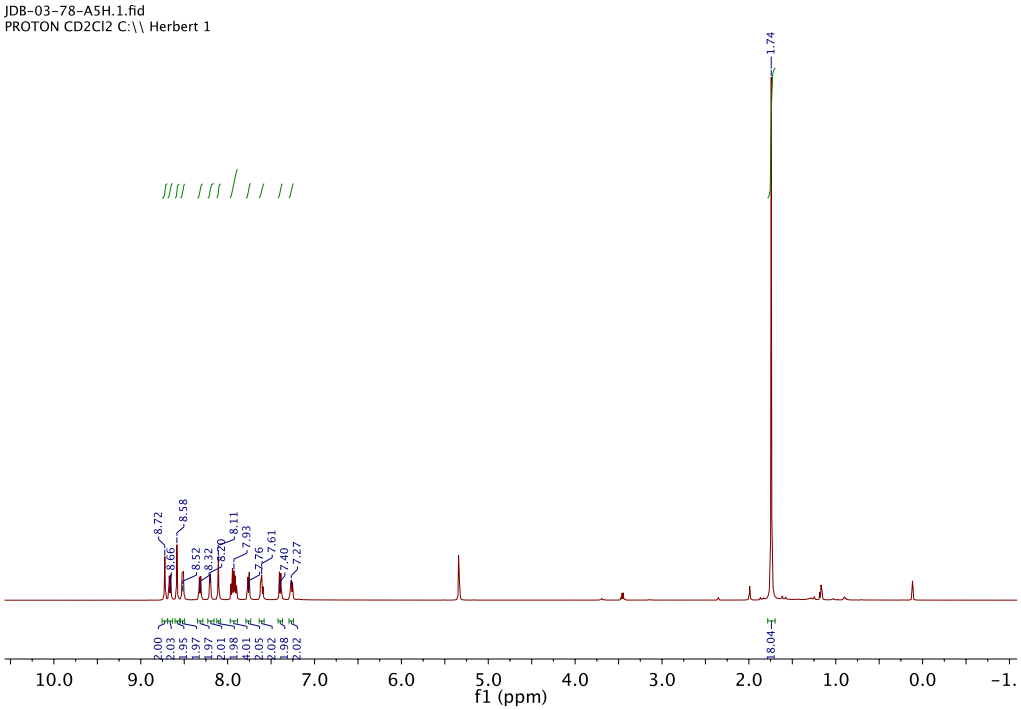

Figure S199. ^1H NMR (500 MHz, CD_2Cl_2, 25°C) of **[10a]**PF_6.

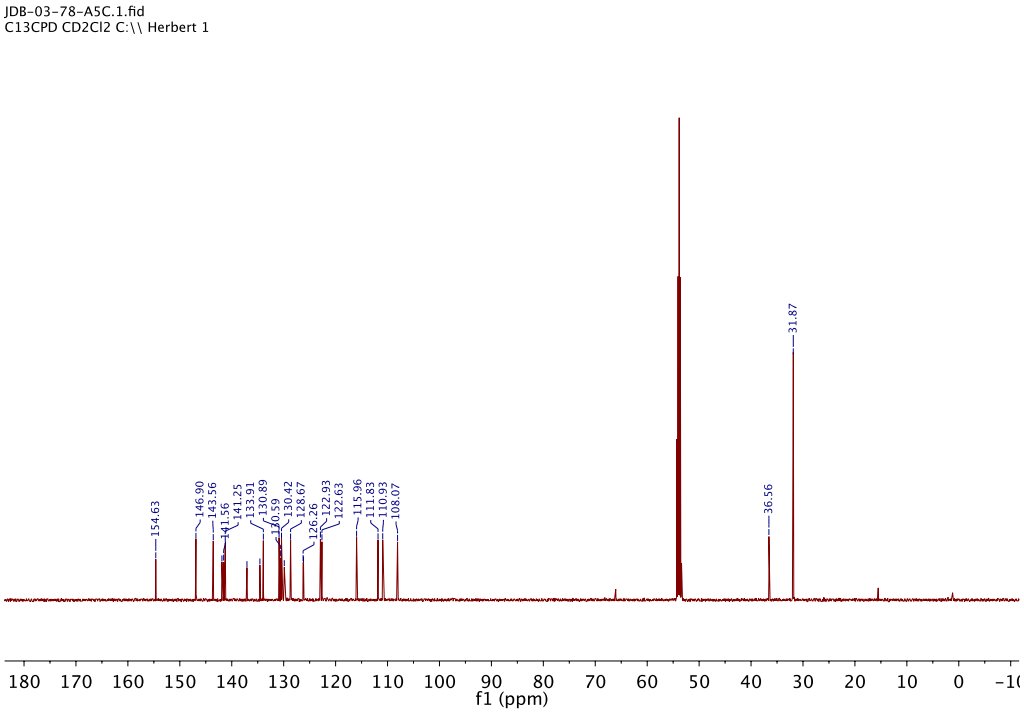

Figure S200. ^{13}C NMR (500 MHz, CD_2Cl_2, 25°C) of **[10a]**PF_6.

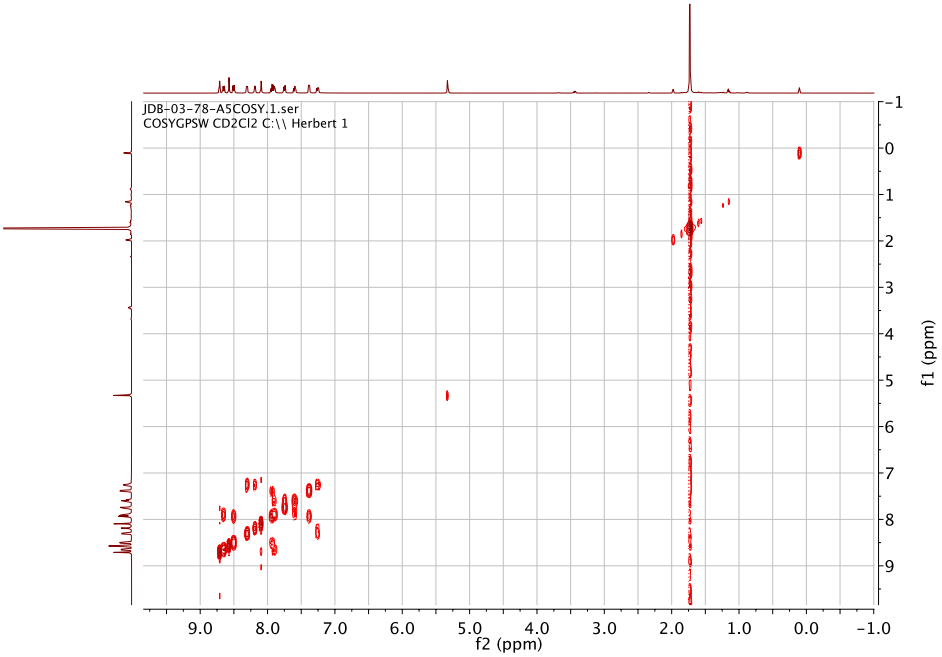

Figure S201. COSY NMR (500 MHz, CD_2Cl_2, 25°C) of **[10a]**PF_6.

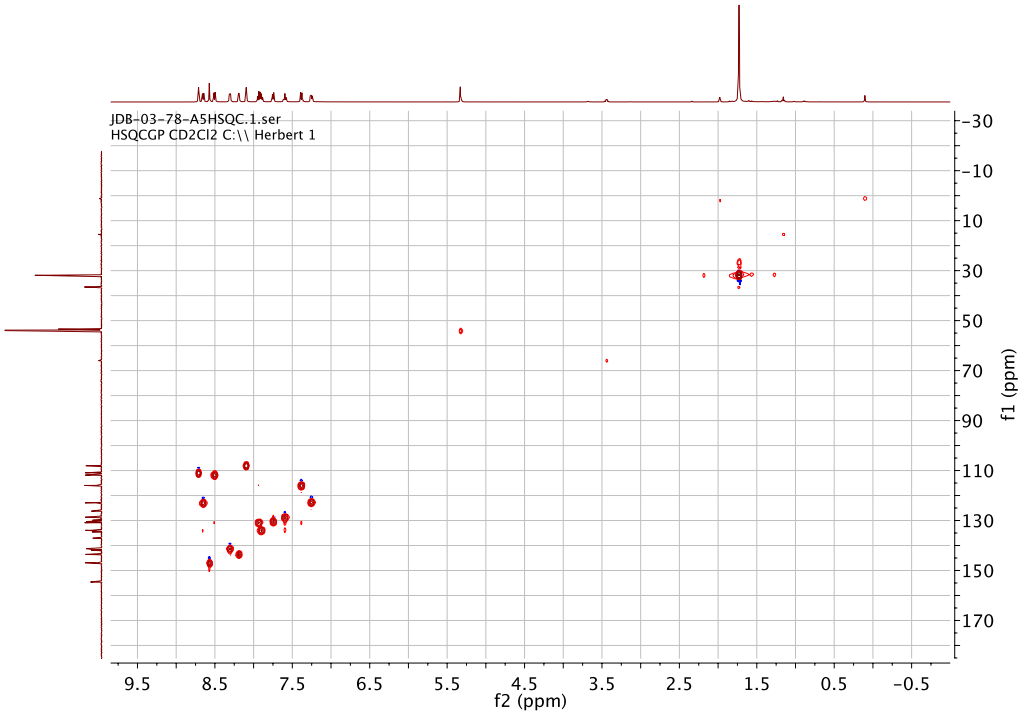

Figure S202. HSQC NMR (500/125 MHz, CD_2Cl_2, 25°C) of **[Ga(**$^{t\mathrm{Bu}}$**L)$_2$]**PF_6.

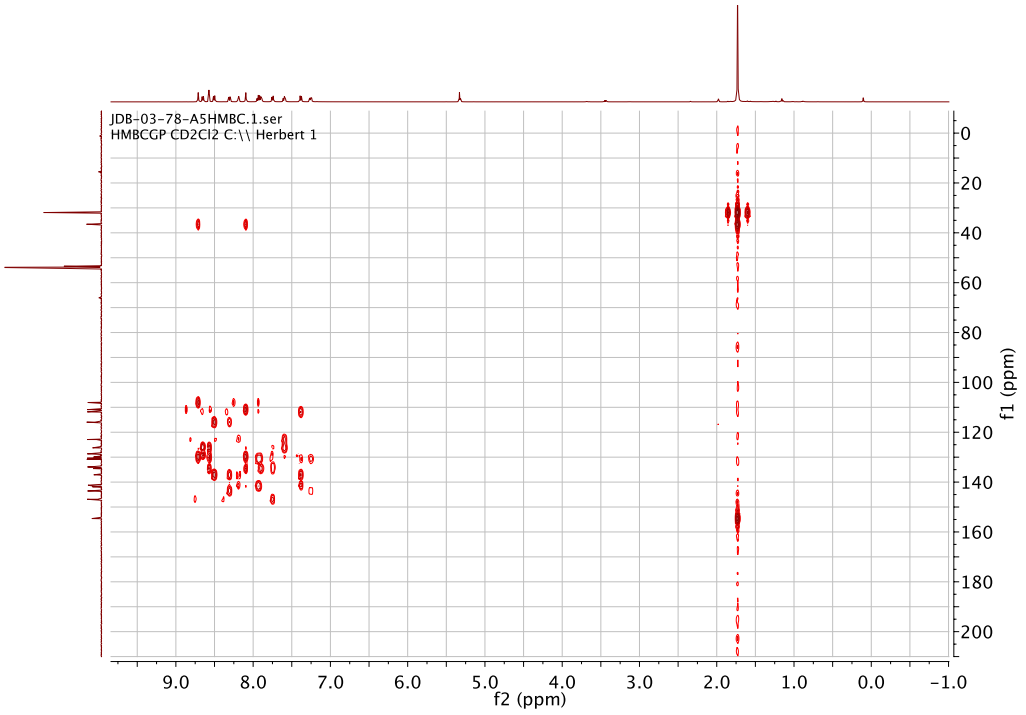

Figure S203. HMBC NMR (500/125 MHz, CD_2Cl_2, 25°C) of **[10a]**PF_6.

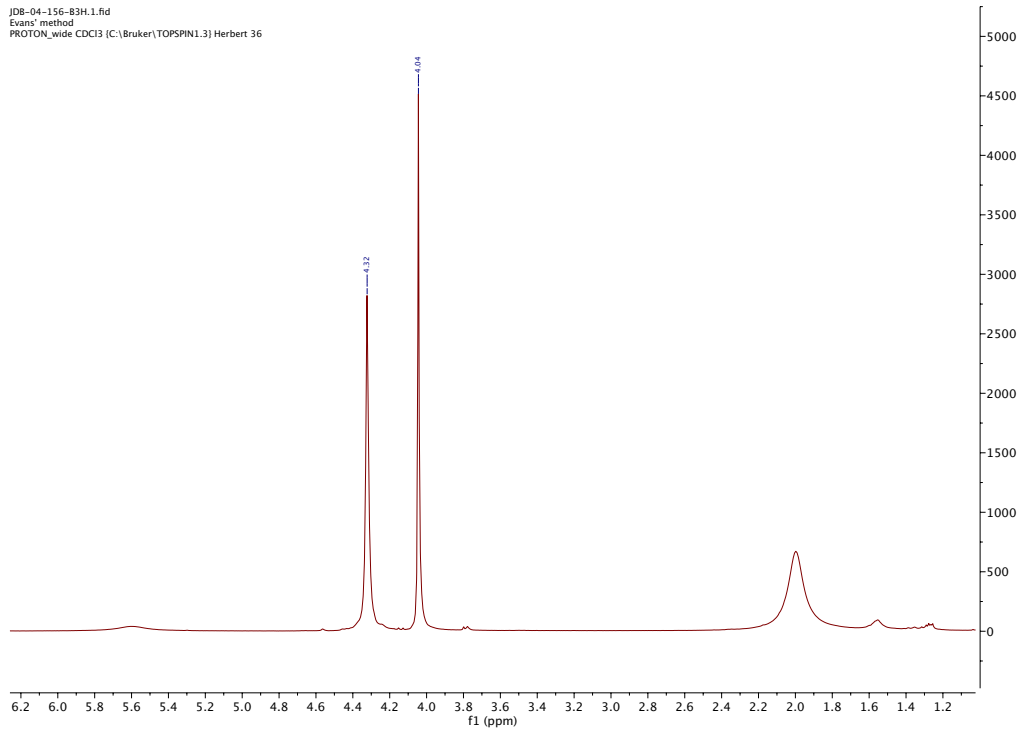

Figure S204. Evans' method NMR (300 MHz, $CDCl_3$, 25°C) of **8a**.

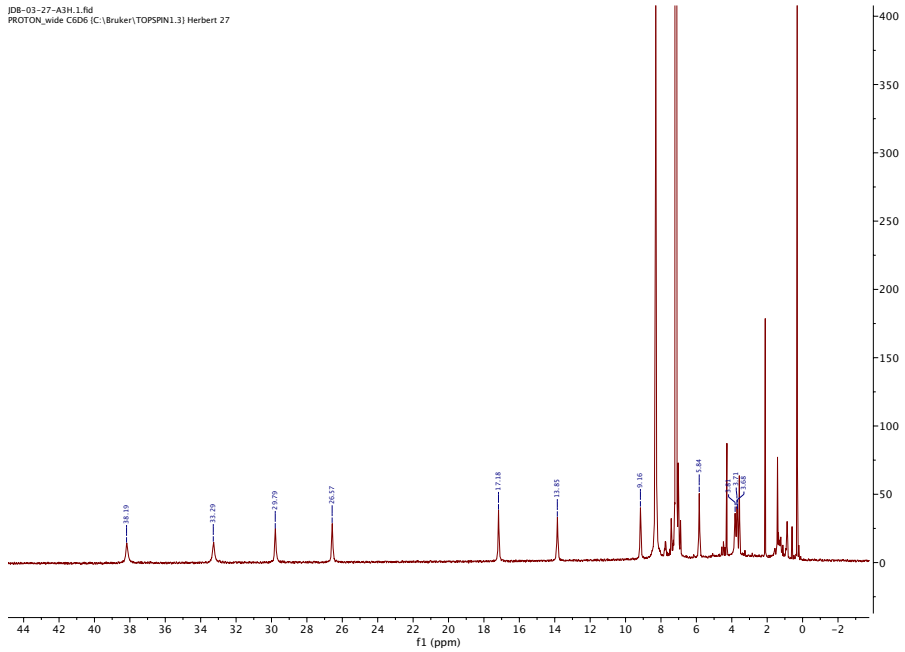

Figure S205. NMR (300 MHz, C_6D_6, 25ºC) of **7a** by reduction of **[7a]**PF_6 with $CoCp_2$

References

(1) Cabrera, P. J.; Yang, X.; Suttil, J. A.; Hawthorne, K. L.; Brooner, R. E. M.; Sanford, M. S.; Thompson, L. T. *J. Phys. Chem. C* **2015**, *119* (28), 15882.

(2) Addison, A. W.; Rao, T. N.; Reedijk, J.; van Rijn, J.; Verschoor, G. C. *J. Chem. Soc., Dalton Trans.* **1984**, No. 7, 1349.

(3) Gaussian 16 Program Package,. Revision C.01 (Gaussian, Inc., Wallingford, CT, 2016).

(4) Zhao, Y.; Truhlar, D. G. *Theor. Chem. Acc.* **2008**, *120* (1–3), 215.

(5) Weigend, F. *Phys. Chem. Chem. Phys.* **2006**, *8* (9), 1057.

(6) Marenich, A. V.; Cramer, C. J.; Truhlar, D. G. *J. Phys. Chem. B* **2009**, *113* (18), 6378.

(7) O'boyle, N. M.; Tenderholt, A. L.; Langner, K. M. *Journal of Computational Chemistry* **2008**, *29* (5), 839.

(8) Lu, T.; Chen, F. *J. Comput. Chem.* **2012**, *33* (5), 580.

(9) Martin, R. L. *J. Chem. Phys.* **2003**, *118* (11), 4775.

(10) Stoll, S.; Schweiger, A. *J. Magn. Reson.* **2006**, *178* (1), 42.

(11) Gaussian 09 Program Package,. Revision B.01 (Gaussian, Inc., Wallingford, CT, 2009).

(12) Cohen, A. J.; Handy, N. C. *Mol. Phys.* **2001**, *99* (7), 607.

(13) Ditchfield, R.; Hehre, W. J.; Pople, J. A. *The Journal of Chemical Physics* **1971**, *54* (2), 724.

(14) Hehre, W. J.; Ditchfield, R.; Pople, J. A. *The Journal of Chemical Physics* **1972**, *56* (5), 2257.

(15) Clark, T.; Chandrasekhar, J.; Spitznagel, G. W.; Schleyer, P. V. R. *Journal of Computational Chemistry* **1983**, *4* (3), 294.

(16) Rassolov, V. A.; Pople, J. A.; Ratner, M. A.; Windus, T. L. *J. Chem. Phys.* **1998**, *109* (4), 1223.

(17) Zhao, Y.; Truhlar, D. G. *J. Chem. Phys.* **2006**, *125* (19), 194101.

(18) Reiher, M.; Salomon, O.; Artur Hess, B. *Theor. Chem. Acc.* **2001**, *107* (1), 48.

(19) Harvey, J. N. *Annu. Rep. Prog. Chem., Sect. C: Phys. Chem.* **2006**, *102*, 203.

(20) Bowman, D. N.; Jakubikova, E. *Inorg. Chem.* **2012**, *51* (11), 6011.

(21) Hirshfeld, F. L. *Theoret. Chim. Acta* **1977**, *44* (2), 129.

(22) Lu, T.; Chen, F.-W. *Acta Chim. Sinica* **2011**, *69* (20), 2393.

(23) Roy, L. E.; Scalmani, G.; Kobayashi, R.; Batista, E. R. *Dalton Trans.* **2009**, No. 34, 6719.

(24) Batista, E. R.; Martin, R. L. In *Encyclopedia of Computational Chemistry*; von Ragu□□ Schleyer, P., Allinger, N. L., Clark, T., Gasteiger, J., Kollman,

P. A., Schaefer, H. F., Schreiner, P. R., Eds.; John Wiley & Sons, Ltd: Chichester, UK, 2004.

(25) GaussView v.6,. (Semichem Inc., Shawnee Mission, KS, 2016).

(26) Ashley, D. C.; Jakubikova, E. *Coord. Chem. Rev.* **2017**, *337*.

(27) Gawelda, W. *J. Am. Chem. Soc.* **2007**, *129*.

(28) Shepard, S. G.; Fatur, S. M.; Rappé, A. K.; Damrauer, N. H. *J. Am. Chem. Soc.* **2016**, *138* (9), 2949.

(29) Handy, N. C.; Cohen, A. J. *Molecular Physics* **2001**, *99* (5), 403.

(30) Hariharan, P. C.; Pople, J. A. *Theoretica Chimica Acta* **1973**, *28* (3), 213.

(31) Braun, J. D.; Lozada, I. B.; Kolodziej, C.; Burda, C.; Newman, K. M. E.; van Lierop, J.; Davis, R. L.; Herbert, D. E. *Nat. Chem.* **2019**, *11* (12), 1144.

(32) Krishnan, R.; Binkley, J. S.; Seeger, R.; Pople, J. A. *The Journal of Chemical Physics* **1980**, *72* (1), 650.

(33) Soda, T.; Kitagawa, Y.; Onishi, T.; Takano, Y.; Shigeta, Y.; Nagao, H.; Yoshioka, Y.; Yamaguchi, K. *Chem. Phys. Lett.* **2000**, *319* (3–4), 223.

(34) Yamaguchi, K.; Takahara, Y.; Fueno, T. In *Applied Quantum Chemistry*; Smith, V. H., Schaefer, H. F., Morokuma, K., Eds.; Springer Netherlands: Dordrecht, 1986; pp 155–184.

(35) Lu, T.; Chen, F. *Journal of Computational Chemistry* **2012**, *33* (5), 580.

(36) Li, Z.; Liu, W. *Journal of Chemical Theory and Computation* **2016**, *12* (1), 238.

(37) Li, Z.; Liu, W. *Journal of Chemical Theory and Computation* **2016**, *12* (6), 2517.